From Walking To Running:
Robust and 3D Humanoid Gait Generation via MPC

Sapienza University of Rome

Dottorato di Ricerca in Automatica, Bioingegneria e Ricerca Operativa - XXXV Ciclo

Filippo Maria Smaldone
ID number 1652946

Advisor
Prof. Giuseppe Oriolo

Co-Advisor
Prof. Leonardo Lanari

Academic Year 2022/2023

Thesis defended on 25 January 2022
in front of a Board of Examiners composed by:

Prof.ssa Paola Cappanera
Prof. Danilo Pani
Prof. Paolo Valigi

From Walking To Running: Robust and 3D Humanoid Gait Generation via MPC
PhD thesis. Sapienza University of Rome

This thesis has been typeset by LaTeX and the Sapthesis class.

Author's email: smaldone@diag.uniroma1.it

Abstract

Humanoid robots are platforms that can succeed in tasks conceived for humans. From locomotion in unstructured environments, to driving cars, or working in industrial plants, these robots have a potential that is yet to be disclosed in systematic every-day-life applications. Such a perspective, however, is opposed by the need of solving complex engineering problems under the hardware and software point of view.

In this thesis, we focus on the software side of the problem, and in particular on locomotion control. The operativity of a legged humanoid is subordinate to its capability of realizing a reliable locomotion. In many settings, perturbations may undermine the balance and make the robot fall. Moreover, complex and dynamic motions might be required by the context, as for instance it could be needed to start running or climbing stairs to achieve a certain location in the shortest time.

We present gait generation schemes based on *Model Predictive Control* (MPC) that tackle both the problem of robustness and tridimensional dynamic motions. The proposed control schemes adopt the typical paradigm of centroidal MPC for reference motion generation, enforcing dynamic balance through the Zero Moment Point condition, plus a whole-body controller that maps the generated trajectories to joint commands. Each of the described predictive controllers also feature a so-called *stability constraint*, preventing the generation of diverging Center of Mass trajectories with respect to the Zero Moment Point.

Robustness is addressed by modeling the humanoid as a *Linear Inverted Pendulum* and devising two types of strategies. For persistent perturbations, a way to use a disturbance observer and a technique for constraint tightening (to ensure robust constraint satisfaction) are presented. In the case of impulsive pushes instead, techniques for footstep and timing adaptation are introduced. The underlying approach is to interpret robustness as a *MPC feasibility* problem, thus aiming at ensuring the existence of a solution for the constrained optimization problem to be solved at each iteration in spite of the perturbations. This perspective allows to devise simple solutions to complex problems, favoring a reliable real-time implementation.

For the tridimensional locomotion, on the other hand, the humanoid is modeled as a *Variable Height Inverted Pendulum*. Based on it, a two stage MPC is introduced with particular emphasis on the implementation of the stability constraint. The overall result is a gait generation scheme that allows the robot to overcome relatively complex environments constituted by a non-flat terrain, with also the capability of realizing running gaits.

The proposed methods are validated in different settings: from conceptual simulations in Matlab to validations in the DART dynamic environment, up to experimental tests on the NAO and the OP3 platforms.

Keywords: humanoid, locomotion, MPC, walking, running, feasibility, LIP, VH-IP.

Acknowledgements

Contents

List of Figures

Chapter 1

Introduction

Robotics and automation are widespread in our society more than people can imagine. From washing machines to cooking and vacuum cleaner robots, one may get overwhelmed in thinking how the quality of our daily life is affected by them. Industry can see these technologies as main characters, ranging from automated assembly lines to stand alone manipulators or additive manufacturing settlements. The medical world is massively introducing robots as a standard feature, while space exploration would not be possible without employing autonomous systems.

Research in robotics has a history of decades and increases its scope year after year with new emerging hardware, conceptual problems, and application fields. This wave of progress is the reflection of a growing enthusiasm both from researchers, who are devoting their career to the area, and from industries, which are the adopters of the results of such research.

Within the numerous domains, this thesis is focused on humanoid robotics. The creation of a human-like machine has inspired humanity since the beginning of its existence. In this view, designing, building, and controlling robots that resemble humans has been a natural and challenging evolution from the first robotics engineering success stories, which date back to the sixties of the last century. Yet, at the time of writing this manuscript, the humanoid robotics field does not see a vast commercial applicability due to many limitations. Humanoid platforms are indeed not reliable enough to be deployed for continuous application in real scenarios. Their cost is too high and they need continuous maintenance. If this could be seen as a limitation under the market perspective, it constitutes a series of opportunities for researchers who spend their efforts in contributing towards the solution of the numerous problems that keep arising day by day.

One of the most challenging aspects of studying humanoids is that there is still not a global consensus on how to address basic problems such as locomotion, motion planning, and perception. The complexity of these platforms encourages the birth of new approaches to solve well established problems, even after decades of studies.

To provide an example, consider the locomotion problem, which constitutes the main theme of this manuscript and let us go through a stream of concepts. Standard bipedal (and legged in general) locomotion is only possible by manipulating the contact forces to move the body. Thus, planning and controlling contact forces is the core of the bipedal locomotion problem. At this point, typical investigations would be how large these forces should be, where and when they should be applied to reach, for instance, a certain body velocity. As intuition suggests, the complexity of the human nature

is projected and emulated by the articulated structure of the humanoid. And thus a reasonable problem would also be to choose the degree of detail that should be put in modeling the robot for planning and control. If increasing the detail yields a more physically consistent solution, it augments, on the other hand, the complexity of the problem that will have to be solved, with the possibility of rendering it not suitable for real-time implementations. This stream of questions can be considered at any level of the locomotion scope, from balancing to loco-manipulation[1].

Such a high level overview of the locomotion problem had the objective to provide a hint of the problems that will be implicitly and explicitly considered within this manuscript. Research community does not have a unified answer yet, but several trends can be identified and will be discussed when revising the state of the art.

1.1 Contribution

This manuscript focuses on two problems within the area of bipedal locomotion, namely *robustness* and *3D walking/running*, both addressed via a *Model Predictive Control* (MPC) formulation. The approach is that of representing the robot dynamics through centroidal models, such as the Linear Inverted Pendulum or the Variable Height Inverted Pendulum. Using descriptive but simple dynamics allows for a higher computational efficiency and an analytical insight on the Optimal Control Problem (OCP) that is solved at each MPC iteration.
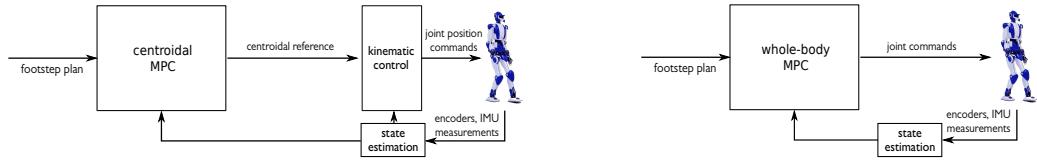
Adopting centroidal models implies addressing the locomotion problem through a hierarchical/decoupled scheme, composed by at least two stages to be solved in rigorous order: the gait generation MPC and the whole-body control block[2], which could either be a kinematic or an inverse dynamics controller. The first stage is in charge of generating the centroidal trajectories to be tracked by the subsequent whole-body controller. On the other hand, a different approach would be to adopt the whole robot dynamics for the gait generation problem, typically involving nonlinear and large size optimization problems, aiming at directly computing joint commands within a unique formulation. Such a way to address locomotion allows to take into account actuation and kinematic limits of the platform and to obtain complex and impressive whole-body motions. A basic scheme comparison can be visualized in Fig. 1.1.

Centroidal approaches demonstrated to work well on physical platforms by numerous experimental reports in the literature and industry, while the whole-body approach is a more recent research direction. As specified above, this thesis follows the first line of formulation of the gait generation problem, adopting the two stage architecture composed by a centroidal MPC and a subsequent whole-body controller. The main contribution of the work can be localized in the theoretical analyses that will be provided along with the proposed algorithms. Given the intrinsic complexity of the problem, a study on the feasibility, recursive feasibility, and stability of a MPC gait generation

---

[1]Even though a specific approach will be used in the thesis, we do not dive into the philosophical discussion on which is the best way to tackle the problem. It is interesting to notice that the discussion is not merely related to the robotics world. In fact, a general methodology in the field of biomechanics is that of addressing the complexity of locomotion through template and anchors [2]. A template is a relatively simple dynamical system describing the behavior of a body when pursuing a specific goal (locomotion for instance). The anchor is a more complex system description in charge of ensuring that the actual subject realizes the template motion. The key point of such method is the possibility to reveal basic principles that do not depend on the complex body structure.

[2]Numerous works also include a stabilization block to improve the performance [3–5].

Figure 1.1: Hierarchical (left) and whole-body (right) schemes. The hierarchical approach, adopted in this work, consists in decomposing the problem in real-time trajectory generation (to be solved first) and control, whereas the whole-body is constituted by a unique controller.

algorithm is hardly ever provided in the literature. Furthermore, the presented methods have the advantage to not require a high computational effort. All the proposed schemes will in practice consist in formulating and solving linear-quadratic problems. This allows to run the methods in low cost and computationally limited physical humanoids.

Let us now review with more detail the main topics of the manuscript.

Disturbance modeling/observation and stability conditions

The aspects that will now be described constitute a medium ground between some conceptual tools and the actual contribution of the thesis. We found that already established concepts were not totally suitable for the present research, so a re-organization and/or an adaptation of them has been required. The considered topics are: disturbance modeling and observation, and stability conditions.

A characterization of the disturbances acting on the humanoid is provided. The idea is that of grouping the possible perturbations in specific sets which will be useful to design robust control strategies. Such a characterization also allows to address the problem of disturbance observation in a way that is particularly useful for practical implementations and analysis.

A fundamental perspective that will be used in the control schemes is that of enforcing stability. To do so, stability constraints in the MPC formulation will be included and their introduction is justified by the existence of stability conditions. In a dedicated chapter this concept will be detailed and adapted to the considered models.

Robustness

Generating robust gaits is a fundamental requirement that constitutes a basic building block for any humanoid application. The word robustness is here intended as the capability of both maintaining *dynamic balance* and *internal stability* in spite of the presence of uncertainties, perturbations, and/or strong pushes. Balance will be addressed through the Zero Moment Point (ZMP) criterion, and thus, paraphrasing, the problem will be on how to guarantee that the ZMP is within the support region in the case of a perturbed gait. Internal stability, on the other hand, refers to the meaningfulness of the generated gait trajectories: the Center of Mass (CoM) must be bounded with respect to the ZMP in order to be realizable by the robot[3]. It must be pointed out that robustness shall be addressed explicitly, because, as testified by many examples both in control literature and in humanoid locomotion, a stable closed loop controller in the

---

[3]We highlight that the concept of stability in legged locomotion does not have a unique definition. It is often linked to the more general concept of viability, for instance. Further details will be provided in the manuscript.

presence of perturbations does not perform as well as a controller that is conceived for such a specific purpose.

In general, the contributions that were presented in the literature address specific aspects of the robustness problem, by for instance focusing on either impulsive or persistent disturbances, such as noise or uncertainties. In this view, an objective of this thesis is to investigate on the possibility of designing a general robustness framework which can cope with perturbations of various kind. The proposed schemes are MPC-based. They exploit the concept of *feasibility region* to manage the various kind of perturbations and to guarantee the feasibility of the MPC at all times. Being defined as the subset of the state space for which the constrained optimization problem to be solved is feasible, the feasibility region allows to introduce tools like the so-called ZMP constraint restriction that, working in conjunction with a disturbance observer, can guarantee robust recursive feasibility in the presence of bounded disturbances. Moreover, if the feasibility is lost due to a strong push, strategies for feasibility recovery can be implemented, by, for example, adapting the step position and timings. The different approaches will be initially presented as separate and later combined under a unified framework.

The robustness contents of the manuscript derive from and extend the concepts of the following works:
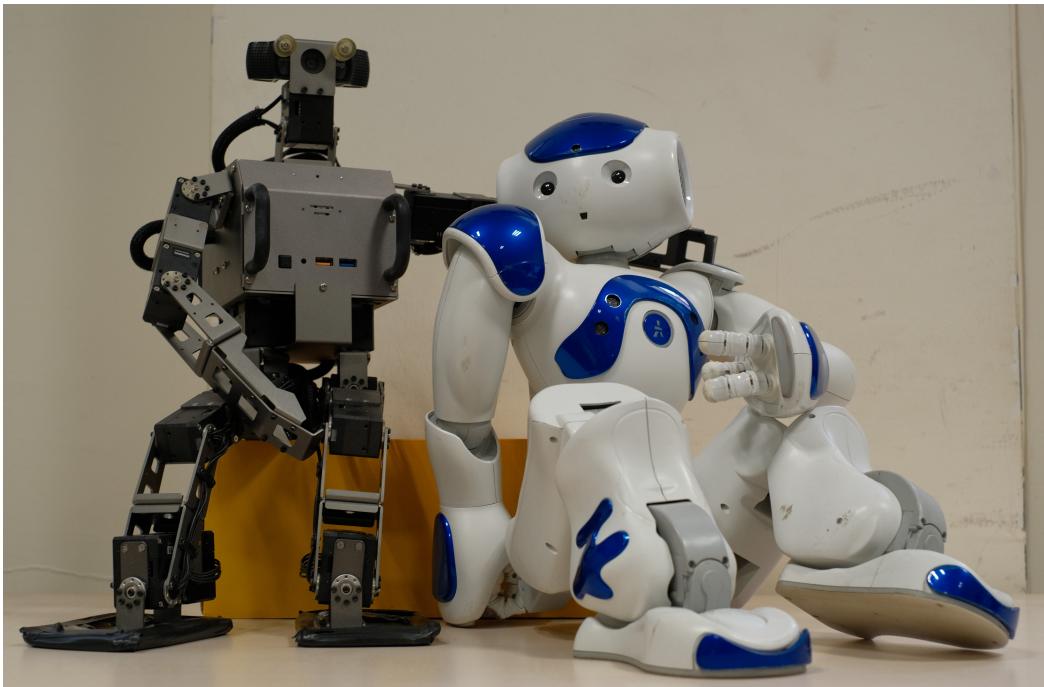
- [6], where the concept of disturbance observer-based MPC gait generation has been introduced;

- [7], where initial theoretical results on robust recursive feasibility have been provided;

- [8], where the problem of step timing adaptation has been addressed by adopting a feasibility point of view;

- [9], which presents a preliminary version of a general framework for robust gait generation;

- [10], that presents a method to handle non-convex kinematic constraints to enhance the robustness of the MPC gait generation scheme.

Tridimensional gait generation

The second aspect that has been tackled in the manuscript is the tridimensional locomotion. The presented scheme is able to generate 3D walking and running in response to an input footstep plan. Typical use cases are stair climbing or passing below obstacles as well as achieving higher locomotion velocities. The problem has been addressed with a MPC formulation using the Variable-Height Inverted Pendulum as prediction model, with particular emphasis on stability. The method is designed to allow for a linear quadratic formulation of the optimization problem to be solved at each time.

The contents of this manuscript that are related to the tridimensional gait generation problem build upon the following contributions:

- [11], where the running gait generation scheme has been introduced for the first time;

- [12], where the scheme is enhanced and explained in detail.

Figure 1.2: NAO and OP-3: the experimental platforms available at the DIAG robotics lab.

Validation

The methodological contributions have been validated following a pipeline that will now be exposed. A first implementation of the ideas is carried in Matlab/Octave. In these environments, the simple centroidal model is used for simulation, without considering the multi-body robot dynamics. This approach allows for fast prototyping, thus encouraging multiple iterations of the controller design.

As soon as the results on simple models are satisfactory, the software is transcribed in C++ to be tested in a dynamic environment with multi-body simulations. This thesis, and the related publications on which it is based on, adopts the Dynamic Animation and Robotics Toolkit (DART). The platform that has been considered for simulation is the position controlled HRP-4. Such a choice favors the use of a kinematic controller for whole-body tracking of the generated MPC trajectories.

By choosing position-based kinematic control for the simulated robots, we ensured continuity with the experimental validation of the methods, conducted on the position controlled small-sized humanoids NAO v5 and Robotis OP-3 (see Fig. 1.2). Although this phase is the most important when proposing a control scheme for robotics, not all the simulation results will have an equivalent experimental counterpart. Dynamic motions involving running, strong push recovery or leg crossing can not be achieved neither on the NAO nor on the OP-3.

1.2 Outline

The manuscript is organized as follows. Chapter 2 will present an overview of the progress in humanoid robotics technology. Historical aspects will be taken into consideration, trying to draw a critical timeline of the milestone events that brought the field to its

present state. A review of the literature related to the specific control topics of the thesis is presented in Chapter 3. We proceed with Chapter 4 that introduces the basic modeling of humanoid robots, followed by Chapter 5 in which the possible sources of perturbation that may act on the robot are discussed. Here, methods for disturbance observation are also discussed. The core concept of stability condition is detailed in Chapter 6. Chapters 7-8-9-10 present gait generation schemes that address the robustness and 3D problem. The thesis is concluded with a final discussion in Chapter 11.

Chapter 2

Humanoid robots

Rockets can be dated back to the thirteenth century. In the battle of Kai-fung-fu, the Chinese army used them against the Mongols. Thus, the idea of a propulsion engine was not a brand new concept when in 1813 William Moore started placing the building blocks of his mathematical treatment for rocket science. William Leitch then introduced the idea of using these vehicles to let humans reach the outer space. Exceptional minds in the field of astronautic theory such as Konstantin Tsiolkovsky, Robert Goddard, Robert Esnault-Pelterie, and Hermann Oberth were not inventors of a whole new branch of engineering, they were rather visionary scientists who gathered the previous knowledge, ideas and perspectives in order to expand humanity towards the sky.
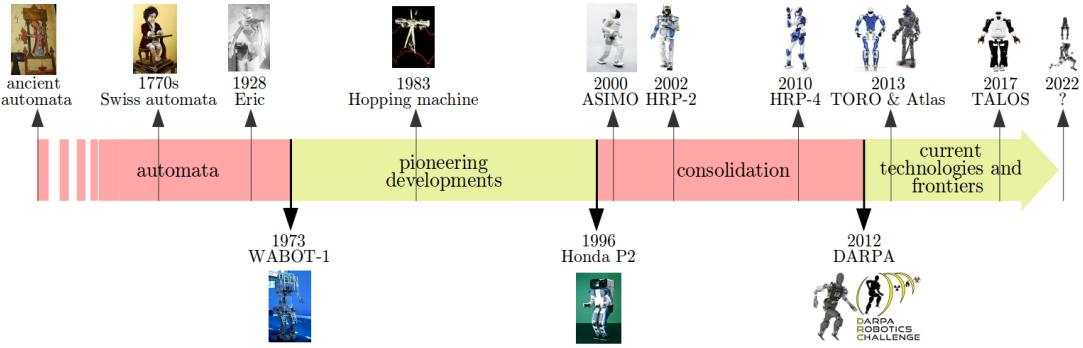
The first artificial objects in space were dated to the forties of the twentieth century, while the first man, Yuri Gagarin, reached space in 1961. Achieving a technology milestone is subordinate to years of research, wrong directions, partial findings, and failures. However, there is one concept that can summarize the whole history of human science and technology: if people can imagine something, this would most likely be realized. No matter when, but one day the goal will be reached in spite of its complexity, and each goal will constitute the starting step for new findings.

Imagination, ideas, and out-of-the-box thinking are fundamental components of the progress. Humanity defines itself within this process and keeps everyday building the world of the future.

The field of humanoid robotics perfectly fits within this description. Trying to mimic with artificial components the perfection of the human body is a gigantic problem, that only the resourcefulness of mankind can face. The scope of this thesis is a specific subset of the vast humanoid robotics area: bipedal locomotion, i.e., a basic requirement for employing humanoids in real world applications. Yet, something that we as humans consider trivial and natural is a rather challenging engineering problem, that will be addressed in this manuscript under a control perspective.

Before analyzing the methodological state of the art concerning the locomotion topic, we believe that providing a technological context would be useful and interesting. This chapter consists in a wide-range overview on the technical development with the following purpose: drawing a sketch of the history of humanoid robotics, trying to understand the process that led to its current status.

We invite non-interested readers to skip this chapter, as it will not contain details on the contribution of the thesis. To provide a summary to those who will not proceed with the reading of it, a time-line is reported in Fig. 2.1. For the convenience of exposition, the treatment is divided into five main time periods: i) the age of automata, ii) pioneering

Figure 2.1: Timeline that briefly wraps up the humanoid robotics development treated along this chapter. Above the line, famous instances are reported, while technology milestones separating the different phases are placed beneath of it. The final period of time unifies both the current technologies and the frontiers of the research, constituting the new generation of humanoids. These two periods are blended as there is not a specific event that can be chosen as a symbolic separation of them.

developments, *iii*) consolidation, *iv*) current technologies and *v*) the new generation.

The age of automata gathers all the attempts conducted throughout history to construct moving machines with human shapes. History is variegated and there is not a unique document that constitutes a univocal beginning of it. For instance, some examples from Greek world will be provided, as well as the famous Swiss automata or metal men used for public expositions, dated back on the beginning for the twentieth century.

The first event that was chosen in this chapter as a turning-point for the subsequent phase is the public presentation of WABOT-1 in 1973, considered as the first full sized programmable legged humanoid. Such a robot launched twenty years of pioneering developments that prepared the ground to the a subsequent and even more influential turning-point, i.e., the public presentation of Honda P2 in 1996. This platform, which later evolved into ASIMO, demonstrated to the world the capabilities of a well built and engineered humanoid, generating enthusiasm and motivation in researchers (and also in the general public). For fifteen years after that point, the progress in the field has become exponential; the number of robots has increased substantially while new research groups in the world have been constituted to start contributing to the advance of such technology. We identify this picture as a consolidation phase, where humanoids became widespread as fundamental research assets in the world.

The subsequent turning point was chosen to be the beginning of the DARPA robotics challenge, launched in 2012. The competition consisted in accomplishing tasks with a robot in "dangerous, degraded, human-engineered environments" and most of the teams participated with humanoid robots. Considering the tremendous mass exposition of the event, this turning point had a double effect. If on one side it further pushed the enthusiasm towards the field by allowing for the consolidation of what are de facto the current humanoid technologies, it also contributed to concretizing the feeling that the technology was not mature enough for practical applications. Since that moment in fact, research on humanoids started focusing more on the limits of the platforms. It is not anymore a matter of feasibility but rather the issue of rendering the technology mature and reliable enough to be deployed in the real world. And this is the point where we are now.

2.1 From the world of ideas...

A long time ago

Robotics begun with a history of ideas and imagination, that started way before than its first successful applications of the twentieth century. Mechanical animals and moving statues were already present in the primordial Jewish mythology. Automata from ancient Greek history are then considered as the first documented examples of machines that were able to execute actions without direct human power. Hero of Alexandria, Ktesibios and Philo of Byzantium were renowned inventors that built these objects, comprising for instance a maid that was mechanically able to pour wine in a cup.

Since then, people have continued building automata throughout history. We can remember the "Book of Ingenious Devices" published in 850 and written by the Banu Musa brothers and the "Book of Knowledge of Ingenious Mechanical Devices" from Al-Jazari, dated to 1206. The latter in particular testifies with detailed descriptions the outstanding achievements of the epoch in automaton development.
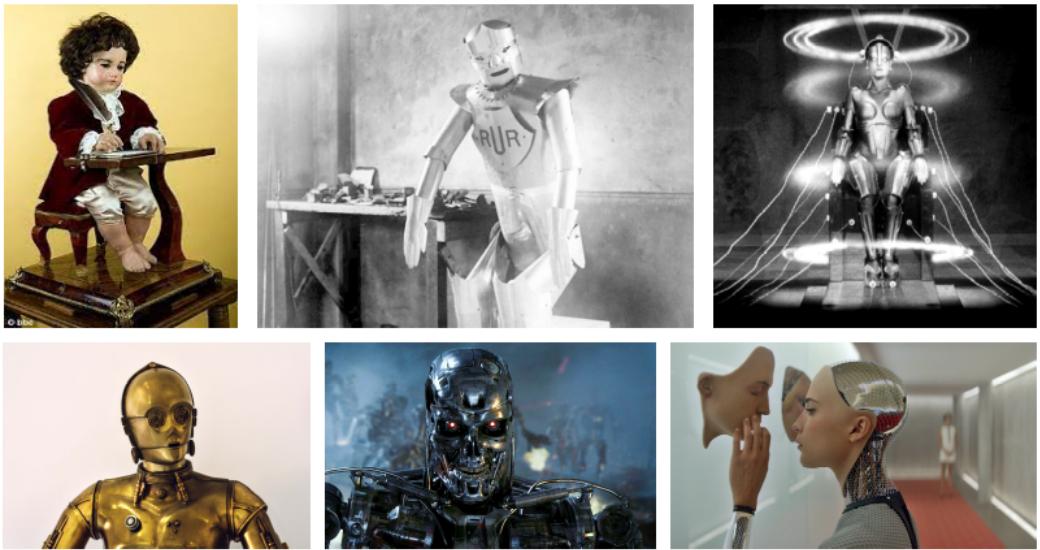
It must be highlighted that the vast majority of these early inventions is related to entertainment. The book of Al-Jarari reports on machines that are "suitable for drinking sessions" as well as on "fountains and musical automata" [13]. This trend, dated back to the Greek inventors, has been propagated throughout the years: from Leonardo da Vinci armored knight [14], passing by the 16th century clockwork monk automaton by Januelo Turriano, to the school of Swiss watchmakers in the 19th century (see Fig.2.2), that was capable of producing mechanisms able to draw or write poems stored in their mechanical memory, composed by gears and springs [15], [16].

A common and underlying feature of automaton history is the attempt in reproducing the human physiology with a machine. This idea itself was a source of wonder and a curiosity stimulus for the public. The common feeling was that the perfection of the human body deserves an effort in studying and replicating it through drawings, paintings, statues, and even moving machines.

Allowing for a pindaric flight, we report an excerpt from an archive newspaper as a concrete example of this general sense of wander. The occasion is the public presentation of Eric the robot in New York. On Wednesday, May 15th of 1929, The Morning Herald wrote: "A great sensation was caused recently in New York by a marvelous mechanical creation vaguely resembling a Knight of the Round Table in full armor, speaking with a voice of a man and so arranged mechanically as to rise, sit and move his arms and legs. It is Eric Robot, with electric eyes...". People in the streets were overwhelmed. The robot, an aluminium composition of armor like parts, was designed and constructed in 1928 for the opening of the exhibition of the Society of model engineers in London. As it can be seen in Figure 2.2, it had three letters engraved in the front of his chest: R.U.R, in honor of the Karel Capek play which is universally considered as the origin of the world "robot".

Science fiction and toys as inspiration

Focusing on humanoid robots, it is interesting to notice that they are part of a common science fiction imaginary, built by novels and movies. Popular culture and media streams indeed play a major role in the social perception of robotics [17] as well as on its development. Shapes blend one in another: the similarity between the humanoid from Metropolis by Fritz Lang and Eric the automaton is undeniable, see Fig. 2.2.

Figure 2.2: Top: The writer Swiss automaton (around 1770), Eric the robot (1928), The Machine Man from Metropolis (1927). Bottom: C-3PO from Star Wars(1977), T-800 from Terminator (1984), Ava from Ex Machina (2015).

Ranging from the Isaac Asimov to Philip K. Dick with its reknown "Do Androids Dream of Electric Sheep?", humanoids have been used as active characters for incredible stories. This inevitably increased the idealized perception of the general public regarding them (and robots in general). Sci-fi authors would see the technology as either a benefit or a course for mankind, spanning from enthusiasm to an uncomfortable view of the future, and providing interesting food for thoughts[1]. The visual impact of cinema, on the other hand, provided further examples of: funny assistants, as C-3PO from Star Wars, human hunters as T-800 from the Terminator, and even disturbing rounded and complex characters such as Ava from Ex Machina, see Fig. 2.2.

Commercial products also contribute towards the gathering of a common robotics imaginary, helping in the definition of a culture. Between the end of 2019 and the beginning of 2020, a robotic exposition took place in Milan [18]. The theme was companion automata. World famous robotic toys were exposed, as the WowWee Robosapien, the Sony Aibo or Digital Dream Lab Vector (former Anki Vector), with the aim of entertaining and amusing visitors. A group of Ubtech Alpha 1S was executing synchronized dances each hour, replicating the same performance known to the public due to a famous Italian TV advertisement. Not only kids were attracted by the exposition: adults re-discovered their childhood dream toys. The exhibition had the objective to celebrate humanity though its capability of imagination, communication and enthusiasm towards the technology. A marginal but interesting detail is that the recurring shape of the exposed robots was human-like.

The underlying claim of this section is that the engineering field of humanoid robotics has a solid cultural, social, and historical background which should not be separated from the technical world. Researchers in the field, while having the delicate goal to establish the fundamentals of a new technology, should also keep in mind the potential

---

[1]Examples: the positive perspective of Star Wars, where humanoids and robots are integrated in the society, and the dramatic point of view presented in Blade Runner, where replicants are more humans than humans.

social impact of their work in shaping not only the concrete future lives of people but also their imaginary.

2.2   ... to the pioneering developments

The first humanoid

Leaving the sphere of automata, entertainment, and imagination, we now focus on the early innovations that opened the path for the field. The first programmable full-sized humanoid robot that was built is WABOT-1 (see Fig. 2.3), developed by a multidisciplinary team lead by professor Ichiro Kato. This pioneering project conducted in Waseda University is considered as the engineering ancestor of contemporary humanoid robots [19, 20]. The idea was to design and implement a multi purpose and versatile system, able to walk, communicate and localize. The first prototype was completed in 1973. At the time, the construction of a programmable humanoid robot was an important challenge perceived within the the idea of replicating human beings through machines. Indeed, professor Kato and his colleagues wrote fourteen years after the completion of the prototype that "It was estimated that the WABOT-1 had the same mental faculty as a one-and-a-half year old child" [19][2].

The WABOT project continued, leading to WABOT-2 (see Fig. 2.3) the anthropomorphic keyboard player that was first presented at the Japanese expo in 1985. This second version was instead a single purpose robot, as it was specifically designed to read the music score and execute it on a keyboard.

Advances through various platforms and concepts
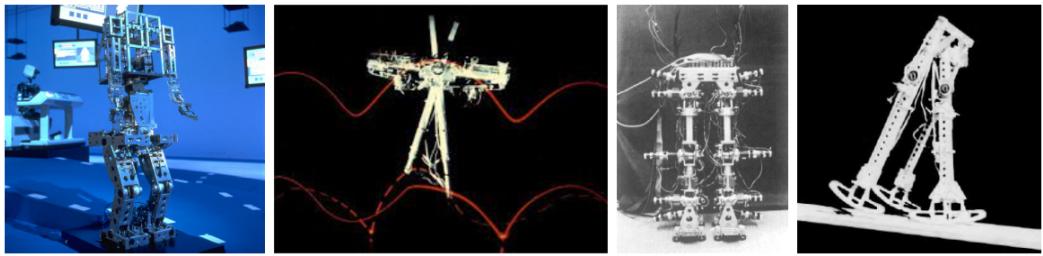
Meanwhile the efforts in theoretical research conducted to the development of ideas and approaches that are still fundamental nowadays. For instance, focusing on the scope of this thesis, the concept of Zero Moment Point for legged locomotion was introduced by Vukobratovic in the late sixties [21, 22].

Impressive hardware and theoretical results were achieved by Marc Raibert, well documented within its milestone book "Legged Robots That Balance" [23]. Raibert started his investigation in 1979 with the construction of an automatic pogostick, that was subsequently improved to the well known hopping machine, see Fig. 2.3. According to Raibert, investigating on legged locomotion was necessary to design machines with improved mobility in rough environments, able to overcome obstacles and to decouple the effect of the terrain on carried loads. He also claimed that addressing the problem under a control perspective would improve the physiological comprehension of human and animal locomotion. The findings of Raibert are still used in the current humanoid (and legged locomotion in general) research: his general ideas are building blocks for motivating legged locomotion research, while some of his control laws have been adopted in various subsequent developments [24–27].

Between the eighties and the nineties, several further results were achieved both in control [28] and hardware implementations of biped robots. We can recall the

---

[2]The peculiarity of this sentence is the willing of the authors to project the technological capabilities of the robot to a human perspective, testifying a sense of wonder of the described technological breakthrough. It would be rare, according to the personal opinion of the author of this thesis, to deduce such a sensation from a contemporary scientific publication.

Figure 2.3: WABOT-1 and WABOT-2 (1973-1986), Raibert hopping machine (1983), biped machine (1992), Passive dynamic walker (1990).

Biper-3 and Biper-4 four degrees of freedom platforms [29], characterized by peculiar ski-like feet to maintain static stability. On the other hand, the biped walking machine adopted in [30, 31], shown in Fig. 2.3, had six degrees of freedom for each leg, i.e., the same kinematic configuration that is nowadays adopted in most of the humanoids. Then, Kajita and his colleagues built a biped with parallel link mechanisms for motor transmission in order to concentrate the mass of the biped (mainly due to the motors) in its body [32], that was extended to the twelve degrees of freedom Meltran II, presented in [33]. They also put in light the effectiveness of addressing the gait generation problem by using simplified models [34].
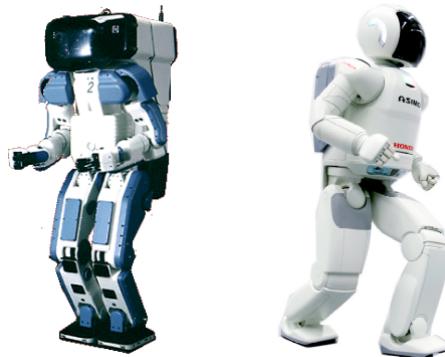
A different investigation was conducted by McGeer [35], who analyzed in detail passive walkers, see Fig. 2.3. These platforms, without control effort and only thanks to their dynamics, can reach a steady state gait similar to that of humans when walking on a proper incline. Studying the motions of a simple and unactuated mechanism allowed for deep analyses [35], opening path for applications to bipedal locomotion control.

2.3 Consolidation

The role of Honda

A wave of enthusiasm towards humanoid robotics derived from the impressive project conducted by HONDA[3]. The company started working in secret on the P series 1986 and the first public demonstrations was only in 1996, followed by contributions in the scientific literature, e.g., [37] where the Honda P2 was described in detail. The idea that moved the company was to add value to human society, by offering a robot oriented at domestic help and elderly care. The objective was to develop a fully autonomous humanoid to operate in known human environments, with the possibility of being tele-operated if necessary. For this reason, the machine was human-sized. P2 was in fact 1.82 m tall, weighted 210 Kg and had 30 degrees of freedom in total, see Fig. 2.4. An advanced control architecture for balancing and locomotion was implemented, involving ZMP, foot landing and body inclination control, that allowed the robot to climb and descend stairs, walk on slopes and carry a 5 Kg payload. Further developments of the project lead to the well known ASIMO (Advanced Step in Innovative MObility) robot [38], see Fig. 2.4, capable of both reliable locomotion and perception. ASIMO was used for extensive demonstrations [39] that increased its fame worldwide as well

---

[3]The vast majority of scientific papers that present new humanoids developed within the first decade of the 2000s refers to the HONDA humanoids as a "trigger" for humanoid robotics research. See for instance [36].

Figure 2.4: HONDA P2 (1996) and ASIMO (2000).

as the public perception of humanoid robotics apart from research laboratories. They suddenly stopped being science fiction characters and became actual machines.

This breakthrough technological demonstration opened the doors for a series of hardware advancements in the field, made by both private companies and public research institutions. Humanoid robotics is by definition a cutting edge technology for which it is required a dense cooperation between academia and industries.

To organize the following treatment, the size of the humanoids will be used as a grouping criterion. According to the author of this thesis in fact, the humanoid size is a fundamental aspect, possibly more determinant than the application for which the robot is conceived. Note that this statement regards the sole consolidation phase of humanoid robotics technologies. As argued in [40], the purpose of the humanoid is also a determinant criterion that leads the choices its design. A similar organization, in fact, will be adopted in the next section. Several authors group humanoids into large, medium and small size [41, 42]. Large sized are those which have the size of an adult human, medium sized of a child, and small sized of around 0.5 meters.

Large and medium-sized humanoids

Large and medium size humanoids require a not negligible economic effort, in terms of hardware components and highly specialized workforce for mechanical and software design. Humanoids have always been conceived as human co-workers, thus requiring to have a height that is comparable to human-targeted spaces. Multiple research oriented projects, that have been conducted from the late nineties up to the first decade of the 2000s, followed this idea.

In 1999 the large size WABIAN humanoid, developed at Waseda Univeristy in Tokyo, was presented [43]. It weighted 107 Kg and was 1.66 m tall. The project later evolved in WABIAN-2 [44], a shorter, 1.53 m, and lighter, 64.5 Kg, platform. These robots were conceived for both engineering and physiological research. A humanoid could in fact be used for testing new algorithms and for acquiring data on kinematic and dynamic quantities that would not be directly measurable on humans, e.g., the required joint torques to perform a motion.

Started in 1998, the long lasting Humanoid Robotic Project had its begin, sustained by the Ministry of Economy Trade and Industry of Japan, brought to the development of platforms that constituted a milestone for humanoid robotics research. It begun with Honda as industrial partner (the platform HRP-1 is an enhanced version of Honda

Figure 2.5: HRP-2 (2002), HRP-4 (2010), Lola (2009), Kojiro (2007).

P3), later substituted by Kawada Industries, and saw the participation of various research institutions such as University of Tokyo and KAIST. The project had the objective of enabling humanoid robots to work in "maintenance tasks of industrial plants, tele-operations of construction machines, human care, security services of home and office, and cooperative works in the open air" [45]. The developed platforms were light and compact (typically being less than 1.5 m tall and weighting less than 50 Kg). Their usability and reliability was improved by the companion simulator OpenHRP [46] that facilitated software development. Overall, the most worldwide famous platforms developed within the HRP project are HRP-2 and HRP-4 [47], see Fig. 2.5.

The HRP project has also addressed several unusual but fundamental aspects related to humanoid robotics. For instance, HRP-3 was constructed to be dust and waterproof, for actual deployment in real-world applications [36]. Other platforms explored the concept of design itself, trying to answer the question "How should a humanoid look like?". A professional mecha designer for comics and animation, Yutaka Izubuchi, was in fact hired to draw the chassis of HRP-2 [46], which was later used also for artistic dance applications [48]. HRP-4C, on the other hand, was conceived as a cybernetic human, designed to resemble a young Japanese female [20]. As opposite to the majority of humanoids, this robot has articulated feet, allowing the researchers to implement physiological walking gaits [49].

We also recall that the HRPs were used to validate, both in simulations and experiments, the conceptual developments of bipedal locomotion that have been fundamental for this thesis, i.e., ZMP preview control and MPC-based gait generation using the Linear Inverted Pendulum model [45, 50]. Moreover, they are still being upgraded and adopted by several research institutions (Japanese and European) [51–55].

Other academic projects also contributed to the advancements of large size humanoid robotics technologies under various aspects. Hubo, developed at the Korea Advanced Institute of Science and Technology (KAIST), was the output of a research focused on adopting low cost components (by preferring commercial rather than custom parts), high rigidity, and simple kinematics [56]. To improve the maneuverability of the platform, the limbs were sized to concentrate the Center of Mass at the torso of the robot. This idea was also implemented by the researchers from Technical University of Munich who designed Lola [57], which, similarly to HRP-4C, has a joint between the forefoot and the heel, see Fig. 2.5. In University of Tokyo, the H7 project was conducted to explore

motion planning and autonomy [58]. On the other hand, iCub from the Italian Institute of Technology (IIT) [59] was conceived as a platform for research in cognitive robotics and human robot interaction.

From private companies we can name Mahru III from Samsung [60] and Reem-B from PAL Robotics [61]. The latter was contrived as a product, i.e., an object that any research institution could buy and conduct its research on. The effort of PAL was oriented in the realization of a reliable and easy to use robot. The company focused then on long battery duration, reaching up to 120 minutes of continuous operation, and autonomy. The latter was intended in the sense that the robot must be able to fully perform its computations online and to reliably localize by only exploiting on board sensing. To this purpose, the platform was equipped with a laser finder on each foot.

Different hardware perspectives have also been investigated. Musculoskeletal structures would allow in principle to exploit the typical synergistic action that continuously happen between antagonistic muscular pairs. This idea motivated the development of Kotaro and Kojiro (see Fig. 2.5) in University of Tokyo by part of the H7 team [62] and successively of Kenshiro [63]. The potentiality of wire actuators towards more physiologically oriented motions in humanoids is enormous, with possible applications in human data retrieval and active car crash tests[4]. However, the hardware implementation and control problems arising from this design choice have discouraged their massive diffusion[5].

Small-sized humanoids

The expensiveness of building a full sized humanoid encouraged the effort of several institutions and companies to construct small sized platforms. To provide a concrete idea on the dimensions, these robots ranged from 0.3 to 0.7 m, weighting at most 9 Kg [64]. The spirit behind such projects was clear: the robot PINO [65], inspired by Pinocchio in its design (see Fig. 2.6), was ironically named by its developers (Kitano Symbiotic Systems Project, Osaka and Keio university and Sony Computer Science Laboratories) as "The Poorman's humanoid project". These kind of robots were built with low cost commercial components, forcing the developers to focus on the software to obtain a reliable performance. Results were in some cases promising, yielding the commercialization of the platform and its mass distribution. Robot PINO was for example converted in a toy and sold to the public by the company ZMP INC, the same happened for Robi [66] characterized by its social skills and its peculiar locomotion engine.
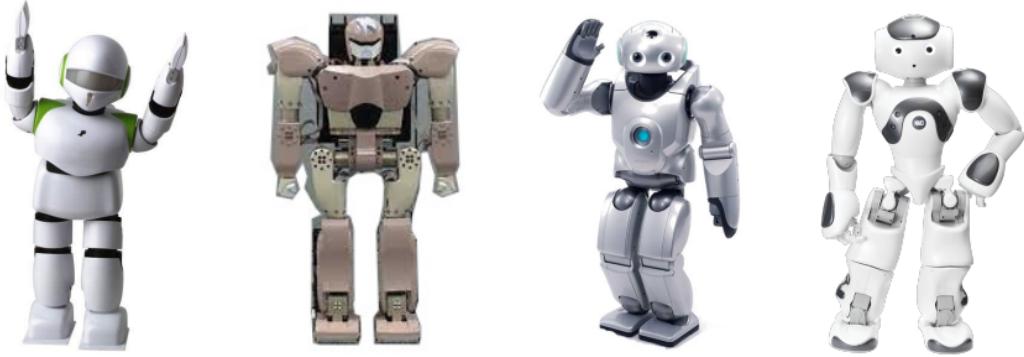
Other platforms worth to be named were the ESYS series [67] by Kitano Symbiotic Systems Project and Aoyama Gakuin University or the UT-μ series from Kyushu University and University of Tokyo [64], see Fig. 2.6. However, the most remarkable results in terms of performance and reliability were obtained by Sony with QRIO and Aldebaran (later acquired by SoftBank Robotics) with NAO.

The expertise that Sony Intelligence Dynamics Laboratory gained in the entertainment project of the Dream Robot, which featured an advanced motion control and the custom actuators SDR-3X, was used to produce QRIO, a 0.6 m tall humanoid that

---

[4]Mannequins are typically adopted. Employing instead an active humanoid would provide a deeper insight on the crash event.

[5]To have a quantitative comparison, the body of Kenshiro has sixty four degrees of freedom. Standard humanoids would approximately range between twenty and thirty.

Figure 2.6: PINO (2000), UT-μ mighty (2005), QRIO (2003), NAO (2006).

weighted 7.3 Kg [68], see Fig. 2.6. Beside the common sensors available in humanoids, it featured accelerometers at the feet, which were also embodied with force sensors. This, together with the improved SDR-4X actuators, allowed for impressive motion control, comprising choreography, stair climbing, running and roller-skating [69]. QRIO was the most advanced small sized humanoid of its time (beginning of the 2000s): its level of engineered integration and its high profile performances in public demonstrations are still nowadays hard to replicate. However, the robot did not have a large distribution as it was only used for corporate advertisements and a reduced set of research projects [70, 71].

On the other hand, NAO (see Fig. 2.6) had (and has) a greater fortune. Its low price and its large scale production allowed for mass distribution between academia, e.g., for the Robocup league or scientific research, or even to the public. It is in fact the most advanced biped humanoid in terms of hardware and software that can be purchased and used by privates at the time of writing this manuscript [72].

2.4 Current technologies

In a span of fifteen years, the effort of various research groups around the world advanced and investigated humanoid robots up to the point in which, de facto, the human species gained the knowledge on how to build a working machine similar to itself. Impressive demonstrations were showcased in scientific publications and in dissemination events, testifying a consolidated and mature technology. Major theoretical advancements accompanied this evolution contributing to the solidity of the field. Yet, at the beginning of the 2010s it started being clear that the reached level of maturity was not enough. Humanoids could not be deployed in controlled industry environments or in disaster areas. To give an example, no robot could be used to provide a concrete help immediately after the Tohoku Earthquake [52]. Furthermore, the majority of humanoids could not interact safely with humans, due to their structure and motor stiffness (mainly position controlled). They were also lacking of robustness during locomotion, compliance, capability to perform dynamic motions, modularity, ease of maintenance. Acknowledging these limitations triggered a brand new series of major developments, which is continuing nowadays.

According to the personal view of the author, it makes more sense to organize the treatment of this section based on conceptual areas rather than the size of the

robot. Exploring the possibility of building a humanoid was the topic of the previous section. With a general consolidation of the field, such perspective started waning at the end of the first decade of the 2000s. If in fact the previous question was "can we build a humanoid robot?", starting from the beginning of $2010s$ the question has been transformed into "how should we build humanoids so that we can actually use them in the proper context?".

The DARPA robotics challenge

The interdependence between academics and industries kept consolidating at the point that it became a mandatory requirement to construct a platform that can comply with the advancements obtained after almost thirty years of dense research. The need of providing a concrete extent to humanoid robotics development started to become more and more felt by researchers and companies. Competitions and large scale projects were launched for this purpose.
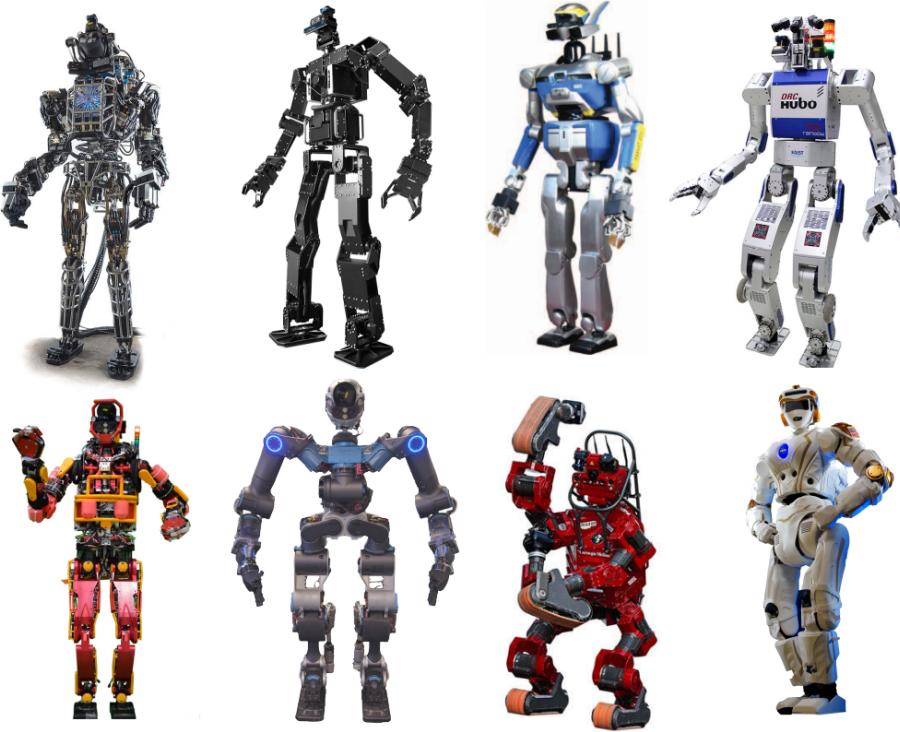
The most famous for both researchers and the general public is the DARPA robotics challenge. Launched by the US Defense Advanced Research Projects Agency in 2012 and concluded in 2015, the project had the objective to boost the progress in semi-autonomous robot deployment for disaster response. In order to score points to win the competitions, the teams had to make their robots (remotely guided by an operator that could only get information from on-board robot sensors) succeed in several tasks such as climb an industrial ladder, open a door and enter a building, close a valve, and drive a vehicle. Some of the major robotics groups in the world took part in the competition which forced them to design advanced solutions for complex real-world problems.

Twenty five were the teams participating in the finals held in California on the 5th and 6th of June 2015. Team KAIST from Korean Advanced Institute of Science and Technology won the competition, scoring all the points in the shortest amount of time.

Although the specifications from DARPA were exclusively task oriented and there was not a mandatory shape for the robot, the vast majority of the platforms were actively balanced humanoids. A task to complete was for instance climbing a ladder, i.e., a typical problem that is easier to solve with a legged robot. Developing a humanoid from scratch is hard, expensive and time consuming. For this reason, seven teams adopted the Boston Dynamics Atlas provided by DARPA, see Fig. 2.7. Other teams used their own platform, adapted from on going research and/or industrial products, such as like THORMANG from Robotis, HRP-2, and Hubo, see Fig. 2.7.

Let us now briefly review some of the participant teams. Team THOR from UCLA chose the humanoid THORMANG [73] for its hardware modularity, composed by commercially available components, such as the Dynamixel actuators. JAXON (Fig. 2.7) was developed in Japan and adopted by the two NEDO companion teams [74, 75], based on the previous research platform STARO. It featured powerful actuators with a joint water cooling system to support long lasting applications and a shock absorbing structure, to be resistant to fall or impacts with the environment. Team AIST participated with an improved version of the well known HRP-2, called HRP-2Kai (Fig. 2.7). The Italian Institute of Technology joined the competition with WALK-MAN [76], an on-purpose developed humanoid, based on the principle of compliance thanks to state of art Series Elastic Actuators, see Fig. 2.7.

The underlying principle that brought to the choice of these type of platforms was that a robot should be structurally similar to a human worker, with two arms and two

Figure 2.7: Atlas (2013), THORMANG (2014), HRP-2Kai (2015), DRC-HUBO+ (2015), JAXON (2015), WALK-MAN (2015), CHIMP (2015), Valkyrie (2013).

legs to perform well in human environments. It should in fact be able to use all four limbs for task execution and locomotion, and be able to get up after an accidental fall.

This idea, although well grounded in practice, did not allow for success. The overall results testified that humanoids were not yet reliable enough. Active balance was in fact a major issue during operations. Several videos in the web from the DARPA competition report humanoid falls during both locomotion and manipulation which involved interaction with the environment. In many cases, the combination between sensing, acting, and hardware configuration did not allow for success.

To prevent this problem, various teams participated in the competition with platforms that were able to passively balance and were also designed to succeed in typical legged robot-oriented problems, like stair climbing. Team RoboSimian proposed an architecture that could both achieve wheeled and crawling locomotion [77]. The robot had four general purpose limbs with seven degrees of freedom each. Four wheels were attached to them so as to be capable of switching to wheeled locomotion when necessary. Team TARTAN Rescue from Carnegie Mellon University developed CHIMP (CMU Highly Intelligent Mobile Platform) a statically stable mobile manipulator which used trailers for locomotion [78, 79] and was capable of stair climbing and passing over debris, see Fig. 2.7. The overall winning team, Team Kaist, participated with DRC-HUBO+ [80, 81], a platform based on its conceptual parents HUBO-1 and HUBO-2. It was a bipedal humanoid capable of a dual-mode locomotion: by squatting, it could reach a posture where two wheels could guarantee static stability during motion.

Compliance and torque control

Several were the research directions triggered by DARPA robotics challege. Many groups maintained the standard kinematic structure of the renown humanoids (ASIMO, HRPs) while focusing on compliance. COMAN by the Italian Institute of Technology was for instance built using joints endowed with torque sensors to enable active torque control and series elastic components for passive compliance. The inherent mechanical compliance of the platform enables safe human-robot interactions at the price of a reduced actuator control bandwidth [82].

The humanoid TORO (Fig. 2.8) from DLR was designed to study whole-body compliance and locomotion, exploiting active torque control [83, 84]. DLR built the platform upon their expertise in developing the well known Light Weight Robots [85]. With its 1.74 m of height, 76.4 Kg weight, and 27 joints, it enabled (and still enables at the time of writing this manuscript) important research and practical results.

TALOS, part of the PAL robotics selling catalogue, is another relevant example of this trend in humanoid robotics (Fig. 2.8). This robot was conceived to maximize both industrial quality and state of the art design, to allow for both repeatability during operations and compliant human-robot interactions [86]. The high quality of the platform is the outcome of the active collaboration between the Gepetto Team of LAAS CNRS and the manufacturer.

Other platforms were built by focusing on the objective of delivering high torque through the motors thanks to hydraulic actuation: the biped TaeMu [87] from Ritsumeikan University, DURUS, created from the collaboration between AMBER lab and SRI international [84], and ATLAS, by Boston Dynamics.

Low cost and modularity

Some research groups focused on modularity and cost reduction. A robot that costs hundreds of thousand euros can only be afforded by a limited number of institutions, limiting its applications. The Poppy Project from Inria Flowers Lab for instance consisted in an open-source modular and 3D printed robot. It was conceived to be light (3.5 Kg weight for a 0.84 m tall structure). Its first application has been a human-robot dance performance [88]. Thanks to its modular and low cost structure, it facilitates iterations over different structure configurations, allowing for instance the investigation on the effect of bent thighs in bipedal robots, see the left image in Fig. 2.8. The same philosophy was followed in Robotics and Mechanisms Laboratory, UCLA, to build BALLU and BALLU2, with a completely different outcome. In order to maximize the safety, the research group proposed a buoyancy assisted biped, where lightweight legs are sustained by helium balloons [89]. The benefits of such structure are that the robot can never fall, it is affordable and light. The drawback is that structure is not robust to wind and physical interactions (Fig. 2.8).

Large projects and case studies

DARPA robotics challenge also triggered further research in disaster response or critical applications for humanoid robots. The Valkyrie platform (Fig. 2.7) was built and used by team from the Johnson Space Center (NASA) to participate with it at the DARPA trials [90]. Valkyrie was 1.87 m tall, weighted 129 Kg, and had forty four degrees of freedom. The expertise and lessons gained in the DARPA trials pushed research

Figure 2.8: Poppy (2012), BALLU2 (2021), TORO (2013), TALOS (2017).

towards complex applications such as Improvised Explosive Device (IED) response tasks [91]. Deploying a robot in these scenarios would for instance involve traversing an uneven terrain, passing though narrow spaces, taking the IED, and eventually securing it in a safety container. Test operations were conducted in semi-autonomy by using a supervisory control approach, in which an operator that could only access the scene through robot sensor data, e.g., cameras, was providing high level commands. The task had to be accomplished in less than one hour, satisfying the hard constraints of both safely handling the IED and remaining charged for all the time of the task. A success rate of 57% was declared, testifying the need of further improvements on both the software and hardware side.

The application of humanoids in large scale industrial environments was also investigated. Finding a way to automatize non added-value tasks that could only be executed by humans was the objective of the Horizon 2020 COMANOID project, which aimed at validating the feasibility of such idea for aircraft manufacturing [55] using HRP-4 and TORO. The final demonstration consisted in climbing a stair to reach the internal of a plane and executing a bracket positioning task before coming back to the starting point. Each one of the two platforms involved in the projects performed a variant of the task, according to its hardware capabilities. In particular, HRP-4 focused more on the stair climbing task (for which a minimal human supervision was required), while TORO on the picking and placing of the bracket.

Before proceeding to the next section, it should be noted that human supervision was required in all of these challenging applications. Hardware and software integration (planning, localization, mapping, control) is not mature enough to guarantee full autonomy in humanoids for prolonged and complex applications.

2.5 The new generation

Where are we now?

We started this treatment from the world of ideas, entertainment, and the enthusiastic perspectives of people. In fact, the willing of recreating the human as a machine has no time. From the ancient world up to the present, this spirit has not changed in substance.

And years of effort brought to the outstanding state-of-the art of humanoid robotics.

There is however something that is missing from the big picture. Humanoids do not work. They are not able to be deployed in the real world. If we think that the first conventional "modern" humanoid, WABOT-1, is dated back to 1973, it is hard to understand how it is possible that in fifty years the technology has not reached yet full maturity. The existing humanoids reported in the chapter are at the moment pure research platforms, i.e., inappropriate for real-life applications [92]. "What are we doing wrong?" could be a good question.

There is no lack of enthusiasm in researchers and several big research projects have been funded in the recent past, so why are humanoids not ready yet for real deployment and commercialization? There is no precise answer to the question, however, some reflections can be conducted upon it.

To begin with, we can build over the interesting and at the same time heavy conclusions of the paper from Kumagai et al, named "Toward Industrialization of Humanoid Robots Autonomous Plasterboard Installation to Improve Safety and Efficiency" and published in 2019 in the IEEE Robotics and Automation Magazine [91]: there is no commercial convenience at the time to adopt humanoids for non-research oriented purposes.

Let us provide an example. Consider the task execution in degraded environments, e.g., for disaster site inspection, that is one of the most promising areas to apply humanoids (see DARPA robotics challenge). In this case the strict need of such technology is limited, as there are many other robots that can more reliably intervene on the site, like drones, crawler mobile manipulators or quadrupeds. Humanoids would be useful in these scenarios only if they could be able to perform as good as (or better than) a human. Yet, this is not the case. Note that we are not discussing here about full autonomy, as the very same limitations would be present even if the robot was tele-operated and the safety issues were not of concern, being for instance the disaster site already damaged. In the DARPA challenge we have seen none of the finalists being able to perform at the same level of a human operator. Disaster response is also the sole case in which the social importance of the application, i.e., preventing a human to risk his life, justifies any cost (that may also comply with the actual prices of current humanoids).

Another interesting example is the daily life application of humanoids, which would introduce them to a wide market. Here, safety and cost would take the highest priority. A customer product must have a proper price to be appealing, while at the same time the robot, once deployed in houses, must be safe for humans. There is not a commercial product satisfying such requirements and yet this big void does not encourage many companies to massively invest in the field.

Great part of the progress is expected from the fundamental research world which is indeed doing its best with its means. However, the generated results have in most cases a long-term utility return in potential commercial applications that may not be sufficient to create a market in the short-medium term. In [92], it is advocated that a minimal effort is devoted in field engineering research targeted to humanoid applications, that would render the state of the art able to comply with the real life task. Notable exceptions are [93–95].

There is a gap to be filled before seeing a large number of companies putting their effort in developing commercial humanoids. They must be built with reliable actuators, possibly small, electric, and torque controlled, so as to allow for compliance

and disturbance rejection while maintaining limited size and noise during operations. The price must be reduced, comprising also maintenance expenses[6]. Large production would reduce the costs and improve the diffusion of the proper components. However, this may still not be enough. On the motion/control side, current algorithms are often dependent on parameters which have to be tuned according to the specific task [55]. They are also not yet robust enough to cope with severe measurement and localization errors.

The new generation of humanoids

The picture from the previous subsection may appear too dark, without encouraging perspectives on the progress of the field. This is not the total reality. There exist people that are focusing their effort in improving the current technology, trying to comply with the specific requirement that an actual deployment of the robot would involve in the specific field of interest. There has not already been a milestone event that can define a clean cut between the current and consolidated research technologies. However, things are moving and what can be called as the *new generation of humanoids* is progressing at the very moment of writing this thesis.

In 2019 Honda presented its new generation platform called E2-DR after abandoning the development of the milestone robot ASIMO. One of the most renowned and impressive humanoid robotics project ever conducted has come to an end, testifying the desire of the company to move towards a more practical functionality of the robot that they are producing. With its 1.68 m of height and 85 Kg weight, the E2-DR platform is conceived as a compact and reliable tool for disaster response. It is dust and waterproof and, on the locomotion side, it can use all its limbs to exploit different configurations and increase its robustness to overcome debris or even climb vertical ladders, see Fig. 2.9. This approach comes from the DARPA lesson, where humanoids have proven their need to exploit various types of locomotion to be resilient enough to the complexity of the environment.

HRP-5P is another example of the new generation of robots, conceived for a specific operational purpose, i.e., large scale manufacturing [91, 96]. The authors motivate their choice by stating that this is the application field in which humanoids may be employed the most. The trade off between required safety, autonomy, cost restriction, and possible market is indeed relatively promising at the current time. Being it able to reach a wide joint range, the platform can manipulate large objects, as demonstrated in a pastelboard application scenario. Still, the overall operation has not reached yet a convenient performance level, taking on average eight times more than a person to execute the task.

Agility Robotics is developing humanoids to be applied in the near future to warehouses or last-mile delivery. The company was built on the solid basis given by years of research at Oregon State University and has two platforms in his catalogue: Cassie, a biped, and Digit, the improved version with arms. At the moment, Agility is mainly selling platforms (just Cassie) for research [97–99] while developing a commercial version for warehouse services. A further example is Tesla, that presented an ambitious plan for humanoid mass distribution[7] [101].

---

[6]Nowadays humanoids break often during operation [94], causing time losses and repair expenses.

[7]As a side observation, the geographic "center of gravity" of humanoid robotics development shifted towards United States and Europe from the original Asian location [100]. This conceptual movement

Figure 2.9: E2-DR (2019), HRP-5P (2019), MIT Humanoid (2021), Kangaroo (2021).

If a certain trend is slowly moving to the concretization of humanoid deployment in real applications, there exists a new interest in fundamental research regarding the possibility of achieving highly dynamic motions. Pushing the limits of the current capabilities of the robots and producing the hardware that is required for it shares the same spirit of old pioneering engineers that started working on the field fifty years ago. Boston Dynamics demonstrated the feasibility of complex and dynamic motions with the new generation of Atlas. New platforms are now coming and new advancements are yet to arrive in the close future. We can report the on-going projects of the MIT humanoid [102] or Kangaroo by PAL robotics [103], which will soon allow for extensive testing of the new methodological progress in dynamic locomotion and, on the other hand, will trigger further research in localization, state estimation and planning (see Fig. 2.9).

Note that all these notable examples are initiatives of single companies and institutions (or at most of the cooperation of a limited number of actors) and do not reflect the general trends. However, if their vision will become reality, they are most likely going to lead the emerging humanoid market.

Remember where we started

Before concluding, we can come back to the ancestral purpose of constructing human-like machines from which this treatment has started, i.e., pure astonishment and entertainment. This area never stopped its niche progress, reaching year after years a high degree of maturity. Such machines do not need perception (or just limited), they operate in safe environments and are often not conceived to navigate. In these ways, the developers can focus on the fluidity and spectacularity of motions. We can report as recent examples of this field the astounding Stuntronics from Disney research, to be employed in theme parks and movies [104], or AMECA from Engineered Arts [105], which can be rented for expositions.

Having ranged from the very beginning of humanoid robotics development up to the latest trends, this chapter has provided an overview on the current platforms, where they come from and where they might be going. Strong bottlenecks in terms of costs, safety, and reliability together with large needs for state-of-the-art improvements prevent their massive diffusion. It is not possible to predict the evolution of the field, however, humanoids keep maintaining a large conceptual fascination over researchers, engineers, and the public, which will ensure a positive gradient of progress throughout the future years.

---

consolidated in the last twenty years and, at the moment, trending manufacturers and research results are located in the occidental world. We keep this as a parenthetical remark, as many complex factors should be analyzed to provide a rigorous picture.

Chapter 3

Literature review

In this chapter, we contextualize the thesis through a literature review. First, a brief introduction on the general gait generation problem for bipedal humanoids will be provided, with particular emphasis on MPC-related approaches. Then, robustness in gait generation and 3D walking-running will be discussed.

3.1 Gait generation problem

Bipedal locomotion is a necessary requirement to render legged humanoids able to accomplish their tasks. Yet, a successful locomotion is subordinate to maintaining balance at all times. The problem of gait generation thus consists in planning trajectories which result in a balanced gait and then realizing them on the robot. There exist several gait types such as walking, crouching and running. In this section, we will review some of the relevant contributions in planar walking, which is considered as the basic problem to solve before moving to more complex gaits.

Two main walking modes are possible: static and dynamic. In static walking, the ground projection of the robot *Center of Mass* (CoM) must always be inside the *support polygon*, defined as the convex hull of the contact surfaces (typically the feet) so as to maintain static balance at all times. This results in a slow gait, that does not resemble the way humans walk. The first successful experiments involving bipedal humanoid locomotion were achieved through this mode, e.g., for the WABOT-1 [19].

Dynamic walking

In dynamic walking instead, the CoM is not constrained to lie above the support polygon of the robot, allowing for faster motions. Here, dynamic balance must be ensured. A fundamental intuition in the gait generation research is due to the introduction of the *Zero Moment Point* (ZMP) [22, 106, 107], corresponding to the point where the horizontal components of the moments of the ground reaction forces is equal to zero. It introduces a key simplification to the dynamic balance problem of planar walking by providing a geometric condition: the ZMP must be inside the support polygon at all times.

To tackle the complexity of the humanoid dynamics, researchers were induced to decompose the problem into lower dimensional sub-problems, i.e., trajectory generation and whole-body tracking of the generated trajectories. Seminal investigations such as [21], [28], and [29], which describes the the first documented experiments on dynamic

walking, embrace this idea with their own declination. A common approach consisted, and is still used in current developments, in considering reduced robot dynamics for trajectory generation. This way was implicitly suggested by the shape of the dynamic model of the humanoid with free-floating base, from which the pendulum dynamics [108] can be obtained from the Centroidal Dynamics (humanoid dynamics projected at its CoM) [109]. Moreover, a further simplification is introduced by neglecting the angular momentum and assuming no variations of the height of the CoM, leading to the definition of the *Linear Inverted Pendulum* (LIP) model.

The LIP, as suggested by the name, relates the CoM to the ZMP through linear dynamics, providing an effective tool for real-time walking pattern generation [107]. Between the last years of the nineties and the first years of the new millennium, investigations based on such a concept brought to effective results and demonstrations [33, 110]. For example, in [111] a method for reactive gait generation has been presented, involving reference ZMP trajectory generation and real-time adaptation. A relevant contribution is that of [3], where preview control is adopted to track a reference ZMP trajectory so as to obtain a stable gait. This paper opened the path for important developments that have been fundamental for the whole humanoid robotics field, i.e., addressing the problem via trajectory optimization and Model Predictive Control.

Divergent component of motion and capture point

A major advantage of the LIP model is its potentiality in highlighting the intrinsic features of the humanoid walking dynamics. Based on it in fact, the *capture point* has been introduced [112, 113], corresponding to the the point on the ground where the robot has to step so as to come to a complete stop. In a broader sense, the concept is also expressed in terms of the maximum number of steps that would be required to the legged system to come to a stop, i.e., the *N*-step capturability. The set of all the points where a legged robot can step to become *N*-step capturable determines the *N-step capture region* for the robot, which has a particular relevance in reactive stepping and push recovery problems. Its strength relies on the fact that the capture regions are expressed in the Euclidean space and thus constitute an expressive mean for reactive stepping controller design [113].

Whereas the capture point identifies an analysis tool or a stepping policy, the strictly related *Divergent Component of Motion* (DCM) [114] is more suitable for gait generation. It corresponds in fact to the unstable mode of the LIP, implicitly conveying a fundamental aspect of the gait generation problem: the geometric ZMP condition does not guarantee dynamic balance by itself as in fact the CoM trajectory may exhibit a divergent evolution if not properly controlled. However, according to its definition, controlling the DCM automatically implies a bounded evolution of the CoM with respect to the ZMP. Different works exploited this concept and rendered it a standard procedure within the locomotion literature [115–117]. By using the concept of *Centroidal Momentum Pivot* (CMP) [118], other authors showed how to also encode the angular momentum within the same simple and effective modeling [119].

MPC-based gait generation

The most relevant contributions for this thesis are those that make use of *Model Predictive Control* (MPC) for gait generation. MPC allows to compute control actions while satisfying constraints and minimizing a cost function, i.e., a performance criterion.

While seeking for optimality, it also accounts for disturbances and model mismatches thanks to its closed-loop receding horizon nature. We refer to [120] for a systematic treatment on the MPC theory. Wieber proposed in [121] an improvement of [3], where the capabilities of a linear MPC scheme applied to bipedal locomotion were shown for the first time. The adopted model was the Cart Table[1] and the objective function was the CoM jerk minimization to generate safe trajectories [50] (bounded CoM with respect to the ZMP), while the dynamic balance condition (ZMP within the support polygon) was enforced as a constraint. This approach opened the path for further investigations from the same research group such as those involving automatic footstep placement [122], stability by applying terminal constraints [123], and recursive feasibility [124]. The tremendous advancement that this approach brought to the state of the art is to demonstrate that trajectory optimization using simple centroidal models could be adopted for real-time bipedal locomotion. At the present time, this still constitutes a valid strategy for gait generation and control.

Intrinsically Stable MPC

The line of research from which this thesis is built upon is the *Intrinsically Stable MPC* (IS-MPC) gait generation scheme, presented for the first time in [125]. It adopts the LIP as prediction model and features an explicit stability constraint in the MPC formulation, derived from the so-called *boundedness condition* [126] which consists in a unique initialization for the DCM ensuring that the CoM does not diverge with respect to the ZMP. Such a specific constraint, different from the other terminal constraints adopted for stability in other works, allowed for rigorous feasibility, recursive feasibility, and stability proofs in [127]. These tools will be the conceptual starting point for the methodologies presented in this manuscript.

Recent developments in centroidal approaches

Optimization-based controller are nowadays the standard for legged robots control. Computers are becoming more and more powerful, allowing to solve large and/or nonlinear optimization problems in a reasonable amount of time (even within a few milliseconds). Recent trends in bipedal locomotion involve adopting the complete expression of the centroidal dynamics [109], which have the full expressiveness to generate walking, running and multi-contact motions [128–132]. In [133], for instance, an optimization problem is solved offline to compute footsteps positions, timing and the trajectories of the centroidal dynamics, allowing to generate walking and running motions over various terrains. Note that other works exploit the centroidal dynamics by representing it through the Single Rigid Body model [134, 135]. In spite of the demonstrated success of adopting online nonlinear optimization for control, there are research groups that still address the problem via linearization while trying to maintain the same motion expressiveness [135],[136].

Whole-body gait generation

Recent research in legged locomotion control is moving towards using the full model of the humanoid in MPC-based schemes. These approaches aim at reducing the

---

[1]The Cart Table model is the inverse of the LIP model.

mismatch between the prediction model and the actual platform with the objective of generating sophisticated and dynamic whole-body motions. The inherent complexity of the complete dynamics require high computational efforts to solve these kind of gait generation problems, addressed with optimization frameworks. Approaches based on Differential Dynamic Programming (DDP) demonstrated impressive simulation [137] and experimental [51] results. More recently, implementations of rigid body dynamics algorithms and efficient derivative computations [138] led to the development of high-performance DDP solvers [139] that are consolidating this area of research, while also opening the path for new problems to solve.

Further results are obtained in [140] which report experiments on the planar robot AMBER-3M. To reduce the prediction horizon of a MPC scheme, the authors propose to design stabilizing terminal constraints based on gaits synthesized offline. A different approach is to focus on how to warm start the optimization problem so as to speed up the computational time and improve the quality of the solution [141]. The same research group reports on successful locomotion experiments using a DDP-based whole-body MPC for the TALOS humanoid in [142]. Other authors exploit instead the inherent structure of the dynamics to design high performance kino-dynamic controllers for multi-contact motion generation [27].

Successful results on whole-body control applied to different robotic platforms are further encouraging the effort in such a general direction. For instance [143] studies the control of a quadruped with a manipulator mounted on the back, while [144, 145] focus on balancing mobile manipulators.

3.2 Robust gait generation problem

One of the objectives of this work is to design a scheme for robust gait generation. Robustness is intended as maintaining dynamic balance and stability (bounded CoM with respect to the ZMP) in spite of the presence of various perturbations. Due to the high complexity of the locomotion problem and the humanoid dynamics, it is not straightforward to design a scheme that is robust against any kind of disturbances, but rather various solutions could be adopted according to the specific circumstances. To provide an example, modifying the step timing and position is suitable for reacting to strong and impulsive pushes, but not as effective for counteracting persistent disturbances. Consider now the example of a human carrying a heavy bag: the natural behavior is to configure the body posture to account for the weight, rather than deviating the path trying to recover from the disturbance effect. It is thus important to present the state of the art in the robustness research field to clarify the various approaches that have been used.

Tube-based MPC

In MPC literature, the problem of robustness has been largely studied. Since MPC relies on solving a constrained optimization problem over a receding horizon, perturbations may render this problem infeasible. A common approach to address the problem is by using robust positive invariant sets. These methodologies are denoted as *tube* MPC [146–151]. The underlying idea is that, by using information on the disturbance bounds, it is possible to use the concept of robust positive invariance to re-shape and restrict the constraints, so that the control action computed by the MPC is ensured to satisfy

the constraints in spite of the presence of the perturbations. Applying tube MPC to humanoid gait generation is not straightforward because such methods are in general intended for set-point regulation or trajectory tracking, they require the system to be stable, and the constraints to be time invariant. Nonetheless, [1] successfully applied robust positive invariance to gait generation and [152] presented a comparative study between tube and stochastic MPC for bipedal locomotion. More recently, [153] used the approach to address the problem of mechanical hip flexibility in Talos.

Disturbance observer-based methods

Even if demonstrated to be effective, the above described approaches have a limited scope: the considered perturbation set need to be limited in magnitude and contain the origin.

A complementary method is to estimate the disturbance and compensate for it. In [154] various state estimators and disturbance observers based on the LIP dynamics are discussed, while [155] presents a method to measure the external force acting on the robot by employing the force sensors located at the feet and the inertial sensor. [156] presents a CoM position estimator, able to measure the equivalent force applied to the humanoid resulting in a CoM offset. This information is shown to be effective to improve the inverse dynamics and to detect imminent falls. Different works [157–159] address the observation of external forces for small sized humanoids, where foot force/torque sensors are often replaced by less expensive force sensing resistors, through which an estimate of the ZMP position is recovered.

The measurement of the external force acting on the robot is used within a preview controller in [160]; other approaches follow a similar procedure while focusing on the divergent component of motion [161, 162]. The MPC based gait generation scheme of [163, 164] uses the measurement of the interaction force coming from human-humanoid physical collaboration.

Adopting a disturbance observation in MPC deserves a particular attention for two reasons. First, proactively accounting for perturbations can conflict with constraint satisfaction, and second, the predictive nature of the controller requires the knowledge of the future disturbance evolution. In [163, 164] the external force is propagated as a constant signal along the prediction horizon with the effect of generating CoM and ZMP trajectories that account for the perturbation. Disturbance observers in MPC is a general open problem that is also studied in standard MPC literature [165–167].

Footstep and timing adaptation

The methods that have been discussed so far work best in the case of noise, small perturbations, or slowly varying persistent disturbances. Humanoids, in practical applications, must also be able to absorb strong external forces by adapting the position and timing of the footsteps. The linear MPC formulation of [122] is able to perform automatic footstep placement to react to pushes. The idea is adopted in [168], where the robustness is enhanced by tuning the cost function via Bayesian optimization and by performing a state projection into the viability kernel to always ensure the generation of a stable gait. Step timing adaptation is as beneficial as footstep adaptation for robustness, however, it can be more complicated, as the mapping between the robot state and the gait time is nonlinear. [169] proposed in fact an approach for adapting step positions and timings based on nonlinear optimization and nonlinear MPC is used

by [170] in order to modify the step timings using time scaling. In [171], first the CoM and swing foot trajectories are interpolated and then the timing is optimized within a double stage MPC scheme. The work [172] proposes a way for fast analytical computation of the stepping position and timing, with application of walking over patches guided by vision. Mixed-Integer Quadratic Programming (MIQP) based MPC can be used to compute step timing and positions using discrete variables [173, 174], with an increased computational time on average to solve the optimization problem.

A line of research consists in using a change of variables to define a linear relation between the footstep position and the current step timing, facilitating the usage of quadratic programs (QP) with linear constraints to optimize for the step timing [175–178]. An analogous idea is also used in [119] where it is proposed to increase the linear velocity of the motion along the disturbance direction.

A different perspective can be found in the works that aim at performing ZMP modulation with angular momentum control. The scheme of [178] is able to combine ankle, hip, stepping and timing strategies in a unique QP controller. [179] proposes a nonlinear MPC formulation to account for angular momentum, footstep positions and CoM height variations, whereas [179] achieves similar results by designing a two stage MPC, composed by a low frequency block that optimizes using the VH-IP model, and a high frequency block that uses the LIP plus flywheel and exploits the concept of Centroidal Momentum Pivot. Interestingly, a disturbance observer is also adopted to estimate the dynamic perturbations acting on the robot so as to increase the performance of the scheme. This work is representative in the sense that it explores the idea of a unique framework for several types of perturbations, conceptually similar to an objective of this manuscript.

Dealing with non-convex kinematically admissible regions

In all the approaches that are able to compute and adapt footstep positions, it is necessary to make sure that the resulting footsteps are kinematically realizable by the robot. This is done by defining an allowed region in which they can be placed. The considered region is in general non-convex and its boundaries depend on both the robot configuration and the environment. Computing such region exactly and directly utilizing it in gait generation may not feasible in a real-time implementation. It is common in fact to approximate it with a convex polytope, as for instance a rectangle.

Using convex polytopes allows to encode the kinematic admissibility condition as a linear constraint when addressing the gait generation with optimization techniques. Many works [180, 181] use in fact Quadratic Programming (QP) for an efficient implementation. Yet, considering a convex polytope can limit the motion of the robot: placing for instance footsteps in front of each other can be quite effective against perturbations, as shown in [182] where the authors use motions pre-computed offline. Adopting non-convex foot placement regions within a MPC formulation yields a non-linear or mixed-integer formulation. For instance, mixed-Integer Quadratic Programming (MIQP) permits to encode the non-convex constraint as a set of mutually exclusive convex constraints by using specific integer variables [128, 183, 184], with extra computational load that may become critical in real-time applications.

Non-convex regions are typically present in obstacle avoidance and it is not a problem when planning offline [185–187], but for real-time implementations convex approximations of the allowed regions are used to render the problem tractable [188].

The Real-Time Iteration (RTI) scheme can be adopted with non-convex constraints by computing time-varying convex approximations of them around a chosen trajectory. An important contribution in this direction is shown in [4] for gait generation with obstacle avoidance. The downside of RTI is that it often lacks of convergence guarantees, and the solution depends on the quality of the initial guess.

3.3 3D walking and running

Another scope of this thesis is the investigation of 3D motions. Addressing the problem with a simplified model allows for high frequency re-planning and control together with the possibility of explicitly addressing the concept of stability. Let us go through the related literature to motivate some of the developments conducted in this manuscript.

Variable height inverted pendulum for walking gait generation

The variation of the vertical component of the CoM is a fundamental requirement to walk over non-plain terrains, e.g., a stairway. An extension of the LIP model that does not fix the height of the CoM is the Variable-Height Inverted Pendulum (VH-IP) model [189].

The main difference between LIP and VH-IP is that the latter presents a non-constant natural frequency, which can either be interpreted as a nonlinear coupling of the dynamics or as a time-varying parameter of the state space. Considering the frequency as a time-varying parameter maintains the dynamics linear and thus simplifies the problem. For example [190] divides the problem in two phases: the design of the vertical motion, conducted offline, and the generation of the horizontal trajectories with a linear time-varying MPC. Under the same interpretation of a linear time-varying system, [191, 192] propose to find a bound for the difference between the VH-IP and LIP, to be used to tighten the ZMP constraint to ensure dynamic balance for the variable height case. A different approach is to constrain the vertical motion to evolve over a specific set of trajectories: in such a way the pendulum frequency can be fixed and the LIP model can be employed for the horizontal component of the motion [193, 194], with the drawback of limiting the possible 3D CoM motions. In [179], it is proposed to accept the nonlinearity of the VH-IP model, which in this case considers also the angular momentum, and to formulate a nonlinear optimization problem for a MPC scheme.

The instability remains a crucial problem when dealing with inverted pendulum dynamics. The decomposition into stable and unstable subsystems, that has been fundamental in planar gait generation through the DCM concept, is possible for the VH-IP only by using a time-varying change of coordinates [195–197]. In the latter work, this has been used for real-time gait generation in a nonlinear MPC framework.

Generation of running gaits using template models

Research on running gaits has historically been conducted in parallel with walking gait generation. We can for instance cite the seminal work of Marc Raibert [23], that was already discussed in the previous chapter as a contribution to the development of hardware platforms, where efficient hopping gaits were demonstrated. As intuition suggests, running requires both a variable CoM height and the existence of flight phases,

where contact with the ground is lost with both the legs of the humanoid. In such a situation the ZMP based approaches for walking using the VH-IP model can not be adopted. Some of these works consider the ZMP as either an input [191, 194, 195, 197] or an output [190, 198], but in the case of flight phases the ZMP results undefined.

A line of research is based on the Spring Loaded Inverted Pendulum (SLIP) as a template model for the running dynamics of the robot [199–201]. The adoption of this model is motivated by several important studies in the biomechanical literature [202, 203]. A method to control the SLIP model consists in the regulation of apex states between subsequent steps. The apex states are the flight states with zero vertical velocity, thus chosen as a representative feature of the steps. The biomechanically based template and anchor paradigm [2] is explicitly used in [204] to control the ATRIAS platform. The work [196] studies hopping on two legs with a quadruped, by using SLIP dynamics. Another example is [205], which optimizes over the derivatives of the leg length to control a SLIP-like spring-mass model that represents the robot while jumping. [206] focuses on the contact forces and the CoM trajectory by using a polynomial encoding to mimic biomechanical data.

Ensuring that the ZMP is inside the support region can be done during support phases, opening for the possibility of ZMP control for running gait generation. These approaches must put particular attention to the contact schedule so as to ensure consistency with the fact that the ZMP is undefined during flight phases. A common method, which will also be adopted within this thesis, is to use the VH-IP when the foot is in contact and a free-falling mass model during flight phases [207–209]. These contributions compute the vertical CoM trajectory first, and then design the ZMP motion during contact phases so as to meet proper boundary conditions that satisfy high level specifications of the running gait. A MPC formulation of an analogous idea is used in [210]. In [211], the authors compute the closed form expression of an optimization problem and use it for control by approximating the balance constraints to promote the efficiency of the scheme. Here, a virtual constraint to impose the contact forces to point towards the CoM (in the same spirit as [193, 194]) is used. A similar approach allows [212] to propose a linear formulation for a unique optimization framework that permits to generate running and walking gaits with adaptive step position and timing.

Chapter 4

Humanoid locomotion dynamics

Legged locomotion is based on contact force modulation. The contact forces generated by the interaction with the environment, thanks to the friction, allow to move the body of the robot. Beside the complex task of regulating the contact forces, the motions involved in walking and running must always be *dynamically balanced.* This fundamental aspect could be described as the capability to maintain postural stability, i.e., not tipping over or falling.

Translating this high-level description into a controller for an articulated legged robotics platform, such as a humanoid, requires an understanding of the underlying dynamics of the locomotion. In this work, we focus on bipedal humanoid gait generation and thus we address this chapter under a walking and running perspective. The generated motions happen through a sequence of *foot contact phases*, defined as a state in which the contact (or the contacts) with the environment is constant. A walking gait is constituted by *double* and *single support phases.* As intuition suggests, in a double support phase both feet are in contact with the ground, whereas in a single support phase a single foot maintains the contact and the other moves towards the subsequent footstep location. The combination of a double and a single support phase constitutes a *step* which has a certain duration, according to both the desired velocity of the motion and the physical limits of the platform. Running, on the other hand, is composed by the alternation of *flight* and *support phases.* The key difference is that in flight phases neither feet are in contact and the robot is only subject to the gravitational force.

Generating a gait consists in computing the proper contact forces that enable *i*) the realization of a certain[1] contact sequence, *ii*) while maintaining the balance. Translating the phenomenon into a condition that can be enforced and/or checked is crucial for solving the gait generation problem. The contact requirement (*i*) has a clear geometric and physical interpretation: position and time, i.e., where and when to place a contact. The balance requirement (*ii*), on the other hand, is related to conditions on the contact forces. They must be within the friction cone to prevent slipping and they must be positive, as the robot in standard settings can only push and not pull from the ground. A wide part of the literature has dealt with balance by assuming sufficient friction at the feet to account only for the unilaterality constraint which can be cast in an intuitive geometric condition on the ZMP, i.e., it must lie within a certain *support region* at all times. In the case of planar walking, such region corresponds to the *support polygon*, defined as the convex hull of the foot contact surfaces.

---

[1]As we have seen in the previous chapter, this can either be specified or computed by the controller.

The key reason for modeling a humanoid (and a legged platform in general) is the understanding on how the contact forces can be realized, i.e., the mapping between them and the joint actuators as well as how the contact forces affect the motion. The answer to the first aspect can be found by looking at the Lagrangian dynamics of the robot. The second aspect has a clearer interpretation by inspecting the so called *centroidal dynamics*, i.e., the humanoid dynamics projected at the CoM. From it, it is possible to derive simple yet highly descriptive models such as the Linear Inverted Pendulum and the Variable Height Inverted Pendulum, at the price of restricting the possible trajectories of the linear and the angular momentum.

These models relate the CoM to the ZMP with a second order differential equation. Addressing the gait generation problem and enforcing balance through them allows for real-time implementation, and in fact there is a large set of success stories in the literature that testify the effectiveness of this approach. The objective of the present chapter is to recapitulate the modeling of humanoid locomotion going through the Lagrangian dynamics up to the simple models obtained from the centroidal dynamics, that will have a dominant role within the manuscript.

4.1 Lagrangian dynamics

We consider in this thesis a humanoid as a multi-body system composed by a number of open kinematic chains[2]: (in general) the torso, the limbs, and the head. It has in total $n + 1$ links and n joints, which define a joint configuration space $\boldsymbol{q}_\mathrm{j} \in \mathbb{R}^n$. We assume that all the joints are actuated by a torque $\boldsymbol{\tau} \in \mathbb{R}^n$. The single joint configuration and torque are denoted as q_j and τ_j for $j = 1, \ldots, n$. Each of the tree structured open kinematic chains of the robot is connected to a *base* link that is not fixed to the world frame. The base link can move in space and thus is represented by a position $\boldsymbol{p}_b \in \mathbb{R}^3$ and an orientation $\boldsymbol{\theta}_b \in \mathbb{R}^3$. The overall configuration space of the free-floating multi-body system is given by the vector

$$\boldsymbol{q} = \begin{bmatrix} \boldsymbol{p}_b \\ \boldsymbol{\theta}_b \\ \boldsymbol{q}_\mathrm{j} \end{bmatrix} \in \mathbb{R}^{6+n}.$$

Bipedal robots can have point or surface feet. To maintain a general formulation, we represent the foot contact through relevant contact points. If the robot has point feet, a single contact point is sufficient for each foot, whereas in the case of a rectangular foot shape four contact points are required [107, 213]. Let us define $\boldsymbol{f}_k \in \mathbb{R}^3$ as the unilateral contact force exchanged with the environment at the $k-$th contact point $\boldsymbol{p}_{f,k}$, where the term unilateral indicates that the orthogonal component of the force to the contact surface is non-negative, i.e.,
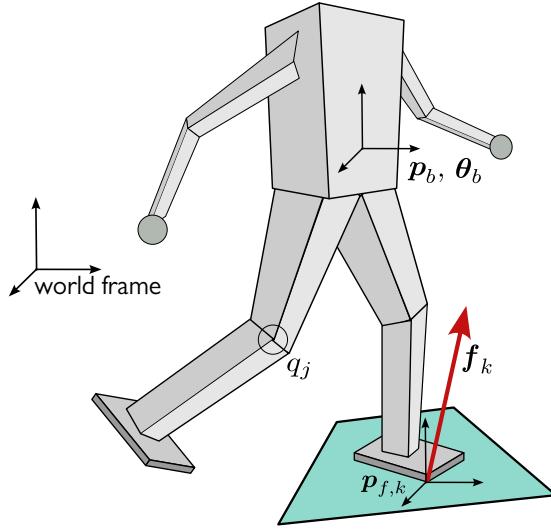
$$\boldsymbol{f}_k^\perp \geq 0.$$

See Fig. 4.1 for a graphical representation of the model.

Contacts are not constant because during locomotion they are established, e.g., hell strike, and broken, e.g., toe off. In the rest of the section, we will not consider the impact dynamics, which would render the model hybrid, and thus the validity of the

---

[2]We do not consider robots with closed kinematic chains.

Figure 4.1: Humanoid robot modelled as a floating base with pose described by $(\boldsymbol{p}_b, \boldsymbol{\theta}_b)$ which constitutes the root for multiple limbs with actuated joints q_j. At contact points $\boldsymbol{p}_{f,k}$ the robot exerts a force $\boldsymbol{f}_k$ on the environment. The robot represented in the figure is in single support and for the sake of clarity a single contact point is drawn.

treatment is restricted to a constant contact phase.

There exist $n + 6$ dynamics equations relating the configuration space and its derivatives to the joint actuation and the contact forces. They are expressed as

$$\begin{bmatrix} \boldsymbol{M}_u \\ \boldsymbol{M}_a \end{bmatrix} \ddot{\boldsymbol{q}} + \begin{bmatrix} \boldsymbol{b}_u \\ \boldsymbol{b}_a \end{bmatrix} = \begin{bmatrix} \boldsymbol{0} \\ \boldsymbol{\tau} \end{bmatrix} + \sum_k \begin{bmatrix} J_{k,u}^T \\ J_{k,a}^T \end{bmatrix} \boldsymbol{f}_k, \tag{4.1}$$

where $\boldsymbol{M}_{\cdot}$ is the inertia matrix, $\boldsymbol{b}_{\cdot}$ is a vector encoding the coriolis, centrifugal and gravitational terms, and $J_{k,\cdot}$ is the $k-$th contact Jacobian. The sum operator is intended to act over all the k contact points.

The Lagrangian dynamics is written so as to highlight its structure and show where the joint torques act on the system. To this purpose the subscript $\square_u$ stands for *underactuated*, while $\square_a$ for *actuated*.

At this point a fundamental observation is that the actuation torques $\boldsymbol{\tau}$ do not directly affect the base coordinates $\boldsymbol{p}_b$ and $\boldsymbol{\theta}_b$. Rather, their effect is that of making the interaction with the environment generate the forces $\boldsymbol{f}_k$ at the contact points, which in turns produce a variation in the momentum of the robot causing a motion in space. This fact allows for a decomposition of the locomotion control problem in two stages: gait generation, to be solved first, and whole-body control [131].

When dealing with unilateral contacts, a further aspect must be considered to account for the physical consistency of the dynamics. The contact forces must be inside the friction cone $\boldsymbol{F}_k$, i.e.,

$$\boldsymbol{f}_k \in \boldsymbol{F}_k.$$

The latter defines the set of realizable contact forces given the friction coefficient μ, that are expressed as

$$\boldsymbol{F}_k = \left\{ f_k \in \mathbb{R}^3 : \sqrt{f_{x,k}^2 + f_{y,k}^2} \le \mu f_{z,k}, f_{z,k} \ge 0 \right\}.$$

4.2   Centroidal dynamics

We now consider the dynamics of the robot projected at its CoM, i.e., the *centroidal dynamics* of the system, which coincides with the Newton–Euler equations of motion. These define the relation between the gravity and contact forces and the derivative of the linear and angular momentum of the whole robot expressed around its CoM (they are not directly affected by the joint actuation), respectively denoted as $\boldsymbol{h}$ and $\boldsymbol{L}$. These two quantities are in general dependent on $(\boldsymbol{q}, \dot{\boldsymbol{q}})$, the mapping can be expressed via the centroidal momentum matrix $\boldsymbol{A}(\boldsymbol{q})$ [109] as

$$\begin{bmatrix} \boldsymbol{h} \\ \boldsymbol{L} \end{bmatrix} = \boldsymbol{A}(\boldsymbol{q})\dot{\boldsymbol{q}}.$$

Some manipulations on the expressions of these equations is instrumental for the intuition behind the adoption of models such as the LIP and the VH-IP.

Let m_i and $\boldsymbol{p}_{l,i}$ be the mass and the position of the $i-$th limb, then the position of the CoM is given by

$$\boldsymbol{p}_c = \frac{\sum_i m_i \boldsymbol{p}_{l,i}}{\sum_i m_i} = \frac{\sum_i m_i \boldsymbol{p}_{l,i}}{m},$$

having defined m as the total mass of the robot. The Newton equation of motion, which describes the balance of the forces, writes as

$$\sum_k \boldsymbol{f}_k = m\ddot{\boldsymbol{p}}_c + m\boldsymbol{g} \tag{4.2}$$

where $\boldsymbol{g}$ is the gravitational acceleration vector. We point out that (4.2) corresponds to $\dot{\boldsymbol{h}}$, i.e., the time derivative of the linear momentum, and that the sum operator is executed over all the contact forces. The Euler equation of motion is instead

$$\sum_k (\boldsymbol{p}_{f,k} - \boldsymbol{p}_c) \times \boldsymbol{f}_k = \dot{\boldsymbol{L}}. \tag{4.3}$$

Flight phases will have a particular significance within this work, as a scheme for running gait generation is one of the contributions. When the contact with the ground is lost, the motion of the centroidal dynamics becomes

$$0 = m\ddot{\boldsymbol{p}}_c + m\boldsymbol{g}$$
$$0 = \dot{\boldsymbol{L}}.$$

The previous equations state that in the case of no contact with the ground the CoM has a free falling evolution given by

$$\ddot{\boldsymbol{p}}_c = -\boldsymbol{g}, \tag{4.4}$$

whereas the angular momentum $\boldsymbol{L}$ remains constant.

Having provided the Newton-Euler equations of motion, we now exploit the terms involved in (4.2) and (4.3) to elaborate on concepts and quantities that will be significant within the thesis.

4.3   Dynamic balance condition

We restrict to the case of a locomotion mode where only the feet can be in contact. To begin with, let us focus on dynamic balancing on a flat ground. This situation corresponds to the case of walking over an even terrain or a slope, provided that no changes in inclinations are present.

The moment balance around a ground point $\boldsymbol{p}_p$ is written as

$$m(\boldsymbol{p}_c - \boldsymbol{p}_p) \times \ddot{\boldsymbol{p}}_c + \dot{\boldsymbol{L}} = m(\boldsymbol{p}_c - \boldsymbol{p}_p) \times \boldsymbol{g} + \sum_k (\boldsymbol{p}_{f,k} - \boldsymbol{p}_p) \times \boldsymbol{f}_k. \qquad (4.5)$$

Equation (4.5) can be interpreted as a non-tilting condition around the ground point $\boldsymbol{p}_p$. Let us now define the *Zero Moment Point* (ZMP) $\boldsymbol{p}_z$ as the point on the ground with respect to which the horizontal components of the moment of the ground reaction forces, namely the contact forces, are equal to zero. In these terms, (4.5) becomes

$$m(\boldsymbol{p}_c - \boldsymbol{p}_z) \times \ddot{\boldsymbol{p}}_c + \dot{\boldsymbol{L}} = m(\boldsymbol{p}_c - \boldsymbol{p}_z) \times \boldsymbol{g} + \boldsymbol{m}_f \qquad (4.6)$$

where $\boldsymbol{m}_f = (0, 0, m_{f,z})$ and $m_{f,z}$ is the vertical component of the moment of the ground reaction forces, in general different from zero.

We introduce the Center of Pressure (CoP), defined as the the point of application on the contact surface of the resultant of the contact forces, defined as

$$\boldsymbol{p}_{cop,xy} = \frac{\sum f_{z,k} \boldsymbol{p}_{f,k,xy}}{\sum_k f_{z,k}}. \qquad (4.7)$$

Note that (4.7) is only defined for the x and y component. Consider now the $\boldsymbol{m}_f$ quantity, we have

$$\sum_k (\boldsymbol{p}_{f,k} - \boldsymbol{p}_z) \times \boldsymbol{f}_k = \boldsymbol{m}_f$$
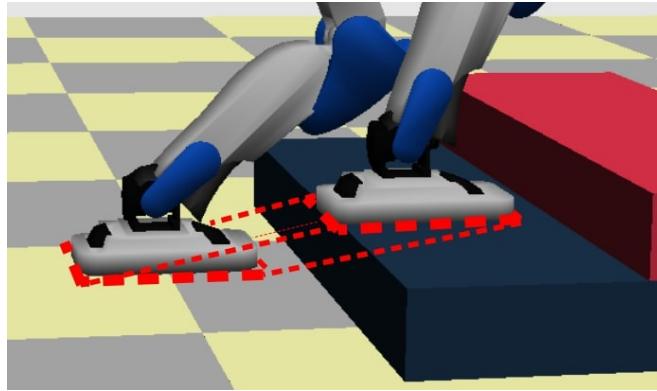
and, dividing by $\sum_k \boldsymbol{f}_{z,k}$, we can notice that the horizontal coordinates of the ZMP corresponds to those of the CoP

$$\boldsymbol{p}_{z,xy} = \boldsymbol{p}_{cop,xy}.$$

Under the hypothesis of flat ground, i.e., coplanar contacts, the CoP and the ZMP coincide. We remark that the hypothesis of flat ground induced the choice of the ZMP as a ground point for the non-tilting condition, which allowed for the validity of such identity.

Considering unilateral contact forces imposes that the CoP is inside the *support polygon* for physical consistency, where the support polygon is defined as the convex hull of the contact points. The same condition is naturally implied also for the ZMP, constituting a necessary geometric constraint to prevent the tilting of the robot. Such concept has been extensively used in the literature, e.g., [3, 33, 110, 121], and so will be in this thesis.

In the case of 3D locomotion, the contact surfaces are in general not coplanar and thus the above described condition does not hold. It is still possible to identify a ZMP, provided that its vertical component is not anymore constrained to lie on the ground. The point in which the horizontal component of the moments of the ground reaction force is equal to zero exists along a line [214], identifying a 3D ZMP.

Figure 4.2: The oblique prism defined by (4.8) when the feet are in contact on different parallel surfaces.

The 3D locomotion problems considered in this thesis will involve environments composed by parallel surfaces. We denote it as *world of stairs*. In such settings, we adopt the approach of [211] as a 3D ZMP geometric condition for dynamic balance. The idea is that of constraining the ZMP to lie within a support region $\boldsymbol{P}$ that constitutes the 3D extension of the support polygon. $\boldsymbol{P}$ is a pyramid with base given by the convex hull of the projections of the foot contact points on an arbitrary plane below all contact surfaces and with the vertex placed at the CoM[3], i.e.,

$$\boldsymbol{P} = \left\{ \boldsymbol{p} : \boldsymbol{p} = \boldsymbol{p}_c + \sum_k \gamma_k (\boldsymbol{p}_{f,k} - \boldsymbol{p}_c), \ \text{with} \ \gamma_k \geq 0 \right\},$$

where the sums are conducted over all the contact points.

The convex hull $\boldsymbol{Z}$ of the contact points is then a subset of the pyramid and can be chosen for the balance condition. We can further require that $\sum_k \gamma_k = 1$ in (4.8) and get

$$\boldsymbol{Z} = \left\{ \boldsymbol{p} : \boldsymbol{p} = \sum_k \gamma_k \boldsymbol{p}_{f,k}, \ \text{with} \ \gamma_k \geq 0, \ \sum_k \gamma_k = 1 \right\}. \tag{4.8}$$

This region corresponds to the support polygon in single support and in double support, when both feet lie in the same plane. In the case of contacts over two different parallel surfaces, (4.8) corresponds to an *oblique prism* delimited by the foot soles, see Fig.4.2.

We conclude this section with a final remark. The discussed geometric conditions on the ZMP are based on the non-tilting condition (4.5) which does not include information on the friction. However, it can be shown that under sufficient friction the ZMP condition is equivalent to the friction cone constraint for the contact forces, which ensures the feasibility of such forces and the stability of the contact [215]. When the hypothesis of sufficient friction loses validity in describing the environment[4], the ZMP condition must be modified to account for it, by for instance shrinking the considered support region [216].

---

[3]The validity of this condition holds when the contact forces point towards the CoM [111]. Although this is a strong assumption, it has been demonstrated to have a practical validity in several contributions [12, 211].

[4]For instance when walking on a slippery terrain.

4.4   Inverted Pendulum models

The paradigm of hierarchical and decoupled approaches for gait generation consists in shaping first the centroidal dynamics trajectories to realize a locomotion task and subsequently computing joint commands that realize them. An insight on the moment balance equation (4.5) reveals important concepts that can be exploited to address the problem.

Let us specify first the notation that will be adopted in the rest of the manuscript. For the components of the CoM we use $\boldsymbol{p}_c = (x_c, y_c, z_c)$, for the ZMP $\boldsymbol{p}_z = (x_z, y_z, z_z)$, and for the angular momentum $\boldsymbol{L} = (L_x, L_y, L_z)$.

The horizontal components of (4.5) write as

$$
\begin{aligned}
m(z_c - z_z)\ddot{x}_c - m(x_c - x_z)(\ddot{z}_c + g) + \dot{L}_y &= 0 \\
m(z_c - z_z)\ddot{y}_c - m(y_c - y_z)(\ddot{z}_c + g) - \dot{L}_x &= 0
\end{aligned}
$$

which can be arranged in

$$
\ddot{x}_c = \frac{(\ddot{z}_c + g)}{(z_c - z_z)}(x_c - x_z) - \frac{\dot{L}_y}{m(z_c - z_z)} \tag{4.9}
$$

$$
\ddot{y}_c = \frac{(\ddot{z}_c + g)}{(z_c - z_z)}(y_c - y_z) + \frac{\dot{L}_x}{m(z_c - z_z)}. \tag{4.10}
$$

Equations (4.9) and (4.10) describe the dynamics of the horizontal components of the CoM (thus encoding the evolution of the horizontal components of the linear momentum) in terms of the evolution of the ZMP and the angular momentum. Let

$$
\lambda = \frac{\ddot{z}_c + g}{z_c - z_z} \tag{4.11}
$$

and consider the following points:

- the quantity λ is non-negative when considering standard locomotion. The nominator of (4.11) is positive for all the motions involving vertical accelerations that is not lower than the gravity acceleration g, which is true for all the cases of interest. The denominator is also positive if the dynamic balance condition for the ZMP is satisfied, that is if the ZMP belongs to the support region defined in (4.8);

- the dynamics (4.9) and (4.10) are inherently unstable. To motivate this statement, consider the case of ZMP placed in the origin with zero angular momentum. The differential equations become

$$
\begin{aligned}
\ddot{x}_c &= \lambda x_c \\
\ddot{y}_c &= \lambda y_c
\end{aligned}
$$

  which correspond to an *inverted pendulum* [217], where λ can be interpreted as the (variable) squared *natural frequency*. Methods to prevent the divergence of the CoM are for example ZMP and angular momentum modulation or stepping strategies;

- the dynamics expressed by (4.9) and (4.10) is nonlinear and the nonlinearity is due to the motion of the vertical component of the CoM: it determines the λ term

and also scales the effect of the angular momentum. The vertical component of (4.2), defining the motion of z_c, is in turns not affected by the horizontal dynamics of the CoM and thus together with (4.9, 4.10) constitutes a triangular system. Such structure will be exploited in the 3D gait generation scheme presented in Chapter 10;

- the inverted pendulum models are obtained neglecting impact dynamics. Nonetheless, their effectiveness has been proven in many applications. Other authors instead consider such phenomenon when using these models [218].

4.4.1 Linear Inverted Pendulum model

To further simplify the dynamics expressed in (4.9) and (4.10), we can assume that the vertical motion of the CoM is constrained to lie on a fixed plane that is parallel to the contact surface, i.e.,

$$z_c = h \qquad \ddot{z}_c = 0,$$

and that the angular momentum around the CoM is equal to zero

$$\boldsymbol{L} = 0.$$

The validity of these assumptions will be enforced through a controller at some point of the gait generation scheme. We also stress that biomechanical observations confirm their physiological consistency in planar walks [219, 220]. Equations (4.9) and (4.10) become

$$\ddot{x}_c \;\; = \eta^2(x_c - x_z) \tag{4.12}$$
$$\ddot{y}_c \;\; = \eta^2(x_c - x_z) \tag{4.13}$$

where

$$\eta^2 = \frac{g}{h}.$$

The dynamics (4.12) and (4.13) are linear, decoupled and do not depend on the angular momentum. They are denoted as the *Linear Inverted Pendulum* (LIP) model. Adopting the LIP for gait generation allows to reduce the dimension of the state space of the centroidal model and to exploit the extensive theory on linear systems that is available in the control literature. In all the contributions presented in this manuscript regarding robust gait generation the LIP model will be adopted.

As already mentioned, the x and y components of the horizontal motion in the LIP model are decoupled. It is thus possible to elaborate on the sole x component with the understanding that all the equations have an identical counterpart for the y component.

The dynamics of the inverted pendulum is unstable. In the case of the LIP, the state space form of (4.12) writes as

$$\begin{bmatrix} \dot{x}_c \\ \ddot{x}_c \end{bmatrix} = \begin{bmatrix} 0 & 1 \\ \eta^2 & 0 \end{bmatrix} \begin{bmatrix} x_c \\ \dot{x}_c \end{bmatrix} + \begin{bmatrix} 0 \\ -\eta^2 \end{bmatrix} x_z \tag{4.14}$$

which highlights that the strate matrix has eigenvalues in $\pm\eta$. This can be further

visualized by operating the following change of coordinates

$$\begin{bmatrix} x_u \\ x_s \end{bmatrix} = \begin{bmatrix} 1 & 1/\eta \\ 1 & -1/\eta \end{bmatrix} \begin{bmatrix} x_c \\ \dot{x}_c \end{bmatrix} \tag{4.15}$$

decoupling the unstable from the stable dynamics and determining the *exponential dichotomy* [221]

$$\dot{x}_u \quad = \eta(x_u - x_z) \tag{4.16}$$
$$\dot{x}_s \quad = -\eta(x_s - x_z). \tag{4.17}$$

The unstable subsystem (4.16) corresponds to the Divergent Component of Motion (DCM) [114], also denoted as Capture Point [112].

The DCM has a dominant role in the gait generation problem as it encodes the intrinsic instability of the CoM/ZMP dynamics. We refer to the Sect. 3.1 for details on the related literature. In the rest of the manuscript the term DCM will be used as a synonym for x_u.

4.4.2   Perturbed Linear Inverted Pendulum model

Consider the case in which an external force $\boldsymbol{f}_{\text{ext}} = (f_{e,x}, f_{e,y}, f_{e,z})$ is acting on the robot at a certain point $\boldsymbol{p}_o = (x_o, y_o, z_o)$ of its body, i.e., a typical scenario of interest when considering the robust gait generation problem. We aim in this section at obtaining an expression of the perturbed dynamics similar to that of (4.12)-(4.13). The moment balance equation with respect to the ZMP (4.6) becomes

$$m(\boldsymbol{p}_c - \boldsymbol{p}_z) \times \ddot{\boldsymbol{p}}_c + \dot{\boldsymbol{L}} = m(\boldsymbol{p}_c - \boldsymbol{p}_z) \times \boldsymbol{g} + \boldsymbol{m}_f + (\boldsymbol{p}_o - \boldsymbol{p}_z) \times \boldsymbol{f}_{\text{ext}}. \tag{4.18}$$

The horizontal components of (4.18) are

$$m(z_c - z_z)\ddot{x}_c - m(x_c - x_z)(\ddot{z}_c + g) + \dot{L}_y \quad = (y_o - y_z)f_{e,z} - (z_o - z_z)f_{e,y}$$
$$m(z_c - z_z)\ddot{y}_c - m(y_c - y_z)(\ddot{z}_c + g) - \dot{L}_x \quad = (z_o - z_z)f_{e,x} - (x_o - x_z)f_{e,z}$$

which can be arranged in

$$\ddot{x}_c \quad = \lambda(x_c - x_z) - \frac{\dot{L}_y}{m(z_c - z_z)} + \frac{(y_o - y_z)f_{e,z} - (z_o - z_z)f_{e,y}}{m(z_c - z_z)} \tag{4.19}$$

$$\ddot{y}_c \quad = \lambda(y_c - y_z) + \frac{\dot{L}_x}{m(z_c - z_z)} + \frac{(z_o - z_z)f_{e,x} - (x_o - x_z)f_{e,z}}{m(z_c - z_z)}. \tag{4.20}$$

We now rewrite (4.19) and (4.20) as

$$\ddot{x}_c = \eta^2(x_c - x_z) + \Delta\lambda(x_c - x_z) - \frac{\dot{L}_y}{m(z_c - z_z)} + \frac{(y_o - y_z)f_{e,z} - (z_o - z_z)f_{e,y}}{m(z_c - z_z)} \tag{4.21}$$

$$\ddot{y}_c = \eta^2(y_c - y_z) + \Delta\lambda(y_c - y_z) + \frac{\dot{L}_x}{m(z_c - z_z)} + \frac{(z_o - z_z)f_{e,x} - (x_o - x_z)f_{e,z}}{m(z_c - z_z)}. \tag{4.22}$$

where we have decomposed the nonlinear term introduced by λ into the sum of a constant part plus a non-linear component $\Delta\lambda$, namely

$$\lambda = \eta^2 + \Delta\lambda.$$

To represent the effect induced by an external force acting on a generic point of the robot together with the effect of the angular momentum around the CoM and the nonlinearities due to the vertical motion, we propose to define

$$w_x \quad = \Delta\lambda(x_c - x_z) - \frac{\dot{L}_y}{m(z_c - z_z)} + \frac{(y_o - y_z)f_{e,z} - (z_o - z_z)f_{e,y}}{m(z_c - z_z)}, \quad (4.23)$$

$$w_y \quad = \Delta\lambda(y_c - y_z) + \frac{\dot{L}_x}{m(z_c - z_z)} + \frac{(z_o - z_z)f_{e,x} - (x_o - x_z)f_{e,z}}{m(z_c - z_z)}, \quad (4.24)$$

in order to obtain a simple expression for the *perturbed* LIP dynamics as

$$\ddot{x}_c \quad = \eta^2(x_c - x_z) + w_x \quad (4.25)$$
$$\ddot{y}_c \quad = \eta^2(x_c - x_z) + w_y. \quad (4.26)$$

This approach corresponds to lumping all the neglected nonlinearities due to the fixed CoM height and zero angular momentum assumptions in a single term together with the effect of the external force. The complexity is thus treated as an exogenous input, interpretable as a disturbance acting on the LIP dynamics (4.12)-(4.13).

We eventually recall that, under the coordinate transformation (4.15), the perturbed LIP can be decomposed into an exponentially stable and unstable subsystem, maintaining the same definition of DCM as for the LIP case. The perturbed DCM dynamics write as

$$\dot{x}_u \quad = \eta(x_u - x_z) + w_x/\eta \quad (4.27)$$
$$\dot{x}_s \quad = -\eta(x_s - x_z) - w_y/\eta. \quad (4.28)$$

4.4.3 Variable Height Inverted Pendulum model

The assumption of constant vertical CoM component is not suitable for describing 3D locomotion, e.g., climbing and descending stairs or running. By assuming zero angular momentum around the CoM while allowing for vertical CoM motions, equations (4.9) and (4.10) become
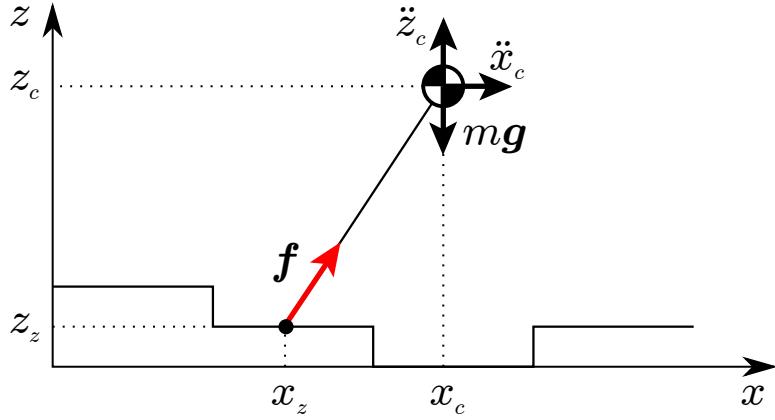
$$\ddot{x}_c \quad = \lambda(x_c - x_z) \quad (4.29)$$
$$\ddot{y}_c \quad = \lambda(y_c - y_z) \quad (4.30)$$

which denote the so-called *Variable Height Inverted Pendulum* (VH-IP) model, see Fig. 4.3. The VH-IP presents a nonlinearity induced by the pendulum natural frequency λ.

The triangular structure of the system (in which the z motion affects the horizontal motion and not the other way around) permits however a further interpretation, that we report here for completeness. The quantity λ can be considered in fact as a time-varying parameter $\lambda(t)$ and thus the state space form of the dynamics (4.29) writes as

$$\begin{bmatrix} \dot{x}_c \\ \ddot{x}_c \end{bmatrix} = \begin{bmatrix} 0 & 1 \\ \lambda(t) & 0 \end{bmatrix} \begin{bmatrix} x_c \\ \dot{x}_c \end{bmatrix} + \begin{bmatrix} 0 \\ -\lambda(t) \end{bmatrix} x_z. \quad (4.31)$$

The repulsive action of the CoM/ZMP displacement on the CoM acceleration is still highlighted, but the change of coordinates (4.15) does not decouple the unstable from the stable mode of the system, as the DCM is now time-varying [117]. It can be shown

Figure 4.3: The VH-IP model on the sagittal plane.

that system (4.31) admits an exponential dichotomy similar to (4.16)-(4.17) provided that $\lambda(t) \in \mathcal{C}^{r-1}, r > 3, 0 < \lambda^m < \lambda(t) < \lambda^M$ and that the limits $\lim_{t \to -\infty} \lambda(t)$ and $\lim_{t \to \infty} \lambda(t)$ exist and are bounded [197, 217, 221].

Let γ and ω be positive and bounded $\mathcal{C}^1$ curves. Under the time-varying change of coordinates

$$\begin{bmatrix} x_u \\ x_s \end{bmatrix} = \begin{bmatrix} \omega & 1 \\ \gamma & -1 \end{bmatrix} \begin{bmatrix} x_c \\ \dot{x}_c \end{bmatrix}, \tag{4.32}$$

(4.31) is transformed into the exponential dichotomy

$$\dot{x}_u \quad = \omega x_u - \lambda x_z \tag{4.33}$$

$$\dot{x}_s \quad = -\gamma x_s + \lambda x_z, \tag{4.34}$$

provided that the Riccati equations

$$\dot{\omega} \quad = \omega^2 - \lambda \tag{4.35}$$

$$\dot{\gamma} \quad = \lambda - \gamma^2$$

are satisfied.

Chapter 5

Perturbations acting on a humanoid

Robustness to perturbations[1] is a core topic of the manuscript. When a disturbance acts on a humanoid, dynamic balance can be compromised. Let us consider for simplicity the LIP model. By rewriting (4.25) as

$$x_z = x_c - \frac{\ddot{x}_c}{\eta^2} + \frac{w_x}{\eta^2},$$

the effect of the perturbation to the ZMP can be understood. The latter is in fact bounded to be within a certain support region for dynamic balance, while the term w_x can lead the ZMP outside of such region if not properly accounted while solving the gait generation problem. We remark that w_x is an acceleration in (4.25) and its measurement unit is m/s^2.

A further aspect can be highlighted by inspecting (4.27). The unstable component of motion results forced by the exogenous input w_x, which can cause the divergence of x_u with respect to the ZMP.

Gait generation schemes that are able to handle perturbations will be presented in Chapters 7-8-9. In the present, we discuss possible physical sources of perturbations. We also discuss two aspects that will be relevant components for our controllers: disturbance modeling and disturbance estimation.

5.1 Sources of perturbations and their model
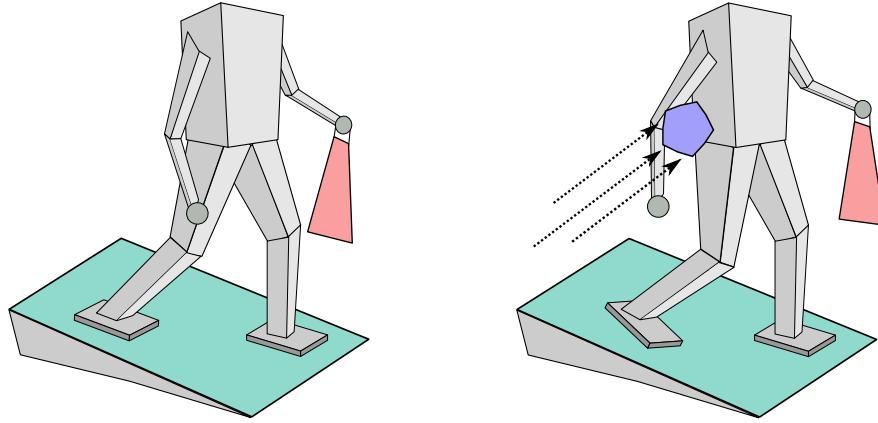
It results convenient for future discussions regarding the development of the proposed methods to categorize and define a terminology for the possible sources of perturbations. We propose the following: *uncertainties*, *persistent disturbances*, and *impulsive disturbances*. See for instance Fig. 5.1.

Uncertainties
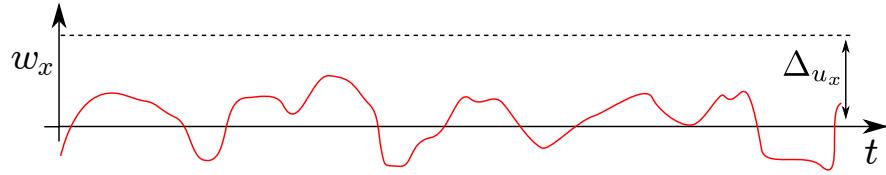
A typical set of perturbations that act on a humanoid is given by uncertainties. Such a word denotes all the quantities that are not explicitly modeled as well as those which differ from the nominal model. They can be generated by low level tracking error in the

---

[1]The terms perturbation and disturbances will be used as synonyms throughout the thesis.

Figure 5.1: A situation in which the robot is affected by perturbations: the humanoid is walking down a slope, while carrying a bag and at a certain point, it is also hit by an object. The slope and the bag can represent persistent sources of disturbance, whereas the hitting object would be modelled as an impulsive perturbation.

Figure 5.2: Example of a plot of the uncertainty over time (red curve) that satisfies (5.1).

actuation and/or measurement noise. Another possible source of uncertainty is given by the first two terms in (4.23)-(4.24), which correspond to the nonlinearities that are neglected when using a LIP model.

The set of the possible uncertainties $\mathcal{W}_{u_x}$, for which

$$w_x \in \mathcal{W}_{u_x} \tag{5.1}$$
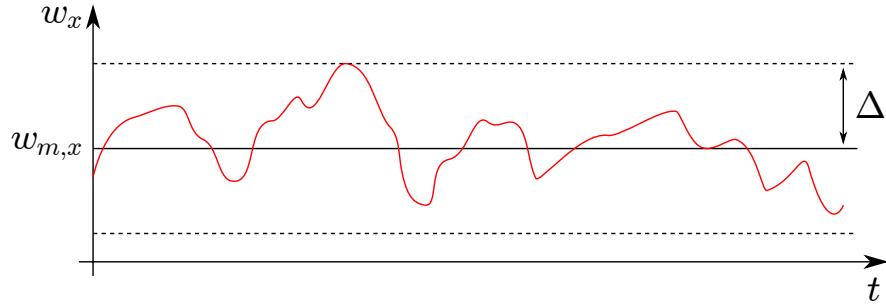
with

$$\mathcal{W}_{u_x} = \{w_x : -\Delta_{u_x} \leq w_x \leq \Delta_{u_x}\}, \tag{5.2}$$
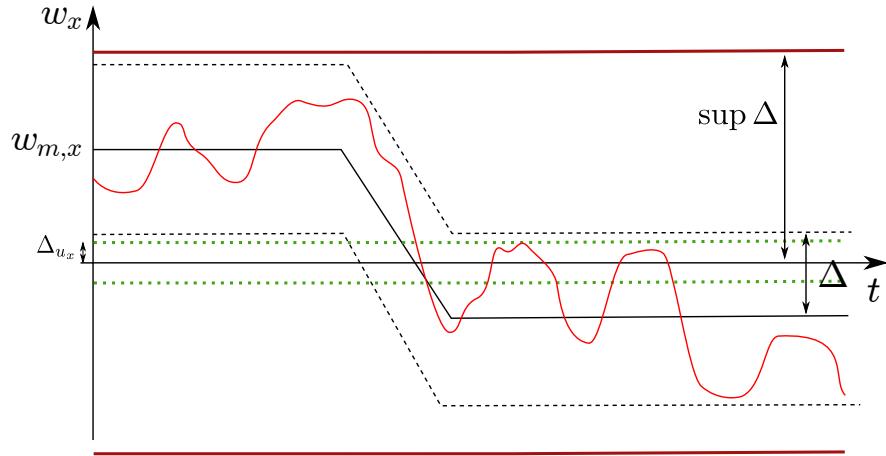
can be estimated with reasonable precision and used to improve the performance of the gait generation scheme [1, 192, 222, 223]. The set $\mathcal{W}_{u_x}$ typically contains the origin in the related literature, unless there exist evidences of specific perturbation bias around which the uncertainties are generated. In the present work, we will always assume that $0 \in \mathcal{W}_{u_x}$, as shown in (5.2) and in Fig. 5.2. Note that (5.1) can be interpreted as a *model* of the uncertainty. A model refers in general to differential or algebraic equations. When no mathematical information is available, it is reasonable to describe the model in terms of all possible realizations, i.e., through a set description. Thus, the set $\mathcal{W}_{u_x}$ represents all the possible realizations of w_x that can exist at a given time instant.

Persistent disturbances

Other external signals acting on the LIP dynamics would be better described as persistent disturbances. Such expression will denote within the thesis all kind of perturbations

Figure 5.3: The evolution of a disturbance w_x (red) that satisfies the assumptions, oscillating in a bounded set around a non-zero midrange $w_{m,x}$.

Figure 5.4: The evolution of a disturbance w_x (red) that satisfies the assumptions, oscillating in a bounded set around a time-varying midrange $w_{m,x}$. This plot also represents the uncertainty set $\mathcal{W}_{u_x}$ (dotted green line) and the set $\sup \mathcal{W}_x$.

that are exogenous (in contrast to uncertainties), are exerted for a prolonged time on the robot, and may have a non-zero bias. Treating them as uncertainties could result in a too conservative controller.

A typical example is walking on a slope. Consider in fact a LIP model in the slope frame: the gravity acceleration will have a non-zero component on the three axes, resulting in a constant disturbance acting on the CoM of the robot [12, 224]. Another set of possible persistent disturbances is the effect of loads. In [6] and [9], it was experimentally shown how a heavy load can deteriorate the gait performance of a humanoid and even leading it to fall if not properly considered by the controllers. A similar effect is originated by the interaction forces in cooperative transportation problems, which have to be properly accounted to maintain the balance [225].

Modeling an exogenous disturbance is not trivial if some information on its nature is not available a priori. Then, for control purposes, hypotheses on the nature of the perturbation must be introduced. We assume

$$
\begin{aligned}
w_x &\in \mathcal{W}_x \\
\dot{w}_x &\in \dot{\mathcal{W}}_x,
\end{aligned}
$$

where $\mathcal{W}_x$ is a disturbance set that in general does not contain the origin. Its definition

together with that of $\dot{\mathcal{W}}_x$ is

$$
\begin{align}
\mathcal{W}_x &= \{w_x : w_{m,x} - \Delta_x \leq w_x \leq w_{m,x} + \Delta_x\} \tag{5.3} \\
\dot{\mathcal{W}}_x &= \{\dot{w}_x : -\dot{\Delta}_x \leq w_x \leq \dot{\Delta}_x\}, \tag{5.4}
\end{align}
$$

with $w_{m,x}$ denoting the *midrange disturbance* and Δ_x the maximum deviation from it. See Fig. 5.3 for a graphical representation of (5.3).

We remark that the disturbance set can be a function of time $\mathcal{W}_x(t)$, implying either a time-varying midrange value or a variable amplitude Δ_x. Furthermore, for physical consistency we have that

$$\mathcal{W}_x \subseteq \sup \mathcal{W}_x$$

with

$$\sup \mathcal{W}_x = \{w_x : \inf(w_{m,x} - \Delta_x) \leq w_x \leq \sup(w_{m,x} + \Delta_x)\}.$$

Any constant or time-varying disturbance set must be bounded within a tolerance limit of the robot[2]. Quantifying the boundaries of such an abstract and conceptual set may not be straightforward (or even not possible). Consider now the following points:

- we chose the expression Δ_x to both distinguish it from Δ_{w_x} and to lighten the notation;

- the value of Δ_x can be chosen so as to contain Δ_{u_x}, thus allowing in practice to model with (5.3) both uncertainties and persistent disturbances. See Fig. 5.4 for a graphical representation. In this case, the effect of high frequency noise, that may be present in $\mathcal{W}_{u_x}$, should be accounted in $\dot{\mathcal{W}}_x$. However, it can be neglected if the entity of the noise is low with respect to that of the persistent disturbances;

- the bound on the disturbance derivatives is implicitly requiring that persistent disturbances are slowly-varying. This hypothesis is not restrictive as impulsive perturbations are gathered in the following type.

Impulsive disturbances

The main source of perturbations that has been studied in the bipedal locomotion literature is given by strong pushes exerted on the humanoid for a limited amount of time. Their strength imposes the robot to perform recovery actions similar to those of humans to maintain the balance, such as modifying the shape of the support polygon by changing the contact locations, delaying or anticipating the switch between contact phases, modulating angular momentum or even the CoM height. Push recovery is one of the most challenging problems in humanoid control, because addressing it involves both the execution of dynamic motions and the capability of taking fast decisions.

The scientific interest generated by the push recovery problem stimulates research and opens new directions for the applicability of the humanoids. In the case of deployment in an industrial or social setting, humanoids must be able to guarantee their operativity, comprising situations where strong pushes incidentally act on them. This can happen due, for instance, to the unexpected collision with a moving object, as depicted in Fig. 5.1.

---

[2]The rationale is the following: $\sup \mathcal{W}_x$ contains all disturbances that can be tolerated without requiring the robot to modify its footstep plan or to assume an unfeasible configuration.

In the thesis, we focus on test cases to validate and benchmark the proposed schemes. In a simulation environment, it is possible to program specific forces to act on a point of the robot for a determined time interval. This is typically the first stage of validation of a robust locomotion algorithm [8, 175, 176]. When dealing instead with hardware platforms in a controlled laboratory environment, two methods are used: direct pushes on the robot [132, 178] or falling objects attached to a rope, constituting a pendulum-like structure that permits a certain repeatability of the experiment [8, 226]. There exist also on-purpose benchmarking setups to conduct a reliable experimental campaign [227], even though they still do not constitute the standard practice in the literature.

It is instrumental at this point to present a mathematical description of the impulsive perturbation. We begin with an example. Consider for instance a force acting on the sole x component of the CoM of the robot, then the impulsive push is modeled as

$$w_x = \begin{cases} 0 & \text{for } t < t_i, \\ f_x/m & \text{for } t_i \leq t < t_f, \\ 0 & \text{for } t \geq t_f, \end{cases} \tag{5.5}$$

where f_x is the force magnitude, m is the total mass of the robot and t_i, t_f are the initial and final time instant of the impulsive disturbance action.

Let us now define $\mathcal{W}_{i_x}$ as the set of all the possible impulsive disturbances acting on the robot. According to our convention for defining the types of perturbations, given a persistent disturbance set $\mathcal{W}_x$, $\dot{\mathcal{W}}_x$, the impulsive disturbance set is defined as

$$\mathcal{W}_{i_x} = \{w_x : w_x \notin \sup \mathcal{W}_x \cap (w_x \notin \mathcal{W}_x \cup \dot{w}_x \notin \dot{\mathcal{W}}_x)\}. \tag{5.6}$$

The model presented in (5.5) belongs to $\mathcal{W}_{i_x}$ for any value of f_x as its derivatives tends to infinity. The definition (5.6) also includes perturbations with bounded derivatives which however exceed the set $\mathcal{W}_x$ as for instance

$$(\sup \mathcal{W}_x \ominus \mathcal{W}_x) \subseteq \mathcal{W}_{i_x}.$$

In this way, disturbances that larger than the boundaries of the considered set $\mathcal{W}_x$ but are within the possibly unknown $\sup \mathcal{W}_x$ (we recall that $\ominus$ denotes the Minkowski difference [228]) are formally part of $\mathcal{W}_{i_x}$. These can just be large but not limited in time perturbations and thus not properly appealable as "impulsive": it is a mere naming choice due to the fact that quantifying $\sup \mathcal{W}_x$ with precision is in general not feasible.

5.2 Estimating the perturbations

We have characterized and modeled in the previous sections the possible sources of perturbations that will be considered in the thesis. It has been shown in numerous contributions, both in control and robotics literature, that having information on the disturbance dramatically improves the control performances. In a few cases it may be possible to have a priori knowledge on the set $\mathcal{W}_x$, as for instance when walking down a known slope or carrying a weight with known mass. When such data are not available, a Disturbance Observer (DO) can be used. This approach is denoted in the literature as Disturbance Observer-Based (DOB) control [229].

For the sake of robustifying the gait generation scheme with respect to persistent

disturbances, in this work we aim at observing either the slowly varying component of the disturbance w_x or the midrange w_m that defines the set $\mathcal{W}_x$. In the case of bipedal locomotion, all the involved quantities, control inputs and states, are intrinsically subject to hard constraints, such as joint and effort limits or the dynamic balance condition. Addressing thus the control problem by estimating the current value of the perturbation would permit to account for the constraint in a proper and proactive way, instead of relying on a pure feedback disturbance rejection. The examples available in the literature [162, 163, 230], showing the validity of this idea, have been a source of inspiration for the development of this thesis.

Here, we present two possible methods to retrieve a disturbance estimate. The reason for discussing two different disturbance observers is that the gait generation schemes that will be detailed in the rest of the thesis do not require a specific form of DO. Any algorithm that provides a measurement of the perturbation can be equivalently employed. We thus provide two alternative candidates.

Impulsive perturbations, due to their limited action in time, are not easily measurable and in fact their rejection is typically based on feedback and not on proactive motions. However, their presence would deteriorate the estimation of persistent slowly varying disturbances by introducing a delayed transient after its occurrence. To account for this issue, we introduce a method to artificially filter the action of eventual pushes.

5.2.1 ZMP based estimate

To begin with, we discuss the simple yet effective method presented in [158]. Given the perturbed LIP model (4.25), we arrange the dynamics to obtain the expression of the disturbance in terms of the CoM and the ZMP as

$$w_x = \ddot{x}_c - \eta^2(x_c - x_z). \tag{5.7}$$

Thus, an estimate $\hat{w}_x$ of w_x can be retrieved by combining CoM position and acceleration to ZMP measurements through (5.7). The CoM position is obtained by either direct kinematics, evaluated at the current encoder readings, or motion capture systems, and the acceleration by an IMU, assuming that the sensor is placed at the robot CoM. The ZMP position is instead inferred by either using Force-Torque Sensors (FTS) or Force Sensing Resistors (FSR).

The platforms adopted for validation experiments in this manuscript have only access to FSRs. Given the location of the FSRs in the foot soles, the ZMP[3] is computed as

$$x_z = \frac{\alpha_l \sum_l x_{l,i} f_{l,i} + \alpha_r \sum_r x_{r,i} f_{r,i}}{\alpha_l \sum_l f_{l,i} + \alpha_r \sum_r f_{r,i}}$$

where the subscipts r, l stand for left and right and then $x_{.,i}$ are the FSR positions at each foot, $f_{.,i}$ the FSR readings, $\alpha_.$ a boolean variable that is equal to 1 when a foot is in contact and 0 otherwise.

The measurement obtained through (5.7) consists in an instantaneous picture of the disturbance, given the current sensor readings. It is not smoothed by filtering dynamics and thus is highly affected by sensor noise. The most productive sources of noise are the IMU and the FSRs. The IMU output is often equipped with an internal filter or processed by the robot framework software provided by the manufacturers. In addition

---

[3]Here, we compute the CoP, that under the assumption of flat ground, corresponds to the CoP.

to the measurement noise, a further criticity arises in the ZMP position measurement when the robot establishes a new contact on the ground at the beginning of a new contact phase during the walk. The effect of impacts on the dynamics is well known [107] and can be modelled. However, due to imperfect impacts with the ground, e.g., when the contact is not established at the designed time instant, or when the foot sole approaches the ground without being perfectly parallel to it, or when elastic deformations happen, the validity of some measurements might be compromised. For this purpose, in experiments a Kalman or low-pass filter must be specifically implemented to process the ZMP measurement.

We conclude the presentation of the estimator with a final observation that will be recalled in further chapters of the thesis. When the robot is not moving, (5.7) becomes

$$w_x = -\eta^2(x_c - x_z).$$

In static equilibrium, the external perturbation is proportional to the CoM/ZMP displacement. A different perspective is: to achieve static equilibrium under the action of a perturbation, the ZMP and the CoM must be displaced by

$$x_z - x_c = \frac{w_x}{\eta^2}. \tag{5.8}$$

5.2.2 Extended state observer

A simple yet effective class of disturbance observers is given by the Extended State Observers (ESO) [231]. With respect to the method presented in the previous section, they allow to both reconstruct the full state and to obtain an asymptotically stable dynamics of the observation error. The underlying idea is that of modeling the disturbance as the output of an exogenous system that is connected to the nominal plant, resulting in the perturbation of the latter. The interconnection is encoded through the state space and then a standard state observer is designed[4].

Consider the state space form of the LIP model (4.12)

$$\begin{bmatrix} \dot{x}_c \\ \ddot{x}_c \\ \dot{x}_z \end{bmatrix} = \begin{bmatrix} 0 & 1 & 0 \\ \eta^2 & 0 & -\eta^2 \\ 0 & 0 & 0 \end{bmatrix} \begin{bmatrix} x_c \\ \dot{x}_c \\ x_z \end{bmatrix} + \begin{bmatrix} 0 \\ 0 \\ 1 \end{bmatrix} \dot{x}_z, \tag{5.9}$$

where the ZMP velocity $\dot{x}_z$ is the control input. The dynamic extension to the first derivative of the ZMP position $\dot{x}_z$ is introduced for consistency with the methods presented in the next chapters of the thesis. Consider now, for the disturbance dynamics, the exosystem

$$\dot{w}_x = 0. \tag{5.10}$$

Given an initial condition $w_x(t_0)$, it will generate a constant disturbance evolution $w_x(t) = w_x(t_0)$.
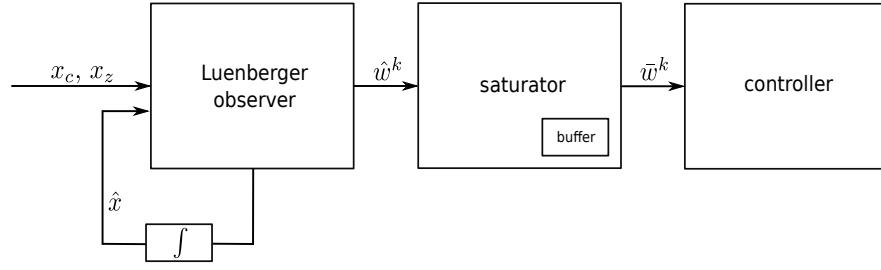
The ESO is designed as a Luenberger observer over the state $\hat{x} = [\hat{x}_c, \ \dot{\hat{x}}_c, \ \hat{x}_z, \ \hat{w}_x]$ as

$$\dot{\hat{x}} = A\hat{x} + B\dot{x}_z + G(H\hat{x} - Hx), \tag{5.11}$$

where the matrices A, B, H are constituted by the interconnection between (5.10) and

---

[4]The considered systems are observable.

Figure 5.5: Block scheme representing the local interconnection between observer, saturator and controller (now depicted as a generic block). The Luenberger observer over the extended state space discussed in Sect. 5.2.2 is reported as an example of a possible disturbance estimator. This scheme highlights how the output of the saturator is used for control and is not fed back to the observer.

(5.9), writing

$$
A = \begin{bmatrix} 0 & 1 & 0 & 0 \\ \eta^2 & 0 & -\eta^2 & 1 \\ 0 & 0 & 0 & 0 \\ 0 & 0 & 0 & 0 \end{bmatrix} \quad B = \begin{bmatrix} 0 \\ 0 \\ 1 \\ 0 \end{bmatrix}
$$
$$
H = \begin{bmatrix} 1 & 0 & 0 & 0 \\ 0 & 0 & 1 & 0 \end{bmatrix},
$$
(5.12)

with G a gain matrix to be computed. H selects the measurable outputs, i.e., the CoM and the ZMP positions, for which the system (5.12) is observable. The construction of G can thus be conducted via pole placement or LQR design.

The asymptotic stability of the observation error implies the exact reconstruction from any initial condition of all the disturbances satisfying (5.10). Different signals will be observed with an error. Although there exist various shapes for the exosystem, choosing a constant signal for modeling is the most neutral assumption and fits with the definition of persistent disturbances given within the chapter. In the literature, this approach has been operated to reconstruct slowly-varying perturbations [232].

5.2.3 Saturator

The objective of the techniques presented in the previous parts of the section is to retrieve a disturbance estimate $\hat{w}_x$. Even though we may know by hypothesis that $w_x \in \mathcal{W}_x$, $w_x \in \sup \mathcal{W}_x$, and $\dot{w}_x \in \dot{\mathcal{W}}_x$, it is possible for the observer to return an estimate that does not belong to these sets. According to the application, it can be instrumental to introduce a filtering stage that we denote as *saturator*.

The idea is that of taking $\hat{w}_x$ as input and producing as output $\bar{w}_x$, a signal which satisfies

$$
\begin{aligned}
\bar{w}_x &\in \mathcal{W}_x \\
\dot{\bar{w}}_x &\in \dot{\mathcal{W}}_x.
\end{aligned}
$$

Let $\hat{w}_k^k = \hat{w}_k(t_k)$, $\bar{w}_k^k = \bar{w}_k(t_k)$, and δ be the sampling interval. At each sampling time t_k, the saturator is formalized as the quadratic program (QP) that is here reported:

$$\begin{cases} \min_{\bar{w}_x^k} (\bar{w}_x^k - \hat{w}_x^k)^2 \\ \\ \text{subject to:} \\ \\ \bullet \;\; w_{m,x} - \Delta_x \leq \bar{w}_x^k \leq w_{m,x} + \Delta_x, \\ \\ \bullet \;\; |\bar{w}_x^k - \bar{w}_x^{k-1}| \leq \delta \dot{\Delta}_x. \end{cases}$$

The saturator QP projects the estimated disturbance inside the persistent disturbance existence set. This will permit a distinction between the control actions against strong pushes from those intended to account for persistent perturbations: the saturator is thus intended as a control oriented processing of the disturbance estimate. Note that the value $\bar{w}_x$ is not fed back to the estimator when a feedback is needed by its design structure, e.g., in the case of the Luenberger observer (5.11), because its stability can be compromised by the induced saturation nonlinearity. This concept is represented in Fig. 5.5. As a final remark, we point out that the implementation of the saturator requires a buffer to store the value of $\bar{w}_x$ at the previous time instant.

5.3   Example

We present now an example of a possible output from the combination "observer plus saturator" depicted in Fig. 5.5. The data were acquired in the DART dynamic environment [233].

The parameters required for the implementation of the observers are set to: $w_{m,x} = \Delta_x = 0.25$ m/s^2, $\dot{\Delta}_x = 0.15$ m/s^3, $h = 0.71$ m, $\eta = 3.72$ s^{-1}, $\delta = 0.01$ s, and
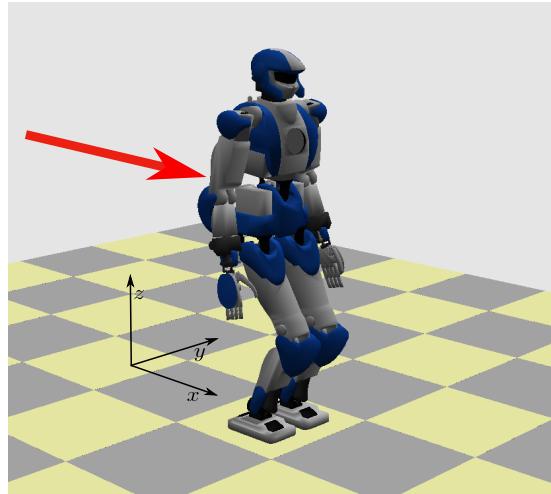
$$G = \begin{bmatrix} 0.90131 & 0.00000 \\ 26.18387 & 0.03266 \\ -0.00000 & 0.50000 \\ 239.94774 & 6.53262 \end{bmatrix},$$

where the Luenberger observer gain matrix G is obtained by pole placement. The simulation setting consists in an HRP-4 robot standing still, subject to an external force with the profile
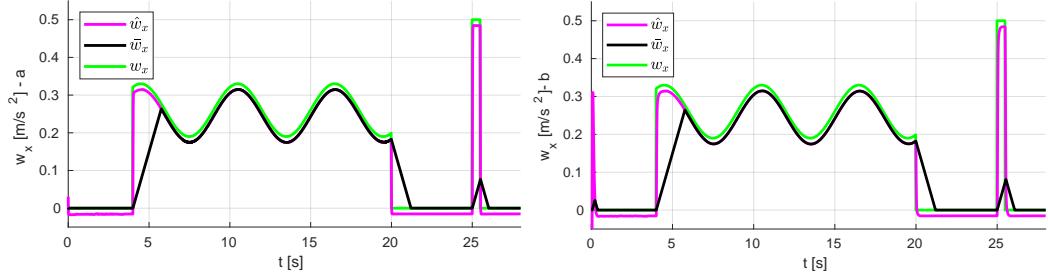
$$w_x = \begin{cases} 0 \text{ m/s}^2 & \text{if } 0 \leq t < t_a, \\ 0.26 + 0.07 \sin(2\pi t/6) \text{ m/s}^2 & \text{if } t_a \leq t < t_b, \\ 0 \text{ m/s}^2 & \text{if } t_b \leq t < t_c, \\ 0.5 \text{ m/s}^2 & \text{if } t_c \leq t < t_d, \\ 0 \text{ m/s}^2 & \text{if } t \geq t_d, \end{cases} \qquad (5.13)$$

where $t_a = 4$ s, $t_b = 20$ s, $t_c = 25$ s, and $t_d = 25.5$ s. A snapshot from the DART environment is reported in Fig. 5.6.

The perturbation w_x is chosen so that $w_x \notin \mathcal{W}_x$, in order to highlight the effect of the saturator. Figure 5.7 displays the $\hat{w}_x$, $\bar{w}_x$ and w_x for the disturbance estimators discussed in Sect.5.2.1-5.2.2. The first plot shows the data in the case of the ZMP based estimate of the disturbance. As it corresponds to an instantaneous measurement of the perturbation, it tracks with negligible delay the original perturbation signal. In the case of rapid variations in the disturbance profile, this method does not present smoothing,

Figure 5.6: Simulation set up in DART. HRP-4 is standing still while an external force (represented as a red arrow) is applied to the CoM of the robot.
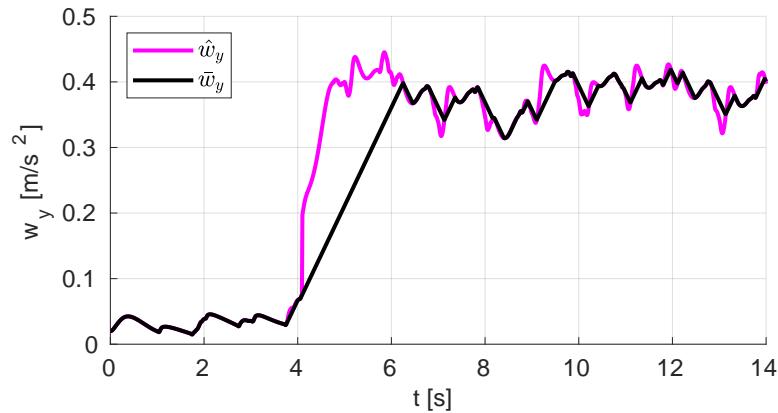
Figure 5.7: Plots of the disturbance and its estimates: (top) ZMP based estimation, (bottom) Luenberger observer.

and the saturator is thus required to limit the derivative of the observation.

The same behavior can be noted in the right hand side plot of Fig. 5.7. Here, $\hat{w}_x$ has smoother transients when the disturbance displays abrupt changes in its profile. The signal estimate is retrieved here with a delay. The Luenberger observer, furthermore, displays a large and fast initial transient, due to the initial observation error. Under a disturbance modeling, it should be interpreted as being part of $\mathcal{W}_{i_x}$ (when in reality no perturbations are acting on the robot). This is a typical situation that further motivates in practice the introduction of a saturator block. It should be noted that this simulation depicts the ideal case, in which the robot is not moving. The full body dynamics matches with high accuracy the LIP model and no sensor noise is considered (in particular, no issues in the ZMP measurement due to imprecise contact). In real experiments, the role of the saturator would be even more evident. To provide a qualitative idea, we reported the disturbance estimate during a noisy[5] walking simulation in Fig. 5.8. A constant disturbance of 0.4 m/s^2 starts acting at $t = 4$ s. Although the observer retrieves a meaningful estimate of the perturbation, the saturator ensures that $\bar{w}_y \in \dot{\mathcal{W}}_y$. We recall that this is useful only to process the disturbance estimate before using it for control. The specific reasons will be clarified in the next chapters.

---

[5]To force noise and imprecise contacts, we de-tuned the gains of the foot tracking task in the inverse kinematics controller.

Figure 5.8: Plots of the disturbance estimate and its saturated version during an "imprecise" walking simulation.

Note eventually that using the saturator to prevent the observer from trying to estimate the impulsive disturbance has also been adopted in [234]. This further confirms that, in the case of bipedal locomotion, it makes sense to compensate for persistent disturbances while using state-based reactive planning for strong pushes.

Chapter 6

The stability condition

The MPC-based gait generation schemes that are proposed in this manuscript will feature a stability constraint. Here, we present the theory motivating this approach.

As shown in Sect. 4.4, the inverted pendulum models have unstable dynamics. We have reported a proper change of coordinate that decomposes the LIP, perturbed LIP and VH-IP models into a stable and an unstable subsystem, casting them into a so called exponential dichotomy. Thus, investigating the stability of such models is fundamental to adopt them for gait generation.

We elaborate in this chapter on the concept of *stability condition*, namely the unique initial condition of the system for which, given a certain input, the state trajectories do not diverge.

The stability condition is formulated on the basis of contributions regarding stable inversion of linear systems [235], control of flexible robots [236], and exact output tracking in the general case of nonlinear nonminimum-phase, possibly time-varying, systems [237, 238]. In [126], the concept was used for gait generation and was named as the *boundedness condition*, consisting in a proper initial condition for the DCM that prevents it from diverging, given a desired ZMP trajectory. Further investigations have also been carried in [197, 217] for the time-varying dynamics of the VH-IP model.

This chapter starts with a motivating example that will allow us to introduce the reader to the subsequent treatment, to recall ideas and methods from the literature, and to clarify relevant concepts. We then discuss the cases of the LIP, perturbed LIP, VH-IP, and a fictitious system constituted by the composition of the VH-IP and the LIP models. A proof of non-divergence of the state trajectories is derived for these specific models.
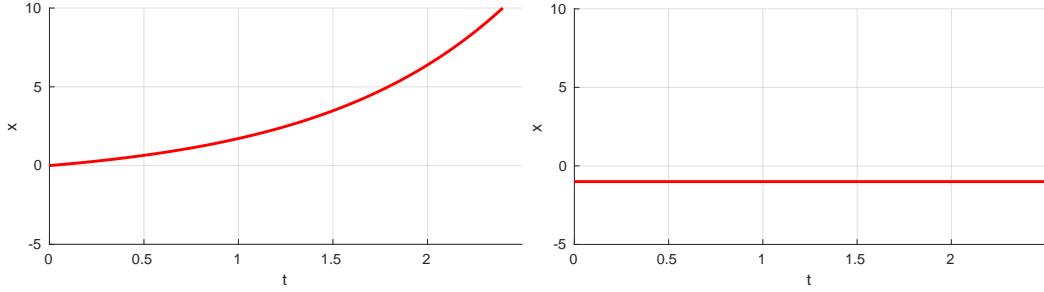
6.1 Introduction to the concept of stability condition

We begin the illustration with a basic example. Consider the scalar system

$$\dot{x} = x + u, \tag{6.1}$$

and let

$$u = \begin{cases} 0 & \text{for } t < 0 \\ 1 & \text{for } t \geq 0. \end{cases} \tag{6.2}$$

Figure 6.1: System (6.1) forced by the step input (6.2): (left) evolving from $x(0) = 0$, (right) evolving from $x(0) = x^*$.

The system, from $x(0) = 0$, evolves as

$$x(t) = e^t - 1.$$

Assume now that

$$x(0) = x^* = -1,$$

then the evolution of the system is

$$x(t) = -1.$$

Given the profile of u, a proper initial condition $x(0) = x^*$ generates a non divergent evolution for system (6.1). Figure 6.1 displays the two system trajectories starting from the two different initial conditions. When evolving from x^*, the divergent free evolution cancels out the divergent forced evolution and the state x remains bounded. The term *boundedness* indicates a non-divergent input-to-state evolution: in this sense, it is not required for the state to converge to an equilibrium of the system (that in this case would be the origin). We denote this as *internal stability*.

It is fundamental to highlight that the choice of the specific initial condition x^* depends on the system dynamics, in particular on the eigenvalues (here $\lambda = 1$) *and* on the complete profile of u, starting from the initial time instant. Initializing a system with a proper x^* requires the exact knowledge of the future control signal. To clarify this statement, let us develop (6.1) into its explicit form:

$$x(t) = e^t x(0) + \int_0^t e^{(t-\tau)} u(\tau) d\tau.$$

The *unique* initial condition from which x remains bounded is identified by

$$x^* = -\int_0^\infty e^{-\tau} u(\tau) d\tau \tag{6.3}$$

and in fact

$$x(t) = e^t x^* + \int_0^t e^{(t-\tau)} u(\tau) d\tau = \int_t^\infty e^{(t-\tau)} u(\tau) d\tau.$$

Wrapping up, we define the stability condition as the *unique* initial condition x^* under which the state trajectories of the system (6.1) remain bounded with respect to a specific input profile. This condition corresponds to an *anticausal* initialization of the system because it will depend on the future evolution of the control input, as it is

evident from (6.3).

The stability condition has also a different interpretation. Given an initial condition $x(0)$, equation (6.3) defines an integral condition for all the possible control policies so that the forced state trajectories of system (6.1) remain bounded. Let us clarify the statement through an example.

Assume we want to force a sinusoidal control input $u = A\sin(\omega t)$ to system (6.1) and that the initial condition is assigned, say $x^* = 1$. Then according to (6.3), we have

$$x^* = -\int_0^\infty e^{-\tau} A \sin(\omega\tau) d\tau = A \left[\frac{e^{-\tau}(\sin(\omega\tau) + \omega\cos(\omega\tau))}{\omega^2 + 1} \right]_0^\infty = \frac{A\omega}{\omega^2 + 1},$$

implying that any sinusoidal signal satisfying the condition $x^* = A\omega/(\omega^2 + 1)$ between pulse and amplitude will result in a non-diverging evolution for the system trajectories. Such a perspective will be fundamental for the implementation of the stability condition through a stability constraint in the proposed MPC-based gait generation schemes.

The example was conducted on a scalar system, but we highlight that the stability condition, as proposed in this chapter, does not present a significant difference when extended to the case of higher dimension linear systems. The sole condition is that the poles are not on the imaginary axis [236–238]. We introduced in Chapter 4 the concept of *exponential dichotomy* [221]. In the case of linear time-invariant systems, this can be interpreted as the property to decompose the dynamics into a stable and an unstable subsystem via a state transformation. The stability condition simply applies to the unstable subsystem (the procedure will be clarified in the following of the chapter).

We conclude this section with a brief discussion on complementary aspects from the literature:

- what we defined here as the stability condition corresponds to the operator $\mathcal{A}$ reported in [237]. The operator is first introduced in the context of stable inversion for linear systems and subsequently extended for nonlinear time-varying systems [237, 238], denoted in this case as $\mathcal{N}$. Let us now recall the stable inversion problem. Consider a system
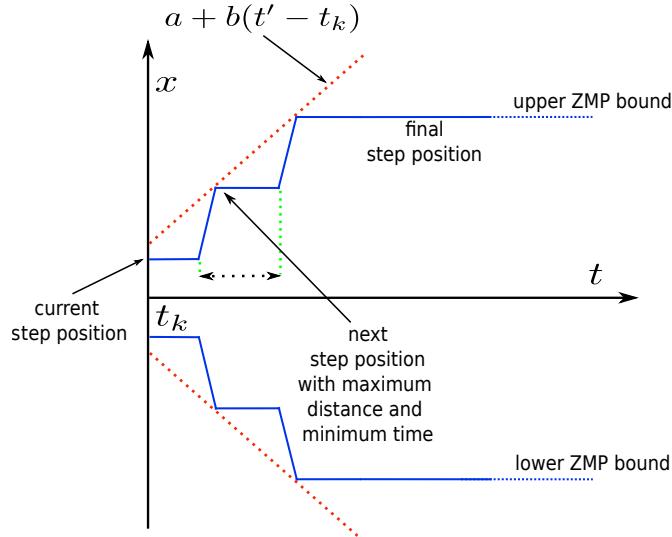
$$\dot{x} = f(x,t) + g(x,t)u$$
$$y = h(x,t)$$

and a desired output y_d. The problem is that of computing a solution x_d, u_d, y_d so that

$$\dot{x}_d = f(x_d,t) + g(x_d,t)u_d$$
$$y_d = h(x_d,t),$$

which can be used as a feedforward term of an output tracking control law. The operator $\mathcal{A}$ is used to compute x_d, u_d, by enforcing the boundary conditions $x(\pm\infty) = 0$ to the dynamics ($\mathcal{N}$ does the same with an iterative procedure). The bounded state trajectory obtained when initializing the system with the exact stability condition x^* is the same as that computed through the operator $\mathcal{A}$. Stable inversion constitutes a generalization of the regulator theory of [239];

- we stated in the previous discussions that the requirement for the computation of a stability condition, as well as to apply the operators $\mathcal{A}$ and $\mathcal{N}$, is that the

Figure 6.2: Given a maximum step length and a minimum step duration, it is possible to geometrically construct the upper bound for the future ZMP trajectory (reported for both positive and negative forward velocity). The oblique parts of the ZMP bounds correspond to the double support phases.

system is hyperbolic, i.e., it does not have the poles[1] on the imaginary axis. [240] showed a technique for stable inversion of non-hyperbolic systems, consisting in perturbing the dynamics to achieve hyperbolicity.

6.2 LIP case

Let t_k be a generic time instant. The stability condition for the LIP corresponds to the unique initialization of the unstable component x_u for which the CoM remains bounded with respect to the ZMP.

Before presenting the condition, we discuss a property of the ZMP trajectory during gaits. In the following, we will use the fact that the future ZMP trajectory is bounded by a linear function

$$|x_z(t') - x_z(t)| \leq a + b(t' - t), \quad \forall t' \geq t, \text{ for some } a, b > 0. \tag{6.4}$$

The ZMP can in fact admit jumps in the case of instantaneous change of contacts[2], but it can not exceed the support region to meet the balance condition, and the latter depends on the kinematic capabilities of the robot. This implies that the ZMP jumps can not be unlimited. The expression of a and b is not relevant for the subsequent elaborations, however we report a graphical way to obtain them for the case of planar walk in Figure 6.2.

We can now formalize the stability condition:

---

[1] Or the eigenvalues of the linearized model, in the case of a nonlinear system.

[2] Assuming instantaneous contact switch during walking is common in the literature, as for instance it simplifies the generation of reference ZMP trajectories or the contact switch management during a gait generation algorithm [3, 175, 197]. This approximation is justified by the biomechanical observation that the single support duration lasts more than the half of the full step duration [241].

Proposition 1 *Assume that (6.4) holds, and that*

$$x_u(t_k) = \eta \int_{t_k}^{\infty} e^{-\eta(\tau - t_k)} x_z(\tau) d\tau, \tag{6.5}$$

then, (4.12) is internally stable, i.e., x_c is bounded with respect to x_z:

$$\exists M > 0 : |x_c(t) - x_z(t)| \leq M, \qquad t \geq t_k.$$

Proof. The unstable subsystem of the LIP

$$\dot{x}_u = \eta(x_u - x_z),$$

if initialized with (6.5), evolves as

$$x_u(t) = \eta \int_t^{\infty} e^{-\eta(\tau - t)} x_z(\tau) d\tau.$$

We add and subtract $x_z(t)$ inside the integral to obtain

$$x_u(t) = \eta \int_t^{\infty} e^{-\eta(\tau - t)} (x_z(\tau) + x_z(t) - x_z(t)) d\tau.$$

The integral can be decomposed in

$$x_u(t) = \eta \int_t^{\infty} e^{-\eta(\tau - t)} x_z(t) d\tau + \eta \int_t^{\infty} e^{-\eta(\tau - t)} (x_z(\tau) - x_z(t)) d\tau$$

of which the first term can be solved being $x_z(t)$ independent from τ, yielding

$$x_u(t) - x_z(t) = \eta \int_t^{\infty} e^{-\eta(\tau - t)} (x_z(\tau) - x_z(t)) d\tau.$$

Let us now consider the module of the previous equation and use the assumption $|x_z(t') - x_z(t)| \leq a + b(t' - t)$ to bound the integral on the right hand side of the previous expression:

$$
\begin{aligned}
|x_u(t) - x_z(t)| &= \left| \eta \int_t^{\infty} e^{-\eta(\tau - t)} (x_z(\tau) - x_z(t)) d\tau \right| \\
&\leq \left| \eta \int_t^{\infty} e^{-\eta(\tau - t)} |x_z(\tau) - x_z(t)| d\tau \right| \\
&\leq \left| \eta \int_t^{\infty} e^{-\eta(\tau - t)} (a + b(\tau - t)) d\tau \right| \\
&= a + \frac{b}{\eta} = M_u,
\end{aligned}
$$

where the passage of the second line is possible due to the positivity of the exponential function. The bound on $|x_u(t) - x_z(t)|$ can be used with (4.16) to deduce that

$$|\dot{x}_u| \leq \eta M_u.$$

To demonstrate the boundedness of the CoM with respect to the ZMP, we proceed by

recalling that the dynamics of the CoM in terms of the evolution of x_u is [162]

$$\dot{x}_c = -\eta(x_c - x_u).$$

By treating x_u as an input, this dynamics has an explicit form given by

$$x_c(t) = x_c(t_k)e^{-\eta(t-t_k)} + \eta \int_{t_k}^{t} e^{-\eta(t-\tau)}x_u(\tau)d\tau.$$

Expanding the integral by parts and using the triangle inequality[3] allows to bound the difference between x_c and x_u as

$$|x_c(t) - x_u(t)| \le \left| (x_c(t_k) - x_u(t_k)) e^{-\eta(t-t_k)} \right| + \left| \int_{t_k}^{t} e^{-\eta(t-\tau)}\dot{x}_u(t)d\tau \right| \le S + M_u.$$

Here, we defined $S = |x_c(t_k) - x_u(t_k)|$ (that is equal to zero when the robot is in static equilibrium) and used the bound on $\dot{x}_u$.

A bound on the possible CoM/ZMP displacement is obtained as

$$|x_c(t) - x_z(t)| \le |x_c(t) - x_u(t)| + |x_u(t) - x_z(t)| \le S + 2M_u = M, \qquad (6.6)$$

thus proving the thesis. ∎

The anticausality of the stability condition (6.5) has a particular interpretation in the case of the LIP model [3, 126]. Solving the gait generation problem using such reduced model consists in computing a bounded CoM trajectory given a desired ZMP profile. In fact, the ZMP is the conceptual input of the LIP dynamics (4.12) as it should be free to vary according to the contact sequence and the balance condition.
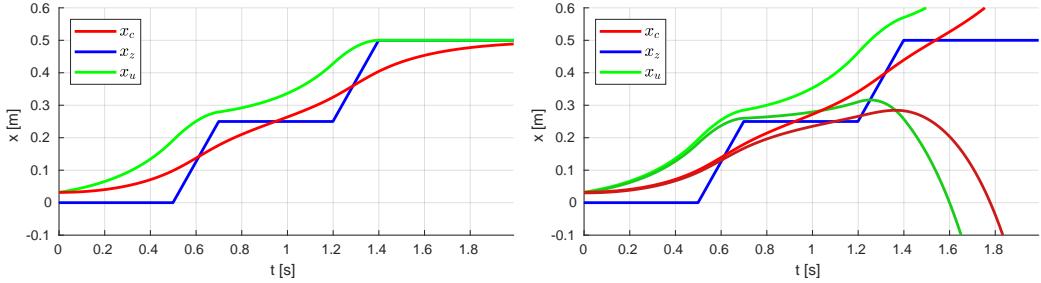
The interesting point is that, in a dynamic gait, the CoM should move in advance with respect to the ZMP. If for instance a step is planned at a certain time t_s, for which a step ZMP profile is planned, the CoM must start its motion before the ZMP jumps from the current to the next step location. A bounded and dynamically stable CoM/ZMP profile implies that the CoM acts based on the *future* evolution of the ZMP [3]. Given a specific ZMP profile, there exists a unique initial condition for which the CoM will not diverge and act according to the dynamics, and it is expressed by (6.5), as shown in Fig. 6.3. The figure reports the CoM/DCM/ZMP trajectories for the motion on the x component when the robot has to perform two steps. When the precise initial condition is met, the CoM remains bounded with respect to the ZMP for the whole time of the motion, whereas a minimum perturbation would cause the divergence of the CoM and the DCM.

We conclude the section with a list of remarks:

- as it was highlighted in the previous paragraphs, anticausality is a key point in dynamic legged locomotion. A method to handle it is to use predictive controllers: they constitute *de facto* the current standard for addressing locomotion problems;

- as briefly discussed in the previous section, the stability condition (6.5) can be interpreted as a constraint on the desired ZMP trajectory, when the LIP has a specific initialization. Such concept is used in [126] for gait generation (and in this

---

[3] $|\alpha + \beta| \le |\alpha| + |\beta|, \ \forall \alpha, \beta \in \mathbb{R}.$

Figure 6.3: CoM/DCM trajectories for an assigned ZMP profile for a two step gait with stride length of 0.25 m, single support duration of 0.5 s and double support duration of 0.2 s (using $h = 0.71$ m, $\eta = 3.72$ s^{-1}). On the left, the state is initialized with the stability condition, whereas on the right a perturbation ϵ of ± 0.001 m is applied to the stability condition, causing the divergence of the CoM (and the DCM) with respect to the ZMP. Note how the CoM starts moving in advance with respect to the ZMP.

thesis, based on [127], to derive the so-called stability constraint in the proposed MPC formulations);

- the stability condition is not robust to perturbations, as shown in Fig. 6.3. Proposition 2 could be formulated as a necessary and sufficient condition for boundedness[4]. In fact, any initial condition

$$x_u(t_k) = \eta \int_{t_k}^{\infty} e^{-\eta(\tau - t_k)} x_z(\tau) d\tau + \Delta x_u(t_k) \qquad (6.7)$$

would result in an evolution

$$x_u(t_k) = \eta \int_{t}^{\infty} e^{-\eta(\tau - t)} x_z(\tau) d\tau + \Delta x_u(t_k) e^{\eta(t - t_k)} \qquad (6.8)$$

which is unbouded. However, applying it as a constraint within an optimzation-based closed-loop controller can still enforce the stability for the LIP as demonstrated in [127];

- the stability condition (6.5) identifies a subset[5] of the viability kernel [50, 113, 176, 243] of the robot. For a given ZMP trajectory contained in the support region, the LIP states satisfying (6.5) at t_k will evolve in the viability kernel and prevent the robot from falling.

6.3 Perturbed LIP case

The effect of a small perturbation on the stability condition causes the divergence of the CoM with respect to the ZMP. It is then important to derive the stability condition in the presence of disturbances. To this purpose, consider:

---

[4]We reported the sole sufficient condition in the proposition to retain a conceptual consistency with the stability constraints that are built over the stability condition in the next chapters. It is only possible, in that cases, to show sufficient conditions for boundedness when the scheme is recursively feasibile.

[5]It is a subset because it depends on an assigned ZMP profile, i.e., a specific footstep position and timing. The viability kernel, on the other hand, depends on the maximum step length and minimum step timing [176, 242].

Proposition 2 *Assume that (6.4) holds, $w_x \in \sup \mathcal{W}_x$, and that*

$$x_u(t_k) = \eta \int_{t_k}^{\infty} e^{-\eta(\tau - t_k)} x_z d\tau - \frac{1}{\eta} \int_{t_k}^{\infty} e^{-\eta(\tau - t_k)} w_x d\tau, \qquad (6.9)$$

then, system (4.25) is internally stable, i.e., x_c is bounded with respect to x_z:

$$\exists M > 0 : |x_c(t) - x_z(t)| \leq M, \qquad t \geq t_k.$$

Proof. The unstable subsystem of the perturbed LIP

$$\dot{x}_u = \eta(x_u - x_z) + w_x/\eta,$$

if initialized with (6.9), evolves as

$$x_u(t) = \eta \int_t^{\infty} e^{-\eta(\tau - t)} x_z(\tau) d\tau - \frac{1}{\eta} \int_t^{\infty} e^{-\eta(\tau - t)} w_x d\tau. \qquad (6.10)$$

We add and subtract $x_z(t)$ inside the first integral to obtain

$$x_u(t) = \eta \int_t^{\infty} e^{-\eta(\tau - t)} (x_z(\tau) + x_z(t) - x_z(t)) d\tau - \frac{1}{\eta} \int_t^{\infty} e^{-\eta(\tau - t)} w_x d\tau.$$

Following the same procedure as for the proof of Prop. 1, we get

$$x_u(t) - x_z(t) = \eta \int_t^{\infty} e^{-\eta(\tau - t)} (x_z(\tau) - x_z(t)) d\tau - \frac{1}{\eta} \int_t^{\infty} e^{-\eta(\tau - t)} w_x d\tau.$$

Considering the module and (6.4), we can write
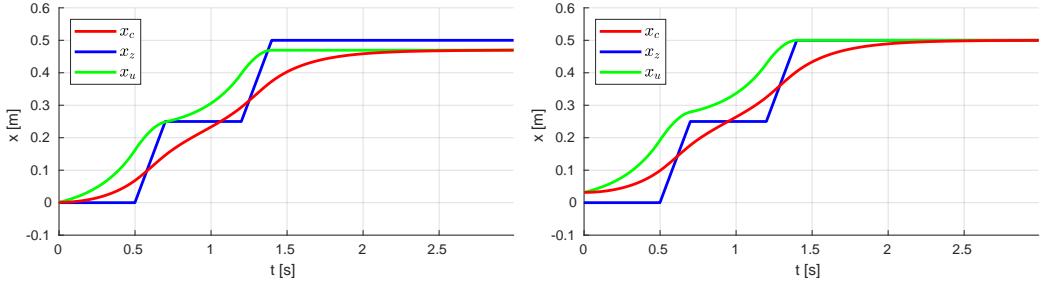
$$
\begin{aligned}
|x_u(t) - x_z(t)| &= \left| \eta \int_t^{\infty} e^{-\eta(\tau - t)} (x_z(\tau) - x_z(t)) d\tau - \frac{1}{\eta} \int_t^{\infty} e^{-\eta(\tau - t)} w_x d\tau \right| \\
&\leq \left| \eta \int_t^{\infty} e^{-\eta(\tau - t)} (x_z(\tau) - x_z(t)) d\tau \right| + \left| -\frac{1}{\eta} \int_t^{\infty} e^{-\eta(\tau - t)} w_x d\tau \right| \\
&\leq \left| a + \frac{b}{\eta} \right| + \left| -\frac{1}{\eta} \int_t^{\infty} e^{-\eta(\tau - t)} \sup \Delta_x d\tau \right| \\
&\leq \left| a + \frac{b}{\eta} \right| + \left| \frac{\sup \Delta_x}{\eta^2} \right| = a + \frac{b}{\eta} + \frac{\sup(w_m + \Delta_x)}{\eta^2} \\
&= M_u
\end{aligned}
\qquad (6.11)
$$

in which we also used the assumptions $|x_z(t') - x_z(t)| \leq a + b(t' - t)$ and $w_x \in \sup \mathcal{W}_x$ to obtain a bound. From (4.27), we deduce that
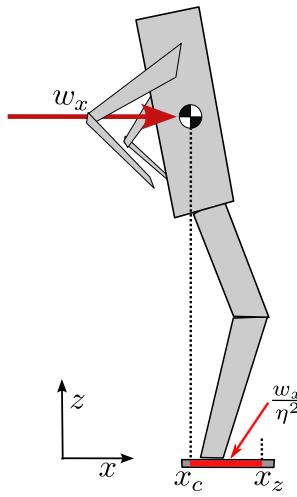
$$|\dot{x}_u| \leq \eta M_u.$$

We now follow the procedure of the conclusion of the proof of Prop. 1. In the perturbed case, the CoM/DCM dynamics are the same as the nominal case, writing

$$\dot{x}_c = -\eta(x_c - x_u)$$

Figure 6.4: CoM/DCM/ZMP trajectories (same parameters as for the previous example). On the left, the state is initialized with the stability condition (6.9) and remains bounded in spite of the presence of the perturbation $w_x(t) = 0.4$ m/s^2. On the right, the unperturbed case is shown. The difference between the two plots is an offset determined by the disturbance trajectory, denoted in the manuscript as a *leaning* against the action of the perturbation.

Figure 6.5: A schematic representation of the leaning behavior at steady state on the sagittal component.

that is expanded in

$$x_c(t) = x_c(t_k)e^{-\eta(t-t_k)} + \eta \int_{t_k}^{t} e^{-\eta(t-\tau)}x_u(\tau)d\tau$$

allowing to get

$$|x_c(t) - x_u(t)| \leq \left|(x_c(t_k) - x_u(t_k))\,e^{-\eta(t-t_k)}\right| + \left|\int_{t_k}^{t} e^{-\eta(t-\tau)}\dot{x}_u(t)d\tau\right| \leq S + M_u.$$

with $S = |x_c(t_k) - x_u(t_k)|$. A bound on the CoM/ZMP displacement is obtained as

$$|x_c(t) - x_z(t)| \leq |x_c(t) - x_u(t)| + |x_u(t) - x_z(t)| \leq S + 2M_u = M, \qquad (6.12)$$

thus proving the thesis. ∎

The proof of Prop. 2 is the same as that of Prop. 1, except for the first part, where the assumption on the finiteness of the disturbance allows for the determination of a bound for $|\dot{x}_u|$.

To conclude the section, we report in Fig. 6.4 a plot (left) of the evolution of the CoM and DCM trajectory in the presence of the disturbance $w_x(t) = 0.4 \text{ m/}s^2$ when initialized with (6.9). The evolution of the LIP state does not present divergence and showcases a displacement with respect to the unperturbed case, shown in the left plot. The displacement appears as a motion towards the effect of the perturbation, as that reported in Fig. 6.5. This behavior, when the simulated robot comes to a stop, is consistent with the static analysis (5.8) of Sect. 5.2.1, and, within the thesis, will be denoted as a *leaning* against the action of the disturbance[6]. The hypothesis $w_x \in \sup \mathcal{W}_x$ from the disturbance model ensures instead a physical consistency with the kinematic and actuation capabilities of the humanoid, constituting a limit on the possible leaning of the robot[7].

6.4 VH-IP case

We reported in Sect. 4.4.3 that the VH-IP model admits the exponential dichotomy (4.33)-(4.34) under the change of coordinates (4.32) provided that the two Riccati equations (4.35)-(4.36) are satisfied. We recall here the the stability condition for the VH-IP [197, 217]:

Proposition 3 *Assume that* $\lim_{t \to \infty} \lambda(t) = \lambda_f < \infty$, $\lim_{t \to \infty} x_z(t) = x_{z,f} < \infty$ *and that*

$$x_u(t_k) = \int_{t_k}^{\infty} e^{-\Omega(t)} \lambda(t) x_z(t) dt, \tag{6.13}$$

where $x_u(t_k) = \omega(t_k) x_c + \dot{x}_c$, $\Omega(t)$ *is the antiderivative of* $\omega(t)$ *such that* $\Omega(0) = 0$. *Then* $x_u(t)$ *remains finite at all times.*

The condition expressed by (6.13) implies solving the nonlinear Riccati differential equation (4.35) when using the stability condition for gait generation. Furthermore, the ZMP trajectory must be bounded. The latter is not a strict assumption (as a humanoid would stop walking at a certain point).

6.5 Combined models

In Chapters 7-8-9, we will implement the stability conditions for the LIP and perturbed LIP as linear equality constraints within a MPC framework. To retain a linear formulation with the possibility of including flight phases when using the VH-IP model, we propose to define time-varying systems of combined models for which a specific stability condition will be derived in this section. Such approach does not require solving a Riccati differential equation.

6.5.1 VH-IP and LIP case

Let δ be a time interval so that the time steps $t_{k+i+1} - t_{k+i} = \delta$, $\forall i \geq 0$, $T_c = \delta C$ a finite time interval, and $t_{k+C} = t_k + T$. The time-varying system defined as

$$\ddot{x}_c = \begin{cases} \lambda^{k+i}(x_c - x_z) & \text{for} \quad t \in [t_{k+i}, t_{k+i+1}), \quad i = 0, \ldots, C-1 \\ \lambda_{\text{LIP}}(x_c - x_z) & \text{for} \quad t \geq t_{k+C}, \end{cases} \tag{6.14}$$

---

[6]In line with [6, 163].

[7]The fact that, according to (5.6), w_x may be part of $\mathcal{W}_{i_x}$ is irrelevant.

with

$$\lambda^{k+i} = \lambda(t_{k+i}) = \frac{\ddot{z}_c^{k+i} + g}{z_c^{k+i} - z_z^{k+i}}$$

and $\lambda_{\mathrm{LIP}} = g/(x_z^{k+C} + h^{k+C})$, consists in a VH-IP model with sampled pendulum frequency over time steps δ for $t \in [t_k, t_{k+C})$ and a time-invariant LIP model for $t \geq t_{k+C}$. Note that we adopt the notation $x_c^k = x_c(t_k)$ for all the states and inputs.

We now formulate a stability condition for system (6.14):

Proposition 4 *Assume that* (6.4) *holds, and that the current state* $(x_c^k, \dot{x}_c^k)$ *satisfies*

$$G\,\Phi(t_{k+C}, t_k) \begin{bmatrix} x_c^k \\ \dot{x}_c^k \end{bmatrix} + \int_{t_k}^{t_{k+C}} G\,\Phi(t_{k+C}, \tau) B(\tau) x_z(\tau) d\tau = x_u^{k+C} \qquad (6.15)$$

where $G = (1 \quad 1/\sqrt{\lambda_{\mathrm{LIP}}})$, *the terms* $\Phi(t_{k+C}, t)$ *and* $B(t)$ *are the state transition and the input matrix for system (6.14) for* $t \in [t_k, t_{k+C})$, *and*

$$x_u^{k+C} = \sqrt{\lambda_{\mathrm{LIP}}} \int_{t_{k+C}}^{\infty} e^{-\sqrt{\lambda_{\mathrm{LIP}}}(\tau - t_{k+C})} x_z(\tau) d\tau. \qquad (6.16)$$

Then, system (6.14) evolves with bounded x_c *with respect to* x_z:

$$\exists M > 0 : |x_c(t) - x_z(t)| \leq M, \qquad t \geq t_k.$$

Proof. System (6.14) is equivalent to a LIP (4.12) for $t \geq t_{k+C}$. Proposition 1 then states that if x_u^{k+C} is given by (6.16), then the subsequent evolution of x_c is bounded with respect to x_z. On the other hand, it is $x_u^{k+C} = G\,(x_c^{k+C} \quad \dot{x}_c^{k+C})^T$, with

$$\begin{bmatrix} x_c^{k+C} \\ \dot{x}_c^{k+C} \end{bmatrix} = \Phi(t_{k+C}, t_k) \begin{bmatrix} x_c^k \\ \dot{x}_c^k \end{bmatrix} + \int_{t_k}^{t_{k+C}} \Phi(t_{k+C}, \tau) B(\tau) x_z(\tau) d\tau.$$
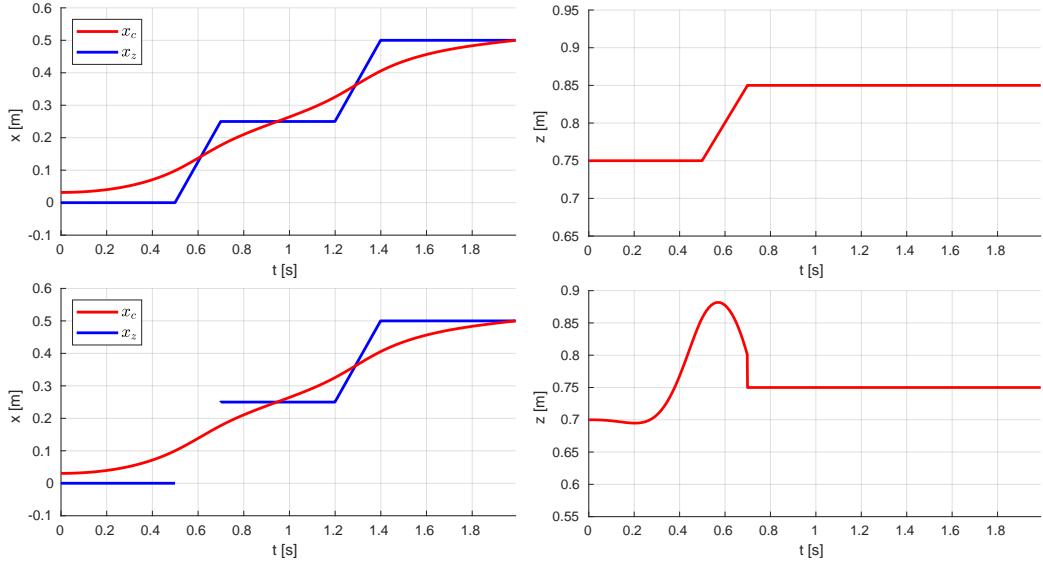
The thesis is then obtained from it. ∎

Equation (6.15) imposes a condition on the state at time $t = t_{k+C}$. Bringing the integral of the left hand side to the right highlights an equation with a similar shape to that of the LIP (6.5), in which a linear combination of the current state must be equal to a certain quantity that depends on the future ZMP trajectory.

It should be noted that Prop. 4 does not rely on any hypotheses on the continuity of λ and x_z, which is instead required in [217][8]. This has a specific advantage. In fact, a feature of system (6.14) is the possibility to model flight phases, provided that they happen within the time range $[t_k, t_{k+C})$. Inside the prediction horizon, the stability condition uses the state transition function that can be properly written for flight phase time steps. This implies that (6.15) works also for running gaits or jumps. Specific implementation details will be provided in Chapter 10.

Figure 6.6 showcases the vertical and horizontal CoM and the ZMP trajectories when applying the stability condition in the case of: (*i*) a CoM height raising, (*ii*) a jumping motion. We chose for the latter a model switching time happening as soon as the robot is supposed to land, without letting it complete the typical biomechanical absorption phase [203]. No significant difference can be observed between the two examples on the

---

[8]Continuity of the ZMP is not strictly required in [197], but such case is not explored within the contribution.

Figure 6.6: Stability condition applied to the combined model composed by a VH-IP and a LIP: (top left and top right) two steps with a CoM height increase during the first double support phase, (bottom left and right) the first of the two steps has a flight phase and in fact the ZMP is not defined during such time. The model switching time is set here to $T = 0.7$ and $\lambda_{\text{LIP}} = 3.72$ s $^{-1}$.

horizontal trajectories, even in the case of strong variations in the vertical CoM motion, which, in the jumping case, comprises both a flight phase and a discontinuity at t_{k+C}.

6.5.2 Perturbed VH-IP and LIP case

It is instrumental to derive a stability condition also for the perturbed version of system (6.14). Consider

$$\ddot{x}_c = \begin{cases} \lambda^{k+i}(x_c - x_z) + w_x & \text{for} \quad t \in [t_{k+i}, t_{k+i+1}) \quad i = 0, \dots, C-1 \\ \lambda_{\text{LIP}}(x_c - x_z) + w_x & \text{for} \quad t \geq t_{k+C}, \end{cases} \tag{6.17}$$

then the stability condition writes as:

Proposition 5 *Assume that* (6.4) *holds,* $w_x \in \sup \mathcal{W}_x$, *and that the current state* $(x_c^k, \dot{x}_c^k)$ *satisfies*

$$G\Phi(t_{k+C}, t_k) \begin{bmatrix} x_c^k \\ \dot{x}_c^k \end{bmatrix} + \int_{t_k}^{t_{k+C}} G\Phi(t_{k+C}, \tau)B(\tau)x_z(\tau)d\tau = $$
$$x_u^{k+C} - \int_{t_k}^{t_{k+C}} G\Phi(t_{k+C}, \tau)Dw_x(\tau)d\tau \tag{6.18}$$

where the disturbance matrix is $D = (0 \ 1)^T$ *and*

$$x_u^k = \sqrt{\lambda_{\text{LIP}}} \int_{t_k}^{\infty} e^{-\sqrt{\lambda_{\text{LIP}}}(\tau - t_k)} x_z(\tau)d\tau - \frac{1}{\sqrt{\lambda_{\text{LIP}}}} \int_{t_k}^{\infty} e^{-\sqrt{\lambda_{\text{LIP}}}(\tau - t_k)} w_x(\tau)d\tau.$$

Then, system (10.21) is internally stable in the sense that

$$\exists M : |x_c(t) - x_z(t)| \leq M, \qquad t \geq t_k.$$

Proof. The demonstration proceeds as for Prop. 4 while using the stability condition (6.9) for the perturbed LIP at time t_{k+C}. ∎

Chapter 7

Robust gait generation using MPC in the presence of persistent disturbances
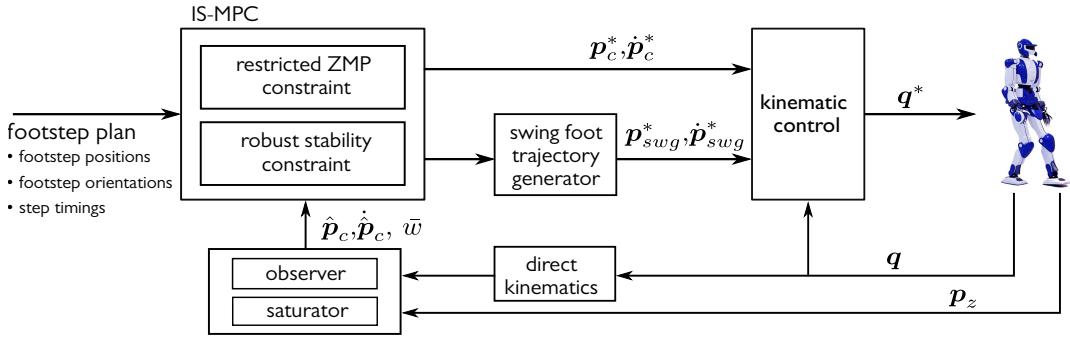
We elaborated until this point on the technical ingredients needed to formulate the gait generation schemes that are the core contribution of this manuscript. The objective of this chapter is thus to formulate and present the first method for generating a humanoid gait under the effect of perturbations. The objective is that of realizing as closely as possible a predefined sequence of footsteps.

As we stated in Chapter 5, perturbations can be of different nature: they can be persistent, such as the effect of gravity when walking on a slope, or impulsive, e.g., a strong push. We focus here on persistent disturbances, i.e., all the signals w_x, endogenous and exogenous, for which it is reasonable to assume that $w_x \in \mathcal{W}_x$ and $\dot{w}_x \in \dot{\mathcal{W}}_x$ (and clearly $w_x \in \sup \mathcal{W}_x$). Note that the sole assumption that is strictly required for the consistency of the method is $w_x \in \sup \mathcal{W}_x$, whereas the others are just used for design.

The approach that is here adopted consists in accounting for the disturbances by generating suitable CoM/ZMP trajectories via MPC rather than modifying the gait pace or the step length to clear the perturbations. This is possible because of the assumption on the disturbance model. Methodologies to generate robust gaits in the case of disturbances such that $w_x \notin \mathcal{W}_x$, $\dot{w}_x \notin \dot{\mathcal{W}}_x$ and/or $w_x \notin \sup \mathcal{W}_x$ will be discussed in the next chapters.

The proposed approach for robust gait generation consists in a linear MPC scheme [127] that uses the perturbed LIP as prediction model, together with two different tools working in conjunction: the robust stability constraint [6], that exploits a disturbance observer, and the ZMP constraint restriction [7]. These ideas were developed as separated contributions in previous works, while here we present a scheme and a theory unifying the two methods.

The underlying philosophy, motivated by the various results in the control literature, is to identify formal guarantees on robustness, given a disturbance set. The feasibility of the proposed scheme under perturbations will be characterized by means of the so called *feasibility region*, i.e., a subset of the state space for which the constrained optimization problem to be solved is feasible. This result will permit to investigate on sufficient conditions for recursive feasibility based on a specific design of the constraints. In particular, the ZMP constraint restriction is modulated to ensure feasibility between

Figure 7.1: Block scheme of the proposed approach. The represented feedback interconnection assumes that the observer reconstructs the centroidal state. If the disturbance estimator is not able to do it, as that of Sect. 5.2.1, the measured ZMP and the output of the direct kinematics go into the MPC block (even though a measurement filtering stage is always recommended).

subsequent sampling intervals and at all times depending on the available knowledge on the disturbance and observer behavior, given a feasible initialization of the problem.

The overall result is a scheme for robust gait generation that has no additional computational burden with respect to a standard MPC formulation [127, 180], while providing robustness guarantees under certain hypotheses. The chapter is concluded with a result section, involving illustrative simulations on the LIP model, as well as multi-body tests in a dynamic environment. Eventually, the scheme is validated through experiments on a NAO and a OP3 humanoid platforms.

7.1 The scheme

Let δ be the duration of the sampling interval adopted for control and let the generic time instant be denoted by $t_k = k\,\delta$. As for the previous chapters, the k superscript for a variable x indicates $x(t_k) = x^k$.

Figure 7.1 shows a block scheme representation of the proposed architecture. At each t_k, the input is given by a part of a planar[1] *footstep plan*, which either comes from a footstep planner or is assigned by an operator. In this chapter we do not provide a description of it. Interested readers can find further information in [127, 185–187]. The footstep planner consists in a sequence of footsteps characterized by their position in space, their timing, and their orientation. The whole footstep plan, from its beginning to its completion, covers a time span T_M.
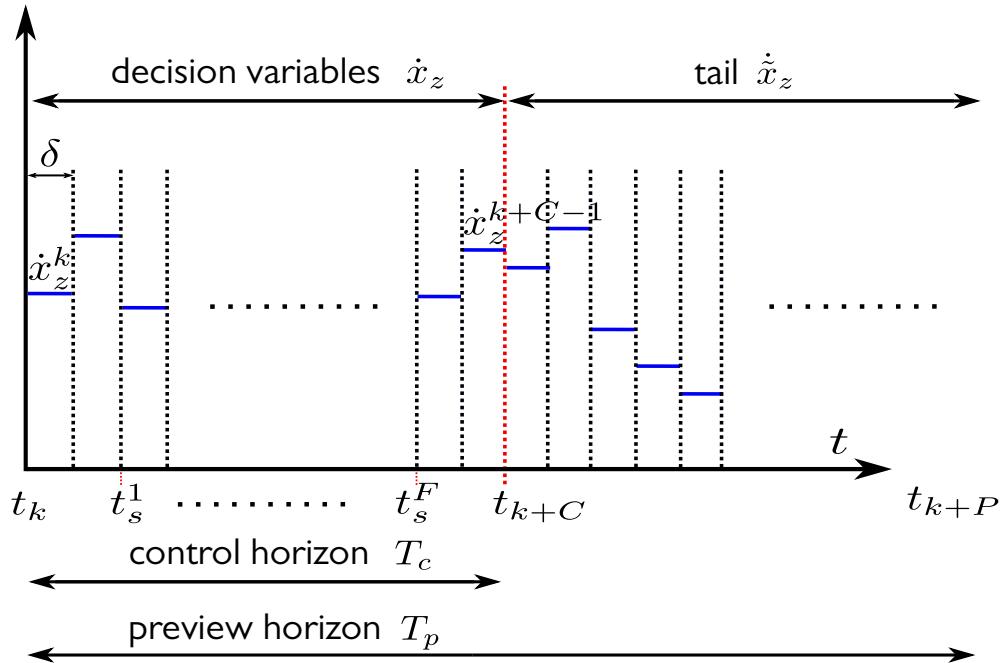
For the sake of compactness, we assume, without loss of generality, that all footstep have the same orientation. This simplifies the exposition by decoupling the sagittal (xz-plane) from the coronal (yz-plane) component, allowing to present the method for the x-axis only, as also shown in Chapter 4. Equations for y will be omitted in the following unless different from their sagittal counterpart.

We represent the generic footstep plan as a sequence of M footstep positions in the x-y plane with the associated timing:

$$X_f^k = (x_f^1, \ldots, x_f^M), \quad Y_f^k = (y_f^1, \ldots, y_f^M), \quad \tau_s^k = (t_s^1, \ldots, t_s^M),$$

where (x_f^j, y_f^j), $j = 1, \ldots, M$, defines the position of the j-th footstep and t_s^j the

---

[1]All footstep lie on the same plane.

Figure 7.2: Representation of the time windows considered in the proposed scheme. The MPC optimization problem is solved over the control horizon T_c, whereas information regarding the footstep plan over the preview horizon $T_p \geq T_c$ is assumed to be available at each time t_k.

corresponding timestamp. At time t_s^j a new double support phase begins. The duration of the j-th step is given by $T_s^j = t_s^{j+1} - t_s^j$, composed by a double and a single support phase. Their duration is respectively T_{ds}^j and T_{ss}^j.

As time passes during operation, it is assumed that a minimum amount of information from the plan, covering a fixed time span generally smaller than T_M, is available to the proposed scheme (thus constituting the actual input). This time interval is denoted as *preview horizon* T_p, which will contain data relative to F footsteps, with $F \leq M$. The preview horizon slides at each time t_k until the full execution of the plan.

The presented architecture is based on Model Predictive Control. A constrained optimization problem, initialized with the current state and disturbance estimate[2], is solved over a receding and finite time window. We denote this temporal span as the *control horizon*, that covers C sampling intervals, i.e., $T_c = C \delta$, with $T_c \leq T_p$. The first sample of the solution of the optimal control problem is used to integrate the adopted prediction model and retrieve a reference position and velocity for the CoM $\boldsymbol{p}_c^*, \dot{\boldsymbol{p}}_c^*$. Together with a reference swing foot pose $\boldsymbol{p}_{swg}^*, \dot{\boldsymbol{p}}_{swg}^*$, the data are processed by a kinematic controller block[3] that is in charge of converting the Cartesian references (and orientations) into joint commands.

---

[2]The scheme of Fig. 7.1 operates, without loss of generality, at a single frequency dictated by the sampling interval δ. When the situation requires operating at various frequencies, e.g., when the MPC and the measurements work at different rates, it is possible to implement solutions such as [244].

[3]This block can be substituted by an inverse dynamics based controller when using a torque controlled humanoid [94].

7.1.1 Prediction and disturbance model

Consider the the perturbed LIP (4.25). We recall the expression of the dynamics to simplify the reading of the rest of the chapter:

$$\ddot{x}_c = \eta^2(x_c - x_z) + w_x, \tag{7.1}$$

where w_x is the perturbation signal. We adopt as prediction model for the proposed MPC formulation the dynamically extended perturbed LIP

$$\begin{bmatrix} \dot{x}_c \\ \ddot{x}_c \\ \dot{x}_z \end{bmatrix} = \begin{bmatrix} 0 & 1 & 0 \\ \eta^2 & 0 & -\eta^2 \\ 0 & 0 & 0 \end{bmatrix} \begin{bmatrix} x_c \\ \dot{x}_c \\ x_z \end{bmatrix} + \begin{bmatrix} 0 \\ 0 \\ 1 \end{bmatrix} \dot{x}_z + \begin{bmatrix} 0 \\ 1 \\ 0 \end{bmatrix} w_x. \tag{7.2}$$

The ZMP velocity $\dot{x}_z$ is selected as input. In line with the MPC formulation, the decision variables are piecewise-constant, namely $\dot{x}_z(t) = \dot{x}_z^k$ for $t \in [t_k, t_{k+1})$, and thus ZMP trajectory is piecewise-linear. This dynamic extension is introduced to generate smooth ZMP profiles. The disturbance w_x, as discussed in Chapter 5, could be either internal (e.g., unmodeled dynamics) or external (e.g., the effect of a carried load).

At this point, we assume that w_x satisfies the modeling of persistent disturbances given in Chapter 5, namely

$$\begin{aligned} w_x &\in \mathcal{W}_x \\ \dot{w}_x &\in \dot{\mathcal{W}}_x, \end{aligned}$$

with

$$\begin{aligned} \mathcal{W}_x &= \{w_x : w_{m,x} - \Delta_x \leq w_x \leq w_{m,x} + \Delta_x\} \\ \dot{\mathcal{W}}_x &= \{\dot{w}_x : -\dot{\Delta}_x \leq w_x \leq \dot{\Delta}_x\}, \end{aligned}$$

with $w_{m,x}$ corresponding to the midrange disturbance, Δ_x the maximum deviation from it, and $\dot{\Delta}_x$ the disturbance derivative bound.

The knowledge of $\mathcal{W}_x$ and $\dot{\mathcal{W}}_x$ is considered to be available, i.e., we have access to a value for the midrange $w_{m,x}$, the maximum deviation Δ_x, and for $\dot{\Delta}_x$. This information can be either inferred by analyzing the possible disturbances that we want the robot to be robust to or by treating the sets as design parameters[4]. Consider the following example. Let the robot be walking on a descending slope with unknown angle θ. The component of gravity tangent to the ground can be seen as a horizontal disturbance $mg \sin \theta$ acting on the robot CoM, with m the robot mass. The value of θ may not be known but it is reasonable to assume it to be contained in a set, given reasonable slopes that a robot can dynamically walk over without footstep re-planning due to friction considerations. We could have for instance $F_{\text{ext,x}}^{\max} = mg \sin \theta^{\max}$ N and $F_{\text{ext,x}}^{\min} = mg \sin 0$ N, which can be then modelled by the formalization of the $\mathcal{W}_x$ set (5.3). In this case, an arbitrary low value can be set for $\dot{\Delta}_x$.

This, however, may not be the case in general. According to the situation, it is also possible that the disturbance knowledge belongs to one of the listed cases:

- A) $w_x \in \sup \mathcal{W}_x$, $\dot{w}_x \in \dot{\mathcal{W}}_x$

---

[4]The reason for this statement will be clarified in the continuation of the chapter.

- B) $w_x \in \sup \mathcal{W}_x$.

Case (A) is when we have information on the maximum variation of the perturbation, but we do not know how large it could be. As we know the limits of the robot, one can formulate a conservative controller based on an arbitrary value representing $\sup \mathcal{W}_x$. Case (B) instead encodes the situation where no information on the disturbance is available at all. We will discuss in the next sections how the unavailability of information on the disturbance affects the guarantees provided by the controller, also providing examples of such a situation.

7.1.2 Restricted ZMP Constraints

To enforce dynamic balance, we constrain the ZMP to be within the support region (4.8), corresponding to the support polygon when walking on a flat ground. The support polygon coincides with the foot sole when the robot is single contact (single support), while during double support phases it includes the area of both feet and a surface in between, obtained by convex hull construction operation. We discuss here the procedure that enables the dynamic balance condition to be formulated as a linear inequality constraint in the MPC, introducing the concept of *moving constraint region*. Furthermore, we present an erosion of this constraint by applying a *restriction function* for robustness purposes.

Moving constraint region

The moving constraint region is a fixed size shape constructed to always be contained within the support polygon. It coincides with the footprint of the foot in contact with the ground during a single support phase, whereas it translates from a support foot to the subsequent during the double support phase so as to always be contained in the convex hull of the contact surfaces (4.8). The motion of the moving constraint happens with a predefined timing law lasting for all T_{ds}^j. See for instance Fig. 7.3.

Under the hypothesis that all footsteps have a fixed orientation[5], the moving constraint region can be represented in terms of the timing law describing its lower and upper bound $x_z^m(t)$, $x_z^M(t)$. The dynamic balance condition is then expressed as

$$x_z^m(t) \le x_z \le x_z^M(t). \tag{7.3}$$

The time-varying bounds $x_z^m(t)$ and $x_z^M(t)$ are constructed on the basis of the footstep plan as follows. Introduce first the piecewise-linear sigmoidal function
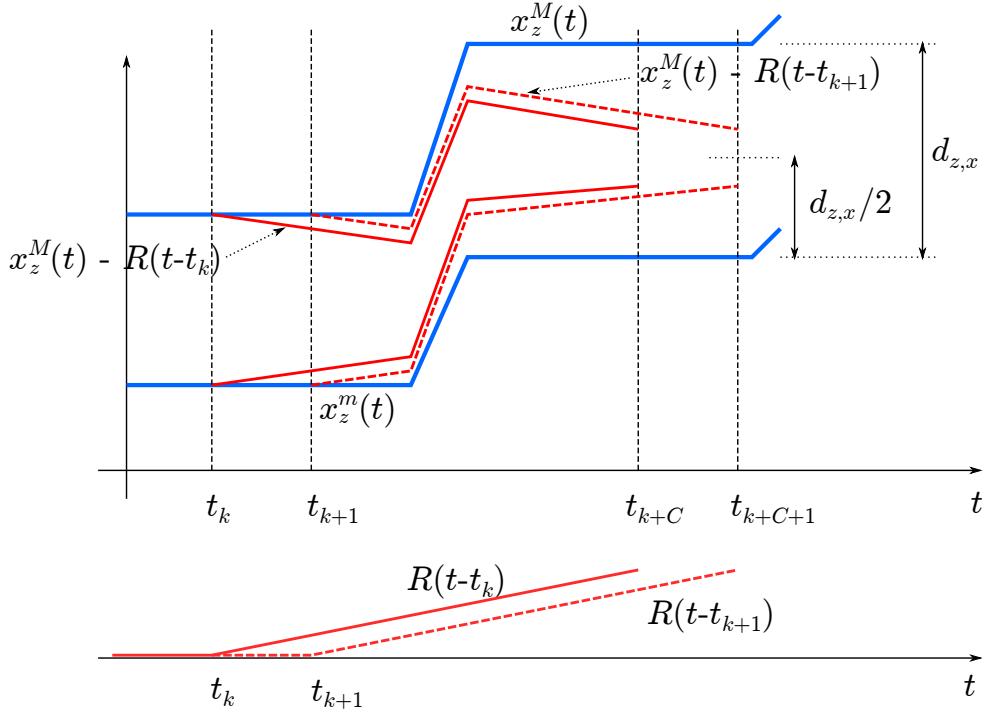
$$\sigma(t, t_i, t_f) = \frac{1}{t_f - t_i} \left(\rho(t - t_i) - \rho(t - t_f) \right), \tag{7.4}$$

with $\rho(t) = t\,\delta_{-1}(t)$ the unit ramp starting at 0, see Fig. 7.4. The bounds of the ZMP constraint (7.3) during the j-th step are then expressed as a function of time as

$$
\begin{aligned}
x_z^m(t) &= x_f^{j-1} + (x_f^j - x_f^{j-1})\sigma(t, t_s^j, t_s^j + T_{ds}^j) - \frac{1}{2}d_{z,x} \\
x_z^M(t) &= x_f^{j-1} + (x_f^j - x_f^{j-1})\sigma(t, t_s^j, t_s^j + T_{ds}^j) + \frac{1}{2}d_{z,x}
\end{aligned}
$$

---

[5]Interested readers can derive from [127] the expression for the constraint when non-fixed orientations are considered.

Figure 7.3: This picture represents the moving constraint region (blue polygonal chain), which constitutes the ZMP constraint for the proposed scheme, and how the restriction function (red polygonal chain) affects it on the x component. For illustration purpose, we considered here a linear restriction function. The restriction is applied to the original ZMP constraints at each time t_k, reducing the size of the moving constraint region over the prediction horizon. Note that the constant traits corresponds to the single support phases, while the oblique to the double support phases.

where $d_{z,x}$ is the support polygon square width. With this choice we are implicitly modeling the footprint as a square, introducing a first degree of conservativity. Thus, the area in between $x_z^m(t)$ and $x_z^M(t)$ is constant

$$x_z^M(t) - x_z^m(t) = d_{z,x}. \tag{7.5}$$

ZMP constraint restriction
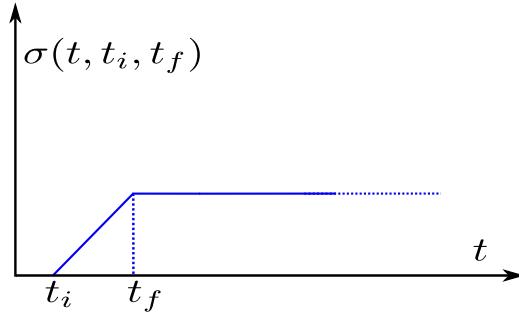
Once formulated the ZMP condition through the moving constraint region (7.3), it is possible to use it directly within the optimization problem of the proposed scheme, as in [122, 127]. We showed however in [7] the gain in terms of robustness when tightening the bounds on the predicted ZMP using a *restriction function*. By means of it, we enforce a *robust ZMP constraint*

$$x_z^m(t) + R(t - t_k) \le x_z \le x_z^M(t) - R(t - t_k), \tag{7.6}$$

corresponding to (7.3) in which the upper and lower bounds are being restricted by the function $R(t)$.

The function $R(t)$ applied to the ZMP constraint, for $t \in [0, T_c]$, has to satisfy

$$0 \le R(t) \le d_{z,x}/2 \quad \text{and} \quad R(0) = 0 \tag{7.7}$$

Figure 7.4: Graphical representation of $\sigma(t, t_i, t_f)$. The linear sigmoidal function begins its inclined trait at time $t = t_i$ and reaches the unitary plateau at time $t = t_f$.

to be denoted as a restriction function. The requirements of (7.7) impose that:

- $R(t)$ must be positive (otherwise it would enlarge the region) and it must not restrict more than the half of the ZMP square width area $d_{z,x}/2$ (being it applied to the upper and lower bound of the ZMP constraint);

- the restriction function only affects the *predicted* ZMP, in order to not modify the available area for the ZMP at the current time instant[6];

- the restriction is applied to the original ZMP constraints at each time step.

An example of (7.6) under the effect of a linear restriction function is reported in Fig. 7.3.

A general concept from the robust MPC literature [146, 147] is that future states are more uncertain: the reachable states by the action of the disturbances will depend on the cumulative effect of the perturbation along the horizon. In line of principle, the restriction, intended as a robustness tool, should act then differently at different stages of the MPC prediction, i.e., eroding more the ZMP constraints towards the end of the horizon (as in Fig. 7.3). This, however, will not necessarily be true in the present case, as it will be shown in the next sections. By now, we simply state that the profile of $R(t)$ will determine the range of disturbances for which the MPC scheme can ensure recursive feasibility.

7.1.3 Robust Stability Constraint

We showed in Chapter 4 that humanoid dynamics are inherently unstable. The unstable subsystem can generate the undesired situation for which the CoM can diverge while the ZMP is contained in the support region.

We recall that the unstable subsystem of the perturbed LIP model writes as

$$\dot{x}_u = \eta \left(x_u - x_z \right) + w_x/\eta$$

for which

$$x_u^k = \eta \int_{t_k}^{\infty} e^{-\eta(\tau - t_k)} x_z(\tau) d\tau - \frac{1}{\eta} \int_{t_k}^{\infty} e^{-\eta(\tau - t_k)} w_x(\tau) d\tau, \tag{7.8}$$

individuates the non causal stability condition (see Chapter 6).

---

[6]It will still indirectly affect the final ZMP trajectory by its effect on the prediction at any particular time.

With the objective of casting the stability condition into a causal constraint for the MPC, we rearrange (7.8) to

$$\eta \int_{t_k}^{t_{k+C}} e^{-\eta(\tau - t_k)} x_z(\tau) d\tau = x_u^k - \tilde{c}_x^k + \tilde{w}_x^k \tag{7.9}$$

with

$$\tilde{c}_x^k = \eta \int_{t_{k+C}}^{\infty} e^{-\eta(\tau - t_k)} x_z(\tau) d\tau \tag{7.10}$$

$$\tilde{w}_x^k = \frac{1}{\eta} \int_{t_k}^{\infty} e^{-\eta(\tau - t_k)} w_x(\tau) d\tau. \tag{7.11}$$

The integral on the left-hand side of (7.9) depends on the MPC decision variables $\dot{x}_z^k, \ldots, \dot{x}_z^{k+C-1}$ as it covers the time span ranging from t_k to t_{k+C}. We then express the piece-wise linear ZMP positions in terms of the piece-wise constant decision variables $\dot{x}_z$ as

$$x_z(t) = x_z^k + \sum_{i=0}^{C-1} \left(\rho(t - t_{k+i}) - \rho(t - t_{k+i+1}) \right) \dot{x}_z^{k+i}, \tag{7.12}$$

where $\rho(t)$ is the unit ramp function. Plugging (7.12) in (7.9) yields

$$\sum_{i=0}^{C-1} (e^{-i\eta\delta} - e^{-(i+1)\eta\delta}) \frac{\dot{x}_z^{k+i}}{\eta} = x_u^k - x_z^k(1 - e^{-\eta T_c}) - \tilde{c}_x^k + \tilde{w}_x^k. \tag{7.13}$$

The terms $\tilde{c}_x^k$ and $\tilde{w}^k$ remain a source of anti-causality which prevents (7.9) from being implemented as a causal equality constraint in the optimization problem of the MPC scheme.

Let us consider first $\tilde{c}_x^k$. It integrates the ZMP trajectory after the end of the control horizon. We denote this part of the trajectory as the *tail*. Computing the exact value of $\tilde{c}_x^k$ is impossible, however [125, 127] proposed three solutions to overcome the problem by *conjecturing* the future ZMP evolution:

- assuming that the robot stops at time t_{k+C}. This approach is denoted as *truncated tail* and corresponds to the methods of [123, 124];

- assuming that the ZMP velocity after t_{k+C} consists in infinite repetitions of the control inputs. The tail in this case is named as *periodic*;

- using a conjectured prediction of the future ZMP based on the information available from the footstep plan within the preview horizon (represented in Fig. 7.2). This approach is denoted as *anticipative tail*.

The anticipative tail $\tilde{x}_z$ retains in most cases a higher similarity to the actual future ZMP trajectory, and in [127] it was shown to bring important feasibility properties to the nominal IS-MPC scheme. We thus adopt it in the proposed scheme for robust gait generation as follows. Consider a ZMP trajectory that corresponds to the centerline of the future support region for t_{k+C} up to t_{k+P}, and stops in place from t_{k+P} up to

infinity

$$\tilde{x}_z(t) = \begin{cases} \dfrac{x_z^M(t) + x_z^m(t)}{2} & \text{for} \quad t \in [t_{k+C}, t_{k+P}) \\ \dfrac{x_z^M(t_{k+P}) + x_z^m(t_{k+P})}{2} & \text{for} \quad t \in [t_{k+P}, \infty). \end{cases} \tag{7.14}$$

Note that the footsteps can not be modified by the present MPC scheme and thus the future ZMP evolution will resemble the conjectured tail profile.

The term $\tilde{w}_x^k$, to be computed, requires information about the future evolution of the disturbance w. We will analyze two cases: (*i*) when the disturbance is fully known, (*ii*) when the disturbance is not known. The latter has a higher relevance for real application and will constitute the actual implementation of the robust stability constraint.

Known disturbance case

When a disturbance is known it is possible to design a control scheme that compensates for it [229]. Linear control theory states for instance that disturbance rejection is even possible by just knowing the class of the disturbance signal (step, ramp,...) [245, 246]. In our setting, however, standard rejection and compensation techniques would fail as they would require a modification to the ZMP trajectory, with an associated risk of violating the dynamic balance constraint. Constraint violation in MPC consists in a loss of feasibility that may yield instability and, in practice, a robot fall.

The constraint (7.9) offers a convenient solution to the problem. Computing (7.11) when w_x is known has no anti-causality issues, and the integral can be evaluated exactly. Using this constraint consists in a form of *indirect compensation* of the disturbance, in the sense that the scheme will generate disturbance aware trajectories rather than trying to reject it. In practice, there will be a displacement between the CoM and the ZMP towards the action of the perturbation. Such observation is consistent with the concept of *leaning* against the disturbance that was introduced in the discussion of Sect. 6.3, e.g., see Figs. 6.4-6.5.

We can recall the discussion of Sect. 5.2.1 to further analyze the benefits of this behavior. Consider in fact a balancing humanoid subject to a constant disturbance $w_x = F_{\text{ext}}/m$, where m is the robot mass. This disturbance results from the effect of a constant force F_{ext} acting on the robot CoM. We can notice at this point that the steady state equation of the perturbed LIP dynamics requires that

$$w_x = -\eta^2(x_c - x_z), \tag{7.15}$$

which corresponds to the steady state solution of the stability constraint[7]

$$x_z - x_c = \frac{1}{\eta} \int_{t_k}^{\infty} e^{-\eta(\tau - t_k)} \frac{F_{\text{ext}}}{m} d\tau = \frac{F_{\text{ext}}}{m \, \eta^2} = \frac{w_x}{\eta^2}. \tag{7.16}$$

The correspondence between (7.15) and (7.16) testifies both the consistency of the stability constraint and the possibility of handling the presence of the disturbance by modifying the CoM position, as the ZMP can not exceed the support polygon.

---

[7]With the locution "steady state solution of the stability constraint" we intend the solution of the MPC at an equilibrium point, when the cost function has no motion requirements, e.g., when minimizing the sole ZMP velocity.

Estimated disturbance

Some kind of perturbations, such as walking on a ramp with a known slope, could be represented as a known disturbance. However, the cases in which the full disturbance evolution is known are rare: relying on the sole stability constraint as presented above would add no robustness improvements in real scenarios.

The general case of interest is that of unknown persistent perturbations within certain sets. We propose here to retrieve a causal implementation of the stability constraint by using an estimate $\bar{w}_x^k$ of the disturbance w_x^k in order to assign a value to the term $w_x(t)$ in (7.9). The disturbance estimate is computed with any estimator, such as those discussed in Chapter 5. A *saturator* block can filter the output of it to be in accordance to the sets $\mathcal{W}_x$ (5.3) and $\dot{\mathcal{W}}_x$. At each sampling time t_k we set

$$w_x(t) = \bar{w}_x^k, \quad t \in [t_k, \infty), \tag{7.17}$$

which corresponds to assuming the disturbance to be constant from t_k up to infinity. This conjecture on the future disturbance evolution, in line with the concept of anticipative tail, is the most neutral, as in the absence of further information any other assumption would be less accurate. In the proposed scheme, we perform indirect compensation of the disturbance through an estimate of it.

Making use of the anticipative tail and the disturbance estimate, the stability constraint writes as

$$\sum_{i=0}^{C-1} (e^{-i\eta\delta} - e^{-(i+1)\eta\delta}) \frac{\dot{x}_z^{k+i}}{\eta} = x_u^k - x_z^k(1 - e^{-\eta T_c}) - \tilde{c}_x^k + \frac{\bar{w}^k}{\eta^2}. \tag{7.18}$$

7.1.4 Quadratic program

It is now instrumental to collect the decision variables over T_c as

$$\dot{X}_z^k = (\dot{x}_z^k, \ldots, \dot{x}_z^{k+C-1}).$$

The proposed MPC scheme for robust gait generation solves at each sampling time t_k the following Quadratic Program (QP)

$$
\begin{cases}
\qquad\qquad \min_{\dot{X}_z^k} \|\dot{X}_z^k\|^2 \\[4pt]
\text{subject to:} \\[4pt]
\quad \bullet \text{ restricted ZMP constraints (7.6)} \\[4pt]
\quad \bullet \text{ robust stability constraints (7.9).}
\end{cases}
$$

The first sample $\dot{x}_z^k$ of the resulting trajectory is used to integrate the prediction model (7.2) and to compute a reference CoM position. This information together with the reference foot pose is sent to the next stage of the scheme, i.e., a kinematic controller to convert them into joint commands.

It might be beneficial to encourage the generated ZMP trajectory to lie at the center of the moving constraint region. To do so, it is sufficient to modify the previous cost function by adding a term of the type $\|X_z^k - X_{mc}^k\|^2$ with a proper weight. The vectors

are defined as

$$X_z^k = (x_z^k \ \ldots \ x_z^{k+C-1})^T \qquad X_{mc}^k = (x_{mc}^k \ \ldots \ x_{mc}^{k+C-1})^T,$$

being x_{mc}^k the center of the moving constraint region.

7.2 Feasibility of the scheme

We analyze in this section the feasibility properties of the robust gait generation scheme that we presented. The discussion follows three stages: first, the concept of feasibility region is introduced and characterized. Second, conditions for robust recursive feasibility of the scheme are derived and discussed for different disturbance knowledge levels. Recursive feasibility depends on the profile of the restriction function and the final part of the analysis covers the design of it.

7.2.1 Feasibility

We characterize the feasibility region of the proposed MPC scheme by means of the following:

Proposition 6 *The QP of the x component of the proposed MPC scheme is feasible at t_k if and only if $x_u^k \in \bar{\mathcal{F}}_x^k$, with*

$$\bar{\mathcal{F}}_x^k = \{x_u : \bar{x}_u^{k,m} \leq x_u \leq \bar{x}_u^{k,M}\}$$

where $\bar{x}_u^{k,m}$, $\bar{x}_u^{k,M}$ are the bounds of the feasibility region, given by

$$\bar{x}_u^{k,m} = \eta \int_{t_k}^{t_{k+C}} e^{-\eta(\tau-t_k)} x_z^m d\tau + \tilde{c}_x^k - \frac{\bar{w}_x^k}{\eta^2} + \eta \int_{t_k}^{t_{k+C}} e^{-\eta(\tau-t_k)} R(\tau-t_k) d\tau$$

$$\bar{x}_u^{k,M} = \eta \int_{t_k}^{t_{k+C}} e^{-\eta(\tau-t_k)} x_z^M d\tau + \tilde{c}_x^k - \frac{\bar{w}_x^k}{\eta^2} - \eta \int_{t_k}^{t_{k+C}} e^{-\eta(\tau-t_k)} R(\tau-t_k) d\tau.$$

Proof. We demonstrate necessity by: multiplying each term in the restricted ZMP constraint (7.6) by $\eta e^{-\eta(t-t_k)}$, integrating from t_k to t_{k+C}, and adding $\tilde{c}_x^k$ and subtracting $\bar{w}_x^k/\eta^2$ on each side of the inequality. Note that we are considering here the implementation of the robust stability constraint that features the saturated disturbance estimate. The center term in the chain of inequalities corresponds to x_u^k thanks to (7.9).
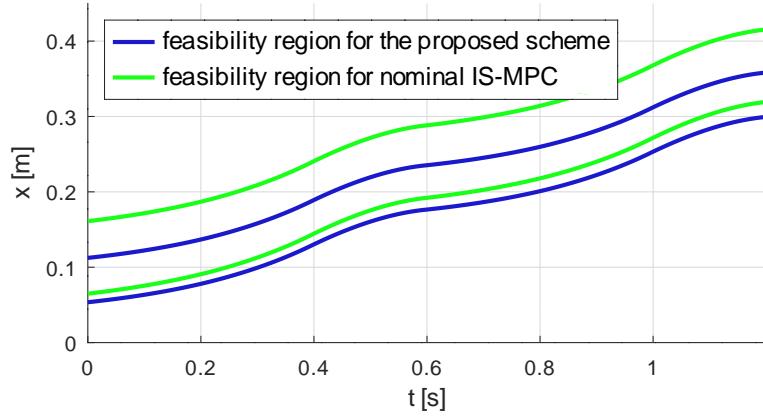
To demonstrate sufficiency we need to show that, if $x_u \in \bar{\mathcal{F}}_x^k$, there exists at least one trajectory satisfying the restricted ZMP and the robust stability constraint. Let us express x_u^k as

$$x_u^k = a\bar{x}_u^{k,m} + (1-a)\bar{x}_u^{k,M} \quad \text{with} \quad a \in [0,1]. \tag{7.19}$$

The ZMP trajectory given by

$$x_z^*(t) = a(x_z^m(t) + R(t-t_k)) + (1-a)(x_z^M(t) - R(t-t_k)) \tag{7.20}$$

is constructed using the parameter a and satisfies the restricted ZMP constraint and the robust stability constraint. The statement can be confirmed by plugging (7.20) in (7.9) and observing that $\tilde{c}_x^k = a\tilde{c}_x^k + (1-a)\tilde{c}_x^k$ and $\frac{\bar{w}_x^k}{\eta^2} = a\frac{\bar{w}_x^k}{\eta^2} + (1-a)\frac{\bar{w}_x^k}{\eta^2}$. ∎

Figure 7.5: The plot shows the evolution of the feasibility region for the x component over the time span corresponding to two steps. We also report the feasibility region for the nominal IS-MPC case, under the same gait parameters. The feasibility region in the proposed robust scheme is translated and eroded with respect to the nominal region.

The bounds $\bar{x}_u^{k,m}$ and $\bar{x}_u^{k,M}$ depend on the upper and lower bound of the ZMP constraint, on the integral of the ZMP tail, on the disturbance estimate, and on the restriction function.

Proposition 6 defines the region for the decoupled problem, presenting the boundaries for the sole x component, and clearly an equivalent proposition can be formalized for the y component. We remark, however, that the whole scheme is feasible at the current time if and only if

$$(x_u^k, y_u^k) \in \bar{\mathcal{F}}_{x,y}^k.$$

We discuss a simple case study in order to present a concrete insight on the feasibility region. In Fig. 7.5, the feasibility region for the proposed robust scheme is shown, together with the feasibility region for the nominal version of IS-MPC [127]. The region is computed over a time span of 1.2 s (two steps), with $d_{z,x} = 0.1$ m, $h = 0.7$ m, $\delta = 0.01$ s, $T_c = 0.7$ s, $T_p = 2$ s. The perturbation consists in a constant signal of 0.6 m/s^2 acting on the CoM. For illustration, the restriction function is chosen to be a linear function as in Fig. 7.3, i.e., $R(t) = rt$ [7], with maximum slope r. We can observe two distinctions between the nominal and the robust feasibility region:

- the nominal feasibility region has a larger width with respect to the nominal region. This depends on restriction function that, by eroding the ZMP constraint, also shrinks the boundaries of the feasibility region by $\pm\eta \int_{t_k}^{t_k+C} e^{-\eta(\tau-t_k)} R(\tau - t_k) d\tau$;

- the robust feasibility region presents a displacement with respect to the nominal region, caused by the disturbance observer term $\bar{w}^k/\eta^2$.

7.2.2 Sufficient Condition for Robust Recursive Feasibility

Under the hypothesis of feasibility at the current time, we now look for a condition that implies the feasibility at the subsequent time instant. This constitutes the first step to derive a sufficient condition for recursive feasibility. Consider the following:

Proposition 7 *Assume that the proposed scheme is feasible at t_k. Then the scheme is feasible at t_{k+1} if the restriction function $R(t)$ is chosen so that*

$$\beta \geq \mu^k + \gamma^k \tag{7.21}$$

where β depends on the restriction function as

$$\beta = \eta \int_{t_{k+1}}^{t_{k+C}} e^{-\eta(\tau - t_{k+1})} R(\tau - t_k) d\tau - \eta \int_{t_{k+1}}^{t_{k+C+1}} e^{-\eta(\tau - t_{k+1})} R(\tau - t_{k+1}) d\tau \tag{7.22}$$

while μ^k and γ^k are defined as

$$\mu^k = \eta \int_{t_{k+C+1}}^{\infty} e^{-\eta(\tau - t_{k+1})} (\tilde{x}_z(\tau) - \tilde{x}'_z(\tau)) d\tau - \eta \int_{t_{k+C}}^{t_{k+C+1}} e^{-\eta(\tau - t_{k+1})} (x_z^M - \tilde{x}_z(\tau)) d\tau$$

$$\gamma^k = \frac{\bar{w}_x^{k+1} - \bar{w}_x^k}{\eta^2} + \frac{1}{\eta} \int_{t_k}^{t_{k+1}} e^{\eta(t_{k+1} - \tau)} (w_x(\tau) - \bar{w}_x^k) d\tau$$

where $\tilde{x}'_z(\tau)$ is the ZMP tail at t_{k+1}.

Proof. The hypothesis of feasibility at time t_k implies that the robust stability constraint (7.9) and restricted ZMP constraint (7.6) are satisfied. Using this information, we can derive a bound on x_u^{k+1}. By integrating the dynamics of x_u we have

$$x_u^{k+1} = e^{\eta\delta} x_u^k - \eta \int_{t_k}^{t_{k+1}} e^{\eta(t_{k+1} - \tau)} x_z(\tau) d\tau + \frac{1}{\eta} \int_{t_k}^{t_{k+1}} e^{\eta(t_{k+1} - \tau)} w_x(\tau) d\tau$$

Plugging (7.9) into the above equation, and using (7.6), we can write

$$\begin{aligned} x_u^{k+1} &\leq \eta \int_{t_{k+1}}^{t_{k+C}} e^{-\eta(\tau - t_{k+1})} (x_z^M - R(\tau - t_k)) d\tau + \\ &\quad \eta \int_{t_{k+C}}^{\infty} e^{-\eta(\tau - t_{k+1})} \tilde{x}_z(\tau) d\tau + \\ &\quad \frac{1}{\eta} \int_{t_k}^{t_{k+1}} e^{\eta(t_{k+1} - \tau)} w_x(\tau) d\tau - \frac{\bar{w}_x^k e^{\eta\delta}}{\eta^2}. \end{aligned}$$

To be feasible at t_{k+1}, x_u^{k+1} must be within the upper bound of the feasibility region at time t_{k+1}, i.e.,

$$\begin{aligned} x_u^{k+1} &\leq \eta \int_{t_{k+1}}^{t_{k+C+1}} e^{-\eta(\tau - t_{k+1})} (x_z^M - R(\tau - t_{k+1})) d\tau + \\ &\quad \eta \int_{t_{k+C+1}}^{\infty} e^{-\eta(\tau - t_{k+1})} \tilde{x}'_z(\tau) d\tau - \frac{\bar{w}_x^{k+1}}{\eta^2}. \end{aligned}$$

A sufficient condition for implying feasibility at t_{k+1} can be derived by imposing that the right-hand side of the penultimate inequality is smaller than that of the last one.

Imposing this condition and arranging the terms yields

$$\eta \int_{t_{k+1}}^{t_{k+C}} e^{-\eta(\tau - t_{k+1})} R(\tau - t_k) d\tau -$$

$$\eta \int_{t_{k+1}}^{t_{k+C+1}} e^{-\eta(\tau - t_{k+1})} R(\tau - t_{k+1}) d\tau +$$

$$\eta \int_{t_{k+C}}^{t_{k+C+1}} e^{-\eta(\tau - t_{k+1})} (x_z^M - \tilde{x}_z(\tau)) d\tau +$$

$$\eta \int_{t_{k+C+1}}^{\infty} e^{-\eta(\tau - t_{k+1})} (\tilde{x}_z'(\tau) - \tilde{x}_z(\tau)) d\tau +$$

$$-\frac{\bar{w}_x^{k+1} - \bar{w}_x^k}{\eta^2} - \frac{1}{\eta} \int_{t_k}^{t_{k+1}} e^{\eta(t_{k+1} - \tau)} (w_x(\tau) - \bar{w}_x^k) d\tau \geq 0.$$

We can now use the definition of β, γ^k and μ^k to obtain the condition (7.21). The same reasoning can be conducted for the lower inequalities and for the y component. ∎

Proposition 7 identifies an inequality to be satisfied to ensure that feasibility at t_k implies feasibility at t_{k+1}. We notice first that

$$\beta^k = \beta \quad \forall k,$$

as it is only affected by the shape restriction function applied at two subsequent time instants[8]. On the other hand, γ and μ depend on t_k. With the aim of providing a time-independent condition for recursive feasibility, we now compute an upper bound for such quantities.

μ^k **Term**

The value of μ^k depends on the variation over time of the ZMP tail and on a further term of which the magnitude is given by the difference between the ZMP bound and the tail. According to the choice of the ZMP tail (7.14), the latter is a constant value equal to $(1 - e^{-\eta\delta}) \frac{d_{z,x}}{2} e^{-\eta T_c}$. The first quantity is instead time varying and we denote it as the *tail mismatch*. In the case of assigned footsteps, $\tilde{x}_z$ corresponds to $\tilde{x}_z'$ for $t \in [t_{k+C+1}, T_{k+P})$, allowing us to write

$$\eta \int_{t_{k+C+1}}^{\infty} e^{-\eta(\tau - t_{k+1})} (\tilde{x}_z(\tau) - \tilde{x}_z'(\tau)) d\tau = \eta \int_{t_{k+P+1}}^{\infty} e^{-\eta(\tau - t_{k+1})} (\tilde{x}_z(\tau) - \tilde{x}_z'(\tau)) d\tau$$

$$\leq \delta e^{-\eta T_p} \frac{1 - e^{-\eta\delta}}{\eta} v_z^{\max}.$$

that can be used to find

$$\mu^k \leq \delta e^{-\eta T_p} \frac{1 - e^{-\eta\delta}}{\eta} v_z^{\max} - (1 - e^{-\eta\delta}) \frac{d_{z,x}}{2} e^{-\eta T_c} = \mu^{\max}. \tag{7.23}$$

The quantity $v_z^{\max}$ in the previous expression is the maximum velocity of the ZMP tail, retrieved from physical considerations on the robot. It should also be noted that the term depending on $v_z^{\max}$ vanishes for $T_p \to \infty$, whereas the second term is negative,

---

[8]It can be verified by the setting $s = \tau - t_k$ as integration variable.

thus contributing to the satisfaction of the recursive feasibility condition.

γ^k **Term**

The quantity γ^k depends on both the *observed disturbance increment over subsequent sampling intervals* and the *observation error*. An upper bound for these quantities must be found. To this purpose, we can exploit the configuration of the proposed scheme: the adoption of the saturated disturbance observer of Sect. 5.2.3 allows to write the following

$$
\begin{aligned}
\gamma^k &= \frac{\bar{w}_x^{k+1} - \bar{w}_x^k}{\eta^2} + \frac{1}{\eta} \int_{t_k}^{t_{k+1}} e^{\eta(t_{k+1}-\tau)}(w_x(\tau) - \bar{w}_x^k)d\tau \\
&\leq \frac{\delta \dot{\Delta}_x}{\eta^2} + \frac{1}{\eta} \int_{t_k}^{t_{k+1}} e^{\eta(t_{k+1}-\tau)} 2\Delta_x d\tau \\
&= \frac{\delta \dot{\Delta}_x}{\eta^2} + \frac{2\Delta_x(e^{\eta\delta} - 1)}{\eta^2} \\
&= \frac{2\Delta_x}{\eta^2}(e^{\eta\delta} - 1)(1 + \alpha) = \gamma^{\max}
\end{aligned}
\tag{7.24}
$$

where we set

$$
\delta \dot{\Delta}_x = 2\alpha\Delta_x(e^{\eta\delta} - 1)
$$

to group the terms in a compact expression. For convenience, the quantity $\dot{\Delta}_x$ is parameterized in terms of α.

After having derived a bound for γ^k and μ^k, we can finally state a condition for recursive feasibility:

Proposition 8 *The proposed scheme is robust recursively feasible for $\forall t \geq t_0$ if it is feasible in t_0 and*

$$
\beta \geq \mu^{\max} + \gamma^{\max}.
\tag{7.25}
$$

Proof. The proposition is demonstrated by substituting (7.23) and (7.24) in (7.21). ∎

We conclude with a list of remarks:

- the inequality for recursive feasibility provides a design guideline: a restriction function can be chosen so as to satisfy it;

- the γ^k term is equal to 0 in the known disturbance case, thus recursive feasibility is ensured if $\beta \geq \mu^{\max}$;

- the stability result of [127] (that states that if the scheme is recursively feasible then it is also internally stable) holds equally in the robust case presented in this manuscript;

- the restriction function requirement (7.7) imposes that there exists an upper bound $\beta^{\max}$ for the quantity β. This happens because β increases as the ZMP constraint is restricted, and thus it cannot increase anymore once the ZMP constraint is shrunk to its limit. An important consequence of this upper limit is that one cannot expect to find a restriction function able to tolerate an arbitrarily large set of

disturbances, because the associated γ^{max} might be such that $\beta^{\mathrm{max}} \geq \mu^{\mathrm{max}} + \gamma^{\mathrm{max}}$ is not satisfied;

- the quantity that, in practice, can generate a violation in the recursive feasibility condition is the disturbance, through the γ^k and γ^{max} terms;

- we can observe from (7.24) that the faster are the perturbation dynamics (i.e., a large $\dot{\Delta}_x$), the larger is the value of the γ^{max} term. The same holds for large values of Δ. The presence of a saturator for the disturbance estimate, on the other hand, would limit the admissible values for the observed disturbance and impose a bound on its derivative, thus governing γ^{max};

- recursive feasibility can also hold when using a non-saturated observer, as in fact, given a certain value for β, (7.21) can be met at each k. In practical situations when $\sup \mathcal{W}_x$ is the sole available information, using an accurate disturbance observer with a tuned restriction function can ensure robustness, even if a formal guarantee is not available. A perturbation estimate saturator is still required to force $\bar{w}^k \in \sup \mathcal{W}_x$;

- conditions of Props. 7-8 are sufficient, implying that there exists a violation tolerance before losing the feasibility of the scheme due to strong perturbations;

- robust recursive feasibility still requires that the system is initialized in a feasible state at t_0. Large midrange values of the disturbance set could introduce large displacements in the feasibility region, so as to render the initial robot state, e.g. of a standing humanoid, infeasible. In these situations, it is sufficient to plan a motion for (x_u, y_u) and recover the feasibility before initializing the proposed scheme.

7.2.3 Design of the restriction function

The restriction function can be used to modulate the β term so as to guarantee robust recursive feasibility for the scheme. By inspecting the expression of the feasibility bounds provided in Proposition 6, it can be inferred that the restriction function also erodes the feasibility region by a total amount of $2\eta \int_{t_k}^{t_k+C} e^{-\eta(\tau-t_k)} R(\tau - t_k)d\tau$. A narrower feasibility region requires a more precise initialization.

It makes sense at this point to investigate on the design of the restriction function $R(t)$. The question is that of finding the function that enables the recursive feasibility via (7.25), while eroding the least possible the feasibility region. We address the investigation by formulating an optimization program:

$$
\begin{cases}
\displaystyle \min_{R(.)} 2\eta \int_{t_k}^{t_k+C} e^{-\eta(\tau-t_k)} R(\tau - t_k)d\tau \\[4mm]
\text{subject to:} \\[2mm]
\quad \bullet \ \text{condition (7.25) for recursive feasibility,} \\[2mm]
\quad \bullet \ R(0) = 0, \\[2mm]
\quad \bullet \ 0 \leq R(t) \leq d_{z,x}/2.
\end{cases}
$$

We aim at computing the restriction function $R(t)$ that minimizes the erosion of the feasibility region, while enforcing the recursive feasibility condition (7.25) as well as the requirements that validate the restriction function definition, given by (7.7).

Instead of directly solving the problem, let us investigate the condition (7.25), here used as a constraint for the program. Without loss of generality, we set $t_k = 0$, yielding

$$\eta \int_\delta^T e^{-\eta(\tau-\delta)} R(\tau) d\tau - \eta \int_\delta^{T+\delta} e^{-\eta(\tau-\delta)} R(\tau-\delta) d\tau \geq \mu^{\max} + \gamma^{\max}$$

which can be cast into

$$\eta e^{\eta\delta} \int_\delta^T e^{-\eta\tau} R(\tau) d\tau - \eta \int_0^T e^{-\eta\tau} R(\tau) d\tau \geq \mu^{\max} + \gamma^{\max}$$

where we performed an integration variable change $(\tau = \tau - \delta)$ in the second integral. The previous inequality can be further arranged as

$$2\eta \int_0^{T_c} e^{-\eta\tau} R(\tau) d\tau \geq 2 \frac{\mu^{\max} + \gamma^{\max} + e^{\eta\delta} \eta \int_0^\delta e^{-\eta\tau} R(\tau) d\tau}{(e^{\eta\delta} - 1)}, \qquad (7.26)$$

having also multiplied both sides by 2.

The left hand side of (7.26) corresponds to the cost function of the problem we are interested at solving. This means that there exists a lower bound for the feasibility erosion, constituting the minimum price to pay in terms of feasibility reduction to ensure (7.25).

The previous consideration introduces a simplification in the optimization problem we are interested in solving, as any restriction function would be optimal with respect to the chosen criterion as long as it satisfies

$$\eta \int_0^{T_c} e^{-\eta\tau} R(\tau) d\tau = \frac{\mu^{\max} + \gamma^{\max} + e^{\eta\delta} \eta \int_0^\delta e^{-\eta\tau} R(\tau) d\tau}{(e^{\eta\delta} - 1)} \qquad (7.27)$$

and $0 \leq R(t) \leq d_{z,x}/2$ for $t \in [\delta, T_c]$. To be consistent with the restriction function definition and to minimize the lower bound (7.27), we set $R(t) = 0$ for $t \in [0, \delta)$, resulting in

$$\eta \int_\delta^{T_c} e^{-\eta\tau} R(\tau) d\tau = \frac{\mu^{\max} + \gamma^{\max}}{(e^{\eta\delta} - 1)}. \qquad (7.28)$$

We can now conclude the discussion we begun in Sect. 7.1.2 regarding the shape of the restriction function. To be effective, it does not have to shrink the allowed ZMP region more towards the end of the prediction horizon provided that (7.28) is satisfied. However, this still constitutes a practical design choice that will be adopted in the following.

Practical design of the restriction function

We can now introduce a practical method to design a restriction function that ensures recursive feasibility and is optimal in the sense of reducing the least possible the feasibility

erosion. Introduce a function $R(t)$ defined as

$$R(t) = \begin{cases} 0 & \text{for } t \in [0, \delta) \\ r(t - \delta) & \text{for } t \in [\delta, t_h) \\ r(t_h - \delta) & \text{for } t \in [t_h, t_C). \end{cases} \tag{7.29}$$

Such function describes a family of piece-wise linear restrictions parametrized by two quantities: the slope r of the initial trait, and the time t_h at which the second, constant, trait begins. This choice is arbitrary and selected for convenience. Plugging the shape (7.29) in (7.28) yields

$$\frac{r}{\eta}(e^{-\eta\delta} - 1)\left((\eta(\delta - t_h) - 1)e^{-\eta t_h} - 1\right) + \\ r(t_h - \delta)(e^{\eta\delta} - 1)(e^{-\eta t_h} - e^{-\eta t_C}) = \mu^{\max} + \gamma^{\max}. \tag{7.30}$$

To compute these parameters we formulate the nonlinear program

$$\begin{cases} \quad \min_{r, t_h} r^2 + (t_h - T_c)^2 \\ \text{subject to:} \\ \quad \bullet\ r \geq 0 \\ \quad \bullet\ r(t_h - \delta) \leq \frac{d_{z,x}}{2} - \epsilon \\ \quad \bullet\ \text{equality (7.30).} \end{cases}$$

The cost function of the problem will both force the restriction to have a minimum slope and the saturation instant t_h to coincide with the end of the prediction horizon. The proposed $R(t)$ will be, in this sense, a linear restriction function with a slope r, which is saturated, when necessary to guarantee $R(t) \leq d_{z,x}$ and equality (7.30).
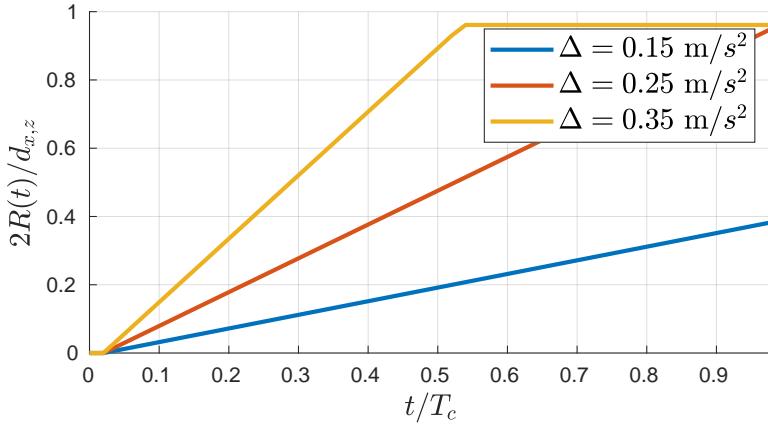
Three plots of restriction functions generated using such optimization problem are shown in Fig. 7.6, obtained with parameters: $\delta = 0.01$ s, $T_c = 0.7$ s, $T_p = 2$ s, $d_{z,x} = 0.1$ m, $\epsilon = 0.005$ m (introduced to prevent the ZMP contraint from becoming an equality), $h = 0.7$ m, $\mu^{\max} = 0.000025$. We set three different values for Δ_x, i.e, 0.15-0.25-0.35 m/s^2, corresponding to $\gamma^{\max} = 0.00023$, $\gamma^{\max} = 0.00061$, $\gamma^{\max} = 0.00099$, while we chose $\alpha = 0.4$ for the disturbance observer saturation block. The slope r increases proportionally to the magnitude of Δ_x. The function is saturated for $\gamma^{\max} = 0.00099$, corresponding to $\Delta_x = 0.35$ m/s^2.

7.3 Simulations
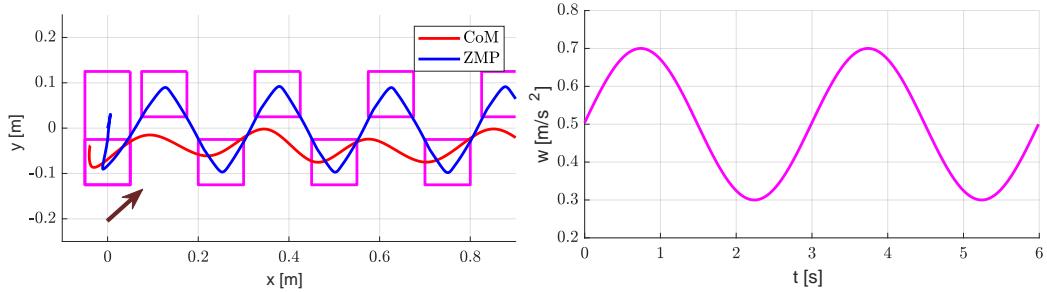
We now validate the proposed gait generation scheme by means of simulations in Matlab and DART.

7.3.1 Matlab simulations

In Matlab simulations, the algorithm is tested on a perturbed LIP model, providing an initial evaluation about the meaningfulness of the idea. We set the following parameters: $\delta = 0.01$ s, $T_c = 0.7$ s, $T_p = 2$ s, $h = 0.75$ m, $d_{z,x} = d_{z,y} = 0.1$ m, $w_{m,x} = w_{m,y} = 0.5$ m/s^2, $\Delta_x = \Delta_y = 0.2$ m/s^2, $\dot{\Delta}_x = \dot{\Delta}_y = 0.2$ m/s^3 ($\alpha = 0.14$),

Figure 7.6: Proposed restriction function with different disturbance ranges.

Figure 7.7: Known disturbance case with slow-varying perturbation: (left) CoM/ZMP trajectory, (right) plot of the disturbance, acting equally on both x and y. The brown arrow on the left plot represents the direction of the disturbance vector.
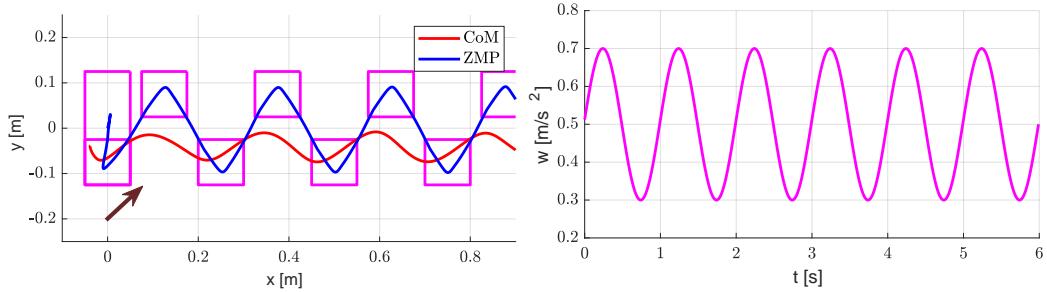
$\mu^{\max} = 0.000025$. We study the case of a forward gait. The single and double support duration is set respectively to $T_{ss} = 0.4$ s and $T_{ds} = 0.2$ s, while the stride length is 0.125 m.

Known disturbance case
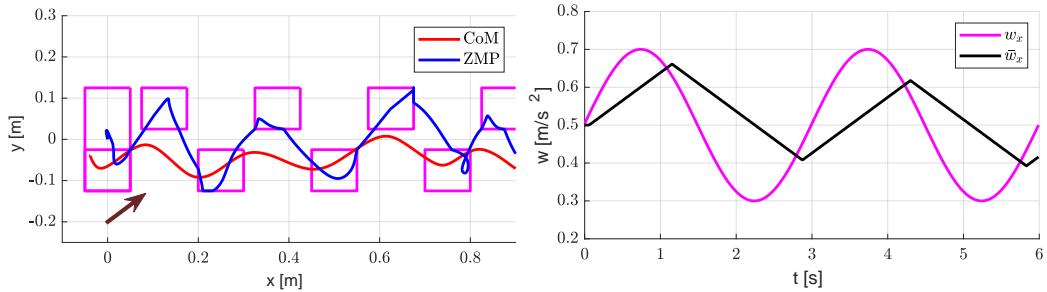
We first consider the case of known disturbance. The restriction function is used with the robust stability constraint which exploits the full knowledge of the perturbation signal. We recall that here recursive feasibility is enforced as long as $\beta \geq \mu^{\max}$, being $\gamma^k = 0$.

Figure 7.7 shows the case of a slow-varying sinusoidal disturbance, whereas Fig. 7.8 displays the same gait under a faster varying disturbance. The perturbations are composed by a constant part plus a sinusoid, i.e., a non-zero midrange value and a time-varying signal.

The CoM/ZMP trajectories reported in both figures do not present a significant difference. The knowledge of the perturbation allows for an *exact indirect compensation* of it, corresponding to a CoM displacement towards the action of it. The ZMP instead remains at the center of the support region, without requiring any modification to account for the disturbance.

Figure 7.8: Known disturbance case with fast-varying perturbation: (left) CoM/ZMP trajectory, (right) plot of the disturbance, acting equally on both x and y. The brown arrow on the left plot represents the direction of the disturbance vector.
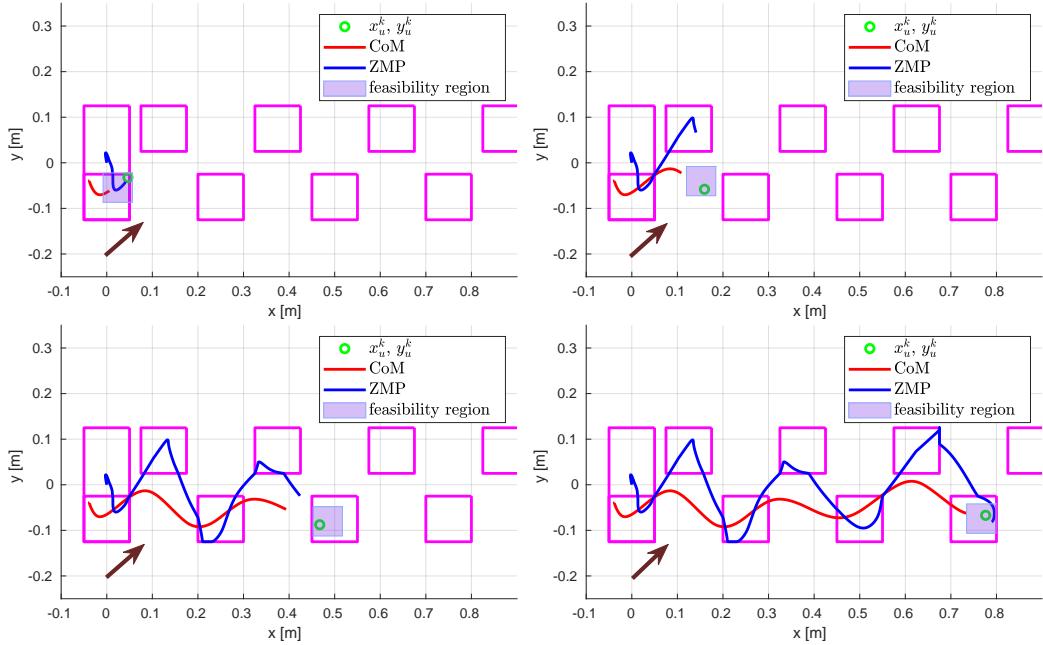
Figure 7.9: Robust gait generation scheme with slow-varying perturbation: (left) CoM/ZMP trajectory, (right) plot of the disturbance, acting equally on both x and y, and its saturated estimate. The brown arrow on the left plot represents the direction of the disturbance vector.

Estimated disturbance case

We now discuss the outcome of the full scheme in the case of observed disturbance in the robust stability constraint. The output of the disturbance estimate is filtered by a saturator block which projects $\bar{w}_{x,y}$ inside $\mathcal{W}_{x,y}$, $\dot{\mathcal{W}}_{x,y}$.

The disturbance chosen for the simulation is such that $w_{x,y} \in \mathcal{W}_{x,y}$, while $\dot{w}_{x,y} \notin \mathcal{W}_{x,y}$. According to (5.6), we have that the perturbation used for simulation belongs to the set of impulsive disturbances $\mathcal{W}_{i_{x,y}}$, being the derivative of the applied signal w_x not part of $\dot{\mathcal{W}}_{x,y}$. This has a major relevance in practical applications, where the definition of a disturbance set is performed in the design phase while in reality it is unpredictable and may change during operations. We will see in the next chapters that these situations may be handled by different locomotion strategies, involving for instance the modification of the footstep locations. On the other hand, it could still be required that the robot executes the footstep plan without variations and we focus here on such a case study. The effect of the saturator is in this case fundamental to prevent the generated trajectory to be affected by the fast disturbance evolution.

Consider first Fig. 7.9. This simulation corresponds to that of Fig. 7.7 for the estimated disturbance case. The generated CoM/ZMP trajectories are more affected by the perturbation than in the known case, but still the gait is stable and no CoM divergence with respect to the ZMP is caused. The expected CoM displacement in the direction of the perturbation is present, mainly caused by the midrange component of it. On the right hand side of the figure, the disturbance together with its saturated estimate is plotted to show the effort of the saturator block to project back the perturbation in

Figure 7.10: The gait is photographed at four different time instants and in all of them the DCM, represented as a green point, is inside the feasibility region, a violet moving square.

the considered set.

We also report four different feasibility region snapshots in Fig. 7.10. The gait is photographed at the random time instants $t = 1.5$ s, $t = 2.5$ s, $t = 4.8$ s, $t = 7.3$ s, and in all of them the DCM (x_u^k, y_u^k) is within the feasibility region. The latter is a squared box that moves along with the gait, as its boundaries are time varying (see Prop. 6).

We then report the case of the same fast-varying disturbance as the known case of Fig. 7.8. Figure 7.11 shows that the effect of the saturator is more accentuated than the previous case, but still the gait retains stability. Figure 7.12 displays instead the gait under the same perturbation when no robustness strategies are enforced. The MPC relies on its pure feedback to reject the perturbations, but the presence of the constraints does not allow for a proper control action that guarantees stability. An analogous outcome happens in the slow-varying disturbance case.
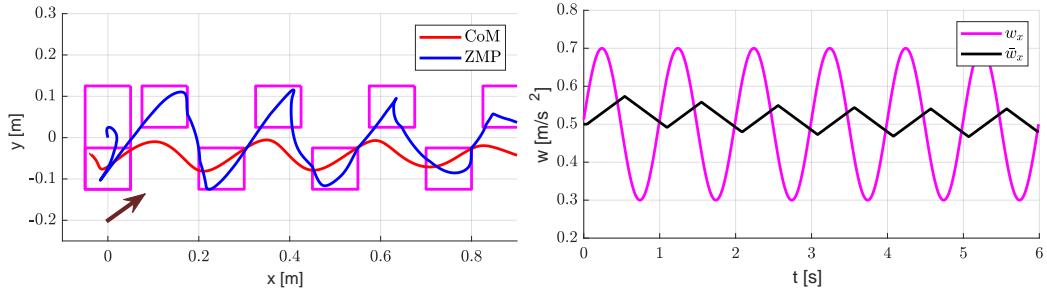
Evaluating recursive feasibility

The fast varying disturbance case offers us the opportunity to quantify how the saturator affects recursive feasibility. The disturbance signal is described by the timing law
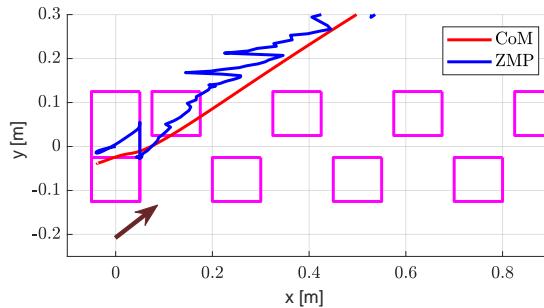
$$w_x = 0.5 + 0.2 \sin(2\pi t) \text{ m/s}^2,$$

for which it is straightforward to verify that $\max \dot{w}_x = 0.4\pi$ m/s². The disturbance derivative set adopted for design is instead bounded by $\dot{\Delta}_x = 0.2$ m/s². The sufficient condition for robust recursive feasibility based on (7.25) would not be met without the saturator. This can be visualized by inspecting Fig. 7.13.

Even if we can find cases where robust recursive feasibility is achieved without using a saturator (provided that the observer is sufficiently responsive and the disturbance is not varying too fast), the saturator consists in a useful tool to obtain theoretical

Figure 7.11: Robust gait generation scheme with fast-varying perturbation: (left) CoM/ZMP trajectory, (right) plot of the disturbance, acting equally on both x and y, and its saturated estimate. The brown arrow on the left plot represents the direction of the disturbance vector. On the bottom, the nominal IS-MPC scheme under the effect of the perturbation is reported, displaying a divergent behavior.

Figure 7.12: The nominal IS-MPC scheme under the effect of the perturbation is reported, displaying a divergent behavior.
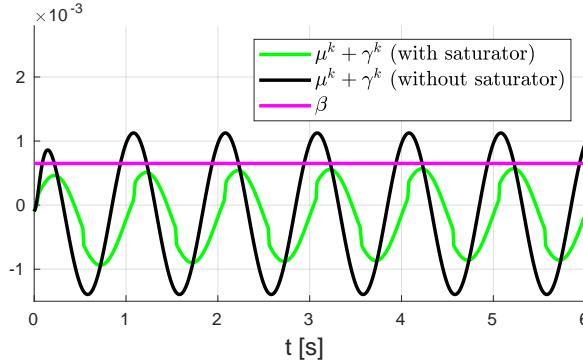
guarantees on the gait generation scheme.

7.3.2 Dart simulations
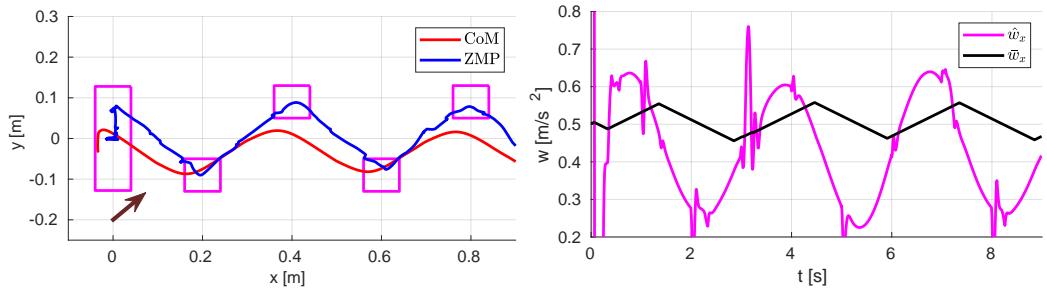
We consider a stage of validation through multi-body simulations in the DART environment [233]. The tests are conducted on the HRP-4 platform, the position controlled full-sized humanoid manufactured by Kawada Industries and developed in the context of a joint project led by Japan's National Institute of Advanced Industrial Science and Technology (AIST) [47]. The kinematic controller runs at 100 Hz and the other parameters are the same of the previous section, except when specified. The QPs of the gait generation scheme are solved with the *hpipm* C library [247].

Evaluation of the robustness to perturbations

We first of all replicate the slow-varying Matlab simulation from the previous section with a variation on the the gait timing, now set to $T_s = 1$ s with $T_{ds} = 0.2$ s, and on the stride length, set to 0.2 m. Figure 7.14 reports the CoM/ZMP trajectories and the disturbance plot. The robot performs the forward walk in spite of the perturbation. Note that the plotted perturbation signals are the output of the observer and the output of the saturator, while the applied disturbance is the same as that of Fig. 7.9. During the walk (see snapshots in Fig. 7.15) the disturbance observer is less precise, being it subject to errors due to the impacts with the ground and imperfect sole contacts. Note

Figure 7.13: Evaluation of the recursive feasibility condition over time (measurement unit is left unspecified being the involved data not interpretable as physical quantities). When using the saturator, we have that $\beta \geq \mu^k + \gamma^k \; \forall k$, as in fact the restriction function has been designed so that $\beta \geq \mu^{\max} + \gamma^{\max}$. On the other hand, without saturator the condition is violated. This can cause a failure for the scheme, unless a proper feasibility recovery action is performed.

Figure 7.14: Dart simulation of forward walk in the presence of a disturbance acting on the CoM of the robot: (left) CoM/ZMP trajectories, (right) disturbance.

that it is here capturing also all the nonlinear effects that are not included in the LIP model. The saturator plays a major role in such situations.
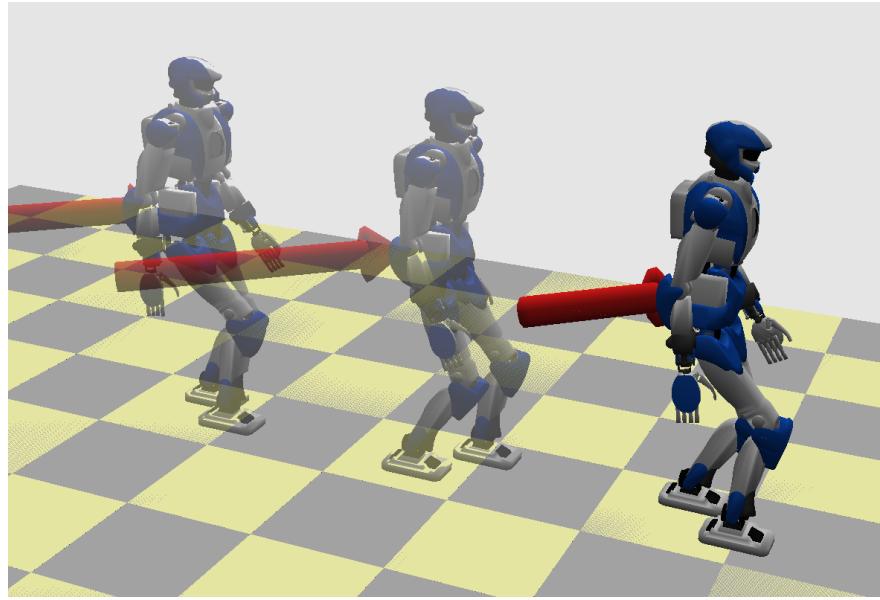
We proceed by investigating the robustness limits of the proposed approach in the case of persistent disturbances directly applied to the robot in correspondence of its CoM. The objective is to quantify the perturbation magnitude that the scheme can withstand given a fixed disturbance set and a certain footstep plan, chosen as representative for an average perturbed walking situation. We used $w_{m,x} = w_{m,y} = 0.25 \text{ m/s}^2$, $\Delta_{x,y} = 0.25 \text{ m/s}^2$, $\dot{\Delta}_{x,y} = 0.2 \text{ m/s}^3$.

We apply constant forces towards the torso of the robot while it is walking forward. The proposed method tolerates constant x-forces in $[-65, 38]$ N and constant y-forces in $[-38, 45]$ N, whereas nominal IS-MPC [127] tolerates constant x-forces in $[-40, 19]$ N and constant y-forces in $[-15, 17]$ N, testifying the benefits in terms of performance yielded by a robustification of the scheme.

Slopes and weight carrying

We now discuss simulations in which the source of perturbation is due to a physical cause and not applied as an artificial force through the simulator.

First, we consider a scenario in which HRP-4 is carrying a 1.5 kg object while walking on a sequence of four ramps with different slopes: 0°(starting point), 2.5°, 4°, 0°(target

Figure 7.15: Snapshots from the dart simulation to show the leaning of the robot against the action of the perturbation. Note that the nominal IS-MPC scheme fails in generating a stable gait under the action of the same disturbance.
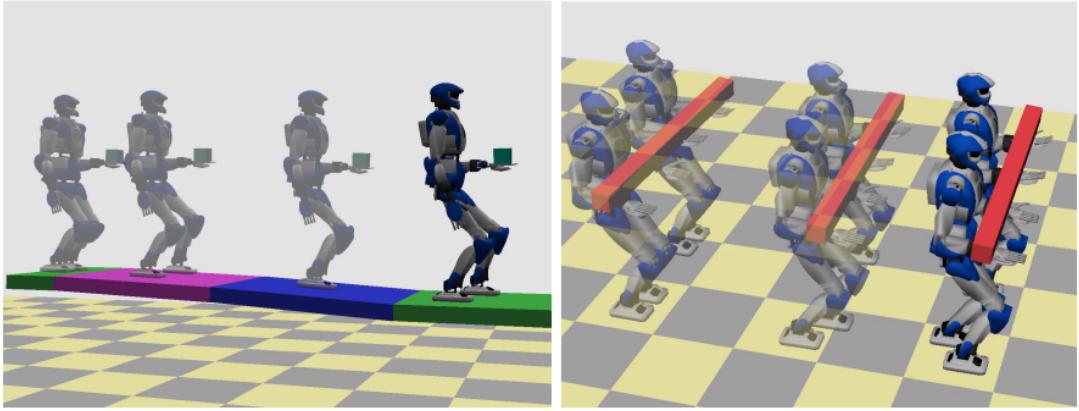
point), as shown in Fig. 7.16 (left). We set $w_{m,x} = 0.45$ m/s^2, $\Delta_x = \Delta_y = 0.2$ m/s^2, $w_{m,y} = 0.125$ m/s^2 and $\dot{\Delta}_x = 0.2$ m/s^3. Thanks to the robustness introduced in the proposed scheme, the robot is able to complete the task without falling (the same simulation conducted with the nominal IS-MPC scheme results in a fall). The objective of this specific result is to show that enforcing robustness with respect to a certain disturbance set is sufficient to withstand a variable disturbance profile.

Then, we show a cooperative transportation task where two HRP-4s walk forward while carrying a 16 kg bar (Fig. 7.16, right). The interaction forces originated during the cooperative transportation and the resultant effect of the carried weight to the robots act as disturbances on the CoM [163, 225]. We set up an independent MPC algorithm for each robot and begin its execution at the same time instant. The humanoids are able to transport the bar without losing balance or incurring into internal stability problems. We highlight that we are not presenting a specific methodology for cooperative transportation, rather we are investigating the effectiveness of the proposed approach in different contexts which may have a practical relevance. As for the previous test, employing the nominal IS-MPC scheme in this situation would result in a fall.
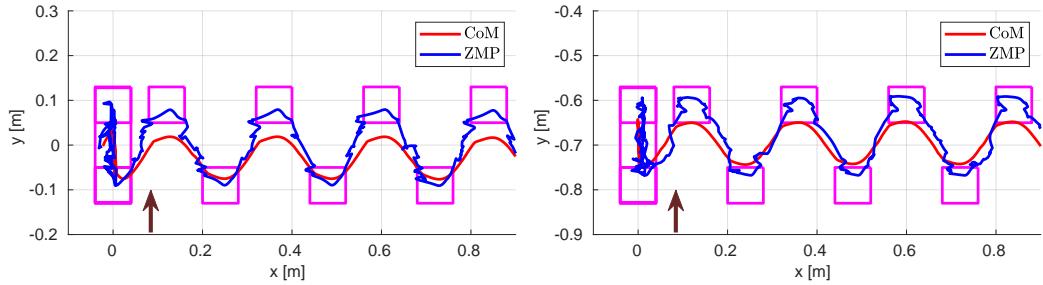
Comparison with different methods

Along the simulation sections, all the results were discussed with respect to the nominal IS-MPC scheme. Providing fair comparisons with approaches from other authors is in general hard: not often a scheme in the literature has comparable features to the presented work nor presents a systematic tuning methodology that prevents possible sources of degradation. Among the state of the art, we selected [1, 152] for the present discussion.

In these works, robust positive invariance is used to enforce robustness: they certainly present analogies with our ZMP constraint restriction approach. These methods perform

Figure 7.16: HRP-4 walking down slopes while carrying a 1.5 Kg wight with its left hand (left), two HRP-4s cooperatively transporting a 16 Kg bar (right).

Figure 7.17: CoM and ZMP trajectories generated by the proposed scheme (left) and [1] (right). The brown arrow in the plots represents the vector of the persistent external disturbance.

very well in the case of perturbations which are bounded within a set that contains the origin, as they do not enforce any form of disturbance observation.
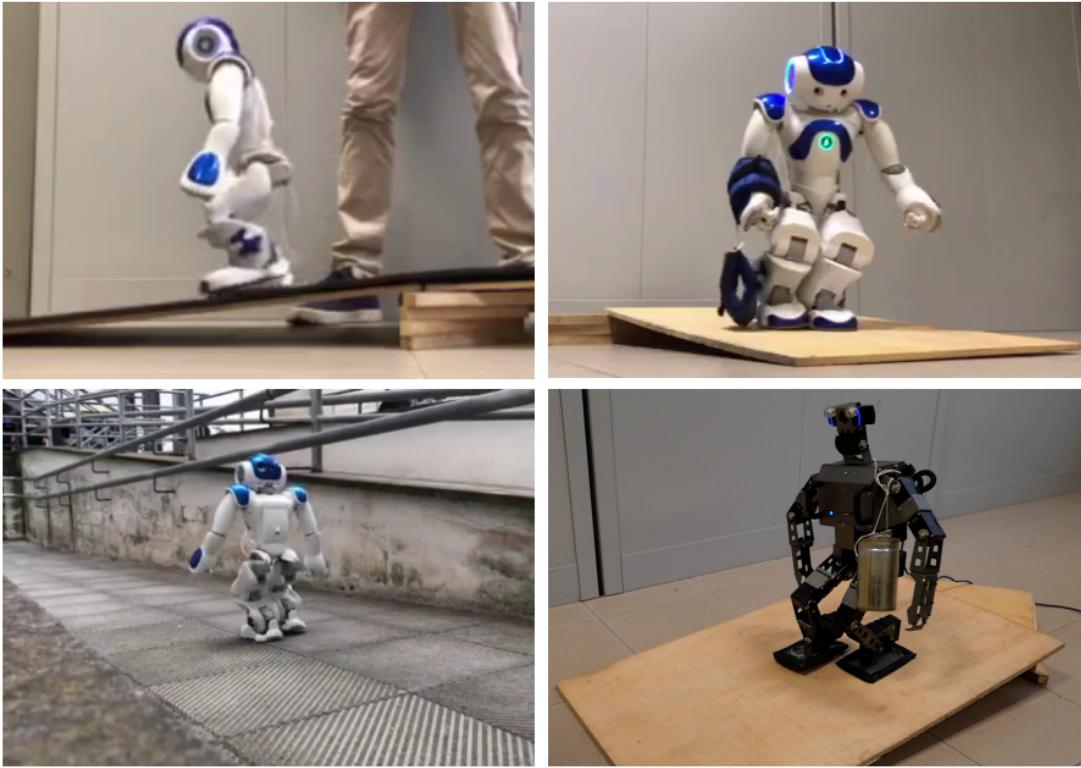
Given this picture, let us consider [1]. The contribution presents a MPC scheme for gait generation, focusing on closed loop robustness. A DCM feedback works in conjunction with the MPC, and thanks to a detailed study on robust positive invariance, the scheme guarantees robust constraint satisfaction. The method requires the computation of the robust positively invariant sets to re-shape the constraints. In our case, we avoid such a computation by addressing robust recursive feasibility via analytic computations on the constraints and then by solving a simple optimization program to compute the restriction parameters.

A measure of the maximum tolerated disturbance is also provided in [1] given the sampling interval, the support polygon width, and the pendulum frequency η, writing as

$$\Delta^{\max,[1]} = \eta^2 \frac{d_z}{2} e^{-\eta\delta}. \tag{7.31}$$

We numerically verified that, under the same hypothesis (no disturbance observation and perturbation set centered in the origin), our scheme can handle the same perturbation as [1]. To do so, we verified whether there existed a feasible restriction function satisfying (7.25) in which $\gamma^{\max}$ is computed by setting $\Delta_x = \Delta^{\max,[1]}$ and $\dot{\Delta}_x = 0$.

Given this first check, we discuss a qualitative difference due to the presence of the observer in our method. Figure 7.17 shows the CoM/ZMP trajectories, obtained from

Figure 7.18: Experiment snapshots: (top left) NAO walking over a sequence of slopes, (top right) NAO walking down a slope while carrying weights, (bottom left) NAO walking down a slope in an outdoor environment, (bottom right) OP3 walking down a slope while carrying a weight.
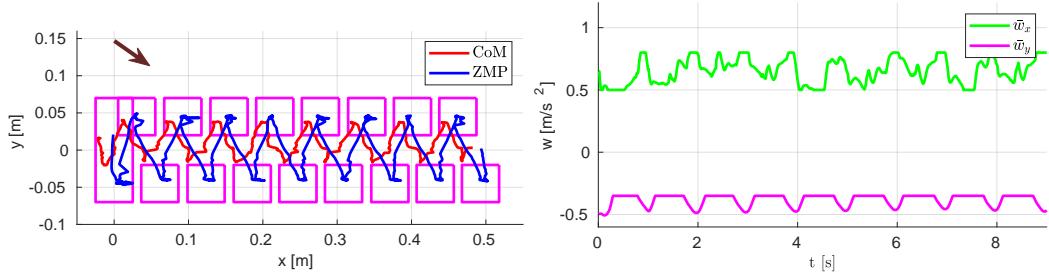
DART, of [1] with respect to the presented approach under the effect of a constant lateral disturbance that is contained inside the considered set. Our scheme generates the usual CoM/ZMP leaning. On the other hand, the outcome [1] shows a displaced ZMP trajectory towards the boundaries of the support polygon.

Given this discussion, we can advocate that the two methods have comparable results. The practical advantage of our scheme relies on the fact that the observer gives help in rejecting possible out-of-range variations in the perturbation. Furthermore, monitoring the feasibility region provides access to a useful information that can trigger recovery behaviors when incurring into critical situations, as it will be detailed in the next chapters.

7.4 Experiments

Simulations in Matlab and Dart confirmed the robustness of the presented scheme. The final stage of validation is to conduct experiments on physical platforms. We used in simulation the full-sized HRP-4 robot which is not available in the laboratory where the research was conducted. The robots that were instead accessible for implementations are NAO and OP3.

NAO is a small sized humanoid (0.58 m tall) weighting 5.3 kg; it has an on-board computer and is endowed with encoders, IMU, and force sensing resistors for state

Figure 7.19: Data from the experiment in which NAO walks down a slope while carrying a weight: (left) CoM/ZMP trajectories, (right) saturated disturbance.

estimation. To provide a further demonstration, a test is also conducted on the OP3 robot (3.5 Kg, 0.51 m tall), which in turns has no force sensing at the foot sole. Experiments on different robots highlight the fact that the proposed scheme is not tailored to a specific platform and can be adapted to different situations without large tuning efforts at the MPC level[9].

In both robots the proposed algorithm runs in real-time over the on-board computer: Intel Atom 1,6 GHz (NAO), INTEL NUC with Intel Core i3-7100U 2x2.40 GHz processor and 8GB 2133MHz RAM (OP3).

Walking down slopes and carrying weights with NAO

We adopted the following parameters: $h = 0.21$ m, $d_{z,x} = d_{z,y} = 0.05$ m, $\delta = 0.05$ s, $T_s = 0.5$ s, $T_{ds} = 0.2$ s, $T_c = 1$ s, $T_p = 2$ s. The kinematic controller runs at 100 Hz and the QPs are solved with the qpOASES library.

In the first experiment, NAO walks over a series of ramps in a lab environment. We set $w_{m,x} = 0.75$ m/s^2, $\Delta_x = 0.3$ m/s^2, $w_{m,y} = 0$ m/s^2 and $\Delta_y = 0.3$ m/s^2, $\alpha = 0.25$. The settings consists in a platform composed by two subsequent ramps of which the slope is respectively 3° and 6°. The robot starts in a balanced rest position and completes the gait without falling. The scheme has also been run outdoor, as shown in Fig. 7.18. Here NAO succeeds in walking down a slope with unknown inclination.

In the second experiment, NAO descends a wooden platform with a 4.5° slope, while carrying two 0.5 kg weights attached to its right arm. We set $w_{m,x} = 0.65$ m/s^2, $\Delta_x = 0.3$ m/s^2, $w_{m,y} = -0.5$ m/s^2, $\Delta_y = 0.3$ m/s^2, and $\alpha = 0.25$. The humanoid maintains dynamic balance, completing the execution of its footstep plan as shown in Fig. 7.18. In Fig. 7.19 the CoM/ZMP trajectories and the observed disturbances recorded from the robot are shown. The data confirm the expected leaning towards the action of the perturbation. Over a set of ten repetitions of the same experiment, we always obtained the same successful outcome. The nominal IS-MPC in the same settings results in a gait which strongly deviates from the straight direction, and, in the vast majority of the runs, the robot falls (eight over ten).

OP3 walking down a slope

To further investigate the robustness of the proposed scheme, we also conducted an experiment on the OP3 platform. In this case, the wooden platform has a slope of 6°, and a 0.3 Kg weight is attached to the left shoulder of the robot. The ZMP measurement

---

[9]Tuning is required by the kinematic controller.

is not available from force sensing at the feet, we thus decided to conduct the experiment by just setting a constant midrange value ($w_{m,x} = 0.7$ m/s^3, $w_{m,y} = 0.3$ m/s^3) without using a disturbance observer.

The QPs are solved with the *hpipm* library, while the kinematic controller runs at 125 Hz. A snapshot of the experiment is reported in Fig. 7.18. This test validates the proposed algorithm over a different platform, highlighting the portability of the scheme.

Chapter 8

Feasibility-driven methods for robust MPC gait generation

We addressed in the previous chapter the problem of gait generation in the presence of persistent disturbances. The peculiarity of the proposed MPC scheme was the possibility to ensure robust recursive feasibility by leveraging the constraints of the optimization problem, with the result of generating disturbance aware CoM/ZMP trajectories. The eventuality of modifying the footstep plan was not considered.

Yet, achieving autonomy in a humanoid platform must also involve being able to adapt to the circumstances in real time based on the state. The form of robustness presented so far is not sufficient for instance when dealing with a disturbance $w_x \notin \sup \mathcal{W}_x$. Including the possibility of modifying the footstep position and timing is thus a fundamental requirement to increase the range of perturbations that the robot can withstand.

This chapter is focused on gait generation using Automatic Footstep Placement (AFP): the MPC scheme is extended with the capability of computing footstep position within the optimization problem. This idea has been initially proposed in [122] and adopted in the nominal Intrinsically Stable MPC formulation [127], which will be exposed in the first section of the chapter.

The novelty and contribution is here given by the feasibility analysis of the IS-MPC with AFP. The feasibility region is derived and a closed form expression of the bounds of it is reported. Such feasibility analysis opens the possibility for reactive planning strategies that improve robustness. The key point that might also be deduced from reading the previous chapter is that robustness in a MPC-based controller (for humanoid locomotion) can be interpreted as a *feasibility problem*. MPC optimizes the trajectories according to the chosen cost function, but its striking advantage with respect to different control techniques consists in the capability of enforcing constraints. In gait generation problems, constraints are more important than the tasks (traduced into costs): balancing and internal stability have priority over the rest. Constraint satisfaction corresponds to feasibility and viceversa, and this fact can be used for robust control.

Consider a simple example. The robot is walking via the architecture of the previous chapter and the MPC is feasible at the current time. Assume then that an external force starts acting at a certain time on the robot. Thanks to the robustness features, the scheme could manage to work properly until the disturbance is within at most $\sup \mathcal{W}_x$, as in fact shown in simulations or experiments. Let us now increase the magnitude

of the applied force in such conceptual experiment. There will be a point in which the DCM is brought outside the feasibility region and the scheme looses its control authority. There is no way for the QP to compute a meaningful solution. Under an engineering point of view, this situation should trigger a safety mode, as the walking pattern generator is not able anymore to generate a balanced motion.

Assume now that as soon as a feasibility loss is detected, the feasibility region is modified so as to encapsulate again the DCM. The feasibility region depends on the constraints which in turns depend on the specific footstep plan (and the robot structure). It means that given a loss of feasibility, there might exist a *different plan* for which the scheme is feasible. This simple idea is at the core of the contribution of this chapter and will be detailed in the following sections.

8.1   IS-MPC with Automatic Footstep Placement

We begin by characterizing the IS-MPC scheme described in [8, 127]. In the same spirit of the robust scheme presented in the previous chapter, the IS-MPC with AFP works over discrete time intervals δ. The generic time instant is denoted by the usual variable t_k.

The input of the scheme is a *candidate* footstep plan, comprising information for M future steps, which are now denoted with the symbols

$$\hat{X}_f^k = (\hat{x}_f^1, \ldots, \hat{x}_f^M), \quad \hat{Y}_f^k = (\hat{y}_f^1, \ldots, \hat{y}_f^M), \quad \hat{\tau}_s^k = (\hat{t}_s^1, \ldots, \hat{t}_s^M).$$

The plan parameters are intended as candidate because the scheme has now the capability of modifying them. The point $(\hat{x}_f^j, \hat{y}_f^j)$, $j = 1, \ldots, M$, defines the position of the j-th candidate footstep and $\hat{t}_s^j$ the corresponding timestamp. At time t_s^j a new double support phase begins. The total duration of the j-th step is given by $\hat{T}_s^j = \hat{t}_s^{j+1} - \hat{t}_s^j$, composed by a double and a single support phase. Their duration is respectively $\hat{T}_{ds}^j$ and $\hat{T}_{ss}^j$.

We still retain the convenient assumption of fixed orientation to simplify the exposition as well as the availability at each t_k of information from the plan for a preview horizont T_p. In IS-MPC with automatic footstep placement, the ZMP velocities and the footstep positions are decision variables

$$\dot{X}_z^k = (\dot{x}_z^k, \ldots, \dot{x}_z^{k+C-1}), \quad X_f^k = (x_f^1, \ldots, x_f^F).$$

At each time step, a constrained optimization problem is solved and the first optimal control variable is used to integrate the model and obtain a reference position and velocity for the CoM $\boldsymbol{p}_c^*, \dot{\boldsymbol{p}}_c^*$, which is sent to a kinematic controller block together with the reference swing foot pose, generated this time by a block that takes the footstep position computed by IS-MPC as input.

8.1.1   Prediction model

We use the LIP (4.12) as prediction model for the IS-MPC. The state space form of the LIP is given by

$$\begin{bmatrix} \dot{x}_c \\ \ddot{x}_c \\ \dot{x}_z \end{bmatrix} = \begin{bmatrix} 0 & 1 & 0 \\ \eta^2 & 0 & -\eta^2 \\ 0 & 0 & 0 \end{bmatrix} \begin{bmatrix} x_c \\ \dot{x}_c \\ x_z \end{bmatrix} + \begin{bmatrix} 0 \\ 0 \\ 1 \end{bmatrix} \dot{x}_z \tag{8.1}$$

where the input is the piece-wise constant ZMP velocity $\dot{x}_z$. Note that we are not considering the effect of the perturbation in (8.1), as we are investigating here the robustness with respect to unpredictable and strong disturbances. In the next chapter, a method to unify the previous chapter to the current will be presented.

8.1.2 ZMP constraints

The ZMP constraints in compact form write now as

$$x_z^m(t, X_f^k, \tau_s^k) \le x_z(t) \le x_z^M(t, X_f^k, \tau_s^k), \tag{8.2}$$

having made explicit the dependency on the footsteps and the timing (that are no more pre-determined based on the plan). In practice, the bounds during the j-th step have the same expression as (7.5)-(7.5), i.e.,

$$
\begin{aligned}
x_z^m(t) &= x_f^{j-1} + (x_f^j - x_f^{j-1})\sigma(t, t_s^j, t_s^j + T_{ds}^j) - \frac{1}{2}d_{z,x}, \\
x_z^M(t) &= x_f^{j-1} + (x_f^j - x_f^{j-1})\sigma(t, t_s^j, t_s^j + T_{ds}^j) + \frac{1}{2}d_{z,x},
\end{aligned}
$$

but the footsteps x_f^j are now decision variables of the MPC, whereas the timings will be determined according to a specific methodology presented in the following sections.

8.1.3 Kinematic constraints

Kinematic constraints are enforced to guarantee that all footsteps comply with the kinematic limits of the humanoid. The position of the footsteps must in fact be inside the Kinematic Admissible Region (KAR). The latter is a function of the kinematic limits of the joints and has in general a non-convex shape. To retain a linear MPC formulation, the j-th predicted footstep must lie within a convex region $\bar{\mathcal{K}}^j$, chosen as a rectangular approximation of the KAR (see Fig. 8.1). The constraint is expressed by
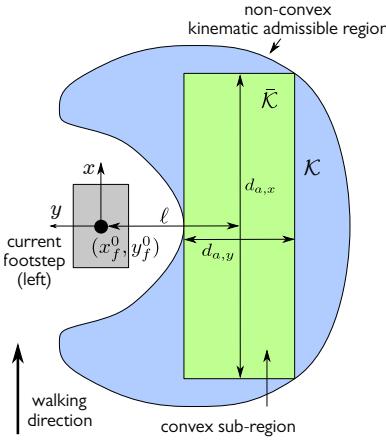
$$(x_f^j, \, y_f^j) \in \bar{\mathcal{K}}^j, \quad j = 1, \dots, F, \tag{8.3}$$

with $\bar{\mathcal{K}}^j$ given by

$$\bar{\mathcal{K}}^j = \left\{ (x, y) : \left| x - x_f^{j-1} \right| \le \frac{d_{a,x}}{2}, \left| y - y_f^{j-1} \pm \ell \right| \le \frac{d_{a,y}}{2} \right\}.$$

The quantities $d_{a,x}$ and $d_{a,y}$ are the dimensions of the chosen rectangular approximation, ℓ is a lateral displacement, and the $\pm$ sign means that the displacement occurs alternatively towards the positive and negative direction of the y axis, depending on the support foot.

We remark that the footstep position should also be constrained by the joint velocity limits of the robot legs. For example, the more the swing foot motion is towards the landing instant, the less the target foot position should be modified. This can be enforced through a constraint [122]. As we are considering walking motions, we assume in this chapter that there is no need to explicitly introduce it. We will rather enforce a similar concept through the step timing adaptation procedure, described in the next sections. In Chapter 10 instead, as faster motions will be considered, such constraint will be part of the proposed MPC formulation.

Figure 8.1: The KAR and its convex approximation. The robot is in single support with the left foot and the sole $\bar{\mathcal{K}}^1$ is represented.

8.1.4 Stability constraint

The stability constraint is derived from the stability condition on the LIP model (6.5). It is expressed in terms of the piece-wise constant ZMP velocity input as

$$\sum_{i=0}^{C-1}(e^{-i\eta\delta} - e^{-(i+1)\eta\delta})\frac{\dot{x}_z^{k+i}}{\eta} = x_u^k - x_z^k(1 - e^{-\eta T_c}) - \tilde{c}_x^k, \tag{8.4}$$

with

$$\tilde{c}_x^k = \eta \int_{t_{k+C}}^{\infty} e^{-\eta(\tau - t_k)}\tilde{x}_z(\tau)d\tau, \tag{8.5}$$

where $\tilde{x}_z$ is equal to (7.14). Note that, beside the disturbance term, the stability constraint is unchanged with respect to the previous chapter, as it does not depend on the footstep positions.

8.1.5 Quadratic program

At the k-th iteration the following QP is solved

$$\min_{\dot{X}_z^k, X_f^k} \|\dot{X}_z^k\|^2 + \mu\|X_f^k - \hat{X}_f^k\|^2$$

subject to:

- ZMP constraints (8.2), for $j = 0, \ldots, F$

- kinematic constraints (8.3), for $j = 1, \ldots, F$

- stability constraint (8.4).

As in the previous chapter, a term in the cost function can be included to promote the generated ZMP trajectory to lie at the center of the moving constraint region.

This QP returns a ZMP velocity trajectory and F modified footstep positions. The first sample $\dot{x}_z^k$ is used to integrate the LIP dynamics and the first computed footstep goes into the swing foot generation module.

8.2 Feasibility region

The feasibility region will now also depend on the kinematic constraints. In the previous chapter, the concept was used for analysis and for the design of the restriction function. Analytical expressions were not required for practical purposes. Here instead, we compute in closed form the boundaries, as they will be used for real-time reactive planning.

8.2.1 Necessary and sufficient condition for feasibility of IS-MPC with AFP

Consider the following:

Proposition 9 *The QP of the sagittal component of the scheme is feasible at t_k if and only if $x_u^k \in \mathcal{F}_x^k$, with*

$$\mathcal{F}_x^k = \{x_u : x_u^{k,m} \le x_u \le x_u^{k,M}\}$$

where

$$
\begin{aligned}
x_u^{k,m} &= \eta \int_{t_k}^{t_{k+C}} e^{-\eta(\tau - t_k)} x_z^m(\tau) d\tau + \tilde{c}_x^k \\
x_u^{k,M} &= \eta \int_{t_k}^{t_{k+C}} e^{-\eta(\tau - t_k)} x_z^M(\tau) d\tau + \tilde{c}_x^k
\end{aligned}
\tag{8.6}
$$

in which

$$
\begin{aligned}
x_z^m(t) &= x_f^{-1} + (x_f^0 - x_f^{-1})\sigma(t, t_s^0, t_s^0 + T_{ds}^0) - \frac{d_{z,x}}{2} - \frac{d_{a,x}}{2}\sum_{j=1}^{F} \sigma(t, t_s^j, t_s^j + T_{ds}^j) \\
x_z^M(t) &= x_f^{-1} + (x_f^0 - x_f^{-1})\sigma(t, t_s^0, t_s^0 + T_{ds}^0) + \frac{d_{z,x}}{2} + \frac{d_{a,x}}{2}\sum_{j=1}^{F} \sigma(t, t_s^j, t_s^j + T_{ds}^j).
\end{aligned}
\tag{8.7}
$$

Proof. We begin with necessity. If IS-MPC is feasible at the current time t_k, the generated ZMP trajectories must satisfy
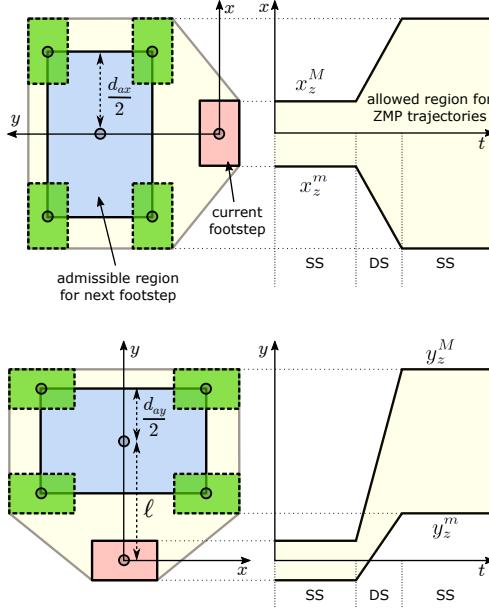
$$x_z^{m,\min}(t) \le x_z \le x_z^{m,\max}(t). \tag{8.8}$$

The values of $x_z^{m,\min}(t)$ and $x_z^{M,\max}(t)$ are given by

$$
\begin{aligned}
x_z^{m,\min}(t) &= \min_{X_f^k} x_z^m(t, x_f^1, \dots, x_f^F) \\
x_z^{M,\max}(t) &= \max_{X_f^k} x_z^M(t, x_f^1, \dots, x_f^F).
\end{aligned}
$$

In practice, we iterate the ZMP constraint (8.2) over the control horizon and use the x component of the kinematic constraint (8.3) to eliminate the dependence on the footstep positions x_f^j for $j = 1, \dots, F$. In this way, $x_z^{m,\min}(t)$ and $x_z^{M,\max}(t)$ account for any possible footstep location (see Fig. 8.2).

Having obtained a bound for the possible ZMP trajectories, we proceed as for Prop. 6: we multiply each term of (8.8) by $\eta\, e^{\eta(t-t_k)}$, integrate over time from t_k to t_{k+C}, add $\tilde{c}_x^k$ on each side, and note that the middle term of the resulting inequality is equal to x_u^k thanks to (6.5), while the outer terms are $x_u^{k,m}$ and $x_u^{k,M}$ according to (8.6).

Figure 8.2: Kinematic constraint (left) and its effect on shaping the bounds on the ZMP trajectory (8.7) (right), for both the x and y components. The green footsteps are placed at the extreme positions compatible with the kinematic constraint (blue region).

Sufficiency can be shown as follows. Let $x_u^k \in \mathcal{F}_x^k$, so that x_u^k is a convex combination of the feasibility region bounds:

$$x_u^k = a x_u^{k,m} + (1-a) x_u^{k,M} \quad \text{with } a \in [0,1].\tag{8.9}$$

Pick now the ZMP trajectory

$$x_z^*(t) = a x_z^{m,\min}(t) + (1-a) x_z^{m,\max}(t),$$

satisfying the ZMP constraint in $[t_k, t_{k+C}]$ for the kinematically admissible sequence of footsteps

$$x_f^j = x_f^{j-1} + \left(\frac{1}{2} - a\right)\frac{d_{a,x}}{2}.$$
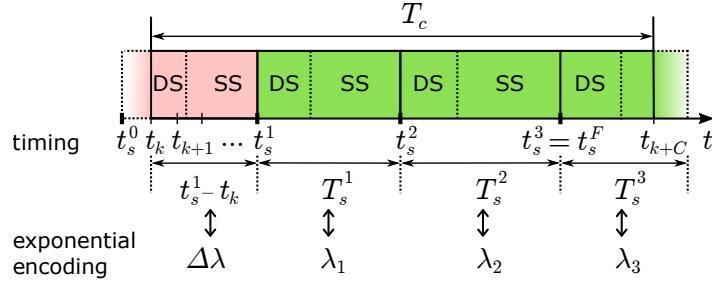
Stability constraint (8.4) is satisfied since

$$x_u^k = \eta \int_{t_k}^{t_{k+C}} e^{-\eta(\tau - t_k)} x_z^*(\tau) d\tau + \tilde{c}_x^k = a x_u^{k,m} + (1-a) x_u^{k,M}$$

is true according to (8.9). We demonstrated sufficiency by showing that, if x_u^k is inside $\mathcal{F}_x^k$, there exists at least a ZMP trajectory and a sequence of footsteps satisfying all constraints. ∎

Proposition 9 is written for the decoupled problem, and an equivalent proposition can be enunciated for the y component. The proof would be identical except for the kinematic constraints, which must incorporate the lateral displacement

$$y_f^j = y_f^{j-1} + \left(\frac{1}{2} - a\right)\frac{d_{a,y}}{2} \pm \ell.\tag{8.10}$$

Figure 8.3: The timings and their relation with the variables $\Delta\lambda, \lambda_j$ within the MPC prediction horizon T_c.

At each time, feasibility for the complete problem holds if and only if

$$(x_u^k, y_u^k) \in \mathcal{F}_{x,y}^k.$$

8.2.2 Computation of the bounds of the feasibility region

We now compute in closed form the bounds (8.6) of the feasibility region $\mathcal{F}^k$. For convenience of later developments, we introduce a parameterization of the step durations: the remaining duration of the *current* step, i.e., the *time-to-step*, is denoted by

$$\Delta\lambda = e^{-\eta(t_s^1 - t_k)},$$

while the subsequent durations are encoded as $\lambda_{1\text{-}F} = \{\lambda_1, \ldots, \lambda_F\}$, where

$$\lambda_j = e^{-\eta T_s^j}.$$

It is also instrumental to define the quantity

$$\nu_j = T_{ds}^j / T_s^j,$$

namely the double support over the whole step ratio.

The bounds (8.6), for t_k in a double support phase, will assume an expression of the type

$$x_u^{k,m/M} = \alpha_{ds,x}^{m/M}(\lambda_{1\text{-}F})\Delta\lambda + \beta_{ds,x}^{m/M}\log\Delta\lambda + \gamma_{ds,x}^{m/M}, \tag{8.11}$$

while, for t_k in a single support phase, the form

$$x_u^{k,m/M} = \alpha_{ss,x}^{m/M}(\lambda_{1\text{-}F})\Delta\lambda + \gamma_{ss,x}^{m/M}. \tag{8.12}$$

The rest of the section will develop the computations of the feasibility boundaries. Non-interested readers can directly proceed to Sect. 8.3. To provide an idea of the expressions to who is going to skip the computation part, we report the coefficients

appearing in (8.11) for $x_u^{k,m}$:

$$\alpha_{ds,x}^m(\lambda_{1\text{-}F}) = \frac{x_f^{-1} - x_f^0}{\eta T_{ds}^0}e^{\eta T_{ss}^0} + \frac{d_{a,x}}{2}\sum_{j=1}^{F}\frac{1-\lambda_j^\nu}{\nu\log\lambda_j}\prod_{i=1}^{j-1}\lambda_i \tag{8.13}$$

$$\beta_{ds,x}^m = \frac{x_f^0 - x_f^{-1}}{\eta T_{ds}^0} \tag{8.14}$$

$$\gamma_{ds,x}^m = (x_f^0 - x_f^{-1})\frac{1+\eta T_s^0}{\eta T_{ds}^0} - \frac{d_{z,x}}{2}(1 - e^{-\eta T_c}) \tag{8.15}$$

$$+x_f^{-1} - x_f^0 e^{-\eta T_c} + F\frac{d_{a,x}}{2}e^{-\eta T_c} + \tilde{c}_x^k. \tag{8.16}$$

We can now begin with the computation of the integrals (8.6). Let us first introduce three auxiliary functions, denoted as Properties, introduced to express the integrals of the piecewise-linear sigmoidal function (7.4). We have

Property 1 *For $t_i < t_k$*

$$P1(t_k, t_i, t_f) = \eta\int_{t_k}^{t_k+C}\sigma(\tau, t_i, t_f)e^{-\eta(\tau-t_k)}d\tau$$

$$= \eta\int_{t_k}^{t_f}\frac{(\tau-t_i)}{(t_f-t_i)}e^{-\eta(\tau-t_k)}d\tau + \eta\int_{t_f}^{t_k+C}e^{-\eta(\tau-t_k)}d\tau \tag{8.17}$$

$$= \frac{1 - \eta(t_i - t_k) - e^{-\eta(t_f-t_k)}}{\eta(t_f - t_i)} - e^{-\eta T_c}.$$

Property 2 *For $t_k < t_i$*

$$P2(t_k, t_i, t_f) = \eta\int_{t_k}^{t_k+C}\sigma(\tau, t_i, t_f)e^{-\eta(\tau-t_k)}d\tau$$

$$= \eta\int_{t_i}^{t_f}\frac{(\tau-t_i)}{(t_f-t_i)}e^{-\eta(\tau-t_k)}d\tau + \eta\int_{t_f}^{t_k+C}e^{-\eta(\tau-t_k)}d\tau$$

$$= \frac{e^{-\eta(t_i-t_k)} - e^{-\eta(t_f-t_k)}}{\eta(t_f - t_i)} - e^{-\eta T_c}. \tag{8.18}$$

Property 3

$$P3 = \eta\int_{t_k}^{t_k+C}e^{-\eta(\tau-t_k)}d\tau = 1 - e^{-\eta T_c}. \tag{8.19}$$

x component: expression of the feasibility bounds during the double support phase

For $t_k \in [t_s^0, t_s^0 + T_{ds}^0]$, by direct computation of the integral that expresses the lower feasibility region bound of the x component, we have

$$x_u^{k,m} = \left(x_f^{-1} - \frac{d_{z,x}}{2} \right) P3 + (x_f^0 - x_f^{-1}) P1(t_k, t_s^0, t_s^0 + T_{ds})$$
$$- \frac{d_{a,x}}{2} \sum_{j=1}^{F} P2(t_k, t_s^j, t_s^j + T_{ds}^j) + \tilde{c}_x^k \tag{8.20}$$

that writes as

$$x_u^{k,m} = \left(x_f^{-1} - \frac{d_{z,x}}{2} \right) (1 - e^{-\eta T_c}) + \frac{x_f^0 - x_f^{-1}}{\eta T_{ds}^0} \left[1 - \eta(t_s^0 - t_k) - e^{-\eta(t_s^0 + T_{ds}^0 - t_k)} \right]$$
$$- (x_f^0 - x_f^{-1})e^{-\eta T_c} - \frac{d_{a,x}}{2} \sum_{j=1}^{F} \frac{1}{\eta T_{ds}^j} \left[e^{-\eta(t_s^j - t_k)} - e^{-\eta(t_s^j + T_{ds}^j - t_k)} \right] + \tag{8.21}$$
$$F \frac{d_{a,x}}{2} e^{-\eta T_c} + \tilde{c}_x^k.$$

Bearing in mind that $t_s^0 = t_s^1 - T_s^0$ and that $t_s^0 + T_{ds}^0 = t_s^1 - T_{ss}^0$, we obtain

$$x_u^{k,m} = \left(x_f^{-1} - \frac{d_{z,x}}{2} \right) (1 - e^{-\eta T_c}) + \frac{x_f^0 - x_f^{-1}}{\eta T_{ds}^0} \left[1 + \eta T_s^0 - \eta(t_s^1 - t_k) - e^{\eta T_{ss}^0} e^{-\eta(t_s^1 - t_k)} \right]$$
$$- (x_f^0 - x_f^{-1})e^{-\eta T_c} - \frac{d_{a,x}}{2} \sum_{j=1}^{F} \frac{1 - e^{-\eta T_{ds}^j}}{\eta T_{ds}^j} e^{-\eta(t_s^j - t_k)} +$$
$$+ F \frac{d_{a,x}}{2} e^{-\eta T_c} + \tilde{c}_x^k. \tag{8.22}$$

Recalling that $\nu_j = T_{ds}^j / T_s^j$, we have $e^{-\eta T_{ds}^j} = \lambda_j^{\nu_j}$ and $\eta T_{ds}^j = -\nu_j \log \lambda_j$. Noting that

$$e^{-\eta(t_s^j - t_k)} = e^{-\eta(t_s^1 - t_k + t_s^2 - t_s^1 + \cdots + t_s^j - t_s^{j-1})}$$
$$= e^{-\eta(t_s^1 - t_k + T_s^1 + \cdots + T_s^{j-1})}, \tag{8.23}$$

expression (8.22) becomes

$$x_u^{k,m} = \left(x_f^{-1} - \frac{d_{z,x}}{2} \right) (1 - e^{-\eta T_c}) + \frac{x_f^0 - x_f^{-1}}{\eta T_{ds}^0} \left[1 + \eta T_s^0 + \log \Delta\lambda - e^{\eta T_{ss}^0} \Delta\lambda \right]$$
$$- (x_f^0 - x_f^{-1})e^{-\eta T_c} + \frac{d_{a,x}}{2} \sum_{j=1}^{F} \frac{1 - \lambda_f^{\nu_j}}{\nu_j \log \lambda_j} \prod_{i=1}^{j-1} \lambda_i \Delta\lambda +$$
$$+ F \frac{d_{a,x}}{2} e^{-\eta T_c} + \tilde{c}_x^k. \tag{8.24}$$

We remark that the first term in the sum contains a product going from 1 to 0 which is conventionally set equal to one. We reorder (8.24) as

$$
\begin{aligned}
x_u^{k,m} =& \frac{x_f^{-1} - x_f^0}{\eta T_{ds}^0} e^{\eta T_{ss}^0} \Delta\lambda + \frac{d_{a,x}}{2} \sum_{j=1}^F \frac{1 - \lambda_j^{\nu_j}}{\nu_j \log \lambda_j} \prod_{i=1}^{j-1} \lambda_i \Delta\lambda \\
&+ \frac{x_f^0 - x_f^{-1}}{\eta T_{ds}^0} \log \Delta\lambda + (x_f^0 - x_f^{-1}) \frac{1 + \eta T_s^0}{\eta T_{ds}^0} - \frac{d_{z,x}}{2}(1 - e^{-\eta T_c}) \\
&+ x_f^{-1} + (F \frac{d_{a,x}}{2} - x_f^0) e^{-\eta T_c} + \tilde{c}_x^k.
\end{aligned}
\tag{8.25}
$$

Grouping the terms of (8.25) leads to (8.13)-(8.14)-(8.15).

x component: expression of the feasibility bounds during the single support phase

For $t_k \in [t_s^0 + T_{ds}^0, t_s^1]$, the solution of the integral of the feasibility region lower bound during the single support is

$$
x_u^{k,m} = \left(x_f^0 - \frac{d_{z,x}}{2}\right) P3 - \frac{d_{a,x}}{2} \sum_{j=1}^F P2(t_k, t_s^j, t_s^j + T_{ds}^j) + \tilde{c}_x^k.
\tag{8.26}
$$

In terms of $\Delta\lambda$, λ_j and making use of (8.18), (8.19), we have

$$
\begin{aligned}
x_u^{k,m} =& \frac{d_{a,x}}{2} \sum_{j=1}^F \frac{1 - \lambda_j^{\nu_j}}{\nu_j \log \lambda_j} \prod_{i=1}^{j-1} \lambda_i \Delta\lambda + \\
& \left(x_f^0 - \frac{d_{z,x}}{2}\right)(1 - e^{-\eta T_c}) + F \frac{d_{a,x}}{2} e^{-\eta T_c} + \tilde{c}_x^k
\end{aligned}
\tag{8.27}
$$

which is easily verified to be linear in $\Delta\lambda$.

The upper bound of the x component of the feasibility region has the same expression as (8.25)-(8.27) unless a proper modification on the sign of the support polygon and kinematic constraint terms.

y component: expression of the feasibility bounds during the double support phase

The y component enforces different kinematic constraints, thus the expression of the feasibility region will differ from that of the x component. For $t_k \in [t_s^0, t_s^0 + T_{ds}^0]$, we have

$$
\begin{aligned}
y_u^{k,m} =& (y_f^{-1} - \frac{d_{z,y}}{2}) P3 + (y_f^0 - y_f^{-1}) P1(t_k, t_s^0, t_s^0 + T_{ds}) \\
&- \sum_{j=1}^F \left(\frac{d_{a,y}}{2} \pm \ell\right) P2(t_k, t_s^j, t_s^j + T_{ds}^j) + \tilde{c}_y^k.
\end{aligned}
\tag{8.28}
$$

Making use of (8.17), (8.18) and (8.19), this bound can be expressed in terms of $\Delta\lambda$, λ_j as

$$
\begin{aligned}
y_u^{k,m} =& \frac{y_f^{-1} - y_f^0}{\eta T_{ds}^0} e^{\eta T_{ss}^0} \Delta\lambda - \sum_{j=1}^{F} \left(-\frac{d_{a,y}}{2} \pm \ell \right) \frac{1 - \lambda_j^{\nu_j}}{\nu_j \log \lambda_j} \prod_{i=1}^{j-1} \lambda_i \Delta\lambda \\
&+ \frac{y_f^0 - y_f^{-1}}{\eta T_{ds}^0} \log \Delta\lambda + (y_f^0 - y_f^{-1}) \frac{1 + \eta T_s^0}{\eta T_{ds}^0} - \frac{d_{z,y}}{2} (1 - e^{-\eta T_c}) \\
&+ y_f^{-1} - y_f^0 e^{-\eta T_c} - \sum_{j=1}^{F} \left(-\frac{d_{a,y}}{2} \pm \ell \right) e^{-\eta T_c} + \tilde{c}_y^k,
\end{aligned}
\tag{8.29}
$$

where the sign alternation of ℓ depends on the support foot. The expression of $y_u^{k,M}$ is found analogously.

y component: expression of the feasibility bounds during the single support phase

For $t_k \in [t_s^0 + T_{ds}^0, t_s^1]$, we have

$$
y_u^{k,m} = \left(y_f^0 - \frac{d_{z,y}}{2} \right) P3 - \sum_{j=1}^{F} \left(\frac{d_{a,y}}{2} \pm \ell \right) P2(t_k, t_s^j, t_s^j + T_{ds}^j) + \tilde{c}_y^k
\tag{8.30}
$$

that in terms of $\Delta\lambda$, λ_j and adopting (8.18), (8.19) becomes
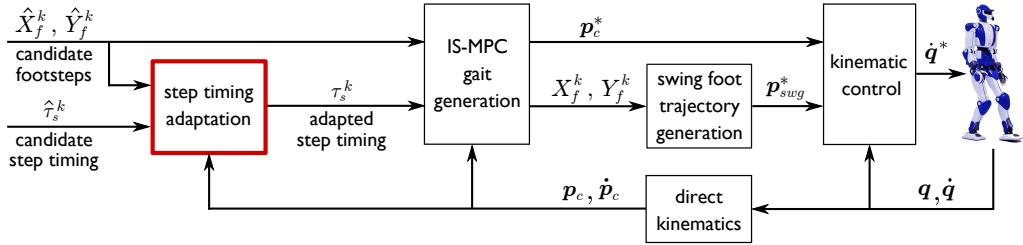
$$
\begin{aligned}
y_u^{k,m} =& -\sum_{j=1}^{F} \left(-\frac{d_{a,y}}{2} \pm \ell \right) \frac{1 - \lambda_j^{\nu_j}}{\nu_j \log \lambda_j} \prod_{i=1}^{j-1} \lambda_i \Delta\lambda \\
&+ (y_f^0 - \frac{d_{z,y}}{2})(1 - e^{-\eta T_c}) - \sum_{j=1}^{F} \left(-\frac{d_{a,y}}{2} \pm \ell \right) e^{-\eta T_c} + \tilde{c}_y^k.
\end{aligned}
\tag{8.31}
$$

8.3 Feasibility-driven step timing adaptation

The scheme presented so far is able by construction to adapt the footsteps so as to counteract the presence of pushes and maintain balance. We showed that at each time instant t_k, the constrained QP of the MPC is guaranteed to be solvable provided that a linear combination of the state of the robot, i.e., the DCM, belongs to a certain feasibility region $\mathcal{F}^k$. The effect of a disturbance can bring (x_u^k, y_u^k) outside such region, and in this case the QP is not able to compute dynamically stable and bounded CoM/ZMP trajectories.

By inspecting the expression of the bounds of the feasibility region in single and double support (8.25)-(8.27)-(8.29)-(8.31), it is immediate to notice their dependence on the step timings, expressed in terms of $\Delta\lambda, \lambda_1, \ldots \lambda_F$: a modification to the timing of the footstep plan corresponds to a modification of the feasibility region $\mathcal{F}^k$. The latter can in fact be re-shaped to recover a loss of feasibility due to, for instance, a strong push. We present in this section a method for Step Timing Adaptation (STA) based on this idea.

The block scheme of the proposed approach is reported in Fig. 8.4. The candidate footstep positions are directly fed to the IS-MPC gait generation block, which was

Figure 8.4: Block scheme of IS-MPC with STA. The step timing adaptation module provides adapted step timings to the IS-MPC block.

described in Sect. 8.1. The candidate timing instead goes through the STA module. If $(x_u^k, y_u^k) \in \mathcal{F}^k$, the timing is not modified. On the other hand, if (x_u^k, y_u^k) exceeds the feasibility boundaries, the timing will be changed so as to re-shape the feasibility region and include the DCM in it. The timing after the STA block is denoted as $\tau_s^k = (t_s^1, \ldots, t_s^F)$. The adapted step timings are then fed to the IS-MPC block, which will use it to build the constraints for the QP.

8.3.1 Conservative estimate of the feasibility region

We formulate the STA problem on the time-to-step, encoded by the $\Delta\lambda$ variable, which is physically constrained to be within the set $[\Delta\lambda^{\min}, \Delta\lambda^{\max}]$, to prevent too fast or too slow stepping. Adapting only $\Delta\lambda$ is motivated by the fact that the current step is the most critical for rejecting a disturbance[1]. Furthermore, the negative exponential function in the integral (8.6) limits the relevance of the $\lambda_1, \ldots \lambda_F$ quantities on shaping such boundaries.

We observed in the previous section that the feasibility bounds are linear in $\Delta\lambda$ during the single support, while in double support the nonlinearity is due to a log function. With the aim of formulating the STA problem as a QP with linear constraints, it is convenient to remove the nonlinearity in $\Delta\lambda$ from the double support bounds (8.25)-(8.29). This is done by observing that $\log \Delta\lambda$ in $[\Delta\lambda^{\min}, \Delta\lambda^{\max}]$ can be bounded above by the tangent computed at

$$\Delta\lambda^{\mathrm{mid}} = (\Delta\lambda^{\min} + \Delta\lambda^{\max})/2,$$

and below by the chord joining $\log \Delta\lambda^{\min}$ and $\log \Delta\lambda^{\max}$. From such procedure, a sub-region of $\mathcal{F}^k$ in double support is obtained:

$$
\begin{aligned}
x_u^{k,m} &\leq \bar{\alpha}_{ds,x}^m \Delta\lambda + \bar{\gamma}_{ds,x}^m = \bar{x}_{u,\mathrm{est}}^{k,m} \\
x_u^{k,M} &\geq \bar{\alpha}_{ds,x}^M \Delta\lambda + \bar{\gamma}_{ds,x}^M = \bar{x}_{u,\mathrm{est}}^{k,M} \\
y_u^{k,m} &\leq \bar{\alpha}_{ds,y}^m \Delta\lambda + \bar{\gamma}_{ds,y}^m = \bar{y}_{u,\mathrm{est}}^{k,m} \\
y_u^{k,M} &\geq \bar{\alpha}_{ds,y}^M \Delta\lambda + \bar{\gamma}_{ds,y}^M = \bar{y}_{u,\mathrm{est}}^{k,M},
\end{aligned}
$$

---

[1]This idea is also argued in [175, 176].

with (reporting the sole expression for the lower bound of the x component)

$$
\begin{aligned}
\bar{\alpha}_{ds,x}^m &= \alpha_{ds,x}^m + \frac{\beta_{ds,x}^m}{\Delta\lambda^{\mathrm{mid}}} \\
\bar{\gamma}_{ds,x}^m &= \gamma_{ds,x}^m + \beta_{ds,x}^m \left(\log \Delta\lambda^{\mathrm{mid}} - 1 \right).
\end{aligned}
$$

We thus define a conservative estimate of $\mathcal{F}^k$ as

$$
\mathcal{F}_{\mathrm{est}}^k = \{ (x_u, y_u) : \bar{x}_{u,\mathrm{est}}^{k,m} \le x_u \le \bar{x}_{u,\mathrm{est}}^{k,M}, \bar{y}_{u,\mathrm{est}}^{k,m} \le y_u \le \bar{y}_{u,\mathrm{est}}^{k,M} \},
$$

where we set

$$
\begin{aligned}
x_u^{k,m} &= \bar{x}_{u,\mathrm{est}}^{k,m} & x_u^{k,M} &= \bar{x}_{u,\mathrm{est}}^{k,M} \\
y_u^{k,m} &= \bar{y}_{u,\mathrm{est}}^{k,m} & y_u^{k,M} &= \bar{y}_{u,\mathrm{est}}^{k,M}
\end{aligned}
$$

in single support phases, so that, by construction, $\mathcal{F}_{\mathrm{est}}^k = \mathcal{F}^k$ during these time instants.
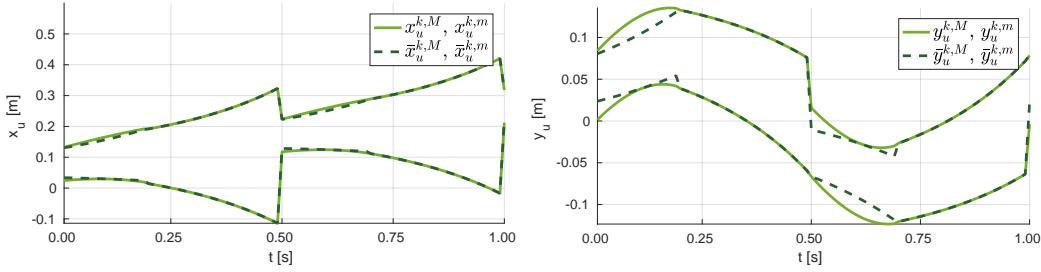
An idea on how the conservative estimate approximates the feasibility region can be gained by inspecting Fig. 8.5. The evolution of $\mathcal{F}^k$ against that of $\mathcal{F}_{\mathrm{est}}^k$ over two steps of duration 0.5 s is shown: $\mathcal{F}_{\mathrm{est}}^k$ coincides with $\mathcal{F}^k$ in single support, and conservatively approximates it during the double support. Figure 8.5 allows for the following considerations:

- at each time t_k, $\mathcal{F}^k$ and $\mathcal{F}_{\mathrm{est}}^k$ are rectangular regions of respective dimensions $(x_u^{k,M} - x_u^{k,m}, y_u^{k,M} - y_u^{k,m})$ and $(\bar{x}_{u,\mathrm{est}}^{k,M} - \bar{x}_{u,\mathrm{est}}^{k,m}, \bar{y}_{u,\mathrm{est}}^{k,M} - \bar{y}_{u,\mathrm{est}}^{k,m})$;

- the center of the $\mathcal{F}^k$ rectangle moves in the space of (x_u, y_u) and its dimensions are time-varying;

- the area of the rectangle monotonically increases starting from the beginning of the double support phase, up to the end of the single support phase, where it is reset to the minimum value;

- in principle, introducing a constraint on the maximum swing foot velocity in the IS-MPC formulation would make the feasibility region during single support phases increase up to a certain point and then start decreasing over time, presenting no discontinuities. However, a swing foot velocity constraint (as that of [122]) requires the knowledge of the swing foot position. This would be an external quantity (with respect to the LIP state and the gait parameters) to be included in the definition of the feasibility region[2]. Rather, we will account for the swing foot velocity limits in the next section, when formulating the QP-STA.

8.3.2 QP-STA

The previous elaboration identified a convenient sub-region to be used in STA. By paying the price of using a slightly conservative estimate of the feasibility region in

---

[2]A related study has been presented in [168] for the characterization of the viability kernel taking into account the swing foot velocity. Unfortunately, the result can not be elaborated and transported in our context for a substantial difference: the feasibility region is tailored to the specific MPC controller and the current time instant, whereas the viability kernel considers all the viable sates given the maximum step length, minimum step timing, and maximum swing foot velocity. In this sense, the feasibility region is a subset of the viability kernel.

Figure 8.5: Bounds of $\mathcal{F}^k$ (solid) vs. $\mathcal{F}^k_{\text{est}}$ (dashed) for both the x and y components over two subsequent steps of 0.5 s, with $T_{ds} = 0.2$ s and $T_{ds} = 0.3$ s.

double support phases, it is possible to formulate the STA problem in a linear-quadratic fashion, by exploiting the linearity of $\mathcal{F}^k_{\text{est}}$ in $\Delta\lambda$.

At time t_k a QP, denoted as QP-STA, is solved to compute the adapted duration of the current step *before* sending the timing vector to IS-MPC:

$$\min_{\Delta\lambda}(\Delta\lambda - \widehat{\Delta\lambda})^2$$

subject to:

- feasibility constraints for x_u and y_u

$$\bar{x}^{k,m}_{u,\text{est}} + \epsilon_x \leq x^k_u \leq \bar{x}^{k,M}_{u,\text{est}} - \epsilon_x$$
$$\bar{y}^{k,m}_{u,\text{est}} + \epsilon_y \leq y^k_u \leq \bar{y}^{k,M}_{u,\text{est}} - \epsilon_y$$

- timing constraints

$$e^{-\eta(t^0_s + T^{\max}_s - t_k)} \leq \Delta\lambda \leq e^{-\eta(t^0_s + T^{\min}_s - t_k)}$$
$$\Delta\lambda \leq e^{-\eta\epsilon_t}$$
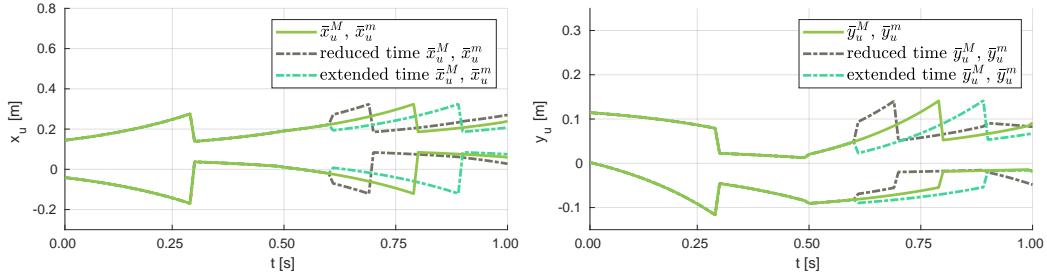
in which:

- $\widehat{\Delta\lambda} = e^{-\eta(\hat{t}^1_s - t_k)}$ is the current candidate timing expressed through the exponential encoding;

- ϵ_x and ϵ_y are non-negative safety margins for the feasibility constraints, to prevent the QP-STA to compute solutions at the boundaries of $\mathcal{F}^k_{\text{est}}$;

- the quantity ϵ_t is given by

$$\epsilon_t = \begin{cases} \hat{T}^0_{ss} + \max\left(|\zeta^k_x - x^0_f|, |\zeta^k_y - y^0_f|\right)/v^{\max}_z & \text{(double support)} \\ \max\left(|x^k_{\text{sw}} - x^{1|k-1}_f|, |y^k_{\text{sw}} - y^{1|k-1}_f|\right)/v^{\max}_{\text{sw}} & \text{(single support)} \end{cases}$$

where $\hat{T}^0_{ss}$ is the candidate duration of the current single support, (ζ^k_x, ζ^k_y) is the center of the moving constraint region at t_k (that follows a fixed timing law in double support phases), $(x^{1|k-1}_f, y^{1|k-1}_f)$ is the target footstep generated by the previous IS-MPC iteration, and $(x^k_{\text{sw}}, y^k_{\text{sw}})$ is the swing foot position at t_k.

The cost function of QP-STA is designed so as to modify the current step duration only if (x^k_u, y^k_u) is outside $\mathcal{F}^k_{\text{est}}$ or if, for any reason, it is required by the timing constraints.

Figure 8.6: Modification of the bounds of $\mathcal{F}_{\text{est}}^k$ in terms of the variations of the time-to-step. The plots were obtained from a simulation in which the robot is walking in the positive x direction. At $\bar{t} = 0.6$ s (left foot swinging), the duration of the current step is reduced/extended by 0.1 s.

If a solution of QP-STA is computed so that $\Delta\lambda \neq \widehat{\Delta\lambda}$, the adapted timestamp of the next step is set to $t_s^1 = t_k + \log(1/\Delta\lambda)/\eta$.
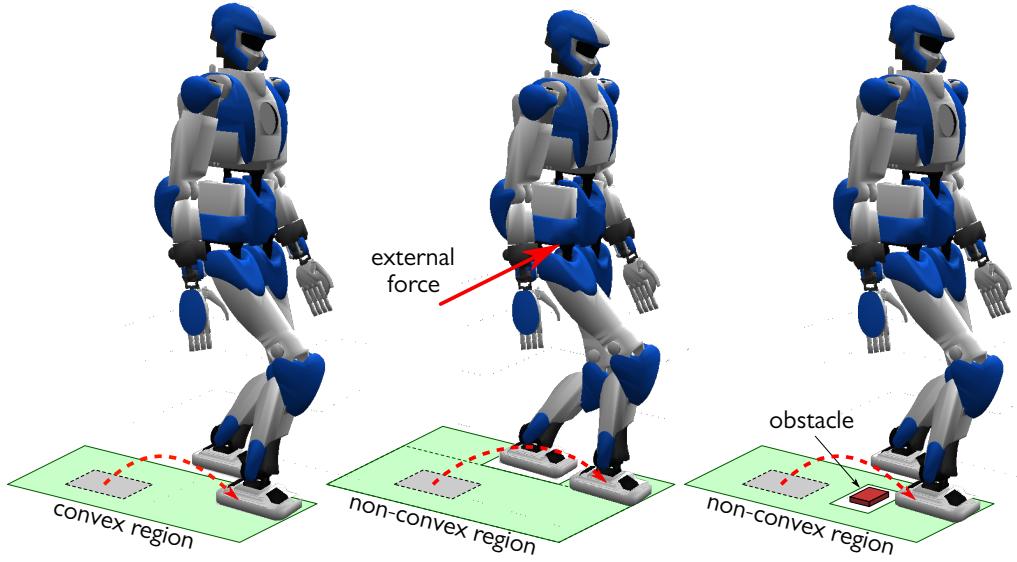
We introduced in the formulation of QP-STA two different timing constraints. The first imposes that any step duration is bounded by $T_s^{\min}$ and $T_s^{\max}$, chosen according to the robot capabilities and the desired motion. Small $T_s^{\min}$ might in fact require high actuation torques, while large $T_s^{\max}$ might lead to slow gaits. The second constraint is introduced for two reasons. It allows to adapt only the duration of the current phase: in double support the time-to-step cannot be reduced below the candidate duration of single support. Moreover, it also ensures that the humanoid has enough time to complete the current step phase given the bounds $v_z^{\max}$ on the ZMP velocity (double support) and $v_{\text{sw}}^{\max}$ on the swinging foot velocity (single support), assumed to be the same over x and y. Such timing bounds are inspired by the swing foot velocity constraint introduced in [122].

Figure 8.6 shows the effect on $\mathcal{F}_{\text{est}}^k$ of a modification to the current time-to-step at a certain time $\bar{t}$:

- a push in the x direction will move x_u towards the same direction. In this case, QP-STA will reduce the current step duration to enlarge $\mathcal{F}_{\text{est}}^k$ along x;

- for a lateral push directed from the support towards the swing leg (positive y), QP-STA will reduce the current step duration to enlarge $\mathcal{F}_{\text{est}}^k$ along y;

- for a lateral push directed from the swing towards the support leg (negative y), QP-STA will extend the current step duration to shift $\mathcal{F}_{\text{est}}^k$ down in y. This happens because of the considered convex sub-region of the KAR (8.3): landing the footstep will result in a feasibility displacement in the wrong direction.

The third bullet of the list may however not be the best strategy to reject a perturbation. Prolonging the current step duration has a limited power to displace the feasibility region towards the push direction when acting from the swing to the support leg. This being the case, two alternatives would act more similarly to physiological intuition:

- landing the current step as soon as possible (while considering the same convex sub-region of the KAR (8.3)) and performing the recovery during the next step;

- allowing for leg crossing by considering a more detailed representation of the KAR.

Figure 8.7: The IS-MPC scheme enforces a convex kinematic constraint (left). However, there are several situations where allowing non-convex steppable regions would improve the capabilities of the scheme with respect to push recovery (meddle) and obstacle avoidance (right).
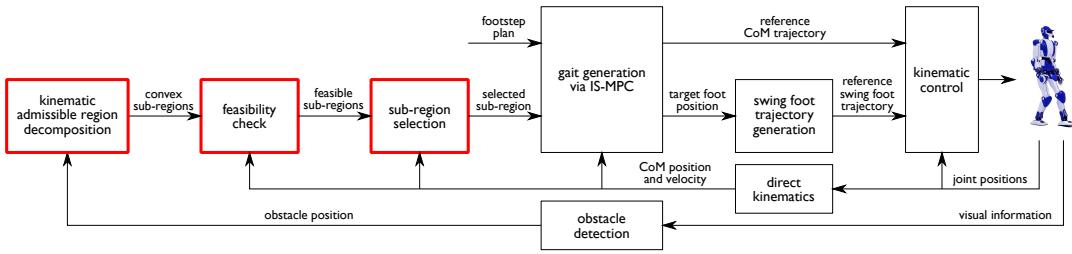
The first idea can be implemented through a simple rule-based state machine, as we showed in [8]. The process is the following. The solution of QP-STA is filtered through a decision block: if the current step duration is computed to be enlarged by QP-STA more than a certain threshold, the minimum step timing is forced so as to make the current step land as soon as possible to achieve a better recovery during the subsequent step. Such a method is based on pure heuristics.

The second bullet instead deals with the possibility of handling non-convex kinematic constraints and will be the topic of the next section.

8.4 Handling non-convex kinematic constraints via the feasibility region

From the previous sections, several limitations due to the convex approximation of the Kinematic Admissible Region (KAR) (8.3) were highlighted. A particular case of push recovery is a suitable example. For pushes directed from the swing towards the support leg, a possible strategy would be to allow the next footstep to be placed in front of the current support foot, and eventually adapt the subsequent footstep position, as shown in Fig. 8.7. A further example is that of obstacle avoidance, where non-steppable regions render the KAR non-convex. Such a situation is depicted in the right hand side picture of Fig. 8.7.

In this section, we extend the scheme described in Sect. 8.1 so as to allow for a non-convex steppable region in order to augment the capabilities of the humanoid in terms of possible rejected disturbances or to allow for the avoidance of small obstacles. Enforcing non-convex constraints in a MPC scheme may undermine the robustness and the real-time capabilities of the numerical solver that is used to obtain the solution. Even if non-linear MPC has been proven to be effective for robot control, the efficiency

Figure 8.8: Block scheme of the IS-MPC with the capability of handling non-convex kinematic constraints.

and reliability of the linear-quadratic formulations is unmatched. To this purpose, we show here how our feasibility theory provides a simple methodology to retrieve a solution of the nonlinear optimization problem that arises from enforcing a non-convex KAR as footstep constraint in the scheme.

The idea is to approximate the KAR with a non-convex polytope and then decompose this approximation into a set of non-overlapping convex sub-regions. At each time, the feasibility of all the QPs resulting from using each separate region as kinematic constraint is evaluated. Then, among the regions generating feasible QPs one is selected based on a certain criterion. The procedure is conducted only for the first footstep inside the control horizon, in the same spirit of the STA described in the previous section. The feasibility evaluation does not add computational load to the scheme as it consists in the evaluation of the closed form expressions of the feasibility bounds. Once a sub-region is selected, a standard QP is solved.
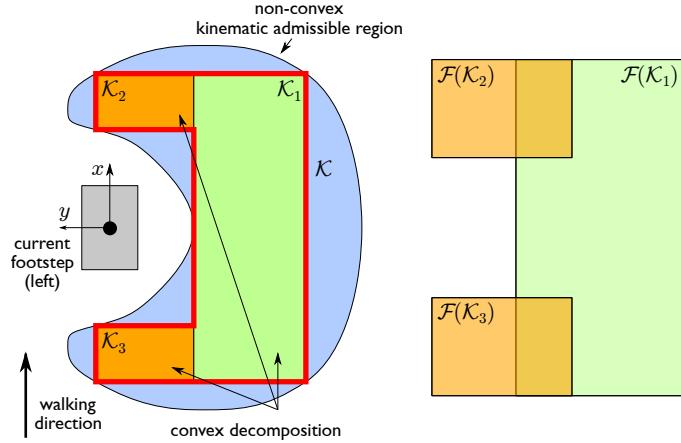
The block scheme of the improved IS-MPC is shown in Fig. 8.8. As usual, a footstep plan is the input. The new modules with respect to the nominal algorithm of Sect. 8.1 are highlighted in red, and in particular:

- in the *kinematic admissible region decomposition* block the KAR region is approximated as a non-convex polytope and then divided into a set of non-overlapping convex sub-regions;

- the *feasibility check* block evaluates the feasibility of each sub-region, i.e., it determines if using the selected convex sub-region as an allowed area for the footsteps results in a feasible QP problem. This blocks outputs a set of feasible convex sub-regions;

- the *sub-region selection* block evaluates all these sub-regions and, according to a specific criterion, chooses a unique feasible sub-region. This region will activate the corresponding kinematic constraint in the QP of the current time step.

Let us now detail the three red blocks of Fig. 8.8.

8.4.1 Kinematic Admissible Region Decomposition

Let $\mathcal{K}$ be a non-convex polytope approximating the original KAR for the first step inside the control horizon. This polytope is larger than $\bar{\mathcal{K}}^1$ (8.3) as shown in Fig. 8.9. The superscript indicating the footstep in the horizon is dropped to enlighten the notation.

Figure 8.9: A possible method to approximate the actual KAR (blue region) with a convex polytope $\mathcal{K}$ (highlighted in red). Note that $\mathcal{K}$ can be decomposed in the union of $\mathcal{K}_1$, $\mathcal{K}_2$ and $\mathcal{K}_3$, where $\mathcal{K}_1$ corresponds to $\bar{\mathcal{K}}^1$ in (8.3) (left). A possible configuration of the corresponding feasibility regions for each sub-region (right). We represented the general case in which non-overlapping kinematic sub-regions correspond to overlapping feasibility regions.

The *kinematic admissible region decomposition* block decomposes $\mathcal{K}$ into a set of N non-overlapping convex sub-regions, i.e.,

$$\mathcal{K} = \bigcup_{\nu=1}^{N} \mathcal{K}_\nu \quad \text{s.t.} \quad \bigcap_{\nu=1}^{N} \mathcal{K}_\nu = \emptyset.$$

For the moment, we do not specify the procedure with which the decomposition is operated. This will depend on the particular application: two possibilities are described in Sects. 8.4.4 and 8.4.5.

8.4.2 Feasibility Check

Any sub-region $\mathcal{K}_\nu$ can be used to construct the kinematic constraint (8.3) for a QP problem that is structurally identical to that of Sect. 8.1. The *feasibility check* block evaluates the feasibility of each QP as

$$(x_u^k, \, y_u^k) \in \mathcal{F}^k(\mathcal{K}_\nu) \tag{8.32}$$
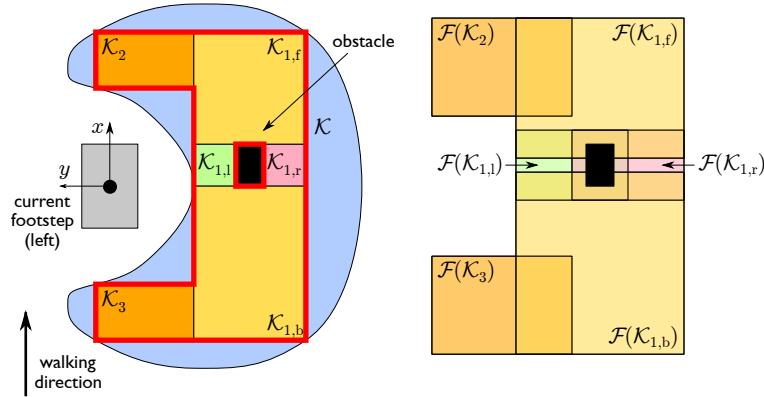
where $\mathcal{F}^k(\mathcal{K}_\nu)$ is the feasibility region corresponding to each kinematic sub-region $\mathcal{K}_\nu$, for $\nu = 1, \dots, N$. In this way, all the feasible regions are identified.

We remark that the feasibility regions corresponding to non-overlapping kinematic sub-regions can overlap. Thus, there might be multiple feasible sub-regions for the current $(x_u^k, \, y_u^k)$.

8.4.3 Sub-Region Selection

The *sub-region selection* block picks a unique sub-region among all the feasible ones. We propose a two stage criterion for the choice.

As a first step, we assign a priority $p(\mathcal{K}_\nu)$ to each sub-region. Lower priority sub-regions are simply discarded, and the choice is restricted to those with higher

---

Figure 8.10: Approximation $\mathcal{K}$ of the KAR (red outline) in the presence of a (black) obstacle (left). Based on the decomposition, the feasibility regions for each kinematic sub-region may be in various configurations, according to the time of evaluation (right). In the represented situation, they overlap.

priority.

The second step is to select, among the remaining candidate regions, the sub-region $\mathcal{K}_\nu$ that maximizes the minimum distance between the boundary $\mathcal{F}^k(\mathcal{K}_\nu)$ and (x_u^k, y_u^k). The further is (x_u^k, y_u^k) from the boundaries of the feasibility region and the more the scheme will be robust to perturbations. Moreover, this will also reduce the probability to change the chosen region at the next time step.

8.4.4 Example of decomposition procedure: allowing leg crossing

Placing one foot in front of the other is a physiological recovery action that humans perform when receiving side pushes directed from the swinging towards the support foot. This is in fact the only way to land with the swing foot in the direction of the perturbation.

For such situations, we consider the KAR approximation in the polytope represented in Fig. 8.9. The kinematic constraint (8.3), which is set $\mathcal{K}_1 \equiv \bar{\mathcal{K}}^1$, is extended with two regions, one in front, $\mathcal{K}_2$, and the other behind, $\mathcal{K}_3$, the stance footstep. The standard and wider region $\mathcal{K}_1$ is assigned priority 1, while the priority of the smaller regions $\mathcal{K}_2$ and $\mathcal{K}_3$ is set to 0. The humanoid will consider a leg crossing maneuver only when required to maintain feasibility. The $\mathcal{K}_1$ region will be preferred otherwise.

8.4.5 Example of decomposition procedure: allowing obstacle avoidance

Obstacles within the KAR imply non-convex constraints. The computed footstep must be within the KAR but outside the obstacle area.

For these scenarios we propose to approximate the KAR as shown in Fig. 8.10. The obstacle is represented as a rectangular area. The rest of the allowed polytope is decomposed in convex sub-regions. In the figure, the obstacle is in $\mathcal{K}_1$, of which the clear space is divided in four parts. The regions in front and behind the support foot $\mathcal{K}_2$ and $\mathcal{K}_3$ are identical to those in the previous subsection. We then introduce for the sub-regions of $\mathcal{K}_1$ the notation $\mathcal{K}_{1,f}$, $\mathcal{K}_{1,b}$, $\mathcal{K}_{1,l}$ and $\mathcal{K}_{1,r}$ (respectively front, back, left

and right with respect to the obstacle). The decomposition is operated by extending $\mathcal{K}_{1,\mathrm{f}}$ and $\mathcal{K}_{1,\mathrm{b}}$ in the y direction, and assigning the remaining space to $\mathcal{K}_{1,\mathrm{l}}$ and $\mathcal{K}_{1,\mathrm{r}}$ (see Fig. 8.10). We remark that there is not a unique way to decompose this polytope into convex sub-regions, and the proposed choice is one of the most natural. We assign priority 1 to the sub-regions $\mathcal{K}_{1,\mathrm{f}}$, $\mathcal{K}_{1,\mathrm{b}}$, $\mathcal{K}_{1,\mathrm{l}}$ and $\mathcal{K}_{1,\mathrm{r}}$, while sub-regions $\mathcal{K}_2$ and $\mathcal{K}_3$ have priority 0.

The proposed procedure for decomposition can easily be extended to the case of different obstacle placements (even multiple), e.g., on the boundary between $\mathcal{K}_1$ and $\mathcal{K}_2$.

8.5   Discussion

We discuss here several aspects of the proposed feasibility-driven methods before reporting simulation and experimental results in the next section.

STA limits

It is not possible to arbitrarily adapt the step timing to recover the feasibility, being the step timing limited by the timing constraints. Given the feasibility and the timing constraints, the only condition that ensures the feasibility of QP-STA itself is that the set of the inequalities characterizing such problem does not describe an empty segment. Such a condition can easily be evaluated at each time by inspecting the constraints of QP-STA. In practice, it constitutes a final check that reveals whether the IS-MPC scheme with STA is able to withstand the perturbations acting on the system at the current time instant.

Obstacle detection

We are not detailing any method for obstacle detection as we assume the robot to be equipped with the proper visual sensors and software to accomplish the task. Details on a possible implementation can be found, for instance, in [248].

Leg crossing for push recovery

Enabling leg crossing recovery at the gait generation level does not ensure that a physical humanoid is able to perform it. Heavy and cumbersome platforms such as TALOS [86] or small robots with large feet like NAO [72] could fail in tracking this kind of motions. On the other hand, studies on Cassie [182] and CogIMon [249] (in simulation) encourage implementing these strategies for the case of light and agile robots. Assuming to have access to a proper platform, a collision free foot trajectory must be to generated.

Accounting for the height of the obstacles

The proposed selection method for the feasible sub-regions does not account for the height of the obstacles. In real applications, their vertical dimension may prevent possible areas to be reached by the swinging foot. To account for this issue, it is sufficient to treat as obstacle all areas that would lead to a foot collision.

Advantages of addressing non-convex KAR through feasibility evaluation

We now discuss some advantages that the presented approach introduces. We first of all recall that the proposed scheme retains the same computational efficiency of standard IS-MPC that has been successfully implemented and tested in various physical humanoid platforms, such as HRP-4, NAO and OP-3 [8, 127].

A possible alternative approach for non-convex constraint handling would be to steer the solution of the optimization problem along the horizon through convex sub-regions that would prevent collision with obstacles [250]. These methods, most suited for navigation planning in the presence of obstacles, can not take into account in real-time the non-convexity, requiring the solution of multiple optimization problems within a single time step. Our feasibility-driven selection allows instead to solve a single QP at each time step that is guaranteed to be feasible.

On the other hand, schemes based on Real Time Iteration, such as [4], would allow to solve a single optimization problem at each time step. To investigate the qualitative differences between that and our method, we tested in Matlab the IS-MPC scheme with non-convex kinematic constraints using a RTI-like formulation. We found that in the case of abrupt changes in the steppable region, e.g., for the presence of a sudden obstacle, the RTI formulation could not find an appropriate solution due to the infeasible initial guess (a strategy for updating the initial guess based on the context should be devised to solve this issue). If in fact the RTI formulation can achieve a similar computational performance to that of IS-MPC with feasibility-driven selection of the kinematic constraints, the latter does not depend on any initial guess and retains guarantees of constraint satisfaction at all times, provided that the DCM is at least within one of the possible feasibility regions corresponding to the convex kinematic sub-regions.

8.6 Simulations

Simulations on Matlab and DART were performed to validate the gain in terms of robustness due to the proposed feasibility-driven approaches.
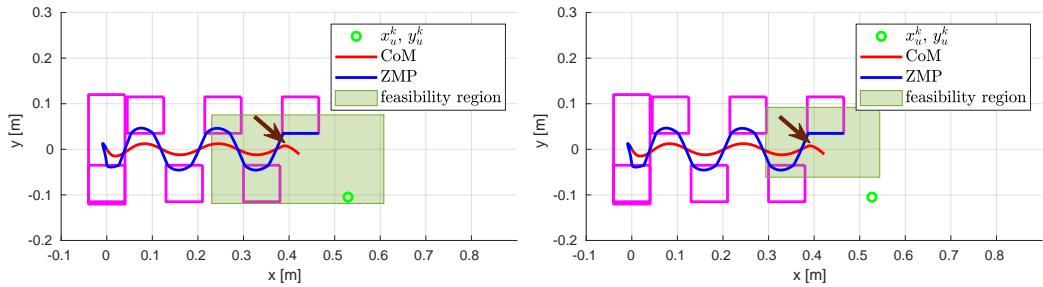
8.6.1 STA simulations on the LIP

The parameters used for the simulations are: $d_{z,x} = d_{z,y} = 0.08$ m, $d_{a,x} = 0.5$ m, $d_{a,y} = 0.16$ m, $\ell = 0.2$ m for the robot (corresponding to the HRP-4 humanoid), $\bar{z}_c = 0.75$ m, $m = 39$ kg, $\delta = 0.01$ s, $T_s^{\min} = 0.2$ s, $T_s^{\max} = 0.65$ s, $T_c = 1$ s, $T_p = 2$ s, $\epsilon_x = \epsilon_y = 0.005$ m, $v_z^{\max} = 1.5$ m/s, $v_{\text{sw}}^{\max} = 1$ m/s. The candidate step timings are all equal with $\hat{T}_s = 0.5$ s of which $\hat{T}_{ds} = 0.2$ s. The QPs are solved with the `quadprog` Matlab solver.

Push Recovery

The typical application of interest in which the STA module can improve the performance of the nominal IS-MPC is a push recovery scenario.

The simulation consists in a forward walk that is perturbed by the action of a push $F_{\text{ext}} = (97.5, -136.5, 0)$ N lasting 0.1 s acting at $t = 2.7$ s. The disturbance is applied at the start of the single support phase of the sixth step.

Figure 8.11: Push recovery simulation on the LIP to validate the IS-MPC with STA module. Feasibility region and (x_u, y_u) at the end of the push ($t = 2.8$ s) with STA (left) and without STA (right).

We compare in Fig. 8.11 the feasibility of the IS-MPC with STA and that of the nominal scheme. Thanks to the STA module, (x_u, y_u) is still inside the feasibility region (green patch, plot on the left) in spite of the push, while in nominal IS-MPC the DCM exceeds the feasibility boundaries (right plot), losing the control authority and inevitably leading to a gait generation failure, i.e., a fall of the humanoid. STA modulates the feasibility region by reducing the duration of the current step by 0.13 s. As the simulation proceeds, we report that it is also necessary to reduce the next double support by 0.14 s to reject the effect of the push. Adaptation at successive instants is required here due to a violation of the conservative estimate $\mathcal{F}_{\text{est}}$, triggering an action from QP-STA.
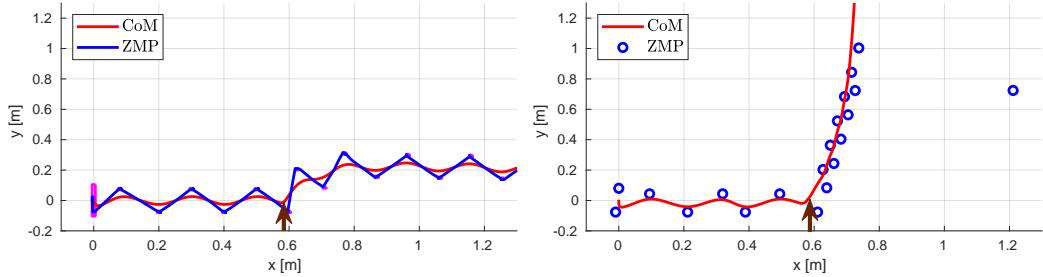
To provide an idea of the general improvement, we ran the simulation under the same settings over various disturbances applied at the same instant. The feasibility driven method tolerates x-forces in $[-260, 304.2]$ N and y-forces in $[-273, 124.8]$ N. The nominal gait generation scheme withstands pushes in $[-136.5, 144.2]$ N on x and $[-93.6, 97.5]$ N on y.

Comparison with DCM-Based Method

Here, we compare the IS-MPC plus STA with a method that is considered significant in the state of the art [175]. This scheme formulates a QP to optimize the footstep locations and timings using ∞-step capturability bounds for the so-called DCM offset, i.e., the difference between the DCM and the ZMP. The ZMP is here assumed to be always at the center of the support foot, being the method formulated for point-foot robots; the double support phase is considered as instantaneous. We kept the same parameters as the previous simulation, but we reduced the support polygon width $d_{z,x}$ and $d_{z,y}$ to 0.01 m in the IS-MPC, aiming at approximating a point-foot situation, and the double support phase to $T_{ds} = 0.05$ s.

At the start of a single support phase, the robot receives a lateral push $F_{\text{ext}} = (0, 226.2, 0)^T$ N lasting 0.1 s. See Fig. 8.12 for the resulting trajectories. IS-MPC with STA adapts to the push and continues its gait, whereas the DCM-based method is not able to recover, displaying a CoM divergence with respect to the ZMP. To provide an idea of the tolerated disturbances, IS-MPC with STA (in the point-foot case) can withstand x-forces in $[-288.6, 290]$ N and y-forces in $[-46.8, 245.7]$ N. The DCM-based method instead tolerates $[-265.2, 265.2]$ N and $[-31.2, 222.3]$ N respectively in x and y.

We identified two possible reasons for the superior performance of our scheme. Our method can exploit the small but not dimensionless feet, and the non-instantaneous

Figure 8.12: Comparison of IS-MPC plus STA (left) with a state of the art method (right). IS-MPC with STA withstands the push while the DCM-based technique displays an unstable behavior.

double support. Second, our stability constraint, based on the stability condition, prevents the CoM/ZMP divergence *at any time*, while the ∞-step capturability constraint of [175] is appropriate *at the start of each step*, so that its use at intermediate instants may lead to failure in critical cases. As a final remark, in the ideal case of point foot, minimum step timing, instantaneous double support and infinite control horizon, the feasibility region $\mathcal{F}^k$ of IS-MPC at the start of a step coincides with the ∞-step capturability region of [175].

8.6.2   Non-convex simulations on the LIP

We report here Matlab simulations to showcase possible applications in which using a non-convex approximation of the KAR results in a strong benefit for the gait. The same parameters as above were used, except for the step duration, set here to $T_s^j = 1$ s, with $T_{ds}^j = 0.3$ s and $T_{ss}^j = 0.7$ s.

Push recovery
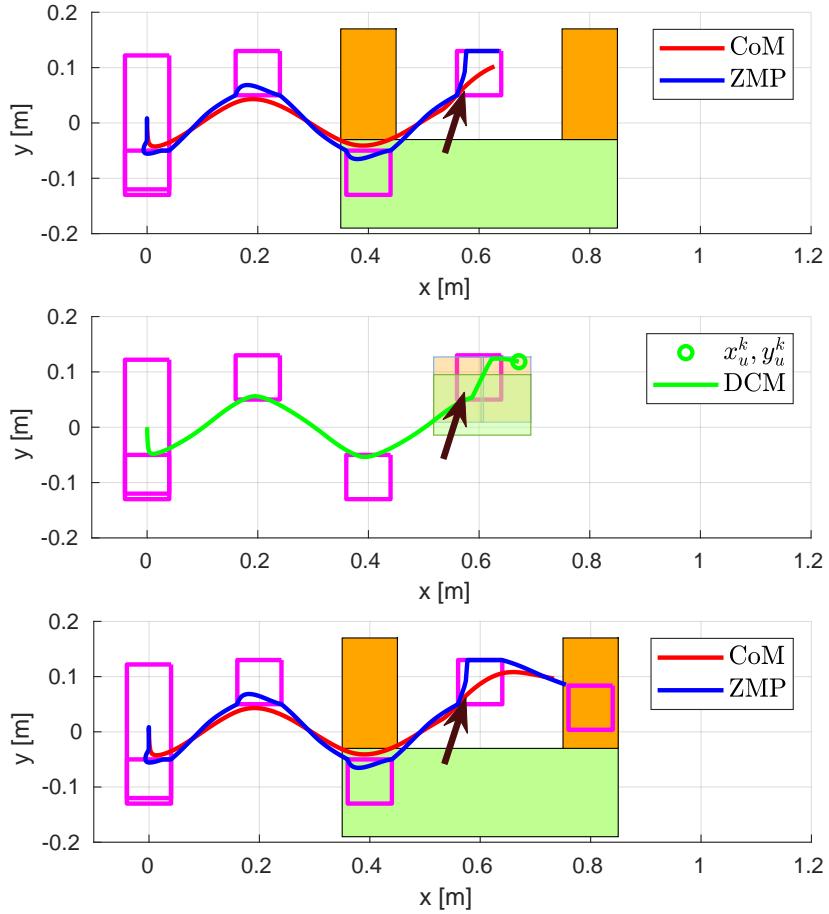
Figure 8.13 shows the simulation in a push recovery scenario, where the disturbance acts from the swing towards the support leg. In the left graph, a $(100, 135, 0)$ N push acts on the system at time $t = 4.45$ s, and as a result the DCM is pushed outside of $\mathcal{F}^k(\mathcal{K}_1)$, as shown in the middle graph. Since it is contained in $\mathcal{F}^k(\mathcal{K}_2)$, the controller can recover by stepping in front of the previous footstep, as shown in the bottom graph, taken at time $t = 4.99$ s. Such maneuver would not be possible in the nominal IS-MPC formulation.

Obstacle avoidance

We consider here the case of obstacle avoidance; plots are in Fig. 8.14. Simply following the footstep plan would lead the robot to step onto the black obstacle with dimensions 0.04 m×0.07 m. Since this is accounted in the process of decomposing the steppable region, the footstep position is modified to make the swing foot land behind the obstacle, inside $\mathcal{K}_{1,b}$. The robot can thus proceed with the gait.

8.6.3   Dynamic simulations

The results of the previous sections are replicated and expanded in the DART dynamic environment, using the full multi-body dynamics of a HRP-4 robot. The kinematic

Figure 8.13: Push recovery simulation. The top and middle plots are taken at time $t = 4.45$ s and show the state right after the push (represented as an arrow). In particular, (x_u^k, y_u^k) is inside $\mathcal{F}^k(\mathcal{K}_2)$, so the push is recovered by putting the right foot in front of the left, as shown in the bottom plot taken at $t = 4.99$ s.

controller of the robot runs at 100 Hz and all the QPs are solved using the *hpipm c* library [247].
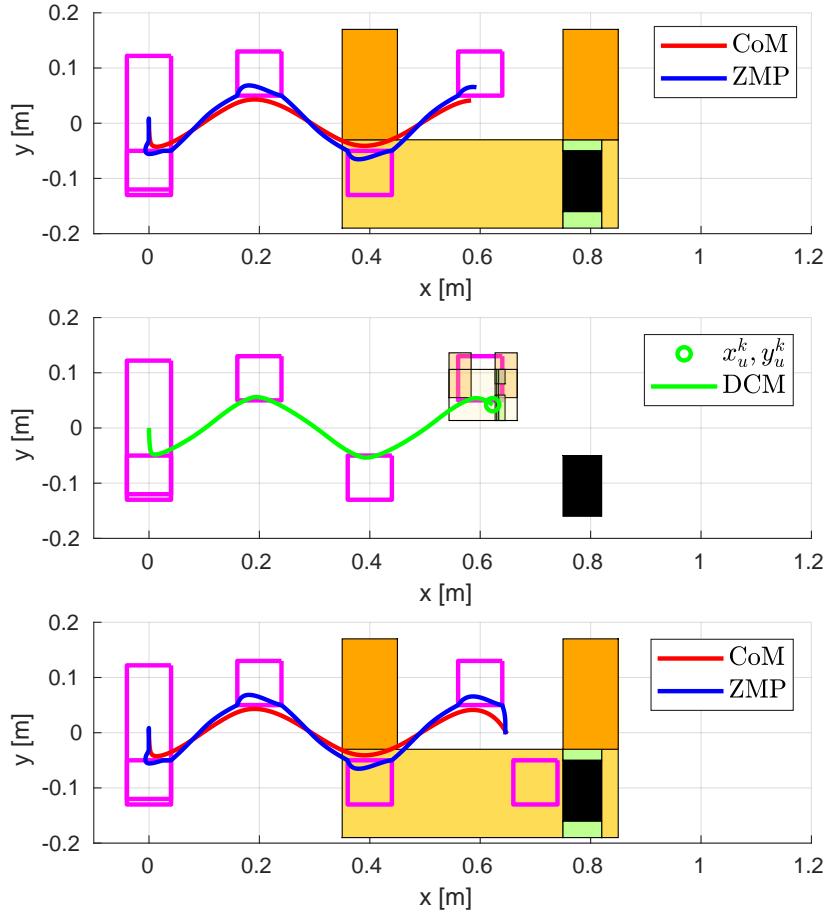
STA

The benefit of adapting the step timing through the STA is tested in push recovery situations. Beside the forward walking case, described in the Matlab simulation section, we also considered the case of backward diagonal walking and walking on the spot. In all scenarios, IS-MPC with STA withstands pushes that would cause the robot to fall without STA. For example, fig. 8.15 shows snapshots of the forward walking test. The outcome of the simulations can be retrieved in: `https://youtu.be/WoYxnzKZeKw`.

We point out that setting up and solving QP-STA takes about 50 μs, appropriate for real-time implementation on physical platforms.

Non-convex
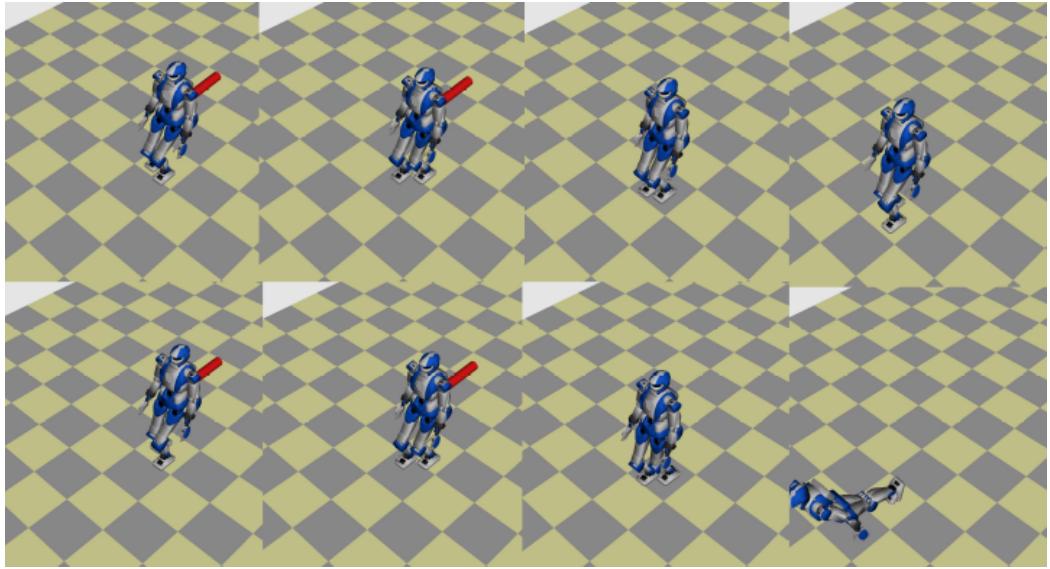
We consider here four different scenarios. The first two tests replicate the LIP simulation, to validate their consistency using the full robot dynamics. The results correspond
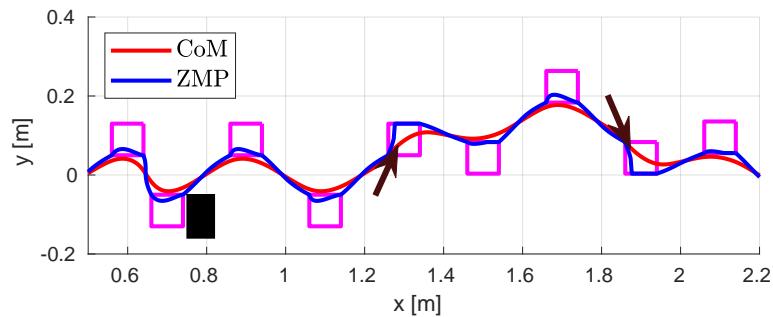
Figure 8.14: Obstacle avoidance simulation. The top and middle plot are taken at time $t = 4.30$ s and show the decomposition of the non-convex polytope when the obstacle is encountered, as well as the position of (x_u^k, y_u^k) at the same time. The bottom plot, taken at $t = 4.85$ s, shows the resulting placement of the next footstep.

to the expectations from Matlab tests. For each of the two cases, push recovery and obstacle avoidance, a simulation using the nominal IS-MPC was performed, to show the benefit of introducing non-convex kinematic constraints. When using the nominal scheme in fact, the robot steps over the obstacle and is not able to recover from the push.

The third simulation involves obstacle avoidance and multiple push recovery, see Fig. 8.16-8.17. The robot encounters the obstacle (with the same size as the previous simulation and a height of 0.02 m) during the fourth step, and then it is subject to two consecutive pushes during the sixth and seventh step, with magnitude $(80, -105, 0)$ N and $(80, 120, 0)$ N. The non-convex kinematic constraints allow for a reactive maneuver that prevents the robot from falling. The fourth simulation consists in walking along a path with multiple obstacles. The animations can be found in `https://drive.google.com/file/d/1DD6Oz0lmA69f6FmjFnK6cnTWv7eovnU_/view`.

Figure 8.15: HRP-4 dynamic simulation: push recovery while walking forward. IS-MPC with STA (top sequence) is able to absorb the disturbance and continue with the gait, without STA (bottom sequence) the robot falls down.
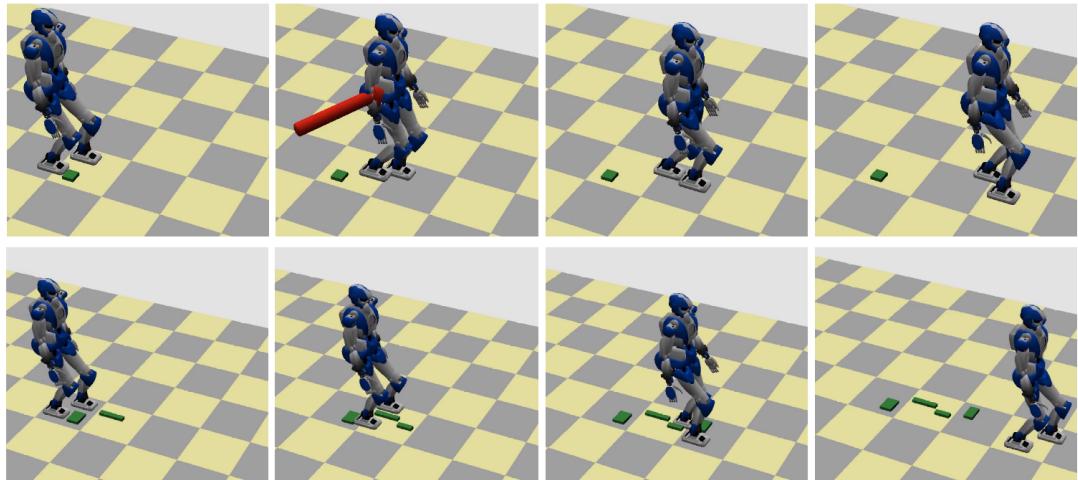
Figure 8.16: CoM/ZMP plot of the multiple push and obstacle avoidance DART simulation.
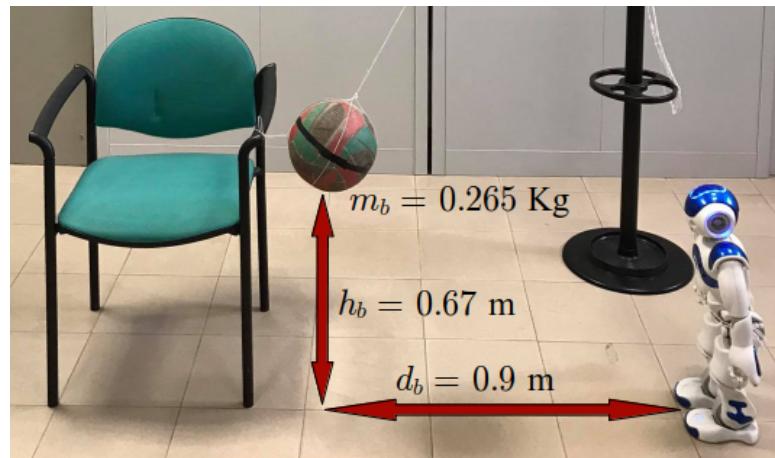
8.7 Experiments

We report here experiments conducted on a NAO robot to validate the STA module. The parameters are now set to: $m = 5.3$ kg, $\bar{z}_c = 0.245$ m, $d_{z,x} = d_{z,y} = 0.05$ m, $d_{a,x} = 0.16$ m, $d_{a,y} = 0.05$ m, $\ell = 0.1$ m, $\delta = 0.05$ s, $T_s^{\min} = 0.3$ s. To perform repeatable push recovery tests, we built the pendulum structure of Fig. 8.18.

Videos of the experimental outcomes can be found at the link: `https://youtu.be/WoYxnzKZeKw`. Thanks to the STA module, the robot withstands pushes that lead the nominal IS-MPC to fail, with a subsequent fall of the robot. Over a set of 10 experiments, IS-MPC with STA had a 90% success rate, whereas IS-MPC without STA recovered in only 20% of the tests.

Figure 8.17: Snapshots from DART simulations using non-convex kinematic constraints: push recovery and obstacle avoidance (top sequence), avoiding multiple obstacle (bottom sequence).

Figure 8.18: Experimental set up for the push recovery experiment.

Chapter 9

A unified scheme for robust MPC gait generation
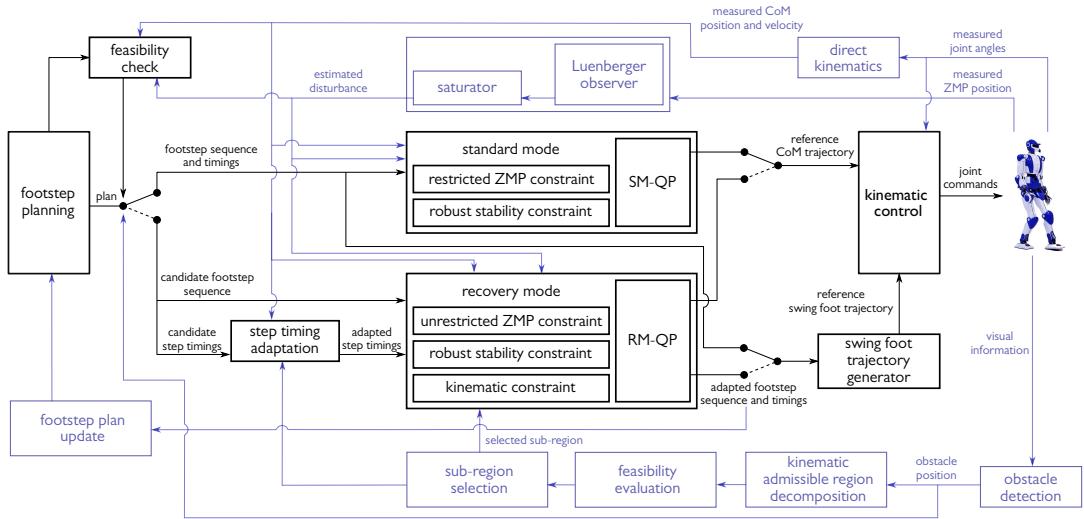
We presented so far two complementary strategies for robust humanoid gait generation. Chapter 7 involved robustness to persistent disturbances, with the aim of investigating on a sufficient condition for recursive feasibility under perturbations. The footstep plan was considered as fixed and not modifiable by the scheme, which could only modulate the ZMP profile to generate a proper CoM trajectory to account for the disturbances. On the other hand, Chapter 8, in the context of a scheme endowed with Automatic Footstep Placement (AFP), stressed the importance of the feasibility region to modify the footstep plan in real-time. Based on it, a Step Timing Adaptation procedure together with a method to handle non-convex kinematic constraints was presented.

The common denominator of both the previous chapters is the feasibility analysis. The subsequent conceptual passage is: can we design a scheme that takes advantage of both the proposed approaches? Or: can we provide guarantees on recursive feasibility while allowing also for the modification of the footstep plan? In this way, a complete gait generation scheme for robustness to persistent and impulsive disturbances could be formulated. To answer this questions, we proceed in this chapter by blending the results of Chapter 7 together with those of Chapter 8 through the introduction of the *modes of operation*, denoted as *standard mode* and *recovery mode*.

The standard is the default operation mode, and corresponds to the scheme of Chapter 7. The robot sticks to the footstep plan while accounting for the persistent disturbances. Here, the disturbance observer and the ZMP constraint restriction are the tools that are used for robustness.

The effect of a strong perturbation (that does not belong to the set of disturbances used for the design of the restriction function) can cause a loss of feasibility. By constantly monitoring the feasibility of the scheme, we propose to switch to an AFP formulation when needed to recover from a loss of feasibility. We denote this mode as *recovery mode*. Here, the Step Timing Adaptation (STA) module together with the non-convex kinematic constraint decomposition in convex sub-regions augments the robust capabilities of the IS-MPC with AFP.

The overall scheme recursively enforces feasibility thanks to both the effect of the restriction function and the active re-shaping of the region during the recovery mode, granting a certain degree of robustness to different kinds of perturbations. This general approach wraps up all the methods proposed so far in the manuscript and concludes

Figure 9.1: Block scheme of the unified robust gait generation scheme.

the block of three the chapters focused on robust gait generation.

9.1   The proposed approach

We consider, as usual, the problem of generating a gait for a humanoid robot under the effect of perturbations, realizing as closely as possible a predefined sequence of footsteps. In this chapter, the considered disturbances involve all the possible types, e.g., $w_x \in \mathcal{W}_x$, $\dot{w}_x \in \dot{\mathcal{W}}_x$, $w_x \in \sup \mathcal{W}_x$, and/or $w_x \in \mathcal{W}_{i_x}$. Note that in practice it is impossible to separate the exact contribution of different sources of perturbation and the proposed modeling is simply used for convenience and control design. We also point out that we are considering a scenario consisting in a flat terrain that can comprise small obstacles. The overall complexity of the environment is low enough to admit the presence of a simple *plan update* procedure which does not require a sophisticated sensor-based re-planning stack. The robot is also assumed to be localized in space and aware of the presence of obstacles (their location is known within the MPC prediction horizon). The latter is clearly a non-trivial assumption, however, we remark that addressing such a problem is not within the scope of the manuscript. The integration with localization and mapping is a parallel research line of the group where this thesis has been conducted, to be integrated with the present contribution in the immediate future.

An overview of the proposed scheme is shown in Fig. 9.1. At each t_k, the input is given by a footstep plan, and, at the start of each iteration, the algorithm performs a *feasibility check*, which determines whether the scheme should operate in *standard mode* or in *recovery mode*. As shown in the previous chapters, the feasibility regions in standard mode, corresponding to that of Chapter 7, and in recovery mode, similar[1] to that of 8, are different. They are respectively named as $\bar{\mathcal{F}}_{x,y}^k$ and $\mathcal{F}_{x,y}^k$.

The feasibility check evaluates if $(x_u^k, y_u^k) \in \bar{\mathcal{F}}_{x,y}^k$. If this is the case, the scheme operates in standard mode, otherwise the recovery mode is activated. The QPs for the standard and recovery mode will be denoted as SM-QP and RM-QP.

---

[1]We will detail the differences in the next section.

As the scheme is also intended to account for the presence of small obstacles, the feasibility check decision also considers possible obstacle detection with a simple logic. If something obstructs the footstep placement, even if the scheme is feasible in standard mode, the recovery mode is activated.

The feasibility check is performed at each iteration and the recovery mode remains active until the feasibility of SM-QP is recovered. Here, commands are generated by solving the optimization problem defined by RM-QP. The outputs are the CoM/ZMP trajectories and the adapted footstep positions, involving also non-convex kinematic constraints and adapted timings via the STA module. The step timing adaptation is performed *after* evaluating the feasibility of the convex sub-regions. In this way, obstacle avoidance and/or leg crossing maneuvers for rejecting swing to support foot pushes are prioritized. The generated footsteps are used to update the footstep plan which is then updated via the *plan update* block, to ensure leg kinematic feasibility for operations in standard mode.

We stress that RM-QP does not enforce a restricted ZMP constraint, in line with the schemes presented in Chapter 8. The reason for this choice is twofold. First, this mode is activated with the goal of recovering from a potential loss of feasibility of the Standard Mode. As opposite to that, the effect of the ZMP constraint restriction is to restrict the feasibility region, as show in Sect. 7.2.1. In this view, considering a restricted ZMP constraint would limit the chances of feasibility recovery. Second, the benefit of the ZMP restriction consists in enforcing recursive feasibility under certain disturbance conditions. When those are in $\mathcal{W}_{i_{x,y}}$, there is no advantage in keeping the restriction, as no methods to account for persistent disturbances has a meaningful effect.

The reference CoM position is computed using the output of the adopted QP at the current time. The next foot landing position and timing are either given by the footstep plan (standard mode) or by the MPC (recovery mode). A swing foot pose is generated accordingly and the Cartesian references are sent to a kinematic controller.

In the rest of the chapter we will detail components of the scheme that are different from those reported in the previous chapters, and present simulation and experimental results.

9.2   Recovery Mode

At the beginning of each iteration the algorithm performs a *feasibility check*. This check returns

- *true* if $(x_u^k, y_u^k) \in \bar{\mathcal{F}}^k$ and the next footstep is not blocked by the presence of an obstacle;

- *false* otherwise.

If the result of the check is true, meaning that SM-QP is feasible, the algorithm can proceed using the standard mode of operation. If the result of the check is false, the recovery mode is activated.

The objective of this mode of operation is to maximize the ability to recover feasibility: footstep positions are QP decision variables and can thus be adapted, the STA module is activated, so that also step timings can be adjusted if needed, and non-convex kinematic constraints are considered. As stated above, once the model hypotheses on w

are violated, standard mode guarantees are lost, and thus it is convenient to remove restrictions in order to maximize the capabilities of feasibility recovery.

We remark the following implementation detail regarding the recovery mode. If the sub-region selection block can not find a feasible region, the original convex kinematic constraint (8.3) is chosen and STA is left free to attempt at recovering the feasibility. In this sense, the scheme of Fig. 8.4 is chosen to be the forced mode of operation when the scheme fails. In such a way it is possible to resume the gait in the case of feasibility recovery due to external actions, e.g., the intervention of an operator.

9.2.1 Recovery Mode QP

The QP to be solved at each time t_k is the same as Sect. 8.1.5, except for the stability constraint, which is instead enforced in its robust version given by (7.9) that we report here for the sake of readability

$$\eta \int_{t_k}^{t_k+C} e^{-\eta(\tau-t_k)} x_z(\tau) d\tau = x_u^k - \tilde{c}_x^k + \frac{\bar{w}_x^k}{\eta^2}. \tag{9.1}$$

Being the saturator block always active, the disturbance estimate in $\bar{w}_x^k$ will not be affected by impulsive pushes, which would rather be sensed through the CoM/ZMP state.

9.2.2 Modification of the feasibility region

Having introduced the robust stability constraint leads to a modification in the feasibility region derived in Sect. 8.2.

Proposition 10 *The QP of the sagittal component of the scheme in recovery mode is feasible at t_k if and only if $x_u^k \in \mathcal{F}_x^k$, with*

$$\mathcal{F}_x^k = \{x_u : x_u^{k,m} \le x_u \le x_u^{k,M}\}$$

where

$$x_u^{k,m} = \eta \int_{t_k}^{t_k+C} e^{-\eta(\tau-t_k)} x_z^m(\tau) d\tau + \tilde{c}_x^k - \frac{\bar{w}_x^k}{\eta^2}$$

$$x_u^{k,M} = \eta \int_{t_k}^{t_k+C} e^{-\eta(\tau-t_k)} x_z^M(\tau) d\tau + \tilde{c}_x^k - \frac{\bar{w}_x^k}{\eta^2}$$

in which

$$x_z^m(t) = x_f^{-1} + (x_f^0 - x_f^{-1})\sigma(t, t_s^0, t_s^0 + T_{ds}^0) - \frac{d_{z,x}}{2} - \frac{d_{a,x}}{2} \sum_{j=1}^{F} \sigma(t, t_s^j, t_s^j + T_{ds}^j)$$

$$x_z^M(t) = x_f^{-1} + (x_f^0 - x_f^{-1})\sigma(t, t_s^0, t_s^0 + T_{ds}^0) + \frac{d_{z,x}}{2} + \frac{d_{a,x}}{2} \sum_{j=1}^{F} \sigma(t, t_s^j, t_s^j + T_{ds}^j).$$

Proof. The proof proceeds as in Sect. 9, with the sole modification of the disturbance term in the stability constraint. All passages can be replicated by accounting also for the additive term $\frac{\bar{w}_x^k}{\eta^2}$. ∎

Figure 9.2: Footstep plan update procedure.

We always recall that we derived the feasibility bounds for the sole x component; the region for y can be derived by substituting in each equation the appropriate coordinate and kinematic constraint.

9.2.3 Footstep plan update

There exists the possibility that in recovery mode the adapted footsteps deviate from the original plan in such a way that, when going back to the standard mode where footsteps are considered as fixed, they might be kinematically not realizable by the humanoid.

We account for this situation in the following way:

- the optimized footsteps $\hat{X}_f^j$, $\hat{Y}_f^j$, for $i = 1, \dots, M$, by the last RM-QP override the corresponding planned footsteps;

- from step $(F + 1)$-th, the footsteps in the plan are translated to ensure that the $(F + 1)$-th footstep is kinematically reachable from the F-th footstep.

The objective of this procedure is to preserve the relative distances between the steps, as shown in Fig 9.2. We adopt such naive method under the hypothesis of a minor presence of obstacles in the environment, which can reasonably be managed by the non-convex kinematic constraint handling pipeline.

9.3 Discussion

We proposed in this chapter a method to combine all the separated contributions in robust gait generation for humanoid robots described in the manuscript. The aim was to gather the best from the different strategies: retain the theoretical insight on robust recursive feasibility as much as possible and use the feasibility-driven recovery capabilities when needed. In this view, the feasibility of the scheme plays a relevant role.

We recall here the perspective given in the preamble of the previous chapter. Robustness can be interpreted as a feasibility problem when dealing with constrained

predictive controllers. Yet, all the proposed development relies on minimal centroidal models, which tend to simplify the complexity of the full platform. Keeping in mind this fact, we stress that the presented methods should not be interpreted as a definitive approach for granting robustness when generating a gait, but rather as starting points for the implementation of more sophisticated approaches which may benefit from the provided analysis.

The balance of bipedal robots, as well as that of other underactuated platforms, can be seen as the control of an inverted pendulum under input constraints, no matter the complexity of the full-body kinematics. This is evident from the internal dynamics of these platforms when studying the locomotion problem using standard control techniques, see for example [145]. Having access to a relatively secure and efficient solution of the gait generation problem at all times using the LIP model could provide a guidance for the implementation of more advanced controllers, employed as an informed initial guess for solving online complex whole-body problems or even used as a back-up strategy.

9.4 Simulations

We present LIP simulations on Matlab to highlight the switching between modes of operation and its effect on the feasibility region, and then validate the approach on DART using the HRP-4 platform.

9.4.1 Simulations on the LIP
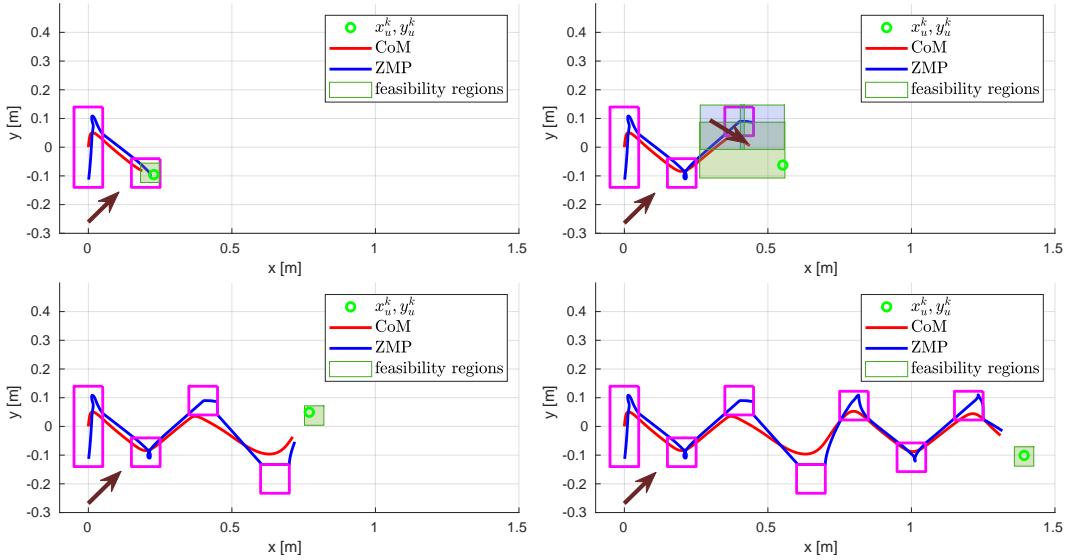
The parameters used for the simulations are: $d_{z,x} = d_{z,y} = 0.08$ m, $\bar{z}_c = 0.75$ m, $m = 39$ kg, $\delta = 0.01$ s, $T_s^{\min} = 0.2$ s, $T_s^{\max} = 1.5$ s, $T_c = 0.7$ s, $T_p = 2.5$ s, $\epsilon_x = \epsilon_y = 0.005$ m, $v_z^{\max} = 2$ m/s, $v_{\text{sw}}^{\max} = 2$ m/s, $w_{m,x} = w_{m,y} = 0.15$ m/s^2, $\Delta_x = \Delta_y = 0.12$ m/s^2, $\alpha = 0.25$. The candidate footsteps are equally spaced with a stride length of 0.2 m in the x direction, the step timings are all equal with $\hat{T}_{ss} = 0.8$ s and $\hat{T}_{ds} = 0.2$ s. The convex kinematic admissible region is described by $d_{a,x} = 0.5$ m, $d_{a,y} = 0.16$ m, $\ell_y = 0.2$ m. To account for possible leg crossing, two sub-regions are added in the same spirit as Fig. 8.9. As they will be used in all the considered simulations, we give here the parameters: $d_{a,x} = 0.15$ m, $\ell_x = 0.175$ m, $d_{a,y} = 0.15$ m, $\ell_y = 0.0$ m.

In all simulations a persistent disturbance is acting on the CoM of the robot in the x and y direction, with $w_x(t) = 0.15 + 0.1\sin(2\pi t/3)$ m/s^2 and $w_y(t) = 0.15 + 0.1\sin(2\pi t/5)$ m/s^2, i.e., $5.85 + 3.9\sin(2\pi t/3)$ N and $5.85 + 3.9\sin(2\pi t/5)$ N.

Persistent and impulsive disturbance

The robot, thanks to the observer and the ZMP constraint restriction, proceeds in standard mode, where the gait generation algorithm is recursively feasible (Fig. 9.3, top left plot) in spite of the presence of the persistent disturbance. The DCM is in fact contained in the feasibility region, represented as a green patch. Note also the peculiar CoM/ZMP displacement due to the robust stability constraint.

At time $t = 2.3$ s, the robot is subject to an external push on the x and y component of respectively 109 N and -136.5 N for a time interval lasting 0.1 s. To recover from a loss of feasibility due to the strong impulsive push, the recovery mode is activated (Fig. 9.3, top right plot). Here, larger and multiple feasibility regions can be noticed. The largest region corresponds to the convex kinematic admissible region used in Sect. 8.6.1. The

Figure 9.3: Persistent and impulsive disturbance simulation. The plot reports snaps of the generated motions at time $t = 1.5$ s, $t = 2.5$ s, $t = 3.5$ s, $t = 6.5$ s. The brown arrow on the bottom left side of the plots describes the direction of the persistent disturbance, whereas the other arrow the direction of the impulsive push. Recovery mode is active in the top right plot.

two smaller regions are on the other hand built using the leg crossing areas of Sect. 8.6.2. The larger region is initially selected, but, due to the strength of the push, adapting the step timing is required. The duration of the step during which the impulsive push happens is reduced to 0.6 s. In particular the single support time is halved. A further step timing adaptation is required in the subsequent step, which is reduced by 0.06 s.

After the second step timing adaptation, the standard mode is resumed (bottom left plot) and a the gait can proceed in a recursively feasible fashion (bottom right plot).

Persistent disturbance with push in the swing to support foot direction
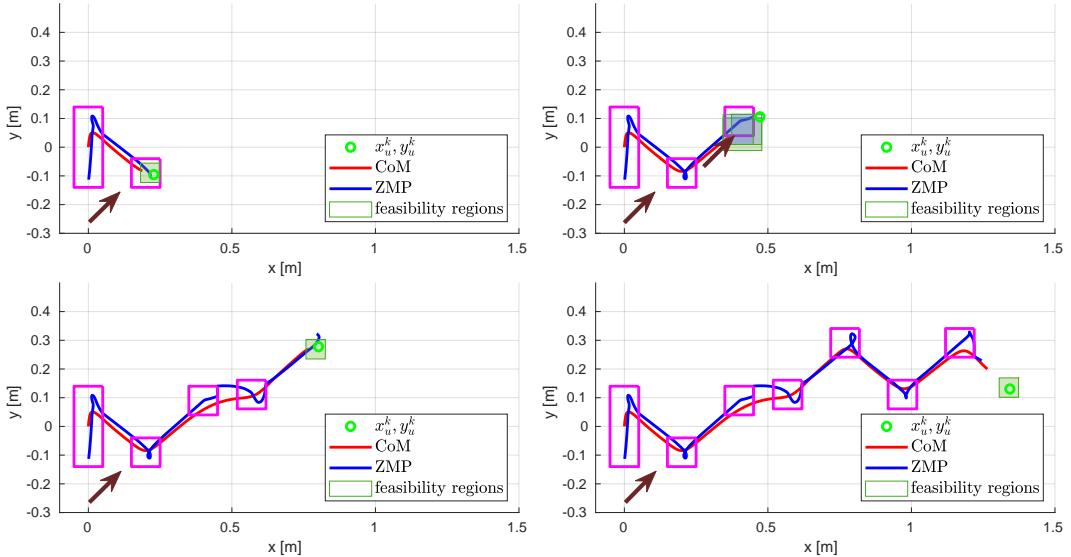
The recursively feasible gait under disturbances (top left plot of Fig. 9.4) is perturbed at time $t = 2.3$ s by a push of 97.5 N and 58.5 N exerted for 0.1 s (top right plot of Fig. 9.4).

The swing to support foot direction of the disturbance promotes the selection of the kinematic sub-region that allows for a leg crossing maneuver in recovery mode (bottom left plot). The footstep is indeed positioned in front of the support foot. A normal gait is then resumed (bottom right plot).

Persistent disturbance with push recovery and avoidance of a small obstacle

The simulation begins with a normal gait (top left plot of Fig. 9.5). An obstacle is placed in the same position of the third planned footstep. At the beginning of the support phase of the second step, the recovery mode is thus activated. The kinematic admissible region is decomposed and the sub-region selection picks the largest region (top right plot of Fig. 9.5), allowing to place the landing foot behind the obstacle.

A push of 78 N on both the x and y direction is applied to the CoM of the robot for 0.1 s during the single support phase of the third step. The recovery mode is again

Figure 9.4: Persistent disturbance with push in the swing to support foot direction simulation. The plot reports snaps of the generated motions at time $t = 1.5$ s, $t = 2.35$ s, $t = 4$ s, $t = 6.5$ s. The brown arrow on the bottom left side of the plots describes the direction of the persistent disturbance, whereas the other arrow the direction of the impulsive push. Recovery mode is active in the top right plot.
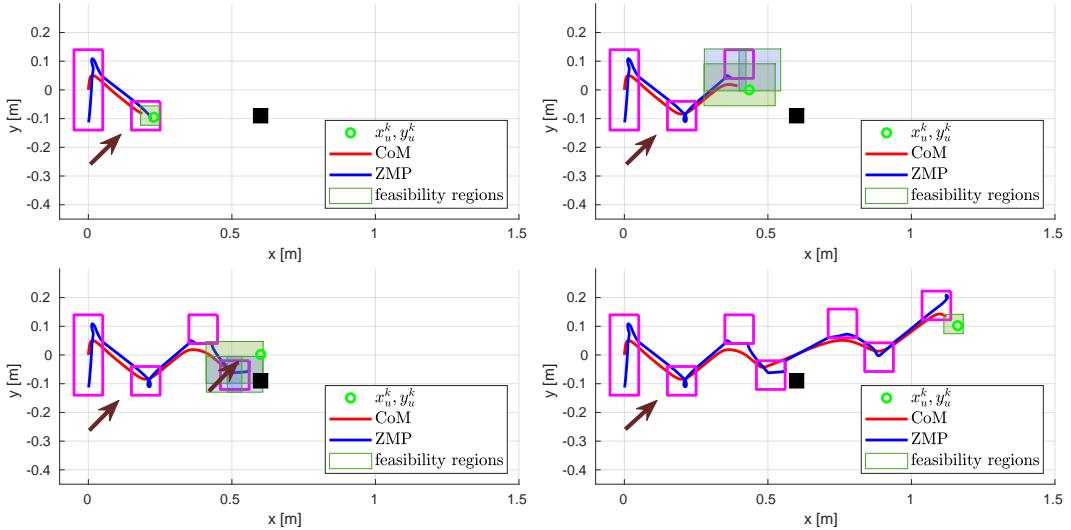
activated (bottom left plot). The planned footstep is placed 0.05 m ahead in the x direction and the step duration is reduced by 0.18 s. Recovery mode is again triggered in the subsequent step, resulting in a further modification of the original plan. The recursively feasible gait is resumed afterwards (bottom right plot).

9.4.2 Dart simulations

Similar settings to the LIP simulations were used for validation in the DART dynamic environment. Some of the parameters were modified to account for the foot size of HRP-4. The value of $d_{a,x} = 0.15\ d_{a,x}$ is set here to 0.6 m, while for the leg-crossing sub-region we have $d_{a,x} = 0.15$ m, $\ell_x = 0.225$ m, $d_{a,y} = 0.15$ m, $\ell_y = 0.0$ m.

Snapshots from the simulations are reported in Fig. 9.6. We considered the following three scenarios: *i)* persistent and impulsive disturbance, *ii)* persistent disturbance with push in the swing to support foot direction, *iii)* persistent disturbance with push recovery and avoidance of a small obstacle. In the last case, the obstacle is placed at $x = 0.68$ m and $y = -0.09$ m. The persistent disturbance has the same magnitude of the LIP simulations in Matlab, while the pushes, although applied at the very same instant and for the same duration, have the values: *i)* $F_{ext} = (60, -60, 0)$ N, *ii)* $F_{ext} = (80, 70, 0)$ N, *iii)* $F_{ext} = (70, -70, 0)$ N. In all cases the robot withstands the disturbances, whereas the nominal IS-MPC scheme showcases failures with a subsequent fall of the robot. Data from the third simulations are plotted in Fig. 9.7.

We considered then a possible application of the proposed approach. Assume that HRP-4 has the objective to carry a box containing a payload of 5 kg from a starting point to a goal destination. The robot may be located in a narrow passage, for which closely following a footstep plan is fundamental to avoid collisions with the environment. The robot can be exposed to unexpected pushes: for instance something could hit the

Figure 9.5: Persistent disturbance with push recovery and avoidance of a small obstacle simulation. The plot reports snaps of the generated motions at time $t = 1.5$ s, $t = 2.8$ s, $t = 3.5$ s, $t = 6.5$ s. The brown arrow on the bottom left side of the plots describes the direction of the persistent disturbance, whereas the other arrow the direction of the impulsive push. The black patch is the obstacle to be avoided. Recovery mode is active in the top right and bottom left plots.
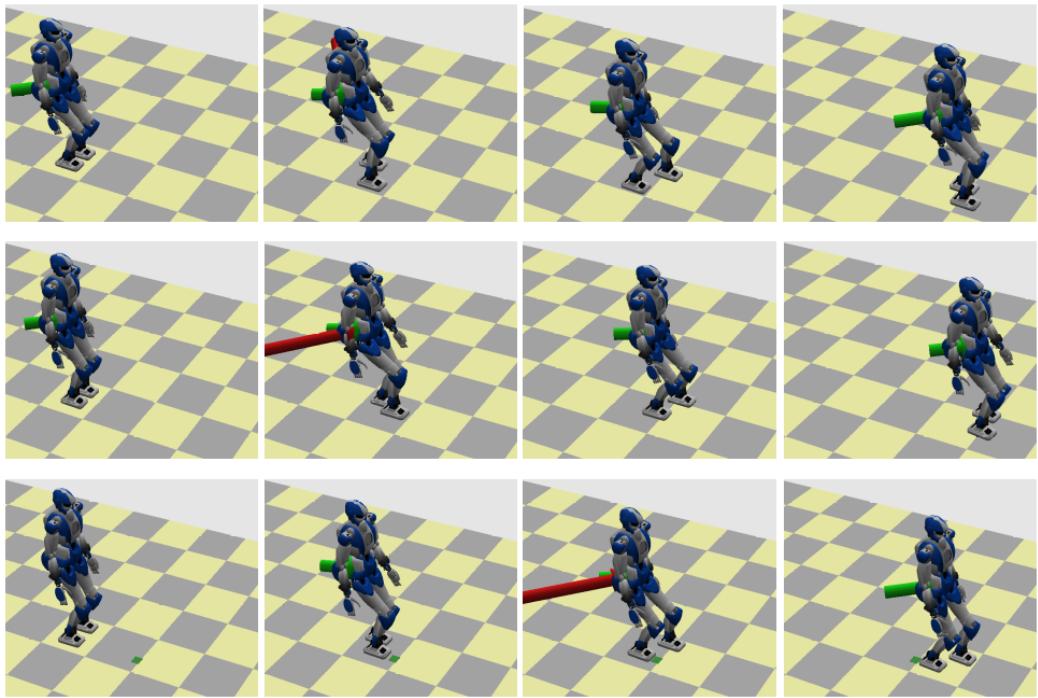
arm of the platform. The ability to slightly adapt footstep position and timings can determine the success of the task in such cases. We simulated a similar scenario, as reported in Fig. 9.8, where locomotion generated by the proposed scheme succeeded in carrying a weight in spite of the push due to a collision with an operating manipulator.

9.5 Experiments

We already shown experiments in the case of persistent and impulsive disturbances. Here, we simply provide an example of the combination of both types of perturbations. We stress that the implementation of the method is partial. NAO is not kinematically able of placing one foot in front of the other during dynamic locomotion without self-collision, due to the foot length and the leg width. We present thus results not involving the non-convex constraint handling.
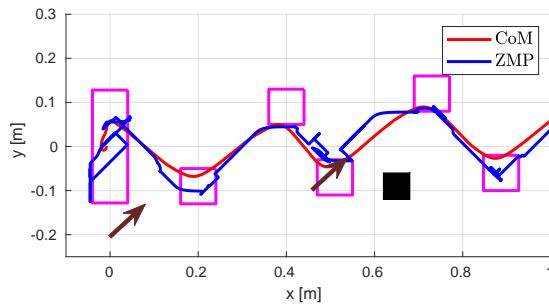
The parameters are: $m = 5.3$ kg, $\bar{z}_c = 0.21$ m, $d_{z,x} = d_{z,y} = 0.05$ m, $d_{a,x} = 0.16$ m, $d_{a,y} = 0.05$ m, $\ell = 0.1$ m, $\delta = 0.05$ s, $T_s = 0.5$ s, $T_{ds} = 0.2$ s. The kinematic controller runs at 100 Hz and the QPs are solved with the qpOASES library.

The setting consists in the robot being hit through the pendulum structure used in the previous chapter, while carrying a 1 kg load with its right arm. The pendulum mass has now a value of 0.670 kg. We set $w_{m,x}(t) = w_{m,x} = 0$ m/s^2, $\Delta = 0.3$ m/s^2, $w_{m,y}(t) = w_{m,y} = 0.45$ m/s^2 and $\Delta = 0.3$ m/s^2. To improve the detection of the impulsive push, IMU measurements are used. The push triggers the activation of the recovery mode, and the disturbance is absorbed by modifying both the step timing and the step position. This experiment was repeated 10 times with a 70% success rate and a successful outcome is shown Fig. 9.9. The realized CoM/ZMP trajectory during this trial is also shown. From the plot, we can recognize the CoM displacement towards
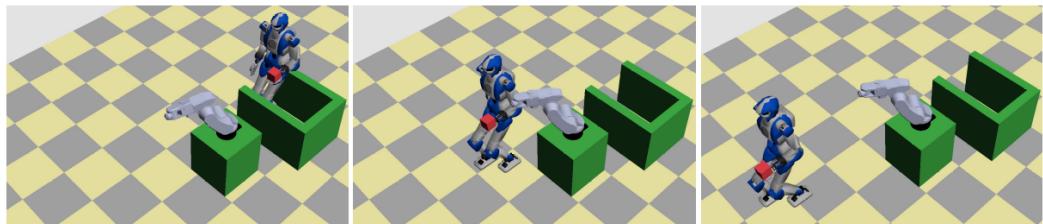
Figure 9.6: Dart simulations: persistent and impulsive disturbance (top sequence), persistent disturbance with push in the swing to support foot direction (meddle sequence), persistent disturbance with push recovery and avoidance of a small obstacle (bottom sequence).
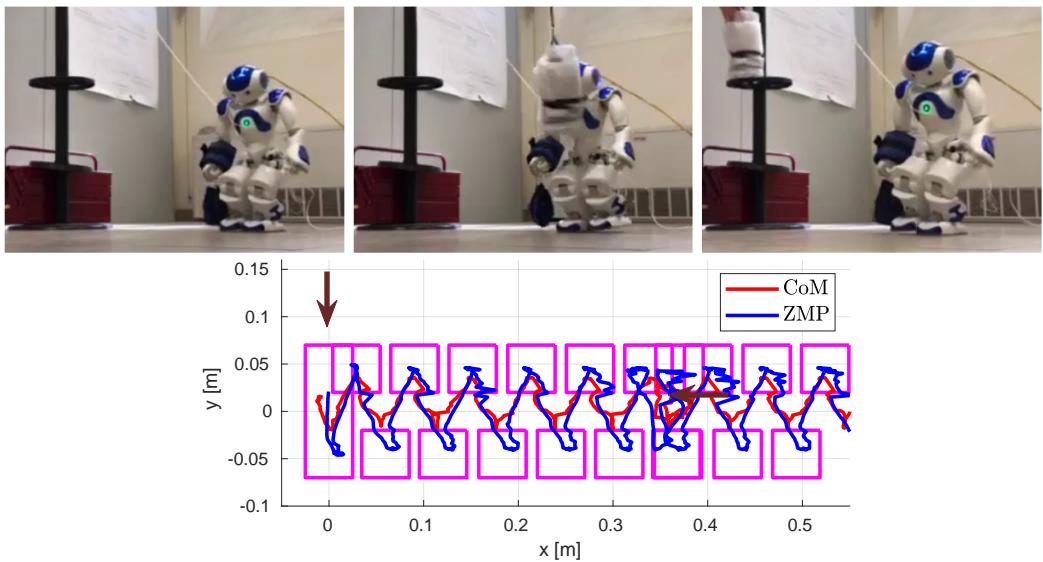
the disturbance direction for all the motion and a footstep adaptation. We report that the timing of the step when the push is received and the subsequent are respectively reduced by 0.15 s and 0.05 s.

Figure 9.7: CoM/ZMP plot of the persistent disturbance with push recovery and avoidance of a small obstacle simulation.

Figure 9.8: Application scenario: HRP-4 carrying a payload while being hit by an operating manipulator.

Figure 9.9: NAO being hit by the pendulum while carrying a weight: snapshots and CoM/ZMP plot.

Chapter 10
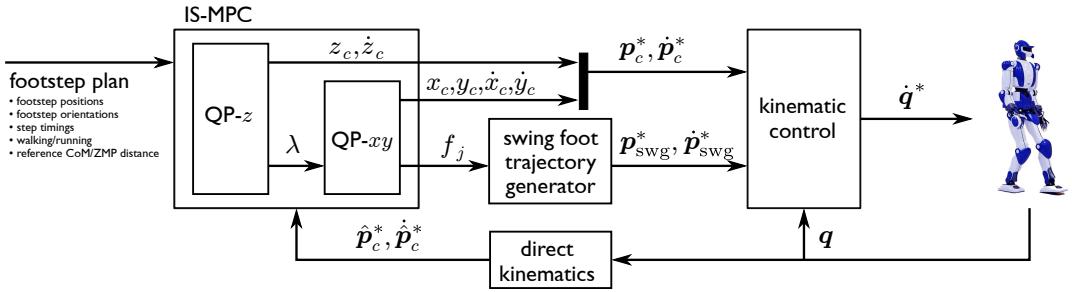
3D walking and running using MPC

This chapter moves towards the design of a MPC-based scheme for dynamic locomotion involving 3D trajectories for the CoM, e.g., stair climbing and running. We consider, as stated in Chapter 4, an environment constituted by horizontal patches of different heights, that we denote as *world of stairs*. We will also present an extension to the case of running over tilted surfaces.

We retain here a centroidal approach composed by a walking pattern generator and a kinematic controller that tracks the reference motions. For the present objective, the LIP model does not provide anymore a sufficient description of the centroidal dynamics. We thus adopt the Variable Height Inverted Pendulum (VH-IP) as prediction model for the MPC.

A two-stage MPC approach is proposed, formulated in such a way to require solving standard QP problems. This is made possible by exploiting the fact that the natural frequency of the VH-IP model can be regarded as a time-varying parameter because, as pointed out in Sect. 4.4.3, the z CoM component is not affected by the horizontal dynamics. At each time, a QP for the vertical CoM motion is solved and with the generated trajectories a subsequent QP is built, providing the solution for the horizontal component. The presented approach has the advantage of allowing for a linear formulation without limiting the possible vertical CoM motions. Linear formulations are in fact already obtained in the literature [194, 211], but they require constraining the pendulum frequency with the result of reducing the achievable CoM motions. Less restrictive approaches, on the other hand, use offline generated trajectories for the z component of the CoM [210].

A further contribution of the chapter is the implementation of the stability condition of Sect. 6.5 as a stability constraint for the horizontal CoM dynamics. The stability condition for combined models, i.e., VH-IP that becomes a LIP after a certain time, was presented in an abstract way, without specifying particular use cases. Here, we demonstrate that such modeling approximates well enough the VH-IP dynamics in the context of a receding horizon controller, with the advantage of allowing to formulate the stability condition as a linear equality constraint, i.e., the same form used in the previous chapters. Another advantage is the possibility of including the presence of flight phases, where the ZMP is not defined. In [197] for instance, the exact stability condition for the VH-IP (reported in Sect. 6.13) was used as a stability constraint for 3D walking.

Figure 10.1: Block scheme of the proposed approach for 3D gait generation.

This was made possible by manipulating the constraint (6.13), while taking (4.35) into account, to render it tractable within the context of nonlinear optimization-based control. This, however, required to fix a profile for the ZMP trajectory, without supporting the presence of flight phases.

The method proposed in the this chapter is validated through dynamic simulations in the DART environment and an experiment on the OP-3 platform. For completeness, a simple footstep planner, that is the required input of the scheme, will also be presented to provide an idea on how to retrieve the parameters and the quantities needed for correct operations.

10.1 IS-MPC for 3D walking and running

The objective is to design a gait generation scheme that tracks a footstep plan, making the humanoid walk over a world of stairs. The scheme (Fig. 10.1) operates over time intervals, $t_{k+1} - t_k = \delta$, and uses the VH-IP as prediction model, that we report here for the sake of readability

$$\ddot{x}_c \quad = \lambda(x_c - x_z) \tag{10.1}$$

$$\ddot{y}_c \quad = \lambda(y_c - y_z) \tag{10.2}$$

$$\ddot{z}_c \quad = \frac{f_z}{m} - g. \tag{10.3}$$

We also recall from Chapter 4 that during flight phases the model boils down to
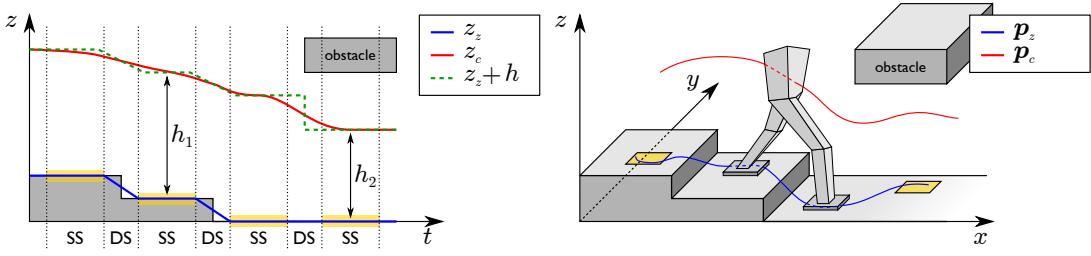
$$\ddot{x}_c \quad = 0 \tag{10.4}$$

$$\ddot{y}_c \quad = 0 \tag{10.5}$$

$$\ddot{z}_c \quad = -g. \tag{10.6}$$

The control inputs are chosen to be the horizontal components of the ZMP (x_z, y_z) and the vertical Ground Reaction Force (GRF) f_z, all of them assumed to be constant over the duration of a single interval. Note two aspects: *i)* that the free falling model is obtained from the VH-IP model for $\lambda = 0$, *ii)* we assume that all footsteps in the plan have the same orientation, taken without loss of generality to be the same of the x axis, with the usual effect of decoupling the motion along the sagittal and coronal plane.

The IS-MPC block receives at each t_k the current footstep plan over a preview horizon T_p. As in the previous chapters, it describes, for $j = 1, \ldots, F$, the 3D positions of the candidate footsteps $(\hat{x}_f^j, \hat{y}_f^j, z_f^j)$ and their timings $(t_s^1, \ldots, t_s^F)$. In this context,

Figure 10.2: Qualitative representation of the generated trajectories over a certain prediction horizon obtained by solving QP-z and QP-xy in sequence. QP-z aims at tracking the reference vertical CoM/ZMP displacement. In this case, h^j is kept constant for the first three steps and lowered in occurrence of the fourth step to pass below an obstacle. The horizontal QP is then solved using the λ profile originated by the previous stage, thus completing the definition of the 3D CoM motion.

however, further information is required: a reference value for the vertical CoM/ZMP displacement[1] h^j over a step and the information whether each step must be performed by walking or running, encoded through the `mode` variables `walk` and `run`. The number of footsteps F in the preview horizon will depend on the duration of each step, which starts at t_s^j and lasts T_s^j, divided in single and double support or single support and flight phase. The single support duration is denoted as T_{ss}^j.

We specify that the presented scheme has the authority to move the footsteps on the horizontal component $(\hat{x}_f^j, \hat{y}_f^j)$ without changing the assigned ground patch: the vertical coordinates z_f^j of the candidate footsteps cannot be modified. This choice, although limiting the possible reactive behaviors, allows for a full decoupling of the problem between the vertical and horizontal components.

The scheme computes at each time a 3D CoM trajectory and adapted footsteps over the control horizon[2] T_c via a two stage formulation of the problem. The first stage is denoted as (QP-z), constituted by a quadratic program where f_z is the optimization variable. The program aims at computing the proper f_z that generates a vertical CoM trajectory minimizing the tracking error with respect to the reference vertical CoM/ZMP displacement. The output of this first stage is the vertical CoM profile over the prediction horizon together with a sequence of time-varying frequency samples λ, given by (4.11). The second stage is also a quadratic program (QP-xy) over the same control horizon, where the ZMP (x_z, y_z) and the footstep positions are the decision variables. The purpose of this stage is to generate the horizontal CoM trajectory resulting in a gait that is both dynamically balanced and internally stable. See Fig. 10.2 for a qualitative example.

The output of the IS-MPC block, constituted by footstep positions and a 3D CoM (and swing foot) reference pose is the input of a kinematic control block that converts the centroidal reference into joint commands. Let us now detail QP-z and QP-x.

---

[1]The reference vertical CoM/ZMP displacement can be used to promote the avoidance of obstacles that may require, for instance, lowering the CoM.

[2]We recall that $T_c = C\delta$ and $T_p = P\delta$.

10.1.1 Vertical QP

The piecewise-constant signal over time steps f_z^{k+i} selects the adopted model: (10.3) when it is positive and (10.6) when it is 0, writing in its general form as

$$\ddot{z}_c = \frac{f_z^{k+i}}{m} - g \qquad \text{for} \quad t \in [t_{k+i}, t_{k+i+1}) \quad i = 0, \dots, C-1.$$

GRF constraint

Slippage can be prevented by ensuring that the computed GRF is inside the friction cone. With the spirit of decoupling the vertical from the horizontal motion, we introduce a simplified constraint [210] expressed by

$$f_z^{k+i} \geq f_z^{\min}. \tag{10.7}$$

In practice, through $f_z^{\min}$ we ensure that the vertical GRF provides sufficient friction. To derive a meaningful value for $f_z^{\min}$ we use a simple Coulomb friction model for single support phases:

$$f_z^{\min} = \frac{m}{\mu} a_{\max},$$

where μ is the friction coefficient and $a_{\max} = \max \sqrt{\ddot{x}_c^2 + \ddot{y}_c^2}$ is the maximum horizontal acceleration of the CoM. Obtaining a value for the latter quantity is in general non trivial: we retrieve it by measures over multiple simulations. Such constraint is for simplicity also used in double support.

To enforce zero vertical GRF when the robot is running, constraint (10.7) is substituted with

$$f_z^{k+i} = 0 \tag{10.8}$$

in compliance with model (10.6).

QP-z

We let the decision variables be collected in a vector

$$F_z^k = (f_z^{k+1} \quad \dots \quad f_z^{k+C-1})^T.$$

For convenience, we group in vectors the predicted state variables
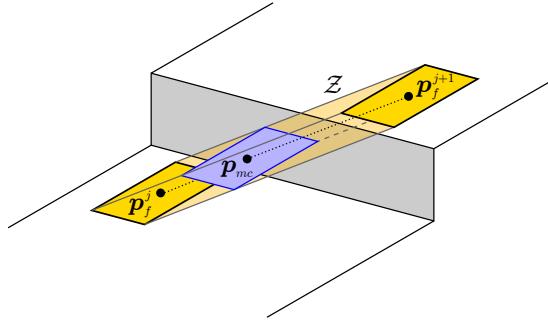
$$\dot{Z}_c^k = (\dot{z}_c^k \quad \dots \quad \dot{z}_c^{k+C-1})^T \qquad Z_c^k = (z_c^k \quad \dots \quad z_c^{k+C-1})^T.$$

Introduce now the vertical ZMP coordinate z_z^{k+i} which is set equal to the vertical component of the moving constraint region z_{mc} and let h^{k+i} be the reference vertical CoM/ZMP displacement; then the reference CoM height is expressed as

$$Z_c^{k,*} = (z_z^k + h^k \quad \dots \quad z_z^{k+C-1} + h^{k+C-1})^T. \tag{10.9}$$

It should be noted that the vertical component of the 3D moving constraint, of which the center is in general expressed as $\boldsymbol{p}_{mc} = (x_{mc} \ y_{mc} \ z_{mc})^T$, is written as

$$z_{mc}(t) = z_f^{j-1} + (z_f^j - z_f^{j-1})\sigma(t, t_s^j, t_s^j + T_{ds}^j) \tag{10.10}$$

Figure 10.3: The moving constraint region is the blue patch in the yellow prism $\mathcal{Z}$ (4.8) that slides between two consecutive footsteps with an assigned timing law, given by (7.4). At any given time, the ZMP must be inside the horizontal slice.

while sharing the same equations (7.5)-(7.5) for the horizontal components. In this sense, we have $z_z^k = z_{mc}(t_k)$. See Fig. 10.3 for a graphical representation.

We can now formulate QP-z as

$$
\left\{
\begin{array}{l}
\displaystyle \min_{F_z^k} \|Z_c^k - Z_c^{k,*}\|^2 + \alpha_z \|\dot{Z}_c^k\|^2 + \beta_z \|\Delta F_z^k\|^2 \\[2ex]
\text{subject to:} \\[1ex]
\quad \bullet \text{ constraint (10.7), for each interval } [t_{k+i}, t_{k+i+1}] \text{ in which the robot is walking;} \\[1ex]
\quad \bullet \text{ constraint (10.8), for each interval } [t_{k+i}, t_{k+i+1}] \text{ in which the robot is running;}
\end{array}
\right.
$$

where α_z, β_z are positive weights. The first two components of the cost function aim at tracking the reference vertical CoM trajectory, while minimizing its velocity. The last term promotes the generation of a smoother profile for f_z by penalizing the difference between subsequent samples of the vertical GRF.

10.1.2 Horizontal QP

The assumption of fixed orientation allows to decouple QP-xy in two separate programs: QP-x and QP-y. As for the previous chapters, we will describe the problem formulation for the sole x component, while specifying the differences with respect to y when required.

For single and double support phases we use (10.1) as prediction model, in which the time-varying λ (4.11) is generated by the result of QP-z. To this purpose, we introduce a sample-and-hold representation of $\lambda(t)$ to obtain a piecewise-time-invariant formulation:

$$
\ddot{x}_c = \lambda^{k+i}(x_c - x_z) \qquad \text{for} \quad t \in [t_{k+i}, t_{k+i+1}), \quad i = 0, \dots, C-1, \tag{10.11}
$$

where

$$
\lambda^{k+i} = \frac{\ddot{z}_c^{k+i} + g}{z_c^{k+i} - z_z^{k+i}}.
$$

During the sampling interval, the model is time-invariant, whereas the value of λ^k is updated at the beginning of each sample. When the robot is in flight phases during running, the prediction model becomes

$$
\ddot{x}_c = 0,
$$

as in fact $f_z^{k+i} = 0$ yielding $\lambda^{k+i} = 0$ in (10.11). Let us now detail the constraints that will be enforced in the QP.

ZMP constraint

The horizontal component of the ZMP constraint is given by the moving constraint region and corresponds to (8.1.2).

Kinematic constraint

We enforce in this chapter, similarly to (8.3), a kinematic constraint given by a convex sub-region of the KAR. The constraint is expressed by

$$(x_f^j, \, y_f^j) \in \bar{\mathcal{K}}^j, \quad j = 1, \ldots, F,$$

where the bounds of $\bar{\mathcal{K}}^j$ are now given by

$$\left| x_f^j - x_f^{j-1} \right| \leq \frac{d_{a,x}(z_f^{j-1}, z_f^j)}{2}, \qquad \left| y_f^j - y_f^{j-1} \pm \ell \right| \leq \frac{d_{a,y}(z_f^{j-1}, z_f^j)}{2}. \tag{10.12}$$

The difference is now that $d_{a,x}(z_f^{j-1}, z_f^j)$ and $d_{a,y}(z_f^{j-1}, z_f^j)$ are functions of z_f^{j-1} and z_f^j. We introduced such a modification to account for the patch height: physical intuition suggests that the more a step is high and the less the humanoid is kinematically able to step further in the horizontal direction. We express the idea through the heuristics

$$d_{a,x}(z_f^{j-1}, z_f^j) = \left(1 - \sigma \frac{|z_f^j - z_f^{j-1}|}{\Delta z_f^{\max}} \right) d_{a,x}^0, \qquad d_{a,y}(z_f^{j-1}, z_f^j) = \left(1 - \sigma \frac{|z_f^j - z_f^{j-1}|}{\Delta z_f^{\max}} \right) d_{a,y}^0,$$

where $\sigma \in (0, 0.5)$, $\Delta z_f^{\max}$ is the maximum step height variation that the robot can tolerate, and $d_{a,x}^0, d_{a,y}^0$ are the original dimensions of the KAR sub-region. The size of the considered KAR sub-region is reduced based on the step height and on the tunable parameter σ[3].

Ground patch constraint

As specified above, footstep adaptation can only be performed over the same ground patch that is assigned by the footstep plan so as to maintain the decoupling between the vertical and the horizontal problem. This condition is enforced through the constraint
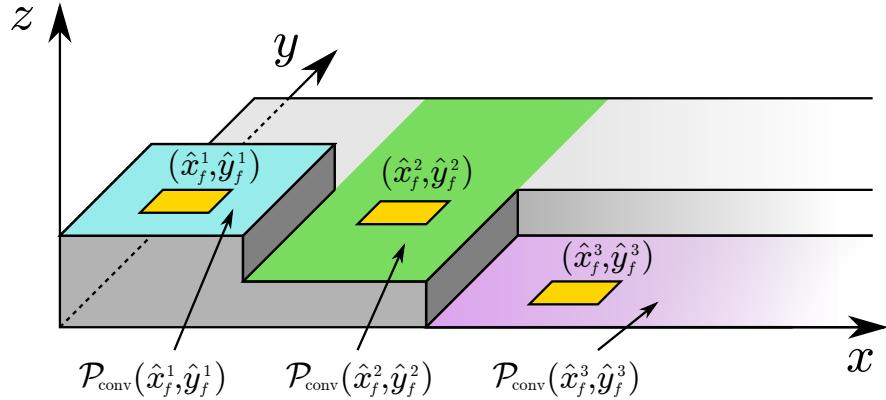
$$(x_f^j, y_f^j) \in \mathcal{P}_{\mathrm{conv}}(\hat{x}_f^j, \hat{y}_f^j) \ominus \mathcal{P}_{\mathrm{foot}}. \tag{10.13}$$

The quantity $\mathcal{P}_{\mathrm{conv}}(x, y)$ expresses a convex subset of the ground patch in which the point (x, y) lies. $\mathcal{P}_{\mathrm{foot}}$ is defined as

$$\mathcal{P}_{\mathrm{foot}} = \{(x, y) : |x| \leq d_{z,x}/2, |y| \leq d_{z,y}/2\}$$

---

[3]For $\sigma \to 1$ the surface of the kinematic constraint tends to vanish. Thus we set the upper bound of the parameter equal to 0.5.

Figure 10.4: Example of a possible patch configuration.

and corresponds to the foot sole size used for gait generation[4]. In this way, we ensure that the considered footstep region is contained in the polytope that is enforced as constraint. If a map of the environment is available, the ground patch constraint can be processed offline[5].

We must point out that if the robot deviates from the plan during the locomotion, it is possible that the ground patch constraint can conflict with the kinematic constraint, yielding an unfeasible problem for the QP. We are not addressing explicitly this limitation of the proposed scheme, which should be handled by updating the footstep plan. To mitigate the issue, we only apply constraint (10.13) to the first footstep in the prediction horizon.

Swing foot constraint

Due to possible motions at higher speeds with respect to walking gaits, we include a constraint that limits the target foot placement of the first step in the prediction horizon according to the current swing foot position, in the same spirit as [122]. The constraint is

$$\left| x_{\text{sw}}^k - x_f^1 \right| \leq (t_s^0 + T_{ss}^0 - t_k)\, v_{\text{sw}}^{\max}, \tag{10.14}$$

where t_s^0 corresponds to the starting time of the current step, T_{ss}^0 the single support duration and $(t_s^0 + T_{ss}^0 - t_k)$ is the time to complete the current single support phase. The quantity $v_{\text{sw}}^{\max}$ can be chosen by estimating the maximum foot Cartesian velocity that the robot can realize. This constraint is only enforced during single support phases.

Stability constraint

The VH-IP model is unstable, as discussed in Sect. 4.4. We propose to adopt for the implementation of a linear stability constraint the model (6.5.1) presented in Sect. 6.5. The dynamics are re-written for readability

$$\ddot{x}_c = \begin{cases} \lambda^{k+i}(x_c - x_z) & \text{for} \quad t \in [t_{k+i}, t_{k+i+1}), \quad i = 0, \dots, C-1 \\ \lambda_{\text{LIP}}(x_c - x_z) & \text{for} \quad t \geq t_{k+C}. \end{cases}$$

---

[4]Note that such quantity is chosen to be slightly smaller than the physical foot sole of the robot to introduce a heuristic robustness margin.

[5]There exist in the literature procedures to perform convex decompositions, such as [128, 183].

This choice corresponds to assuming that the vertical motion of the CoM disappears after the control horizon and sets to a fixed CoM height, i.e., the VH-IP dynamics becomes LIP dynamics. Neglecting the vertical CoM variations after T_c is a reasonable assumption given the receding horizon nature of the controller and the fact that the decision variables are only covered by the prediction horizon (for which the VH-IP model is employed). We presented in Sect. 6.5 a stability condition for such a combined model, i.e.,

$$G\,\Phi(t_{k+C}, t_k) \begin{bmatrix} x_c^k \\ \dot{x}_c^k \end{bmatrix} + \int_{t_k}^{t_{k+C}} G\,\Phi(t_{k+C}, \tau) B(\tau) x_z(\tau) d\tau = x_u^{k+C} \qquad (10.15)$$

with

$$x_u^{k+C} = \sqrt{\lambda_{\text{LIP}}} \int_{t_{k+C}}^{\infty} e^{-\sqrt{\lambda_{\text{LIP}}}(\tau - t_{k+C})} \tilde{x}_z(\tau) d\tau.$$

Here, we show how to convert it into a stability constraint. We begin with the state transition matrix $\Phi(t_{k+C}, t)$ and the input matrix $B(t)$, specifying these terms at time t_{k+i} of the control horizon which can either correspond to a support or a flight phase. The state transition matrix from t_{k+i} to t_{k+C} is given by

$$\Phi(t_{k+C}, t_{k+i}) = \prod_{j=i}^{C-1} \Phi_{k+j} \qquad i = 0, \ldots, C-1, \qquad (10.16)$$

where for support time steps we have

$$\Phi_{k+j} = \begin{pmatrix} \cosh(\sqrt{\lambda^{k+j}}\delta) & \frac{\sinh(\sqrt{\lambda^{k+j}}\delta)}{\sqrt{\lambda^{k+j}}} \\ \sinh(\sqrt{\lambda^{k+j}}\delta)\sqrt{\lambda^{k+j}} & \cosh(\sqrt{\lambda^{k+j}}\delta) \end{pmatrix}$$

and

$$\Phi_{k+j} = \begin{pmatrix} 1 & \delta \\ 0 & 1 \end{pmatrix}$$

for flight phase intervals. Regarding the input matrix, we have

$$B(t_{k+i}) = \begin{pmatrix} 1 - \cosh(\sqrt{\lambda^{k+i}}\delta) \\ -\sinh(\sqrt{\lambda^{k+i}}\delta)\sqrt{\lambda^{k+i}} \end{pmatrix} \qquad \text{and} \qquad B(t) = \begin{pmatrix} 0 \\ 0 \end{pmatrix}$$

respectively for support and flight instants.

Plugging (10.16) into (10.15) and rearranging the terms leads to the stability constraint

$$G \sum_{i=0}^{C-1} \prod_{j=i}^{C-1} \Phi_{k+j} B_{k+i} x_z^{k+i} = \sqrt{\lambda_{\text{LIP}}} \int_{t_{k+C}}^{\infty} e^{-\sqrt{\lambda_{\text{LIP}}}(\tau - t_{k+C})} \tilde{x}_z(\tau) d\tau - G \prod_{i=0}^{C-1} \Phi_{k+i} \begin{pmatrix} x_c^k \\ \dot{x}_c^k \end{pmatrix}.$$
$$(10.17)$$

The anticipative tail (7.14) is used to conjecture the value of $\tilde{x}_z$.

Horizontal QP

Let us collect the decision variables in

$$X_z^k = (x_z^k \; \ldots \; x_z^{k+C-1})^T \qquad X_f^k = (x_f^1 \; \ldots \; x_f^F)^T,$$

the candidate footsteps in

$$\hat{X}_f^k = (\hat{x}_f^1 \; \ldots \; \hat{x}_f^F)^T,$$

and the x coordinate of the center of the moving constraint region in

$$X_{mc}^k = (x_{mc}^k \; \ldots \; x_{mc}^{k+C-1})^T.$$

Introduce also the ZMP increment vector $\Delta X_z = (x_z^{k+1} - x_z^k \; \ldots \; x_z^{k+C} - x_z^{k+C-1})^T$.
The QP-x is expressed as

$$\min_{X_z^k, X_f^k} \|X_z - X_{mc}^k\|^2 + \alpha_x \|\Delta X_z\|^2 + \beta_x \|X_f^k - \hat{X}_f^k\|^2$$

subject to:

- ZMP constraints, (8.2);

- kinematic constraints, (10.12), for $j = 1, \ldots, F$;

- ground patch constraints (10.13), for $j = 1$;

- swing foot constraint (10.14), for $j = 1$;

- stability constraint (10.17).

The cost function aims at tracking the reference ZMP position as well as the candidate footstep placement, while penalizing large ZMP increments. An analogous problem QP-y is formulated for the y component, the only difference being that the kinematic constraint is given by the second expression in (10.12).

All constraints are not applied at the same time, in particular:
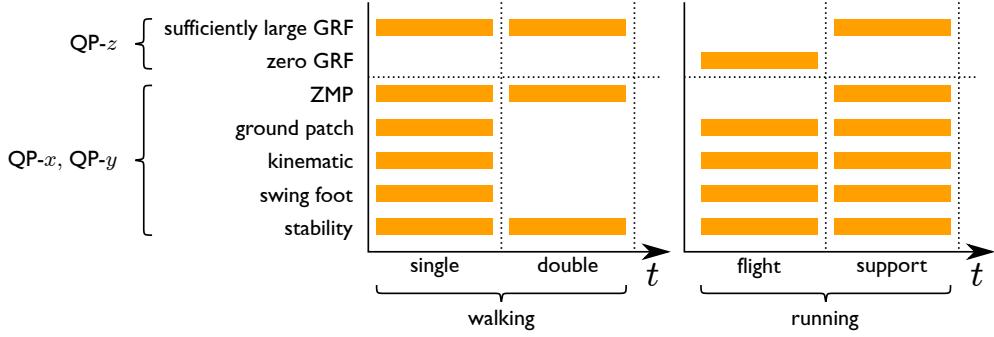
- the ZMP constraint is not enforced during flight phase samples;

- the ground patch, kinematic, and swing foot constraints are not enforced during double support phases.

Figure 10.5 wraps up the constraint activation schedule for both QP-xy and QP-z.

10.2   Running over tilted surfaces

We consider here the case of running over tilted surfaces. In running gaits no double support phases are involved and this allows to use similar arguments to the previous sections to enforce dynamic balance in single support.

When a foot is in contact with a tilted surface, a higher friction is required to avoid slipping because the tangential component of the GRF is also in charge of compensating for the tangential component of gravity. In the case of parallel surfaces it was sufficient to impose a minimum value for the vertical GRF (10.7). To retain a similar constraint here, we increase the minimum required vertical GRF by scaling the right side of (10.7)

Figure 10.5: Constraint activation schedule over a step.

by an appropriate coefficient, depending on the maximum slope of the ground. Given the full knowledge of the map, it is possible to assign a scaling term for each tilted patch.

We express, for consistency with the previous treatment, the position of the CoM and ZMP in a frame oriented as the tilted patch, where the z axis is normal to the patch plane. The vertical CoM dynamics is thus

$$\ddot{z}_c = \frac{f'_z}{m} - g'_z, \tag{10.18}$$

while the horizontal dynamics writes as

$$\ddot{x}_c = \lambda(x_c - x_z) + g'_x \tag{10.19}$$
$$\ddot{y}_c = \lambda(y_c - y_z) + g'_y, \tag{10.20}$$

where g'_x, g'_y and g'_z correspond to the component of the gravity vector in the tilted plane frame. These can be interpreted as known disturbances, given the knowledge of the patch orientation.

The scheme for running over tilted surfaces is thus equivalent to that exposed in the previous sections of the chapter, with a different stability constraint. Let us consider in fact the combined model given by

$$\ddot{x}_c = \begin{cases} \lambda^{k+i}(x_c - x_z) + g'_x & \text{for} \quad t \in [t_{k+i}, t_{k+i+1}) \quad i = 0, \ldots, C-1 \\ \lambda_{\mathrm{LIP}}(x_c - x_z) + g'_x & \text{for} \quad t \geq t_{k+C}. \end{cases} \tag{10.21}$$

For such model we presented in Sect. 6 the stability condition (6.18) which can be cast in the stability constraint

$$G \sum_{i=0}^{C-1} \prod_{j=i}^{C-1} \Phi_{k+j} B_{k+i} x_z^{k+i} = \sqrt{\lambda_{\mathrm{LIP}}} \int_{t_{k+C}}^{\infty} e^{-\sqrt{\lambda_{\mathrm{LIP}}}(\tau - t_{k+C})} \tilde{x}_z(\tau) d\tau$$
$$- G \sum_{i=0}^{C-1} \prod_{j=i}^{C-1} \Phi_{k+j} D g_x^{',k+i} - G \prod_{i=0}^{C-1} \Phi_{k+i} \begin{pmatrix} x_c^k \\ \dot{x}_c^k \end{pmatrix} \tag{10.22}$$

and used in the horizontal QP when required by the plan[6].

_____

[6]The knowledge of the plan and the map should also be used to generate a proper swing foot trajectory that is consistent with the tilted patch configuration.

10.3 Velocity-driven footstep planner

Before discussing simulation and experimental results, we present a simple method to generate the required input data for the scheme. Let us assume that a forward velocity command v and an *elevation map*, i.e., a 3D map of the environment, are given.

We follow here the heuristics of [127] for which a change in the reference velocity implies a variation in the footstep placement and timing. Let us consider a triplet of cruise parameters $(\bar{v}, \bar{L}, \bar{T})$, where $\bar{v} = \bar{L}/\bar{T}$, being $\bar{L}$ a stride length and $\bar{T}$ the step duration[7]. Then, given a deviation from $\bar{v}$, the effect on the step length and duration is expressed as

$$v = \bar{v} + \Delta v = \frac{\bar{L} + \Delta L}{\bar{T} - \Delta T}.$$

We impose $\Delta L = \alpha \Delta T$ with $\alpha > 0$ and derive the corresponding expression for the step duration as a response to the reference v

$$T = \bar{T}\,\frac{\alpha + \bar{v}}{\alpha + v},$$

which has to be divided into phases (single/double or support/flight). Human biomechanics [203] suggests that the double support duration constitutes the 20-40% of the step duration. The proportion should be inverted in the presence of running flight phases. Realizing human-like running with a humanoid robot requires highly performing actuators and can be dangerous for the mechanical structure if not properly designed. Hence, we adopt here the same double support duration proportion for flight phases.

The associated step length is calculated as $L = vT$. In this way, the value of L increases as the reference command v is increased. To distinguish walking from running steps, we set a step length threshold $L_{\max}$ and command the scheme to generate a running step (`mode = run`) when $L > L_{\max}$ or a walking step (`mode = walk`) when $L \leq L_{\max}$. Regarding the y direction, the footsteps simply alternates with a fixed foot distance with respect to the initial CoM position.

We showed how to compute the triplet $(L^j, T^j, \texttt{mode}^j)$ for each step. The candidate horizontal footstep location is obtained from it, given the starting position of the robot. It is then necessary to associate a specific ground patch $\mathcal{P}^j(\hat{x}_f^j, \hat{y}_f^j)$ to each footstep. To do this, we simply check where each footstep has been placed by the planner and pick the relative ground patch. However, some of the candidate footsteps can be unfeasible as they may not be completely contained inside the corresponding patch (being for instance placed at the border). This being the case, we perform the following procedure for each of the unfeasible footstep positions: we translate towards the previous footstep the section of the plan that starts from the unfeasible step until it is fully contained inside a ground patch.

Further useful heuristics might be introduced. For instance, a practical rule is that of setting a step with zero sagittal stride each time two footsteps are located at two different heights[8].

To conclude the set of data which define a 3D plan, we need to assign the reference CoM/ZMP displacement h^j. We simply set it as a constant reference value $h^j = \bar{h}$,

---

[7]These can be for instance obtained from the default walking gait provided by the manufacturer.

[8]This prevents the robot from executing large foot motions to reach patches of different height, increasing the robustness and the repeatability of the locomotion [54].

while we modify it when required by the specific task or due to the presence of vertical obstacles.

10.4 Simulations

We evaluate the performance of the presented scheme through a set of dynamic simulations in DART. The considered platform is the HRP-4 humanoid. We point out that the method does not account for joint actuation limits, implying that possible infeasible motions can be generated. The main objective here is to validate the dynamic stability on a simulated multi-body system and thus we do not enforce the torque limits in the simulation: the robot could in principle execute any motion without saturating the actuators. However, the joint torque can be retrieved from the simulator and the feasibility of the motion can be evaluated. The scheme parameters can also be tuned so as to obtain meaningful joint torque values, reducing for instance the flight phase duration, the step length or acting on the reference CoM height. We also recall that at the time of writing the manuscript, a limited number of humanoid platforms is conceived to perform dynamic running in a 3D environment, e.g., Atlas by Boston Dynamics or on-going projects such as the MIT humanoid [102] and Kangaroo by PAL Robotics.
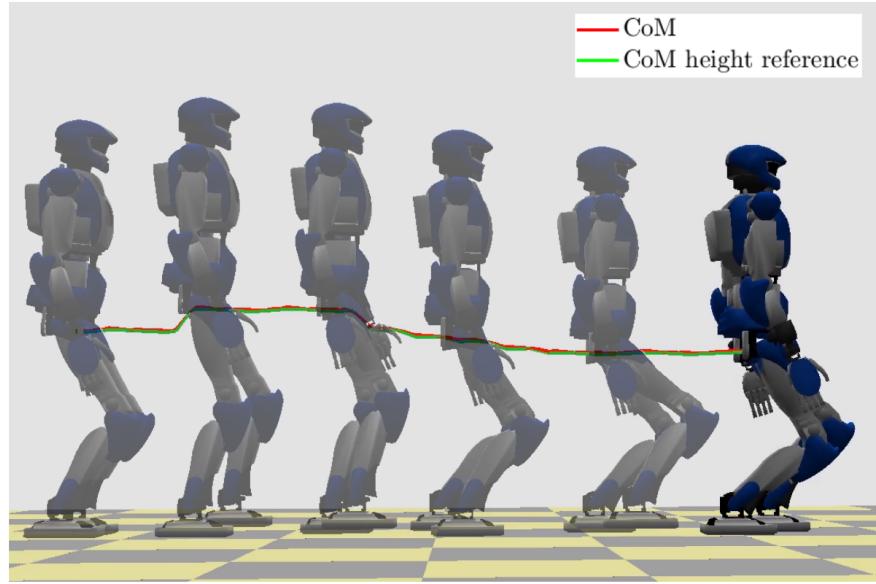
The parameters are the following: sampling time $\delta = 0.01$ s, control horizon $T_c = 0.7$ s, preview horizon $T_p = 1.8$ s, $f_z^{\min} = 114$ N, $d_{z,x} = d_{z,y} = 0.08$ m, $d_{a,x} = 1$ m, $d_{a,y} = 0.12$ m, $\ell = 0.25$ m. The weights of the cost functions are $\alpha_z = \beta_z = 10^{-5}$, $\alpha_x = \alpha_y = 1$ and $\beta_x = \beta_y = 10^4$, while λ_{LIP} is updated at each iteration using the desired value of λ at the end of the control horizon, i.e., $\lambda_{\mathrm{LIP}} = 9.81/(h^{k+C} - z_z^{k+C})$. In all the simulations the kinematic controller runs at 100 Hz, while the vertical and horizontal QPs are solved using *hpipm* [247].

The video of the results can be found in `https://www.frontiersin.org/articles/10.3389/frobt.2022.876613/full`.
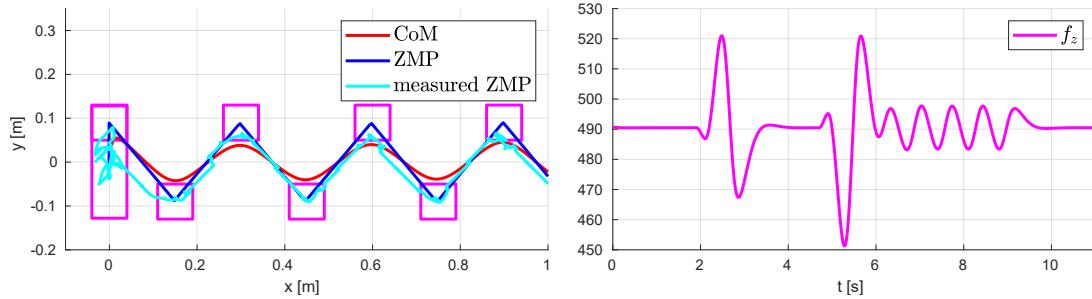
10.4.1 Walking on flat ground: variation of the CoM height

We begin the validation by considering a walking task over a unique ground patch. In this initial test, the footstep plan is manually assigned: the positions are spaced by 0.15 m along x, and displaced by ± 0.18 m on the y. The step duration is 0.7 s, divided in 0.5 s for the single support and 0.2 s for the double support. We assigned a time-varying profile for the vertical CoM/ZMP displacement. It begins with 0.7 m for the first four steps, then is raised to 0.77 m for four subsequent steps. In the next five steps the reference value is progressively decreased by 0.02 m, until reaching the final value of 0.58 m. Walking with variable CoM height can be used for the transition between walking and crouching as well as for passing below an obstacle.

We display simulation snapshots and data in Figs. 10.6-10.7. The vertical CoM motion can be visualized in Fig. 10.6, represented with respect to the reference value. The first plot of Fig. 10.7 shows the CoM and ZMP trajectory in the (x, y) plane for the first eleven seconds of the gait. The boundedness of the CoM trajectory with respect to the ZMP testifies the validity of the stability constraint that has been implemented for the 3D CoM motion case. The second plot reports the vertical GRF computed by QP-z. This quantity acts as a control input that generates the desired CoM height profile. The smoothness of f_z is obtained through the cost function of QP-z.

Figure 10.6: Walking on flat ground with variable CoM height: stroboscopic motion.
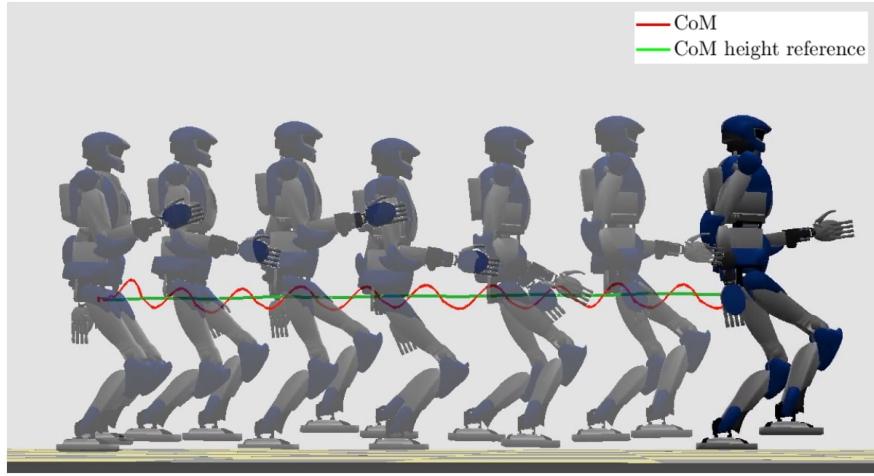
Figure 10.7: Walking on flat ground with variable CoM height: CoM/ZMP trajectories (left) and vertical GRF (right). The measured ZMP trajectory is also reported in the first plot.

10.4.2 Running on flat ground
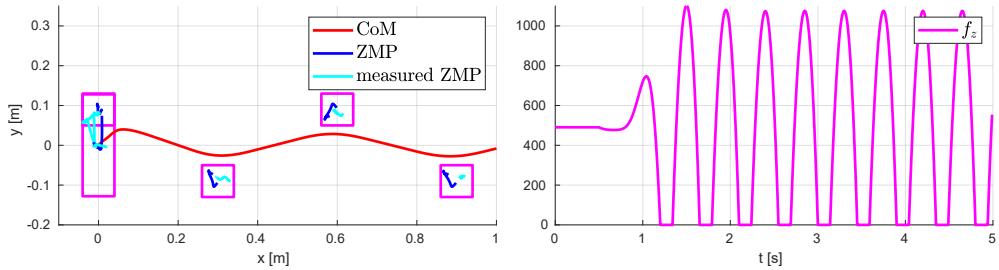
We now consider a stride length of 0.3 m in the x direction with a the step duration of 0.45 s, divided in 0.3 s for the single support phase and 0.15 s for the flight phase. An initial walking step on the place is planned for transitioning to the running gait from the initial standing position. The vertical CoM/ZMP displacement is $h = 0.7$ m. The arm swing is coordinated with the gait frequency, while the amplitude is empirically assigned, similarly to what was done in [24].

The vertical CoM motion, that can be visualized in Figs. 10.8, has a similar profile to human biomechanics [202, 203]. Running gaits are characterized by the alternation between an *absorption* and a *generation* phases: absorption consists in a horizontal deceleration that drives the descent of the CoM. On the other hand, in the generation phase the CoM accelerates horizontally and rises in height until reaching an apex. The consistency of the simulated humanoid motion with this description can be evaluated by inspecting the video.

The data reported in 10.9 show the horizontal CoM/ZMP trajectories and the vertical GRF. The ZMP trajectory is discontinuous because it is not defined during the flight phases, and the CoM trajectory is bounded (always between the footsteps). The

Figure 10.8: Running on flat ground: stroboscopic motion.

Figure 10.9: Running on flat ground: CoM/ZMP trajectories (left) and vertical GRF (right). The measured ZMP trajectory is also reported in the first plot.
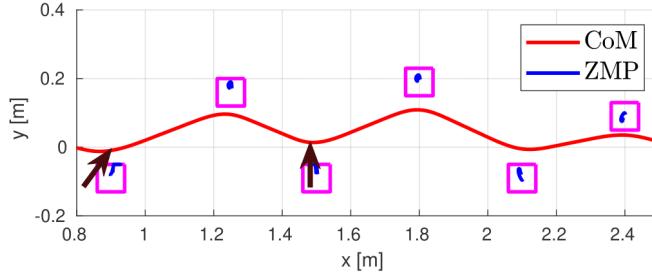
vertical GRF has a smooth profile during the support phases. There exists however a discontinuity, not easily distinguishable in the present plot as quite low with respect to the force peaks, when transitioning from support to flight phases and viceversa. This phenomenon is due to the friction constraint enforced by the vertical QP when the foot is in contact with the ground. We also recall that the effect of the last term in the QP-z cost function mitigates such a discontinuity.

In this simulation the robot reaches a maximum forward velocity of 1.25 m/s. Higher velocities can be achieved by improving the kinematic controller with stabilizers [54].
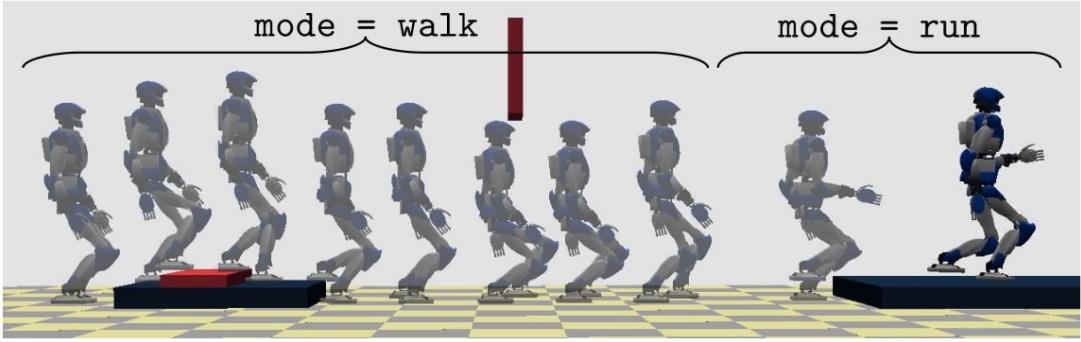
As a further validation, we considered a push recovery case, where HRP-4 is pushed twice by forces lasting 0.1 s of respectively $(50, 75, 0)$ N and $(0, 75, 0)$ N. By adapting the footstep positions, the robot clears the disturbance and proceeds with the gait (Fig. 10.10). The simulation video reports also the case where no footstep adaptation is considered: the pushes destabilize the robot leading it to fall.

10.4.3 Walking and running in a world of stairs

We now present a simulation in a world of stairs with also the presence of an overhanging obstacle along the path. The footstep plan is computed from the planner of Sect. 10.3, in which the chosen parameters are: $\alpha = 0.4$, $\bar{T} = 0.9$ s, $\bar{L} = 0.3$ m, and $L_{\max} = 0.35$ m. The reference velocity v is 0.3 m/s and increased to 1.15 m/s after 16 s. The complete elevation map is assumed to be available offline and, based on it, the ground patches

Figure 10.10: CoM/ZMP trajectory on the horizontal plan for the push recovery scenario.

Figure 10.11: Stroboscopic representation of the motion of HRP-4 in the world of stairs.
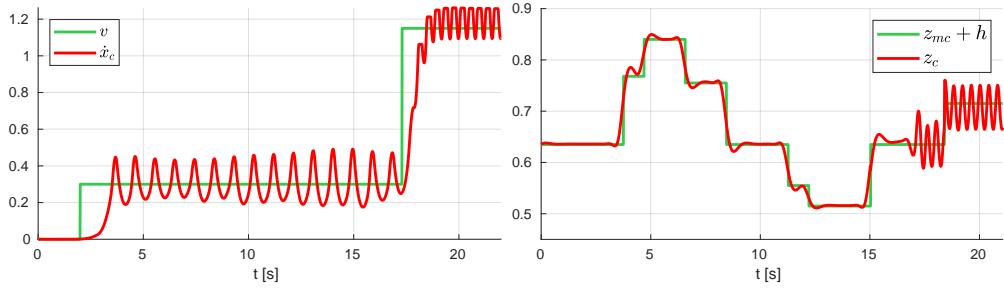
are assigned to the footsteps as well as the reference vertical CoM/ZMP displacement, that is selected in order to account for the presence of the obstacle.

The robot begins in the walking mode (`mode = walk`) with a step duration of 0.94 s, of which 0.74 s is for the single support phase and 0.2 s is for the double support phase, and a stride length on the x direction of 0.28 m. In this phase, stairs are climbed and descended, and the CoM height is modified to pass below the obstacle. The reference velocity is changed after 16 s and the plan updates the stride length to 0.48 m, implying a change in the gait mode (`mode = run`). The new step duration is 0.44 s, with 0.24 s for the single support phase and 0.2 s for the flight phase. A stroboscopic representation of the whole motion can be visualized in Fig. 10.11. We display then in Fig. 10.12 the tracking of the reference sagittal velocity and the vertical CoM height. The performance testifies the meaningfulness of feeding the planner output to the gait generation scheme to succeed in a certain task.

10.4.4 Running over tilted surfaces

We conclude the set of simulations by discussing the case of running in an environment with two ramps (inclined by ± 8 degrees) placed across the x path. A footstep plan is generated with the planner of Sect. 10.3 in response to the input velocity $v = 0.35$ m/s, that is switched to 1.1 m/s before the first ramp and then set back to the initial value after the second. The planner parameters are: $\alpha = 0.4$, $\bar{T} = 0.7$ s, $\bar{L} = 0.3$ m, $L_{\max} = 0.35$ m. The ground patch for each tilted plane is assigned offline based on the map.

The motion can be visualized in Fig. 10.13. The plots of Fig. 10.14 display the horizontal and vertical trajectories for five steps of the running gait. The proposed form of indirect disturbance compensation results in a CoM trajectory that leans against the

Figure 10.12: Walking and running in a world of stairs: reference and actual sagittal velocity (left), reference and actual CoM height (right).

effect of the perturbation introduced by the gravity when in contact with the tilted surface.
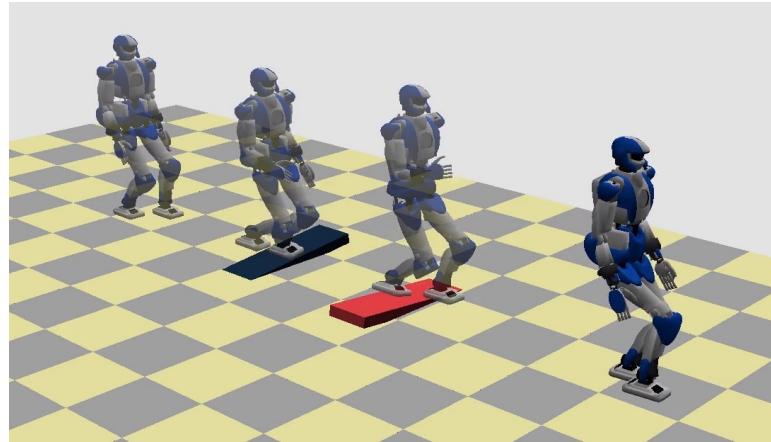
10.5   Experiments

The scheme was tested on the small sized humanoid OP3, manufactured by ROBOTIS. The same parameters of the dynamic simulations were used, except for the sampling time $\delta = 0.008$ s, $f_z^{\min} = 5$ N, $d_{z,x} = d_{z,y} = 0.05$ m, as well as those of the kinematically admissible region, that have been changed to $d_{a,x} = 0.3$ m, $d_{a,y} = 0.05$ m, with lateral displacement $\ell = 0.1$ m.
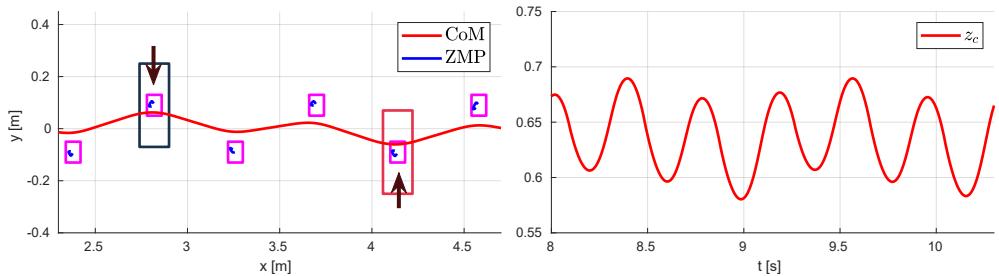
The environment is constituted of two ground patches, namely the floor and an elevated platform, and a vertical obstacle that is placed along the path. A footstep plan is generated with: $\alpha = 0.4$, $\bar{T} = 0.6$ s, $\bar{L} = 0.07$ m, $L_{\max} = 0.15$ m. The reference velocity is chosen as 0.12 m/s, resulting in a candidate step length on the x direction of 0.07 m, while on the y direction the distance between the footsteps is ± 0.09 m. In order to climb the step and place the whole foot on the elevated ground, the eighth candidate step has a distance on the x component of 0.15 m. The reference CoM height is 0.22 m at the beginning of the experiment. This value is modified to account for the presence of the obstacle and set back to the starting value after it. Figure 10.15 reports snapshots of the motion in four phases: initial walk, stair climbing, obstacle avoidance and final pose.

The scheme is implemented on the robot computer (INTEL NUC with Intel Core i3-7100U 2x2.40 GHz processor and 8GB 2133MHz RAM) in real time. The QPs have 87 decision variables ($T_c/\delta = 0.7/0.008$), while the number of constraints varies depending on which are active at a particular time (see Fig. 10.5): QP-z always has exactly 87 constraints, while the total number for QP-xy oscillate around 180.
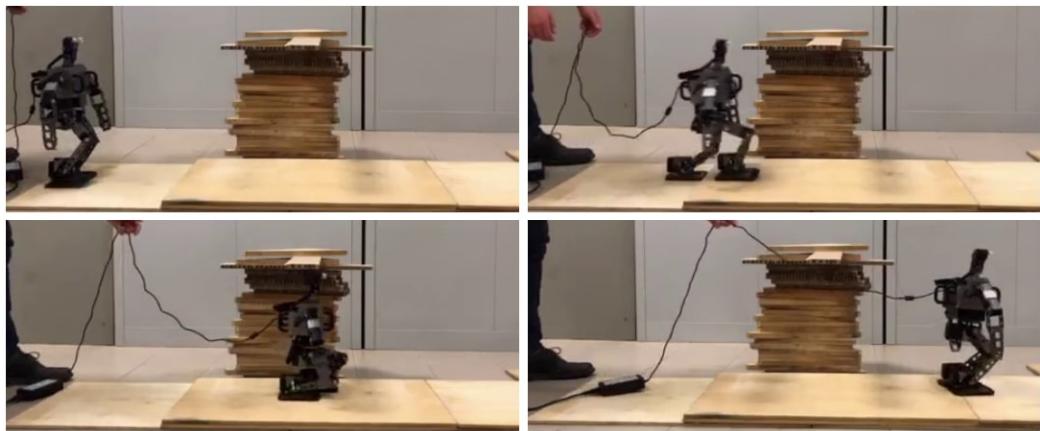
The experiment validates the framework on a small sized humanoid. The advantage of the proposed scheme is that a minimal tuning is required when switching to a different platform (the tuning effort is located on the sole kinematic or whole-body controller block). Furthermore, the method is computationally light, requiring only to solve standard QPs.

Figure 10.13: Stroboscopic motion of the tilted surface running.

Figure 10.14: Running over tilted surfaces. CoM/ZMP trajectories (left) and CoM height (right). The sole running part of the simulation is here reported. The black arrow represents the equivalent disturbance caused by the tangential component of the gravity when stepping on the tilted patch.

Figure 10.15: Snapshots from the experiment where OP3 walks forward, climbs a stair and passes below an obstacle. The cable attached to the robot back is used for power supply and does not sustain nor perturb the motion.

Chapter 11

Conclusions

11.1 Final summary

The problems addressed in this thesis were two: robust and 3D gait generation, using centroidal models. The two aspects, although presented in separate chapters, have in common the concept of stability constraint, derived from the stability conditions discussed in Chapter 6.

Robustness to persistent disturbances has been tackled with a disturbance observer and the ZMP constraint restriction in Chapter 7. The scheme that has been presented uses the LIP as prediction model and achieves robustness by modulating the CoM/ZMP displacement, while not allowing for footstep nor timing adaptation. The main objective of the chapter was to identify conditions for robust recursive feasibility under the effect of bounded disturbances.

The concept of feasibility region has been used in Chapter 8 to design a step timing adapter and a method to handle non-convex kinematic constraints in the presence of different perturbations, i.e., strong impulsive pushes. The core idea of the chapter is that by exploiting the feasibility region, it is possible to encode reactive behaviors that modify the footstep plan and subsequently the constraints of the QP of the MPC.

Eventually, a unified scheme that adopts all the robustness features introduced in Chapters 7 and 8 is presented in Chapter 9. Thanks to the modes of operation, the gait generation algorithm can retain the advantages of both the presented perspectives: exploiting the benefits of disturbance observer and ZMP constraint restriction for robust recursive feasibility as a default mode of operation, while using STA and non-convex kinematic constraints as a feasibility recovery tool in the presence of unpredictable strong pushes.

The 3D gait generation problem is addressed in Chapter 10. Here, a two stage MPC is proposed, using the VH-IP as prediction model. At each time step, the vertical CoM component is generated first by solving a QP and the result is used to formulate a subsequent QP for the horizontal motion. Thanks to the two stage formulation and the receding horizon nature of the controller, a stability constraint is proposed based on a specific stability condition obtained for a fictitious system that approximates the VH-IP dynamics after the control horizon by neglecting the vertical CoM variations.

The peculiarity of the presented methods rely on the adoption of stability constraints. They restrict the feasibility of the QPs, but this information can be quantified and even leveraged to devise tuning independent robustness strategies. The centroidal approach formulation also permits the implementation of such methods on the computer of low

cost humanoid platforms, as demonstrated in the experiments on NAO and OP3.

In the next section we will discuss possible directions for the prosecution of the work.

11.2 Future works

A practical aspect that is required to consolidate the presented schemes is their integration with localization and real-time planning stacks. As we stated during the exposition, footstep adaptation in response to perturbations may cause a significant deviation from the original contact plan. We provided naive solutions to the issue, but investigating techniques in the spirit of [187, 251, 252] is required to increase the practical usability of the methods developed in the manuscript.

Then, a prosecution of the work could be a further exploitation of the feasibility region for footstep and contact planning. The methodology of inserting a feasibility-driven plan modification block before solving IS-MPC could be exploited to address different problems. We know how the support polygon and external forces affect the shape of the region and then a possible investigation could be how to design a contact-augmented gait with negligible computational effort. With "contact-augmented", we intend the standard bipedal locomotion with the possible presence of wall contacts with the arms to enhance the dynamic balance capabilities of the robot when, for instance, performing very large steps or climbing tall stairs, in a similar way to [253].

A further interesting line of research which could be addressed is the area of contact uncertainty. Contact stability is a key aspect in legged locomotion [254]. Beside contact force considerations, issues like imprecise or unknown contact time as well as the presence of irregularities over the contact surface can destabilize the robot. Recent developments [255]-[256] propose a risk sensitive optimal control to address part of the problem. This framework can generate motions with adaptive impedance so that the contact uncertainty has a reduced effect on the performance of the platform. Borrowing general concepts from this idea and using them in IS-MPC could improve the proposed scheme in terms of robustness to disturbances which may not be modeled as those of Chapter 5.

The previous work prosecutions can be seen as immediate extensions of the thesis contents: let us now move towards a higher problem abstraction level. The feasibility analysis of Chapter 7-8 can be used as a certificate on the boundedness of the generated CoM/ZMP trajectories and as a tool for robustness. A legitimate question would be: how can we translate it to a whole-body MPC setting? It is clear that conducting the same reasoning would not be manageable. Rather, it would make more sense to blend the concept of stability constraint in a whole-body optimization context in order to design proper final costs or terminal constraints. Let us see how it could be done. The nonlinear stable inversion theory [237, 238, 240] provides us a procedure to compute bounded state x_d and input u_d trajectories for a nonlinear system given a desired output y_d to track, so that the system dynamics

$$\dot{x}_d = f(x_d) + g(x_d)u_d$$
$$y_d = h(x_d)$$

is satisfied. Inverting the humanoid dynamics in a semi real-time fashion (e.g., two or three times per second) based on the desired task y_d would provide the triplet (u_d, x_d, y_d) that can be used to design terminal cost/constraints for the whole-body

MPC. A practical way could be to adapt the procedure of Prop. 4 and [145] to this specific context. By construction, the terminal constraint will identify a stable manifold, that will be independent of the cost function and of the length of the prediction horizon[1]. A possible advantage could be to alleviate the effect of tuning on the stability of a whole-body gait generation scheme and the need of a shorter optimization horizon. Encouraging results of similar ideas have been reported in [123, 140, 145] and motivate a possible research effort in this direction.

---

[1]On the other hand, the method would require a sufficiently large preview knowledge of y_d, as in [127].

Bibliography

[1] N. A. Villa and P. Wieber. Model predictive control of biped walking with bounded uncertainties. In *17th IEEE-RAS Int. Conf. on Humanoid Robots*, pages 836–841, 2017.

[2] Robert J Full and Daniel E Koditschek. Templates and anchors: neuromechanical hypotheses of legged locomotion on land. *Journal of experimental biology*, 202 (23):3325–3332, 1999.

[3] S. Kajita, F. Kanehiro, K. Kaneko, K. Fujiwara, K. Harada, K. Yokoi, and H. Hirukawa. Biped walking pattern generation by using preview control of zero-moment point. In *2003 IEEE Int. Conf. on Robotics and Automation*, pages 1620–1626, 2003.

[4] Maximilien Naveau, Manuel Kudruss, Olivier Stasse, Christian Kirches, Katja Mombaur, and Philippe Souères. A reactive walking pattern generator based on nonlinear model predictive control. *IEEE Robotics and Automation Letters*, 2(1): 10–17, 2016.

[5] Stéphane Caron. Biped stabilization by linear feedback of the variable-height inverted pendulum model. In *2020 IEEE International Conference on Robotics and Automation (ICRA)*, pages 9782–9788. IEEE, 2020.

[6] Filippo M. Smaldone, Nicola Scianca, Valerio Modugno, Leonardo Lanari, and Giuseppe Oriolo. Gait generation using intrinsically stable MPC in the presence of persistent disturbances. In *19th IEEE-RAS Int. Conf. on Humanoid Robots*, pages 682–687, 2019.

[7] Filippo M. Smaldone, Nicola Scianca, Valerio Modugno, Leonardo Lanari, and Giuseppe Oriolo. ZMP constraint restriction for robust gait generation in humanoids. In *2020 IEEE Int. Conf. on Robotics and Automation*, pages 8739–8745, 2020.

[8] Filippo Smaldone, Nicola Scianca, Leonardo Lanari, and Giuseppe Oriolo. Feasibility-driven step timing adaptation for robust MPC-based gait generation in humanoids. In *IEEE RA-L*, volume 6, pages 1582–1589, 2021.

[9] Filippo M Smaldone, Nicola Scianca, Leonardo Lanari, and Giuseppe Oriolo. Robust mpc-based gait generation in humanoids. In *I-RIM 3D*, 2020.

[10] Andrew S Habib, Filippo M Smaldone, Nicola Scianca, Leonardo Lanari, and Giuseppe Oriolo. Handling non-convex constraints in mpc-based humanoid gait

generation. In *IEEE/RSJ International Conference on Intelligent Robots and Systems (IROS)*. IEEE, 2021.

[11] Filippo M Smaldone, Nicola Scianca, Leonardo Lanari, and Giuseppe Oriolo. Mpc-based gait generation for humanoids: from walking to running. In *I-RIM 3D*, 2021.

[12] Filippo Maria Smaldone, Nicola Scianca, Leonardo Lanari, and Giuseppe Oriolo. From walking to running: 3d humanoid gait generation via mpc. *Frontiers in Robotics and AI*, page 149.

[13] Gunalan Nadarajan. Islamic automation a reading of al-jazari's the book of knowledge of ingenious mechanical devices (1206). 2019.

[14] Sven Behnke. Humanoid robots-from fiction to reality? *Künstliche Intell.*, 22(4): 5–9, 2008.

[15] https://themadmuseum.co.uk/history-of-automata.

[16] Teun Koetsier. On the prehistory of programmable machines: musical automata, looms, calculators. *Mechanism and Machine theory*, 36(5):589–603, 2001.

[17] Nina Merz, Maximilian Huber, Freimut Bodendorf, and Jörg Franke. Science-fiction movies as an indicator for user acceptance of robots in a non-industrial environment. In *Proceedings of the 2020 on Computers and People Research Conference*, pages 142–143, 2020.

[18] http://www.iorobotto.com/.

[19] Ichiro Kato, Sadamu Ohteru, Katsuhiko Shirai, Toshiaki Matsushima, Seinosuke Narita, Shigeki Sugano, Tetsunori Kobayashi, and Eizo Fujisawa. The robot musician 'wabot-2'(waseda robot-2). *Robotics*, 3(2):143–155, 1987.

[20] Shuuji Kajita, Kenji Kaneko, Fumio Kaneiro, Kensuke Harada, Mitsuharu Morisawa, Shin'ichiro Nakaoka, Kanako Miura, Kiyoshi Fujiwara, Ee Sian Neo, Isao Hara, et al. Cybernetic human hrp-4c: A humanoid robot with human-like proportions. In *Robotics Research*, pages 301–314. Springer, 2011.

[21] Miomir Vukobratovic and Davor Juricic. Contribution to the synthesis of biped gait. *IEEE Transactions on Biomedical Engineering*, (1):1–6, 1969.

[22] Miomir Vukobratović and Juri Stepanenko. On the stability of anthropomorphic systems. *Mathematical biosciences*, 15(1-2):1–37, 1972.

[23] Marc H Raibert. *Legged robots that balance.* MIT press, 1986.

[24] Shuuji Kajita, Takashi Nagasaki, Kazuhito Yokoi, Kenji Kaneko, and Kazuo Tanie. Running pattern generation for a humanoid robot. In *Proceedings 2002 IEEE International Conference on Robotics and Automation (Cat. No. 02CH37292)*, volume 3, pages 2755–2761. IEEE, 2002.

[25] Gerardo Bledt, Patrick M Wensing, and Sangbae Kim. Policy-regularized model predictive control to stabilize diverse quadrupedal gaits for the mit cheetah. In *2017 IEEE/RSJ International Conference on Intelligent Robots and Systems (IROS)*, pages 4102–4109. IEEE, 2017.

[26] Fanny Risbourg, Thomas Corbères, Pierre-Alexandre Léziart, Thomas Flayols, Nicolas Mansard, and Steve Tonneau. Real time footstep planning and control of the solo quadruped robot in 3d environments. 2022.

[27] Avadesh Meduri, Paarth Shah, Julian Viereck, Majid Khadiv, Ioannis Havoutis, and Ludovic Righetti. Biconmp: A nonlinear model predictive control framework for whole body motion planning. *arXiv preprint arXiv:2201.07601*, 2022.

[28] Fumio Miyazaki and Suguru Arimoto. A control theoretic study on dynamical biped locomotion. 1980.

[29] Hirofumi Miura and Isao Shimoyama. Dynamic walk of a biped. *The International Journal of Robotics Research*, 3(2):60–74, 1984.

[30] C-L Shih and William A Gruver. Control of a biped robot in the double-support phase. *IEEE transactions on systems, man, and cybernetics*, 22(4):729–735, 1992.

[31] Ching-Long Shih, William A Gruver, and Tsu-Tian Lee. Inverse kinematics and inverse dynamics for control of a biped walking machine. *Journal of Robotic Systems*, 10(4):531–555, 1993.

[32] Shuuji Kajita, Tomio Yamaura, and Akira Kobayashi. Dynamic walking control of a biped robot along a potential energy conserving orbit. *IEEE Transactions on robotics and automation*, 8(4):431–438, 1992.

[33] Shuuji Kajita and Kazuo Tani. Experimental study of biped dynamic walking. *IEEE Control Systems Magazine*, 16(1):13–19, 1996.

[34] Shuuji Kajita and Kazuo Tani. Study of dynamic biped locomotion on rugged terrain-derivation and application of the linear inverted pendulum mode. In *Proceedings. 1991 IEEE International Conference on Robotics and Automation*, pages 1405–1406. IEEE Computer Society, 1991.

[35] Tad McGeer et al. Passive dynamic walking. *Int. J. Robotics Res.*, 9(2):62–82, 1990.

[36] Kenji Kaneko, Kensuke Harada, Fumio Kanehiro, Go Miyamori, and Kazuhiko Akachi. Humanoid robot hrp-3. In *2008 IEEE/RSJ International Conference on Intelligent Robots and Systems*, pages 2471–2478. IEEE, 2008.

[37] K. Hirai, M. Hirose, Y. Haikawa, and T. Takenaka. The development of honda humanoid robot. In *Proceedings. 1998 IEEE International Conference on Robotics and Automation (Cat. No.98CH36146)*, volume 2, pages 1321–1326 vol.2, 1998. doi: 10.1109/ROBOT.1998.677288.

[38] Y. Sakagami, R. Watanabe, C. Aoyama, S. Matsunaga, N. Higaki, and K. Fujimura. The intelligent asimo: system overview and integration. In *IEEE/RSJ International Conference on Intelligent Robots and Systems*, volume 3, pages 2478–2483 vol.3, 2002. doi: 10.1109/IRDS.2002.1041641.

[39] https://web.archive.org/web/20160722094926/http://asimo.honda.com/news/asimo-walks-the-red-carpet-for-robots-premiere/newsarticle_0031/.

[40] Olivier Stasse and Thomas Flayols. An overview of humanoid robots technologies. *Biomechanics of Anthropomorphic Systems*, pages 281–310, 2019.

[41] Nikolaos G Tsagarakis, Martin Sinclair, Francesco Becchi, Giorgio Metta, Giulio Sandini, and Darwin G Caldwell. Lower body design of theicub'a human-baby like crawling robot. In *2006 6th IEEE-RAS International Conference on Humanoid Robots*, pages 450–455. IEEE, 2006.

[42] Louis Hawley, Rémy Rahem, and Wael Suleiman. External force observer for small-and medium-sized humanoid robots. *International Journal of Humanoid Robotics*, 16(06):1950030, 2019.

[43] Jin'ichi Yamaguchi, Eiji Soga, Sadatoshi Inoue, and Atsuo Takanishi. Development of a bipedal humanoid robot-control method of whole body cooperative dynamic biped walking. In *Proceedings 1999 IEEE International Conference on Robotics and Automation (Cat. No. 99CH36288C)*, volume 1, pages 368–374. IEEE, 1999.

[44] Yu Ogura, Hiroyuki Aikawa, Kazushi Shimomura, Hideki Kondo, Akitoshi Morishima, Hun-ok Lim, and Atsuo Takanishi. Development of a new humanoid robot wabian-2. In *Proceedings 2006 IEEE International Conference on Robotics and Automation, 2006. ICRA 2006.*, pages 76–81. IEEE, 2006.

[45] Kenji Kaneko, Fumio Kanehiro, Shuuji Kajita, Kazuhiko Yokoyama, Kazuhiko Akachi, Toshikazu Kawasaki, Shigehiko Ota, and Takakatsu Isozumi. Design of prototype humanoid robotics platform for hrp. In *IEEE/RSJ International Conference on Intelligent Robots and Systems*, volume 3, pages 2431–2436. IEEE, 2002.

[46] Hirohisa Hirukawa, Fumio Kanehiro, Kenji Kaneko, Shuuji Kajita, Kiyoshi Fujiwara, Yoshihiro Kawai, Fumiaki Tomita, Shigeoki Hirai, Kazuo Tanie, Takakatsu Isozumi, et al. Humanoid robotics platforms developed in hrp. *Robotics and Autonomous Systems*, 48(4):165–175, 2004.

[47] Kenji Kaneko, Fumio Kanehiro, Mitsuharu Morisawa, Kazuhiko Akachi, Go Miyamori, Atsushi Hayashi, and Noriyuki Kanehira. Humanoid robot hrp-4-humanoid robotics platform with lightweight and slim body. In *2011 IEEE/RSJ International Conference on Intelligent Robots and Systems*, pages 4400–4407. IEEE, 2011.

[48] Oscar E Ramos, Nicolas Mansard, Olivier Stasse, Christophe Benazeth, Sovannara Hak, and Layale Saab. Dancing humanoid robots: Systematic use of osid to compute dynamically consistent movements following a motion capture pattern. *IEEE Robotics & Automation Magazine*, 22(4):16–26, 2015.

[49] Shuuji Kajita, Mitsuharu Morisawa, Kanako Miura, Shin'ichiro Nakaoka, Kensuke Harada, Kenji Kaneko, Fumio Kanehiro, and Kazuhito Yokoi. Biped walking stabilization based on linear inverted pendulum tracking. In *2010 IEEE/RSJ International Conference on Intelligent Robots and Systems*, pages 4489–4496. IEEE, 2010.

[50] Pierre-Brice Wieber. Viability and predictive control for safe locomotion. In *2008 IEEE/RSJ International Conference on Intelligent Robots and Systems*, pages 1103–1108. IEEE, 2008.

[51] Jonas Koenemann, Andrea Del Prete, Yuval Tassa, Emanuel Todorov, Olivier Stasse, Maren Bennewitz, and Nicolas Mansard. Whole-body model-predictive control applied to the hrp-2 humanoid. In *2015 IEEE/RSJ International Conference on Intelligent Robots and Systems (IROS)*, pages 3346–3351. IEEE, 2015.

[52] Kenji Kaneko, Mitsuharu Morisawa, Shuuji Kajita, Shin'ichiro Nakaoka, Takeshi Sakaguchi, Rafael Cisneros, and Fumio Kanehiro. Humanoid robot hrp-2kai—improvement of hrp-2 towards disaster response tasks. In *2015 IEEE-RAS 15th International Conference on Humanoid Robots (Humanoids)*, pages 132–139. IEEE, 2015.

[53] Shuuji Kajita, Mehdi Benallegue, Rafael Cisneros, Takeshi Sakaguchi, Shin'ichiro Nakaoka, Mitsuharu Morisawa, Hiroshi Kaminaga, Iori Kumagai, Kenji Kaneko, and Fumio Kanehiro. Biped gait control based on spatially quantized dynamics. In *2018 IEEE-RAS 18th International Conference on Humanoid Robots (Humanoids)*, pages 75–81. IEEE, 2018.

[54] Stéphane Caron, Abderrahmane Kheddar, and Olivier Tempier. Stair climbing stabilization of the hrp-4 humanoid robot using whole-body admittance control. In *2019 International Conference on Robotics and Automation (ICRA)*, pages 277–283, 2019. doi: 10.1109/ICRA.2019.8794348.

[55] Abderrahmane Kheddar, Stéphane Caron, Pierre Gergondet, Andrew Comport, Arnaud Tanguy, Christian Ott, Bernd Henze, George Mesesan, Johannes Englsberger, Máximo A Roa, et al. Humanoid robots in aircraft manufacturing: The airbus use cases. *IEEE Robotics & Automation Magazine*, 26(4):30–45, 2019.

[56] Ill-Woo Park, Jung-Yup Kim, Jungho Lee, and Jun-Ho Oh. Mechanical design of the humanoid robot platform, hubo. *Advanced Robotics*, 21(11):1305–1322, 2007.

[57] Sebastian Lohmeier, Thomas Buschmann, and Heinz Ulbrich. Humanoid robot lola. In *2009 IEEE International Conference on Robotics and Automation*, pages 775–780. IEEE, 2009.

[58] Koichi Nishiwaki, James Kuffner, Satoshi Kagami, Masayuki Inaba, and Hirochika Inoue. The experimental humanoid robot h7: a research platform for autonomous behaviour. *Philosophical Transactions of the Royal Society A: Mathematical, Physical and Engineering Sciences*, 365(1850):79–107, 2007.

[59] Giorgio Metta, Giulio Sandini, David Vernon, Lorenzo Natale, and Francesco Nori. The icub humanoid robot: an open platform for research in embodied cognition. In *Proceedings of the 8th workshop on performance metrics for intelligent systems*, pages 50–56, 2008.

[60] Woong Kwon, Hyun K Kim, Joong Kyung Park, Chang Hyun Roh, Jawoo Lee, Jaeho Park, Won-Kuk Kim, and Kyungshik Roh. Biped humanoid robot mahru iii. In *2007 7th IEEE-RAS International Conference on Humanoid Robots*, pages 583–588. IEEE, 2007.

[61] Ricardo Tellez, Francesco Ferro, Sergio Garcia, Esteban Gomez, Enric Jorge, Dario Mora, Daniel Pinyol, Joan Oliver, Oriol Torres, Jorge Velazquez, et al. Reem-b: An autonomous lightweight human-size humanoid robot. In *Humanoids 2008-8th IEEE-RAS International Conference on Humanoid Robots*, pages 462–468. IEEE, 2008.

[62] Ikuo Mizuuchi, Yuto Nakanishi, Yoshinao Sodeyama, Yuta Namiki, Tamaki Nishino, Naoya Muramatsu, Junichi Urata, Kazuo Hongo, Tomoaki Yoshikai, and Masayuki Inaba. An advanced musculoskeletal humanoid kojiro. In *2007 7th IEEE-RAS International Conference on Humanoid Robots*, pages 294–299. IEEE, 2007.

[63] Yuto Nakanishi, Yuki Asano, Toyotaka Kozuki, Hironori Mizoguchi, Yotaro Motegi, Masahiko Osada, Takuma Shirai, Junichi Urata, Kei Okada, and Masayuki Inaba. Design concept of detail musculoskeletal humanoid "kenshiro"-toward a real human body musculoskeletal simulator. In *2012 12th IEEE-RAS International Conference on Humanoid Robots (Humanoids 2012)*, pages 1–6. IEEE, 2012.

[64] Tomomichi Sugihara, Kou Yamamoto, and Yoshihiko Nakamura. Hardware design of high performance miniature anthropomorphic robots. *Robotics and Autonomous Systems*, 56(1):82–94, 2008.

[65] Fuminori Yamasaki, Tatsuya Matsui, Takahiro Miyashita, and Hiroaki Kitano. Pino the humanoid: A basic architecture. In *Robot Soccer World Cup*, pages 269–278. Springer, 2000.

[66] Kerstin S Haring, David Silvera-Tawil, Tomotaka Takahashi, Katsumi Watanabe, and Mari Velonaki. How people perceive different robot types: A direct comparison of an android, humanoid, and non-biomimetic robot. In *2016 8th international conference on knowledge and smart technology (kst)*, pages 265–270. IEEE, 2016.

[67] Takayuki Furuta, Tetsuo Tawara, Yu Okumura, Masaharu Shimizu, and Ken Tomiyama. Design and construction of a series of compact humanoid robots and development of biped walk control strategies. *Robotics and Autonomous Systems*, 37(2-3):81–100, 2001.

[68] Toru Ishida. Development of a small biped entertainment robot qrio. In *Micro-Nanomechatronics and Human Science, 2004 and The Fourth Symposium Micro-Nanomechatronics for Information-Based Society, 2004.*, pages 23–28. IEEE, 2004.

[69] Kenichiro Nagasaka, Yoshihiro Kuroki, Shinya Suzuki, Yoshihiro Itoh, and Jinichi Yamaguchi. Integrated motion control for walking, jumping and running on a small bipedal entertainment robot. In *IEEE International Conference on Robotics and Automation, 2004. Proceedings. ICRA'04. 2004*, volume 4, pages 3189–3194. IEEE, 2004.

[70] Andrew G Brooks and Ronald C Arkin. Behavioral overlays for non-verbal communication expression on a humanoid robot. *Autonomous robots*, 22(1):55–74, 2007.

[71] Sonia Chernova and Manuela Veloso. Teaching collaborative multi-robot tasks through demonstration. In *Humanoids 2008-8th IEEE-RAS International Conference on Humanoid Robots*, pages 385–390. IEEE, 2008.

[72] David Gouaillier, Vincent Hugel, Pierre Blazevic, Chris Kilner, Jérôme Monceaux, Pascal Lafourcade, Brice Marnier, Julien Serre, and Bruno Maisonnier. Mechatronic design of nao humanoid. In *2009 IEEE international conference on robotics and automation*, pages 769–774. IEEE, 2009.

[73] Seung-Joon Yi, Stephen McGill, Larry Vadakedathu, Qin He, Inyong Ha, Michael Rouleau, Dennis Hong, and Daniel D Lee. Modular low-cost humanoid platform for disaster response. In *2014 IEEE/RSJ International Conference on Intelligent Robots and Systems*, pages 965–972. IEEE, 2014.

[74] Yohei Kakiuchi, Kunio Kojima, Eisoku Kuroiwa, Shintaro Noda, Masaki Murooka, Iori Kumagai, Ryohei Ueda, Fumihito Sugai, Shunichi Nozawa, Kei Okada, et al. Development of humanoid robot system for disaster response through team nedo-jsk's approach to darpa robotics challenge finals. In *2015 IEEE-RAS 15th International Conference on Humanoid Robots (Humanoids)*, pages 805–810. IEEE, 2015.

[75] Kunio Kojima, Tatsuhi Karasawa, Toyotaka Kozuki, Eisoku Kuroiwa, Sou Yukizaki, Satoshi Iwaishi, Tatsuya Ishikawa, Ryo Koyama, Shintaro Noda, Fumihito Sugai, et al. Development of life-sized high-power humanoid robot jaxon for real-world use. In *2015 IEEE-RAS 15th International Conference on Humanoid Robots (Humanoids)*, pages 838–843. IEEE, 2015.

[76] Nikolaos G Tsagarakis, Darwin G Caldwell, Francesca Negrello, Wooseok Choi, Lorenzo Baccelliere, Vo-Gia Loc, J Noorden, Luca Muratore, Alessio Margan, Alberto Cardellino, et al. Walk-man: A high-performance humanoid platform for realistic environments. *Journal of Field Robotics*, 34(7):1225–1259, 2017.

[77] Sisir Karumanchi, Kyle Edelberg, Ian Baldwin, Jeremy Nash, Jason Reid, Charles Bergh, John Leichty, Kalind Carpenter, Matthew Shekels, Matthew Gildner, et al. Team robosimian: semi-autonomous mobile manipulation at the 2015 darpa robotics challenge finals. *Journal of Field Robotics*, 34(2):305–332, 2017.

[78] Anthony Stentz, Herman Herman, Alonzo Kelly, Eric Meyhofer, G Clark Haynes, David Stager, Brian Zajac, J Andrew Bagnell, Jordan Brindza, Christopher Dellin, et al. Chimp, the cmu highly intelligent mobile platform. *Journal of Field Robotics*, 32(2):209–228, 2015.

[79] G Clark Haynes, David Stager, Anthony Stentz, J Michael Vande Weghe, Brian Zajac, Herman Herman, Alonzo Kelly, Eric Meyhofer, Dean Anderson, Dane Bennington, et al. Developing a robust disaster response robot: Chimp and the robotics challenge. *Journal of Field Robotics*, 34(2):281–304, 2017.

[80] Hyoin Bae, Inho Lee, Taejin Jung, and Jun-Ho Oh. Walking-wheeling dual mode strategy for humanoid robot, drc-hubo+. In *2016 IEEE/RSJ International Conference on Intelligent Robots and Systems (IROS)*, pages 1342–1348. IEEE, 2016.

[81] Taejin Jung, Jeongsoo Lim, Hyoin Bae, Kang Kyu Lee, Hyun-Min Joe, and Jun-Ho Oh. Development of the humanoid disaster response platform drc-hubo+. *IEEE Transactions on Robotics*, 34(1):1–17, 2018.

[82] Zhibin Li, Nikos G Tsagarakis, and Darwin G Caldwell. Walking trajectory generation for humanoid robots with compliant joints: Experimentation with coman humanoid. In *2012 IEEE International Conference on Robotics and Automation*, pages 836–841. IEEE, 2012.

[83] Bernd Henze, Alexander Werner, Maximo A Roa, Gianluca Garofalo, Johannes Englsberger, and Christian Ott. Control applications of toro—a torque controlled humanoid robot. In *2014 IEEE-RAS International Conference on Humanoid Robots*, pages 841–841. IEEE, 2014.

[84] Johannes Englsberger, Alexander Werner, Christian Ott, Bernd Henze, Maximo A Roa, Gianluca Garofalo, Robert Burger, Alexander Beyer, Oliver Eiberger, Korbinian Schmid, et al. Overview of the torque-controlled humanoid robot toro. In *2014 IEEE-RAS International Conference on Humanoid Robots*, pages 916–923. IEEE, 2014.

[85] Gerd Hirzinger, Norbert Sporer, Alin Albu-Schaffer, M Hahnle, Rainer Krenn, Antonio Pascucci, and Markus Schedl. Dlr's torque-controlled light weight robot iii-are we reaching the technological limits now? In *Proceedings 2002 IEEE International Conference on Robotics and Automation (Cat. No. 02CH37292)*, volume 2, pages 1710–1716. IEEE, 2002.

[86] Olivier Stasse, Thomas Flayols, Rohan Budhiraja, Kevin Giraud-Esclasse, Justin Carpentier, Joseph Mirabel, Andrea Del Prete, Philippe Souères, Nicolas Mansard, Florent Lamiraux, et al. Talos: A new humanoid research platform targeted for industrial applications. In *2017 IEEE-RAS 17th International Conference on Humanoid Robotics (Humanoids)*, pages 689–695. IEEE, 2017.

[87] Sang-Ho Hyon, Daisuke Suewaka, Yuki Torii, and Narifumi Oku. Design and experimental evaluation of a fast torque-controlled hydraulic humanoid robot. *IEEE/ASME Transactions on Mechatronics*, 22(2):623–634, 2016.

[88] Matthieu Lapeyre, Pierre Rouanet, Jonathan Grizou, Steve Nguyen, Fabien Depraetre, Alexandre Le Falher, and Pierre-Yves Oudeyer. Poppy project: open-source fabrication of 3d printed humanoid robot for science, education and art. In *Digital Intelligence 2014*, page 6, 2014.

[89] Hosik Chae, Min Sung Ahn, Donghun Noh, Hyunwoo Nam, and Dennis W Hong. Ballu2: A safe and affordable buoyancy assisted biped. *Frontiers in Robotics and AI*, page 290, 2021.

[90] Nicolaus A Radford, Philip Strawser, Kimberly Hambuchen, Joshua S Mehling, William K Verdeyen, A Stuart Donnan, James Holley, Jairo Sanchez, Vienny Nguyen, Lyndon Bridgwater, et al. Valkyrie: Nasa's first bipedal humanoid robot. *Journal of Field Robotics*, 32(3):397–419, 2015.

[91] Iori Kumagai, Mitsuharu Morisawa, Takeshi Sakaguchi, Shin'ichiro Nakaoka, Kenji Kaneko, Hiroshi Kaminaga, Shuuji Kajita, Mehdi Benallegue, Rafael Cisneros,

and Fumio Kanehiro. Toward industrialization of humanoid robots: Autonomous plasterboard installation to improve safety and efficiency. *IEEE Robotics & Automation Magazine*, 26(4):20–29, 2019.

[92] Christopher G Atkeson, Benzun P Wisely Babu, Nandan Banerjee, Dmitry Berenson, Christoper P Bove, Xiongyi Cui, Mathew DeDonato, Ruixiang Du, Siyuan Feng, Perry Franklin, et al. No falls, no resets: Reliable humanoid behavior in the darpa robotics challenge. In *2015 IEEE-RAS 15th International Conference on Humanoid Robots (Humanoids)*, pages 623–630. IEEE, 2015.

[93] Olivier Stasse, Kevin Giraud-Esclasse, Edouard Brousse, Maximilien Naveau, Rémi Régnier, Guillaume Avrin, and Philippe Souères. Benchmarking the hrp-2 humanoid robot during locomotion. *Frontiers in Robotics and AI*, 5:122, 2018.

[94] N Ramuzat, G Buondonno, S Boria, and Olivier Stasse. Comparison of position and torque whole-body control schemes on the humanoid robot talos. In *2021 20th International Conference on Advanced Robotics (ICAR)*, pages 785–792. IEEE, 2021.

[95] Noelie Ramuzat, Olivier Stasse, and Sebastien Boria. Benchmarking whole-body controllers on the talos humanoid robot. *Frontiers in Robotics and AI*, 9, 2022.

[96] Kenji Kaneko, Hiroshi Kaminaga, Takeshi Sakaguchi, Shuuji Kajita, Mitsuharu Morisawa, Iori Kumagai, and Fumio Kanehiro. Humanoid robot hrp-5p: An electrically actuated humanoid robot with high-power and wide-range joints. *IEEE Robotics and Automation Letters*, 4(2):1431–1438, 2019.

[97] Taylor Apgar, Patrick Clary, Kevin Green, Alan Fern, and Jonathan W Hurst. Fast online trajectory optimization for the bipedal robot cassie. In *Robotics: Science and Systems*, volume 101, page 14, 2018.

[98] Jacob Reher, Wen-Loong Ma, and Aaron D Ames. Dynamic walking with compliance on a cassie bipedal robot. In *2019 18th European Control Conference (ECC)*, pages 2589–2595. IEEE, 2019.

[99] Zhongyu Li, Xuxin Cheng, Xue Bin Peng, Pieter Abbeel, Sergey Levine, Glen Berseth, and Koushil Sreenath. Reinforcement learning for robust parameterized locomotion control of bipedal robots. In *2021 IEEE International Conference on Robotics and Automation (ICRA)*, pages 2811–2817, 2021. doi: 10.1109/ICRA48506.2021.9560769.

[100] Ambarish Goswami and Prahlad Vadakkepat. *Humanoid robotics: a reference.* Springer, 2019.

[101] https://spectrum.ieee.org/tesla-optimus-robot.

[102] Matthew Chignoli, Donghyun Kim, Elijah Stanger-Jones, and Sangbae Kim. The mit humanoid robot: Design, motion planning, and control for acrobatic behaviors. *arXiv preprint arXiv:2104.09025*, 2021.

[103] https://pal-robotics.com/robots/kangaroo/. 2021.

[104] Craig Causer. Disney tech: Immersive storytelling through innovation. *IEEE Potentials*, 38(5):10–18, 2019. doi: 10.1109/MPOT.2019.2919851.

[105] https://www.engineeredarts.co.uk/. 2021.

[106] Miomir Vukobratović and Branislav Borovac. Zero-moment point—thirty five years of its life. *International journal of humanoid robotics*, 1(01):157–173, 2004.

[107] P.-B. Wieber, R. Tedrake, and S. Kuindersma. Modeling and control of legged robots. In *Handbook of Robotics*, pages 1203–1234. Springer, 2016.

[108] J Furusho and M Masubuchi. A theoretically motivated reduced order model for the control of dynamic biped locomotion. 1987.

[109] David E Orin, Ambarish Goswami, and Sung-Hee Lee. Centroidal dynamics of a humanoid robot. *Autonomous robots*, 35(2):161–176, 2013.

[110] Shuuji Kajita, Fumio Kanehiro, Kenji Kaneko, Kazuhito Yokoi, and Hirohisa Hirukawa. The 3d linear inverted pendulum mode: A simple modeling for a biped walking pattern generation. In *Proceedings 2001 IEEE/RSJ International Conference on Intelligent Robots and Systems. Expanding the Societal Role of Robotics in the the Next Millennium (Cat. No. 01CH37180)*, volume 1, pages 239–246. IEEE, 2001.

[111] Tomomichi Sugihara, Yoshihiko Nakamura, and Hirochika Inoue. Real-time humanoid motion generation through zmp manipulation based on inverted pendulum control. In *Proceedings 2002 IEEE International Conference on Robotics and Automation (Cat. No. 02CH37292)*, volume 2, pages 1404–1409. IEEE, 2002.

[112] J. Pratt, J. Carff, S. Drakunov, and A. Goswami. Capture point: A step toward humanoid push recovery. In *6th IEEE-RAS Int. Conf. on Humanoid Robots*, pages 200–207, 2006.

[113] Twan Koolen, Tomas De Boer, John Rebula, Ambarish Goswami, and Jerry Pratt. Capturability-based analysis and control of legged locomotion, part 1: Theory and application to three simple gait models. *The international journal of robotics research*, 31(9):1094–1113, 2012.

[114] T. Takenaka, T. Matsumoto, and T. Yoshiike. Real time motion generation and control for biped robot - 1st report: Walking gait pattern generation. In *2009 Int. Conf. on Intelligent Robots and Systems*, pages 1084–1091, 2009.

[115] Johannes Englsberger, Christian Ott, Máximo A Roa, Alin Albu-Schäffer, and Gerhard Hirzinger. Bipedal walking control based on capture point dynamics. In *2011 IEEE/RSJ International Conference on Intelligent Robots and Systems*, pages 4420–4427. IEEE, 2011.

[116] Manuel Krause, Johannes Englsberger, Pierre-Brice Wieber, and Christian Ott. Stabilization of the capture point dynamics for bipedal walking based on model predictive control. *IFAC Proceedings Volumes*, 45(22):165–171, 2012.

[117] Michael A Hopkins, Dennis W Hong, and Alexander Leonessa. Humanoid locomotion on uneven terrain using the time-varying divergent component of motion. In *2014 ieee-ras international conference on humanoid robots*, pages 266–272. IEEE, 2014.

[118] Marko B Popovic, Ambarish Goswami, and Hugh Herr. Ground reference points in legged locomotion: Definitions, biological trajectories and control implications. *The international journal of robotics research*, 24(12):1013–1032, 2005.

[119] R. J. Griffin, G. Wiedebach, S. Bertrand, A. Leonessa, and J. Pratt. Walking stabilization using step timing and location adjustment on the humanoid robot, Atlas. In *IEEE/RSJ Int. Conf. on Intelligent Robots and Systems*, pages 667–673, 2017.

[120] Eduardo F Camacho and Carlos Bordons Alba. *Model predictive control*. Springer science & business media, 2013.

[121] Pierre-Brice Wieber. Trajectory free linear model predictive control for stable walking in the presence of strong perturbations. In *6th IEEE-RAS Int. Conf. on Humanoid Robots*, pages 137–142, 2006.

[122] Andrei Herdt, Holger Diedam, Pierre-Brice Wieber, Dimitar Dimitrov, Katja Mombaur, and Moritz Diehl. Online walking motion generation with automatic footstep placement. *Advanced Robotics*, 24(5-6):719–737, 2010.

[123] Alexander Sherikov, Dimitar Dimitrov, and Pierre-Brice Wieber. Whole body motion controller with long-term balance constraints. In *2014 IEEE-RAS International Conference on Humanoid Robots*, pages 444–450. IEEE, 2014.

[124] Matteo Ciocca, Pierre-Brice Wieber, and Thierry Fraichard. Strong recursive feasibility in model predictive control of biped walking. In *2017 IEEE-RAS 17th International Conference on Humanoid Robotics (Humanoids)*, pages 730–735. IEEE, 2017.

[125] Nicola Scianca, Marco Cognetti, Daniele De Simone, Leonardo Lanari, and Giuseppe Oriolo. Intrinsically stable MPC for humanoid gait generation. In *16th IEEE-RAS Int. Conf. on Humanoid Robots*, pages 101–108, 2016.

[126] Leonardo Lanari, Seth Hutchinson, and Luca Marchionni. Boundedness issues in planning of locomotion trajectories for biped robots. In *14th IEEE-RAS Int. Conf. on Humanoid Robots*, pages 951–958, 2014.

[127] Nicola Scianca, Daniele De Simone, Leonardo Lanari, and Giuseppe Oriolo. MPC for humanoid gait generation: Stability and feasibility. *IEEE Transactions on Robotics*, 36(4):1171–1188, 2020.

[128] Robin Deits and Russ Tedrake. Footstep planning on uneven terrain with mixed-integer convex optimization. In *2014 IEEE-RAS Int. Conf. on Humanoid Robots*, pages 279–286, 2014.

[129] Scott Kuindersma, Robin Deits, Maurice Fallon, Andrés Valenzuela, Hongkai Dai, Frank Permenter, Twan Koolen, Pat Marion, and Russ Tedrake. Optimization-based locomotion planning, estimation, and control design for the atlas humanoid robot. *Autonomous robots*, 40(3):429–455, 2016.

[130] Justin Carpentier, Steve Tonneau, Maximilien Naveau, Olivier Stasse, and Nicolas Mansard. A versatile and efficient pattern generator for generalized legged locomotion. In *2016 IEEE International Conference on Robotics and Automation (ICRA)*, pages 3555–3561. IEEE, 2016.

[131] Justin Carpentier and Nicolas Mansard. Multicontact locomotion of legged robots. *IEEE Transactions on Robotics*, 34(6):1441–1460, 2018. doi: 10.1109/TRO.2018. 2862902.

[132] Giulio Romualdi, Stefano Dafarra, Giuseppe L'Erario, Ines Sorrentino, Silvio Traversaro, and Daniele Pucci. Online non-linear centroidal mpc for humanoid robot locomotion with step adjustment. In *2022 International Conference on Robotics and Automation (ICRA)*, pages 10412–10419. IEEE, 2022.

[133] Alexander W Winkler, C Dario Bellicoso, Marco Hutter, and Jonas Buchli. Gait and trajectory optimization for legged systems through phase-based end-effector parameterization. *IEEE Robotics and Automation Letters*, 3(3):1560–1567, 2018.

[134] Yanran Ding, Abhishek Pandala, Chuanzheng Li, Young-Ha Shin, and Hae-Won Park. Representation-free model predictive control for dynamic motions in quadrupeds. *IEEE Transactions on Robotics*, 37(4):1154–1171, 2021.

[135] Junjie Shen and Dennis Hong. Convex model predictive control of single rigid body model on so (3) for versatile dynamic legged motions. In *2022 IEEE International Conference on Robotics and Automation (ICRA)*, 2022.

[136] Wanchao Chi, Xinyang Jiang, and Yu Zheng. A linearization of centroidal dynamics for the model-predictive control of quadruped robots. In *2022 International Conference on Robotics and Automation (ICRA)*, pages 4656–4663. IEEE, 2022.

[137] Yuval Tassa, Tom Erez, and Emanuel Todorov. Synthesis and stabilization of complex behaviors through online trajectory optimization. In *2012 IEEE/RSJ International Conference on Intelligent Robots and Systems*, pages 4906–4913. IEEE, 2012.

[138] Justin Carpentier, Guilhem Saurel, Gabriele Buondonno, Joseph Mirabel, Florent Lamiraux, Olivier Stasse, and Nicolas Mansard. The pinocchio c++ library: A fast and flexible implementation of rigid body dynamics algorithms and their analytical derivatives. In *2019 IEEE/SICE International Symposium on System Integration (SII)*, pages 614–619. IEEE, 2019.

[139] Carlos Mastalli, Rohan Budhiraja, Wolfgang Merkt, Guilhem Saurel, Bilal Hammoud, Maximilien Naveau, Justin Carpentier, Ludovic Righetti, Sethu Vijayakumar, and Nicolas Mansard. Crocoddyl: An efficient and versatile framework for multi-contact optimal control. In *2020 IEEE International Conference on Robotics and Automation (ICRA)*, pages 2536–2542. IEEE, 2020.

[140] Manuel Y Galliker, Noel Csomay-Shanklin, Ruben Grandia, Andrew J Taylor, Farbod Farshidian, Marco Hutter, and Aaron D Ames. Bipedal locomotion with nonlinear model predictive control: Online gait generation using whole-body dynamics. *arXiv preprint arXiv:2203.07429*, 2022.

[141] Ewen Dantec, Rohan Budhiraja, Adria Roig, Teguh Lembono, Guilhem Saurel, Olivier Stasse, Pierre Fernbach, Steve Tonneau, Sethu Vijayakumar, Sylvain Calinon, Michel Taix, and Nicolas Mansard. Whole body model predictive control with a memory of motion: Experiments on a torque-controlled talos. In *2021 IEEE International Conference on Robotics and Automation (ICRA)*, pages 8202–8208, 2021. doi: 10.1109/ICRA48506.2021.9560742.

[142] Ewen Louis Dantec, Maximilien Naveau, Pierre Fernbach, Nahuel Villa, Guilhem Saurel, Olivier Stasse, Michel Taïx, and Nicolas Mansard. Whole-body model predictive control for biped locomotion on a torque-controlled humanoid robot. 2022.

[143] Jean-Pierre Sleiman, Farbod Farshidian, Maria Vittoria Minniti, and Marco Hutter. A unified mpc framework for whole-body dynamic locomotion and manipulation. *IEEE Robotics and Automation Letters*, 6(3):4688–4695, 2021. doi: 10.1109/LRA.2021.3068908.

[144] Maria Vittoria Minniti, Farbod Farshidian, Ruben Grandia, and Marco Hutter. Whole-body mpc for a dynamically stable mobile manipulator. *IEEE Robotics and Automation Letters*, 4(4):3687–3694, 2019. doi: 10.1109/LRA.2019.2927955.

[145] Marco Kanneworff, Tommaso Belvedere, Nicola Scianca, Filippo M Smaldone, Leonardo Lanari, and Giuseppe Oriolo. Task-oriented generation of stable motions for wheeled inverted pendulum robots. 2022.

[146] L. Chisci, J. A. Rossiter, and G. Zappa. Systems with persistent disturbances: predictive control with restricted constraints. *Automatica*, 37(7):1019–1028, 2001.

[147] D.Q. Mayne, M.M. Seron, and Sasa V. Raković. Robust model predictive control of constrained linear system with bounded disturbances. *Automatica*, 41:219–224, 2005. doi: 10.1016/j.automatica.2004.08.019.

[148] Gabriele Pannocchia, James B. Rawlings, and Stephen J. Wright. Conditions under which suboptimal nonlinear MPC is inherently robust. *Systems & Control Letters*, 60:747–755, 2011. doi: 10.1016/j.sysconle.2011.05.013.

[149] E. C. Kerrigan. *Robust Constraint Satisfaction: Invariant Sets and Predictive Control*. PhD thesis, Department of Engineering - University of Cambridge, 2000.

[150] S Raković and D.Q. Mayne. A simple tube controller for efficient robust model predictive control of constrained linear discrete time systems subject to bounded disturbances. *IFAC Proceedings Volumes (IFAC-PapersOnline)*, 16, 01 2005.

[151] D. Limon, I. Alvarado, and Teodoro Alamo. Robust tube-based MPC for tracking of constrained linear systems with additive disturbances. *Journal of Process Control*, 20:248–260, 03 2010. doi: 10.1016/j.jprocont.2009.11.007.

[152] Ahmad Gazar, Majid Khadiv, Andrea Del Prete, and Ludovic Righetti. Stochastic and robust MPC for bipedal locomotion: A comparative study on robustness and performance. *arXiv preprint arXiv:2005.07555*, 2020.

[153] Nahuel Villa, Pierre Fernbach, Nicolas Mansard, and Olivier Stasse. Addressing flexibility in biped locomotion with robust control and closed-loop model-predictive control. In *Humanoids*, 2022.

[154] B. J. Stephens. State estimation for force-controlled humanoid balance using simple models in the presence of modeling error. In *IEEE Int. Conf. on Robotics and Automation*, pages 3994–3999, 2011.

[155] Kenji Kaneko, Fumio Kanehiro, Mitsuharu Morisawa, Eiichi Yoshida, and Jean-Paul Laumond. Disturbance observer that estimates external force acting on humanoid robots. In *12th IEEE International Workshop on Advanced Motion Control (AMC)*, pages 1–6, 2012.

[156] X Xinjilefu, Siyuan Feng, and Christopher G Atkeson. Center of mass estimator for humanoids and its application in modelling error compensation, fall detection and prevention. In *2015 IEEE-RAS 15th International Conference on Humanoid Robots (Humanoids)*, pages 67–73. IEEE, 2015.

[157] Tommaso Mattioli and Marilena Vendittelli. Interaction force reconstruction for humanoid robots. *IEEE Robotics and Automation Letters*, 2(1):282–289, 2016.

[158] L. Hawley and W. Suleiman. External force observer for medium-sized humanoid robots. In *2016 IEEE-RAS Int. Conf. on Humanoid Robots*, pages 366–371, Nov 2016. doi: 10.1109/HUMANOIDS.2016.7803302.

[159] Louis Hawley, Rémy Rahem, and Wael Suleiman. Kalman filter based observer for an external force applied to medium-sized humanoid robots. In *IEEE/RSJ Int. Conf. on Intelligent Robots and Systems*, pages 1204–1211, 2018.

[160] Stefan Czarnetzki, S′oren Kerner, and Oliver Urbann. Observer-based dynamic walking control for biped robots. *Robotics and Autonomous Systems*, 57(8): 839–845, 2009.

[161] Robert J Griffin, Alexander Leonessa, and Alan Asbeck. Disturbance compensation and step optimization for push recovery. In *IEEE/RSJ Int. Conf. on Intelligent Robots and Systems*, pages 5385–5390, 2016.

[162] J. Englsberger, G. Mesesan, and C. Ott. Smooth trajectory generation and push-recovery based on divergent component of motion. In *IEEE/RSJ Int. Conf. on Intelligent Robots and Systems*, pages 4560–4567, 2017.

[163] Don Joven Agravante, Alexander Sherikov, Pierre-Brice Wieber, Andrea Cherubini, and Abderrahmane Kheddar. Walking pattern generators designed for physical collaboration. In *IEEE Int. Conf. on Robotics and Automation*, pages 1573–1578, 2016.

[164] Don Joven Agravante, Andrea Cherubini, Alexander Sherikov, Pierre-Brice Wieber, and Abderrahmane Kheddar. Human-humanoid collaborative carrying. *IEEE Transactions on Robotics*, 35(4):833–846, 2019.

[165] Jun Yang, Shihua Li, Xisong Chen, and Qi Li. Disturbance rejection of ball mill grinding circuits using dob and mpc. *Powder Technology*, 198(2):219–228, 2010.

[166] Jun Yang, Wei Xing Zheng, Shihua Li, Bin Wu, and Ming Cheng. Design of a prediction-accuracy-enhanced continuous-time mpc for disturbed systems via a disturbance observer. *IEEE Transactions on Industrial Electronics*, 62(9): 5807–5816, 2015.

[167] Xing Fang and Wen-Hua Chen. Model predictive control with preview: Recursive feasibility and stability. *IEEE Control Systems Letters*, 2022.

[168] Mohammad Hasan Yeganegi, Majid Khadiv, Andrea Del Prete, S. Ali A. Moosavian, and Ludovic Righetti. Robust walking based on mpc with viability guarantees. *IEEE Transactions on Robotics*, pages 1–16, 2021. doi: 10.1109/TRO.2021.3127388.

[169] Przemyslaw Kryczka, Petar Kormushev, Nikos Tsagarakis, and Darwin G Caldwell. Online regeneration of bipedal walking gait optimizing footstep placement and timing. In *IEEE/RSJ Int. Conf. on Intelligent Robots and Systems*, pages 3352–3357, 2015.

[170] N. Bohórquez and P. Wieber. Adaptive step duration in biped walking: A robust approach to nonlinear constraints. In *2017 IEEE-RAS 17th International Conference on Humanoid Robotics (Humanoids)*, pages 724–729, Nov 2017.

[171] S. Caron and Q. Pham. When to make a step? tackling the timing problem in multi-contact locomotion by TOPP-MPC. In *2017 IEEE-RAS 17th International Conference on Humanoid Robotics (Humanoids)*, pages 522–528, Nov 2017.

[172] Yuta Kojio, Yuki Omori, Kunio Kojima, Fumihito Sugai, Yohei Kakiuchi, Kei Okada, and Masayuki Inaba. Footstep modification including step time and angular momentum under disturbances on sparse footholds. *IEEE Robotics and Automation Letters*, 5(3):4907–4914, 2020.

[173] Aurelien Ibanez, Philippe Bidaud, and Vincent Padois. Emergence of humanoid walking behaviors from mixed-integer model predictive control. In *IEEE/RSJ Int. Conf. on Intelligent Robots and Systems*, pages 4014–4021, 2014.

[174] M. R. O. A. Maximo, C. H. C. Ribeiro, and R. J. M. Afonso. Mixed-integer programming for automatic walking step duration. In *IEEE/RSJ Int. Conf. on Intelligent Robots and Systems*, pages 5399–5404, 2016.

[175] M. Khadiv, A. Herzog, S. A. A. Moosavian, and L. Righetti. Step timing adjustment: A step toward generating robust gaits. In *2016 IEEE-RAS 16th International Conference on Humanoid Robots (Humanoids)*, pages 35–42, Nov 2016.

[176] M. Khadiv, A. Herzog, S. A. A. Moosavian, and L. Righetti. Walking control based on step timing adaptation. *IEEE Transactions on Robotics*, pages 1–15, 2020.

[177] Milad Shafiee, Giulio Romualdi, Stefano Dafarra, Francisco Javier Andrade Chavez, and Daniele Pucci. Online DCM trajectory generation for push recovery of torque-controlled humanoid robots. In *19th IEEE-RAS Int. Conf. on Humanoid Robots*, 2019.

[178] Hyobin Jeong, Inho Lee, Jaesung Oh, Kang Kyu Lee, and Jun-Ho Oh. A robust walking controller based on online optimization of ankle, hip, and stepping strategies. *IEEE Transactions on Robotics*, 35(6):1367–1386, 2019.

[179] Jiatao Ding, Chengxu Zhou, Songyan Xin, Xiaohui Xiao, and Nikolaos G Tsagarakis. Nonlinear model predictive control for robust bipedal locomotion: exploring angular momentum and com height changes. *Advanced Robotics*, 35(18): 1079–1097, 2021.

[180] Andrei Herdt, Nicolas Perrin, and Pierre-Brice Wieber. Walking without thinking about it. In *2010 IEEE/RSJ Int. Conf. on Intelligent Robots and Systems*, pages 190–195, 2010.

[181] Angelo Bratta, Romeo Orsolino, Michele Focchi, Victor Barasuol, Giovanni Gerardo Muscolo, and Claudio Semini. On the hardware feasibility of nonlinear trajectory optimization for legged locomotion based on a simplified dynamics. In *2020 IEEE Int. Conf. on Robotics and Automation*, pages 1417–1423, 2020.

[182] Zhaoyuan Gu, Nathan Boyd, and Ye Zhao. Reactive locomotion decision-making and robust motion planning for real-time perturbation recovery. *arXiv preprint arXiv:2110.03037*, 2021.

[183] Robin Deits and Russ Tedrake. Computing large convex regions of obstacle-free space through semidefinite programming. In *Algorithmic foundations of robotics XI*, pages 109–124. Springer, 2015.

[184] Bernardo Aceituno-Cabezas, Carlos Mastalli, Hongkai Dai, Michele Focchi, Andreea Radulescu, Darwin G. Caldwell, José Cappelletto, Juan C. Grieco, Gerardo Fernández-López, and Claudio Semini. Simultaneous contact, gait, and motion planning for robust multilegged locomotion via mixed-integer convex optimization. *IEEE Robotics and Automation Letters*, 3(3):2531–2538, 2018. doi: 10.1109/LRA.2017.2779821.

[185] Joel Chestnutt, Manfred Lau, German Cheung, James Kuffner, Jessica Hodgins, and Takeo Kanade. Footstep planning for the honda asimo humanoid. In *Proceedings of the 2005 IEEE international conference on robotics and automation*, pages 629–634. IEEE, 2005.

[186] Armin Hornung, Andrew Dornbush, Maxim Likhachev, and Maren Bennewitz. Anytime search-based footstep planning with suboptimality bounds. In *2012 12th IEEE-RAS International Conference on Humanoid Robots (Humanoids 2012)*, pages 674–679. IEEE, 2012.

[187] Paolo Ferrari, Nicola Scianca, Leonardo Lanari, and Giuseppe Oriolo. An integrated motion planner/controller for humanoid robots on uneven ground. In *18th European Control Conf.*, pages 1598–1603, 2019.

[188] Daniele De Simone, Nicola Scianca, Paolo Ferrari, Leonardo Lanari, and Giuseppe Oriolo. MPC-based humanoid pursuit-evasion in the presence of obstacles. In *2017 IEEE/RSJ Int. Conf. on Intelligent Robots and Systems*, pages 5245–5250, 2017.

[189] Twan Koolen, Michael Posa, and Russ Tedrake. Balance control using center of mass height variation: Limitations imposed by unilateral contact. In *2016 IEEE-RAS Int. Conf. on Humanoid Robots*, pages 8–15, 2016.

[190] Andrei Herdt, Nicolas Perrin, and Pierre-Brice Wieber. Lmpc based online generation of more efficient walking motions. In *2012 12th IEEE-RAS International Conference on Humanoid Robots (Humanoids 2012)*, pages 390–395. IEEE, 2012.

[191] Kai Hu, Christian Ott, and Dongheui Lee. Online human walking imitation in task and joint space based on quadratic programming. In *2014 IEEE International Conference on Robotics and Automation (ICRA)*, pages 3458–3464. IEEE, 2014.

[192] Camille Brasseur, Alexander Sherikov, Cyrille Collette, Dimitar Dimitrov, and Pierre-Brice Wieber. A robust linear mpc approach to online generation of 3d biped walking motion. In *2015 IEEE-RAS 15th International Conference on Humanoid Robots (Humanoids)*, pages 595–601. IEEE, 2015.

[193] Johannes Englsberger, Christian Ott, and Alin Albu-Schäffer. Three-dimensional bipedal walking control using divergent component of motion. In *2013 IEEE/RSJ International Conference on Intelligent Robots and Systems*, pages 2600–2607. IEEE, 2013.

[194] Alessio Zamparelli, Nicola Scianca, Leonardo Lanari, and Giuseppe Oriolo. Humanoid gait generation on uneven ground using intrinsically stable mpc. *IFAC-PapersOnLine*, 51(22):393–398, 2018.

[195] Michael A Hopkins, Dennis W Hong, and Alexander Leonessa. Humanoid locomotion on uneven terrain using the time-varying divergent component of motion. In *2014 ieee-ras international conference on humanoid robots*, pages 266–272. IEEE, 2014.

[196] Shenggao Li, Hua Chen, Wei Zhang, and Patrick M Wensing. Quadruped robot hopping on two legs. In *IEEE/RSJ International Conference on Intelligent Robots and Systems (IROS)*, pages 7448–7455. IEEE, 2021.

[197] S. Caron, A. Escande, L. Lanari, and B. Mallein. Capturability-based pattern generation for walking with variable height. *IEEE Transactions on Robotics*, pages 1–20, 2019. doi: `10.1109/TRO.2019.2923971`.

[198] Camille Brasseur, Alexander Sherikov, Cyrille Collette, Dimitar Dimitrov, and Pierre-Brice Wieber. A robust linear mpc approach to online generation of 3d biped walking motion. In *2015 IEEE-RAS 15th International Conference on Humanoid Robots (Humanoids)*, pages 595–601. IEEE, 2015.

[199] Patrick M Wensing and David E Orin. High-speed humanoid running through control with a 3d-slip model. In *2013 IEEE/RSJ International Conference on Intelligent Robots and Systems*, pages 5134–5140. IEEE, 2013.

[200] Gorkem Secer and Uluc Saranli. Control of planar spring–mass running through virtual tuning of radial leg damping. *IEEE Transactions on Robotics*, 34(5): 1370–1383, 2018.

[201] Gorkem Secer and Ali Levent Cinar. A momentum-based foot placement strategy for stable postural control of robotic spring-mass running with point feet. *Proceedings of the 2020 IEEE International Conference on Intelligent Robots and Systems (IROS) Las Vegas, NV, USA (Virtual)*, 2020.

[202] Reinhard Blickhan. The spring-mass model for running and hopping. *Journal of biomechanics*, 22(11-12):1217–1227, 1989.

[203] Tom F Novacheck. The biomechanics of running. *Gait & posture*, 7(1):77–95, 1998.

[204] Behnam Dadashzadeh, Hamid Reza Vejdani, and Jonathan Hurst. From template to anchor: A novel control strategy for spring-mass running of bipedal robots. In *2014 IEEE/RSJ International Conference on Intelligent Robots and Systems*, pages 2566–2571. IEEE, 2014.

[205] Xiaobin Xiong and Aaron D Ames. Bipedal hopping: Reduced-order model embedding via optimization-based control. In *2018 IEEE/RSJ Int. Conf. on Intelligent Robots and Systems*, pages 3821–3828, 2018.

[206] Johannes Englsberger, Paweł Kozłowski, Christian Ott, and Alin Albu-Schäffer. Biologically inspired deadbeat control for running: from human analysis to humanoid control and back. *IEEE Transactions on Robotics*, 32(4):854–867, 2016.

[207] Shuuji Kajita, Takashi Nagasaki, Kenji Kaneko, and Hirohisa Hirukawa. Zmp-based biped running control. *IEEE robotics & automation magazine*, 14(2):63–72, 2007.

[208] Toru Takenaka, Takashi Matsumoto, Takahide Yoshiike, and Shinya Shirokura. Real time motion generation and control for biped robot-2 nd report: Running gait pattern generation. In *2009 IEEE/RSJ International Conference on Intelligent Robots and Systems*, pages 1092–1099. IEEE, 2009.

[209] Ryosuke Tajima, Daisaku Honda, and Keisuke Suga. Fast running experiments involving a humanoid robot. In *2009 IEEE International Conference on Robotics and Automation*, pages 1571–1576. IEEE, 2009.

[210] Donghyun Ahn and Baekkyu Cho. Online jumping motion generation via model predictive control. *IEEE Transactions on Industrial Electronics*, 2021.

[211] Tomomichi Sugihara, Kenta Imanishi, Takanobu Yamamoto, and Stéphane Caron. 3D biped locomotion control including seamless transition between walking and running via 3D ZMP manipulation. In *2021 IEEE Int. Conf. on Robotics and Automation*, pages 6258–6263, 2021.

[212] Mahrokh Ghoddousi Boroujeni, Elham Daneshman, Ludovic Righetti, and Majid Khadiv. A unified framework for walking and running of bipedal robots. In *2021 20th International Conference on Advanced Robotics (ICAR)*, pages 396–403. IEEE, 2021.

[213] Mario Selvaggio, Jonathan Cacace, Claudio Pacchierotti, Fabio Ruggiero, and Paolo Robuffo Giordano. A shared-control teleoperation architecture for nonprehensile object transportation. *IEEE Transactions on Robotics*, 38(1):569–583, 2021.

[214] Philippe Sardain and Guy Bessonnet. Forces acting on a biped robot. Center of pressure-zero moment point. *IEEE Transactions on Systems, Man, and Cybernetics-Part A: Systems and Humans*, 34(5):630–637, 2004.

[215] Hirohisa Hirukawa, Shizuko Hattori, Kensuke Harada, Shuuji Kajita, Kenji Kaneko, Fumio Kanehiro, Kiyoshi Fujiwara, and Mitsuharu Morisawa. A universal stability criterion of the foot contact of legged robots-adios zmp. In *Proceedings 2006 IEEE International Conference on Robotics and Automation, 2006. ICRA 2006.*, pages 1976–1983. IEEE, 2006.

[216] Stéphane Caron, Quang-Cuong Pham, and Yoshihiko Nakamura. Zmp support areas for multicontact mobility under frictional constraints. *IEEE Transactions on Robotics*, 33(1):67–80, 2016.

[217] John Hauser, Alessandro Saccon, and Ruggero Frezza. Achievable motorcycle trajectories. In *2004 43rd IEEE Conference on Decision and Control (CDC)(IEEE Cat. No. 04CH37601)*, volume 4, pages 3944–3949. IEEE, 2004.

[218] Xiaobin Xiong and Aaron Ames. 3-d underactuated bipedal walking via h-lip based gait synthesis and stepping stabilization. *IEEE Transactions on Robotics*, 2022.

[219] Marko Popovic, Andreas Hofmann, and Hugh Herr. Angular momentum regulation during human walking: biomechanics and control. In *IEEE International Conference on Robotics and Automation, 2004. Proceedings. ICRA'04. 2004*, volume 3, pages 2405–2411. IEEE, 2004.

[220] Steven A Gard, Steve C Miff, and Arthur D Kuo. Comparison of kinematic and kinetic methods for computing the vertical motion of the body center of mass during walking. *Human Movement Science*, 22(6):597–610, 2004. ISSN 0167-9457. doi: https://doi.org/10.1016/j.humov.2003.11.002.

[221] W.A Coppel. Dichotomies and reducibility. *Journal of Differential Equations*, 3 (4):500–521, 1967. ISSN 0022-0396. doi: https://doi.org/10.1016/0022-0396(67) 90014-9.

[222] Nahuel Alejandro Villa, Johannes Englsberger, and Pierre-Brice Wieber. Sensitivity of legged balance control to uncertainties and sampling period. *IEEE Robotics and Automation Letters*, 4(4):3665–3670, 2019.

[223] Diana Serra, Camille Brasseur, Alexander Sherikov, Dimitar Dimitrov, and Pierre-Brice Wieber. A newton method with always feasible iterates for nonlinear model predictive control of walking in a multi-contact situation. In *2016 IEEE-RAS 16th International Conference on Humanoid Robots (Humanoids)*, pages 932–937. IEEE, 2016.

[224] Filippo M Smaldone, Nicola Scianca, Valerio Modugno, Leonardo Lanari, and Giuseppe Oriolo. Zmp constraint restriction for robust gait generation in humanoids. In *2020 IEEE International Conference on Robotics and Automation (ICRA)*, pages 8739–8745. IEEE, 2020.

[225] Louis Hawley and Wael Suleiman. Control framework for cooperative object transportation by two humanoid robots. *Robotics and Autonomous Systems*, 115: 1–16, 2019.

[226] Juan José Alcaraz-Jiménez, D Herrero-Pérez, and H Martínez-Barberá. Robust feedback control of zmp-based gait for the humanoid robot nao. *The International Journal of Robotics Research*, 32(9-10):1074–1088, 2013.

[227] R Conti, F Giovacchini, L Saccares, N Vitiello, Jose L Pons, and D Torricelli. What do people expect from benchmarking of bipedal robots? preliminary results of the eurobench survey. In *International Symposium on Wearable Robotics*, pages 132–136. Springer, 2018.

[228] Luis Montejano. Some results about Minkowski addition and difference. *Mathematika*, 43(2):265–273, 1996.

[229] Shihua Li, Jun Yang, Wen-Hua Chen, and Xisong Chen. *Disturbance observer-based control: methods and applications*. CRC press, 2014.

[230] Baek-Kyu Cho, DongHyun Ahn, YoungBum Jun, and Paul Oh. A posture balance controller for a humanoid robot using state and disturbance-observer-based state feedback. *Journal of Intelligent & Robotic Systems*, 95(2):331–349, 2019.

[231] Xiaoxia Yang and Yi Huang. Capabilities of extended state observer for estimating uncertainties. In *2009 American control conference*, pages 3700–3705. IEEE, 2009.

[232] Wen-Hua Chen, Donald J Ballance, Peter J Gawthrop, and John O'Reilly. A nonlinear disturbance observer for robotic manipulators. *IEEE Transactions on industrial Electronics*, 47(4):932–938, 2000.

[233] Jeongseok Lee, Michael Grey, Sehoon Ha, Tobias Kunz, Sumit Jain, Yuting Ye, Siddhartha Srinivasa, Mike Stilman, and C. Liu. Dart: Dynamic animation and robotics toolkit. *The Journal of Open Source Software*, 3:500, 02 2018. doi: 10.21105/joss.00500.

[234] Jiatao Ding, Linyan Han, Ligang Ge, Yizhang Liu, and Jianxin Pang. Robust locomotion exploiting multiple balance strategies: An observer-based cascaded model predictive control approach. *IEEE/ASME Transactions on Mechatronics*, 2022.

[235] P Moylan. Stable inversion of linear systems. *IEEE Transactions on Automatic Control*, 22(1):74–78, 1977.

[236] Leonardo Lanari and J Wen. Feedforward calculation in tracking control of flexible robots. In *Proc. 30th IEEE Conf. Decision Control*, pages 1403–1408, 1991.

[237] S Devasia and B Paden. Exact output tracking for nonlinear time-varying systems. In *Proceedings of 1994 33rd IEEE Conference on Decision and Control*, volume 3, pages 2346–2355. IEEE, 1994.

[238] S. Devasia, Degang Chen, and B. Paden. Nonlinear inversion-based output tracking. *IEEE Transactions on Automatic Control*, 41(7):930–942, 1996. doi: 10.1109/9.508898.

[239] A. Isidori and C.I. Byrnes. Output regulation of nonlinear systems. *IEEE Transactions on Automatic Control*, 35(2):131–140, 1990. doi: 10.1109/9.45168.

[240] Santosh Devasia. Approximated stable inversion for nonlinear systems with nonhyperbolic internal dynamics. *IEEE Transactions on Automatic Control*, 44 (7):1419–1425, 1999.

[241] Roger A Mann and John Hagy. Biomechanics of walking, running, and sprinting. *The American journal of sports medicine*, 8(5):345–350, 1980.

[242] Mohammad Hasan Yeganegi, Majid Khadiv, Andrea Del Prete, S Ali A Moosavian, and Ludovic Righetti. Robust walking based on mpc with viability guarantees. *IEEE Transactions on Robotics*, 2021.

[243] Pierre-Brice Wieber. On the stability of walking systems. In *Proceedings of the international workshop on humanoid and human friendly robotics*, 2002.

[244] Arnaud Tanguy, Daniele De Simone, Andrew I. Comport, Giuseppe Oriolo, and Abderrahmane Kheddar. Closed-loop mpc with dense visual slam - stability through reactive stepping. In *2019 International Conference on Robotics and Automation (ICRA)*, pages 1397–1403, 2019. doi: 10.1109/ICRA.2019.8794006.

[245] Richard C.. Dorf and Robert H Bishop. *Modern control systems*. Pearson Prentice Hall, 2008.

[246] Alberto Isidori. *Sistemi di controllo*. Siderea, 1998.

[247] Gianluca Frison and Moritz Diehl. HPIPM: a high-performance quadratic programming framework for model predictive control. *arXiv preprint arXiv:2003.02547*, 2020.

[248] Hyobin Jeong, Joon-Ha Kim, Okkee Sim, and Jun-Ho Oh. Avoiding obstacles during push recovery using real-time vision feedback. In *2019 IEEE/RSJ Int. Conf. on Intelligent Robots and Systems*, pages 483–490, 2019.

[249] Songyan Xin, Chengxu Zhou, and Nikos Tsagarakis. New cross-step enabled configurations for humanoid robot. In *2018 IEEE-RAS 18th International Conference on Humanoid Robots (Humanoids)*, pages 1–9. IEEE, 2018.

[250] Changliu Liu, Chung-Yen Lin, and Masayoshi Tomizuka. The convex feasible set algorithm for real time optimization in motion planning. *SIAM Journal on Control and Optimization*, 56(4):2712–2733, 2018.

[251] Nicola Scianca, Paolo Ferrari, Daniele De Simone, Leonardo Lanari, and Giuseppe Oriolo. A behavior-based framework for safe deployment of humanoid robots. *Autonomous Robots*, 45(4):435–456, 2021.

[252] Ruben Grandia, Fabian Jenelten, Shaohui Yang, Farbod Farshidian, and Marco Hutter. Perceptive locomotion through nonlinear model predictive control. *arXiv preprint arXiv:2208.08373*, 2022.

[253] Philipp Seiwald, Shun-Cheng Wu, Felix Sygulla, Tobias FC Berninger, Nora-Sophie Staufenberg, Moritz F Sattler, Nicolas Neuburger, Daniel Rixen, and Federico Tombari. Lola v1. 1–an upgrade in hardware and software design for dynamic multi-contact locomotion. In *2020 IEEE-RAS 20th International Conference on Humanoid Robots (Humanoids)*, pages 9–16. IEEE, 2021.

[254] Stéphane Caron, Quang-Cuong Pham, and Yoshihiko Nakamura. Stability of surface contacts for humanoid robots: Closed-form formulae of the contact wrench cone for rectangular support areas. In *2015 IEEE International Conference on Robotics and Automation (ICRA)*, pages 5107–5112. IEEE, 2015.

[255] Brahayam Pontón, Stefan Schaal, and Ludovic Righetti. On the effects of measurement uncertainty in optimal control of contact interactions. In *Algorithmic foundations of robotics XII*, pages 784–799. Springer, 2020.

[256] Bilal Hammoud, Majid Khadiv, and Ludovic Righetti. Impedance optimization for uncertain contact interactions through risk sensitive optimal control. *IEEE Robotics and Automation Letters*, 6(3):4766–4773, 2021.